THE UNIVERSITY *of* EDINBURGH

New Cofacial Binuclear Complexes for the Oxygen Reduction Reaction and Selective Anion Binding

Aline M. J. Devoille

A Thesis Submitted for the Degree of

Doctor of Philosophy

At the

The University of Edinburgh

2011

Declaration

The work presented in this thesis is original work of the author, except where specific reference has been made to other sources. It was composed by the author and has not been submitted, in whole or in part, for any other degree.

Aline M. J. Devoille

May 2011

Abstract

This thesis describes the design, synthesis and reactivity of bimetallic complexes of doubly-pillared Schiff-base calixpyrrole ligands.

Chapter One introduces the oxygen reduction reaction in light of the global energy scenario at present and in the future. Compounds and materials known to catalyse this reaction are discussed, with particular focus on transition metal complexes of pyrrole-containing macrocycles and the ability of these compounds to act as catalysts in redox reactions.

Chapter Two describes the design and synthesis of several of the macrocyclic ligands developed during this project. The wide range of metals and geometries supported by one of the ligands, H_4L, are outlined and include complexes of alkali-metals (Li, K), a rare earth metal (Mg), transition metals (Pd, Fe) and an actinide (UO_2^{2+}).

Chapter Three presents the use of $[Co_2(L)]$ for the reduction of dioxygen to water. The redox behaviour of the complex and its ability to reversibly bind oxygen were evaluated. The catalytic activity of $[Co_2(L)]$ was investigated in solution by UV-Vis spectrophotometry and electrochemically by rotating ring-disk electrochemistry.

In Chapter Four, the ability of $[Zn_2(L)]$ to bind anions is described. Isothermal microcalorimetry, NMR, UV-Visible spectrophotometry, and fluorophotometry were used to study the de-aggregation of the anion free complex and the subsequent anion binding event. The stability of the complexes was estimated by DFT calculations.

Chapter Five outlines the synthesis of complexes of L for other transition metals relevant to small molecule activation.

Chapter Six contains a conclusion and suggestions on further investigations to carry out.

Chapter Seven presents the full experimental details and analytical data for this work.

Acknowledgements

I would like to thank my supervisor, Dr Jason B. Love, for his encouragement and guidance. I really appreciated that you always make yourself available to discuss the project and share your expertise, it has been of great help and I gained invaluable knowledge from it. Thank you also for arranging the collaboration with Prof Sessler in Austin, it has been a very beneficial experience for me and it helped me become a more independent in research.

My thanks also go to Prof Polly L. Arnold and all the past and present members of the Love and the Arnold groups. It has been a pleasure to work (and socialise) with all of you. You all make the lab a stimulating, fun and friendly place, which is a highly valuable support when chemistry goes its own way. A special thank has to go to Dr Jean-Charles Buffet for having been so enthusiastic to help and to share experimental and theoretical knowledge, Dr Manuel Volpe for getting me started with crystallography and Dr Stephen Mansell for reading and commenting on my thesis.

I am grateful to Prof Sessler for giving me the opportunity to stay at Austin for a month, to his group for the friendly welcome I received and to Nathan Bill for his help with the ITC experiments. I warmly thank Elisabeth Karnas for making my stay so enjoyable and giving me such a good taste of the Austin way of life: live country music, two-step dancing, base ball matches…

I would also like to acknowledge the help of Dr Patricia Richardson for DFT calculations and fluorescence spectroscopy, Mr Juraj Bella and Dr Marika Decremoux for NMR spectroscopy and every one else who assisted me in my work, especially with X-ray crystallography, mass spectroscopy, EPR, elemental analyses.

My thanks also go to my parents who always supported and encouraged me in my studies and through all my choices.

Thank you to all the friends I made in Edinburgh, I am so happy I met you and let’s face it, there is nothing like a good “raclette” with all of you!

Finally, to Nico, I would not have taken up this challenge without your enthusiasm about moving to the UK together; I would not have succeeded without your continuous support. For that and much more: thank you so much!

Abbreviations

BCA	Bis-Corrole Anthracene
BCB	Bis-Corrole Biphenyl
BCD	Bis-Corrole Dibenzofurane
BCO	Bis-Corrole Dibenzofurane
BCS	Bis-Corrole Dibenzothiophenyl
BCX	Bis-Corrole Xanthene
BCY	Generic Bis-Corrole
C*c*	Cytochrome *c*
CCDC	Cambridge Crystallographic Data Centre
C*c*O	Cytochrome *c* Oxydase
CE	Counter Electrode
CV	Cyclic Voltametry
ΔE	Energy of binding
DFT	Density Functional Theory
DME	Dimethoxyethane
DMF	Dimethylformamide
DMSO	Dimethyl Sulfoxide
DOSY	Difusion Ordered NMR spectroscopy
DPA	Diporphyrin Anthracene
DPB	Diporphyrin Biphenyl
DPD	Diporphyrin Dibenzofurane
DPDM	Methoxyaryl substituted Diporphyrin Dibenzofuran
DPO	Diporphyrin Dibenzofurane
DPOx	Diporphyrin Diphenylether
DPS	Diporphyrin Dibenzothiophenyl
DPX	Diporphyrin Xanthene
DPXM	Methoxyaryl substituted Diporphyrin Xanthene
DPY	Generic Pacman Diporphyrin
ε	Extinction coefficient

E'	$(E_p^a+E_p^c)/2$
E_0	Standard redox potential
$E_{1/2}$	Half-wave potential
EI-MS	Electron Impact Mass Spectroscopy
E_p^a	Anodic electrode potential
E_p^c	Cathodic electrode potential
EPG	Edge Plane Graphite
EPR	Electron Paramagnetic Resonance
esd	Estimated standard deviation
ESI-MS	Electrospray Ionisation
FAB-MS	Fast Atom Bombarding Mass Spectroscopy
Fc	Ferrocene
FTF	"Face-to-face"
HOMO	Highest Occupied Molecular Orbital
I	Nuclear spin
I_p^a	Anodic electrode current
I_p^c	Cathodic electrode current
ITC	Isothermal Microcalorimetry
K	Binding constant
λ	Wavelength
LUMO	Lowest Unoccupied Molecular Orbital
μ_{eff}	Effective magnetic moment
μ_s	Spin only magnetic moment
μ_{l+s}	Magnetic moment with orbital contribution
N”	*Bis*(trimethylsilyl)amide
NHE	Normal Hydrogen Electrode
NMR	Nuclear Magnetic Resonance
OEC	Oxygen Evolving Complex
OEP	2,3,7,8,12,13,17,18-Octaethyl-21H,23H-porphine
ORR	Oxygen Reduction Reaction
PCA	Porphyrin Corrole Anthracene
PCB	Porphyrin Corrole Biphenyl
PCD	Porphyrin Corrole Dibenzofurane

PCET	Proton Coupled Electron Transfer
PCO	Porphyrin Corrole Dibenzofurane
PCOx	Porphyrin Corrole Diphenylether
PCS	Porphyrin Corrole Dibenzothiophenyl
PCX	Porphyrin Corrole Xanthene
PCY	Generic Prophyrin Corrole
PEM-FC	Polymer Electrolyte Membrane Fuel Cell
ppm	Part per million
PS(II)	Photosystem (II)
py	Pyridine
RDE	Rotating Disk Electrode
RE	Reference Electrode
RRDE	Rotating Ring Disk Electrode
SCE	Saturated Calomel Electrode
TFA	Trifluoroacetic Acid
THF	Tetrahydrofuran
WE	Working Electrode

Table of contents

Chapter 1 – Introduction.

1.1 Energy: the challenge for tomorrow

Energy is probably the biggest global challenge of the 21st century. The energy demand is proportional to the planet's population and to economic growth, both of which are expected to increase significantly in the coming decades. The world population is expected to increase from about 6.1 billion in 2001 to about 9.4 billion by 2050 and it is estimated that the energy demand will have doubled by the middle of the century and tripled by 2100 (compared to 2001 and provided that technological advances meet the expected targets to save energy).[1] In the mean time, our current economy is based largely on fossil fuels which generate large amounts of green house gases such as carbon dioxide.[2] It is now widely acknowledged that the anthropologic CO_2 emitted since the industrial revolution is already causing important damage to the environment and that drastic action needs to be taken to limit the consequences. Most studies agree that global warming needs to be kept under 2 °C compared to pre-anthropologic levels to avoid its most serious effects and this target has been accepted by the European Council in March 2007.[3] After considering several energy scenarios, it was acknowledged that this should be achieved if the atmospheric CO_2 concentration is maintained lower than 400 ppm and meeting the target is very unlikely if it rises to 550 ppm or above.[1, 4] In addition, the CO_2 release needs to peak within this decade and consistently diminish from there. Achieving these goals appears very challenging as we still rely mostly on high carbon-footprint fuels. There is therefore an urgent need for the development of large scale, carbon free, renewable energy alternatives to meet the demand of tomorrow.[1] This matter is so important that out of ten leading chemists interviewed by Nature in January 2011, four clearly set renewable energies as the priority for the forthcoming decades.[5] Furthermore, addressing the energy problem is very likely to be the key not only to environmental security but also to economic and political security.[6]

Numerous alternative energy sources can be considered and amongst them solar and wind energy are seen to be the most promising, mainly because they are renewable and have a high energy potential.[2, 6, 7] For example, the sun shines more energy on Earth in one day than we currently use in a whole year.[6] Solar and wind energies are readily available but their low energetic density and their intermittent nature are probably their main drawbacks: energy conversion and storage technologies need to be developed to overcome this issue. As electricity and chemical bonds are two dense and convenient ways of storing energy, they appear as the most likely solutions.[7, 8] As a result, hydrogen is seen by many as a promising option for large scale energy storage.

1.2 Fuel cells

1.2.1 Hydrogen as an energy carrier

Hydrogen is the most abundant element in the universe but it does not occur naturally as a single element on Earth. Instead, it is combined with other elements such as oxygen, carbon or nitrogen. As a result, the use of dihydrogen as a fuel requires its extraction first, and therefore hydrogen is an energy carrier. This contrasts to fossil fuels, nuclear energy, solar energy or wind energy which are primary energies.[9] Historically, hydrogen was obtained from coal and was the main component of “town gas”; nowadays most of the dihydrogen is produced by the reforming of hydrocarbons.[2, 10] Alternatively, dihydrogen can be obtained from the water splitting reaction which presents several advantages, which include: the absence of polluting by-product (dioxygen is the only by-product)[10, 11] and the closed cycle constituted by the production and consumption of energy (the fuel is generated from water splitting and water is regenerated as hydrogen is combusted). This means that the natural oxygen-water balance is not affected and environmental issues are avoided. Furthermore, an energy vector relying on water would be politically-safer than fossil fuels as most countries rely on foreign oil at the moment.[10] Currently, the primary applications for hydrogen are mobile devices.[2, 9, 12] For hydrogen to be a viable fuel for the future, the whole process from its production to its final use needs to be environment friendly. Therefore, the advantages of the water splitting path are

clear but this process requires energy and the source of this has to be carefully considered. Solar and wind energy are more desirable than nuclear energy, for example. The materials used in manufacturing the electrolyser, energy collectors (photovoltaics, windmills, etc.) and fuel cells are also to be considered.[12-14] Most of these issues are beyond the scope of this thesis and the following discussion will focus on the fuel cells, in particular the reactions occurring at the cathodic electrode, which are most relevant to the research presented herein.

1.2.2 Polymer electrolyte membrane hydrogen fuel cell

A fuel cell is a device used to generate electricity by rearrangement of chemical bonds. One of the big advantages of a fuel cell is its efficiency. Indeed, the thermodynamic efficiency of burning hydrogen gas is 10 to 20% while the use of dihydrogen in a fuel cell can theoretically lead to 93% efficiency. Currently, efficiencies of around 30% can be achieved when the cell efficiency as well as the energy used to produce and compress the fuel are accounted for.[15] Among the different types of fuel cells available, the proton electrolyte membrane fuel cell (PEM-FC) is the most appropriate for mobile application such as transportation, computers or cell phones because it operates at fairly low temperatures (60 to 80 °C), has a high power density and does not require pre-heating time.[16] Furthermore, very thin components can be manufactured which allows the production of high power density within a small space.[12]

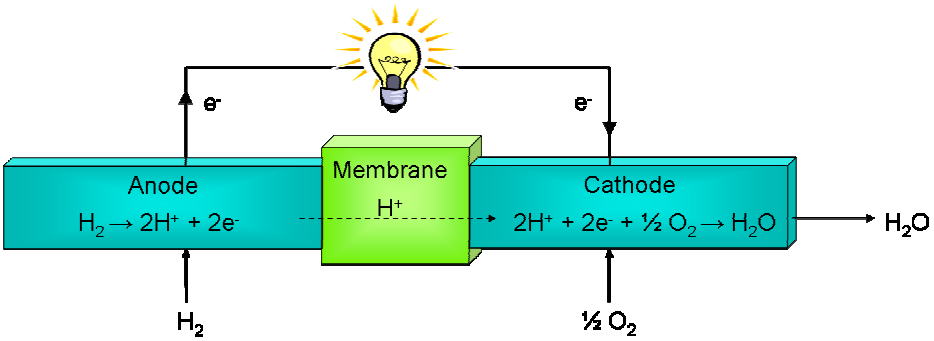

Figure 1.1: Representation of a hydrogen fuel cell.

A PEM-FC (**Figure 1.1**) consists of two electrodes, the anode and the cathode, separated by a membrane which, crucially, is permeable to protons but does not

conduct electrons.[16] At the anode, the fuel is oxidised to generate protons and electrons. The protons travel trough the membrane by osmosis to the cathode. The electrons are transported to the cathode through an external circuit generating a current. Oxygen is supplied at the cathode and its reduction using four electrons and four protons generates water. Chemically, the overall process can be summarised as follows for the hydrogen fuel cell:

$$H_2 \longrightarrow 2\,H^+ + 2\,e^- \qquad E_0 = 0\ V\ vs.\ RHE \qquad (1.1)$$

$$\tfrac{1}{2}O_2 + 2\,H^+ + 2\,e^- \longrightarrow H_2O \qquad E_0 = 1.23\ V\ vs.\ RHE \qquad (1.2)$$

$$H_2 + \tfrac{1}{2}O_2 \longrightarrow H_2O + \text{electrical power} + \text{heat} \qquad \Delta E_0 = 1.23\ V \qquad (1.3)$$

The use of a different fuel (such as methanol, methane or natural gas) or a mixture of fuel affects the anodic reaction only; as such, the following discussion focussing on the cathodic half-cell remains valid in the general case.

The half-reactions occurring at each of the two electrodes are multiple electron transfers and are coupled to multiple proton transfers, and as such they are called multiple Proton Coupled Electron Transfers (PCET). These reactions are not spontaneous and an efficient fuel cell requires efficient catalysts to manage the appropriate proton-electron inventory both at the anode and at the cathode. The low temperature of operation of a PEM-FC makes the role of the catalyst even more important.[17] The oxidation of hydrogen at the anode of a fuel cell is quite a facile reaction but the reduction of oxygen at the cathode is, in contrast, more difficult due to the large kinetic barrier,[18] as illustrated by the 1.23 V potential of the reaction. Also, O_2 needs to be fully reduced to water which involves the breaking of the strong O=O bound (498 $kJ.mol^{-1}$).[17] The following sections focus on the Oxygen Reduction Reaction (ORR) and materials that are capable of catalysing it.

1.2.3 The challenge of oxygen reduction for fuel cell technology

The use of fuel cells on a large scale still represents a technological challenge in terms of fuel production, storage and use.[14] For the PEM-FC, for example, the durability and production cost of the membrane remain limiting factors, and new catalysts need to be engineered for the manufacture of the appropriate electrodes. At the moment, both electrochemical half-reactions in fuel cells are catalysed by

platinum-based electrodes, which is an issue for a number of reasons. The first and most obvious drawback of platinum is its cost, at around 59000 $.kg^{-1}$ at the start of 2011[19] while non-noble alternatives could be much cheaper (for example, around the same date, Co: 40 $.kg^{-1}$,[20] Fe ore: 0.14 $.kg^{-1}$).[21] In addition to this, platinum is a very rare metal in the Earth's crust,[22] with an abundance of 0.005 ppm (Co: 25 ppm, Fe: 5630 ppm)[23] and this prevents its use on a large scale. Platinum ore is only present in a very limited number of areas around the globe, mainly in South Africa and Russia, and this raises geopolitical issues.[24] Finally, the performances of the precious metal as a catalyst are relatively limited when compared to the theoretically attainable value.[17]

The chemical properties of the metals affect its suitability for catalytic applications in fuel cells. Platinum-based electrodes require fairly high loadings of the metal, especially at the cathode where the kinetically slow oxygen reduction is carried out.[25] In addition, platinum is quite sensitive to contaminants[26] and to methanol, which is a major issue for direct methanol fuel cells. From the electrochemical point of view, the precious metal generates a cathodic onset around 0.9-1.0 V *vs.* NHE, which represents a 0.2-0.3V over-potential (E_0 = 1.23V for the four electron reduction of oxygen, **(1.2)**).[27] Finally, the reduction is not selective towards the four-electron process and some undesired, partially-reduced species are also produced.

1.2.4 Criteria for the evaluation of a catalyst

For a catalyst to have potential applications on a large scale for the reduction of oxygen, its production has to be easy, cheap and from readily available starting materials. The electrochemical and chemical stability of the catalyst under the operating conditions of the fuel cell is also critical for durability issues (*i.e.* high turn over numbers are required).[28] From an electrochemical point of view, the catalyst needs to yield large current densities (*i.e.* a high turn over frequency is required) and carry out the reaction at a low over-potential to ensure high efficiency. In practice, this means that the on-set potential needs to be as close as possible to the standard

reduction potential of oxygen to water to enable the cathodic over-potential η_c to be low. This is directly linked to the efficiency ς of the cell:[15]

$$\varsigma = 1 - \frac{\eta_a + \eta_c}{\Delta E^o} \qquad \textbf{(1.4)}$$

where η_a and η_c are the over-potentials at the anode and the cathode respectively, and ΔE_0 is the total cell potential (ΔE_0 = 1.23 V for the hydrogen fuel cell, **(1.3)**).

Finally, the catalyst needs to be highly selective towards the four-electron reduction of oxygen to produce water (**Figure 1.2**). The alternative two-electron process is more facile and produces hydrogen peroxide. This reactive species can decompose the catalyst and the electrolyte membrane, and the selectivity of the catalyst is very important for the durability of the fuel cell. In addition, a two-electron process also generates less power density than a four-electron process as the energy stored in the chemical bond is not efficiently utilised.

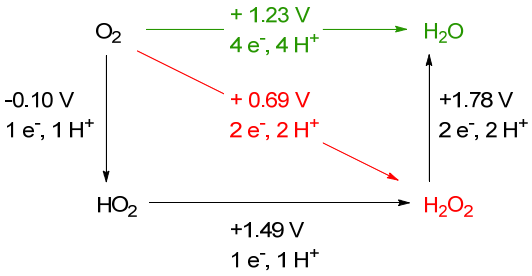

Figure 1.2: Standard reduction potentials of oxygen *vs.* NHE (E°) in acidic medium with the corresponding electron(s) and proton(s) balance.

1.3 Alternative to platinum catalysts

1.3.1 Overview of non-platinum catalysts developed to date

Even though platinum currently remains the best compromise as a cathode catalyst for fuel cells, it is fairly ill-suited to carry out this reaction according to the above criteria. As a result, the search for efficient, cheaper alternatives receives a lot of attention. Numerous materials show activity towards the reduction of oxygen and among the most widely studied are other precious metals, alloys of precious and non-precious metals, ruthenium-based catalysts, non-precious metal calcogenides,

nitrides, oxides, oxynitride, carbonitrides, enzymes, metal complexes, and metal-free catalysts such as carbon allotropes. Many of the above catalysts have also been studied whilst supported on a conducting material electrode (carbon or metal-based). This subject has been intensively reviewed in the past decade[15, 17, 29, 30] and for the scope of this thesis, only the progress on nitrogen-donor macrocycle-based catalysts will be detailed further.

1.3.2 Nitrogen-containing macrocyclic complexes

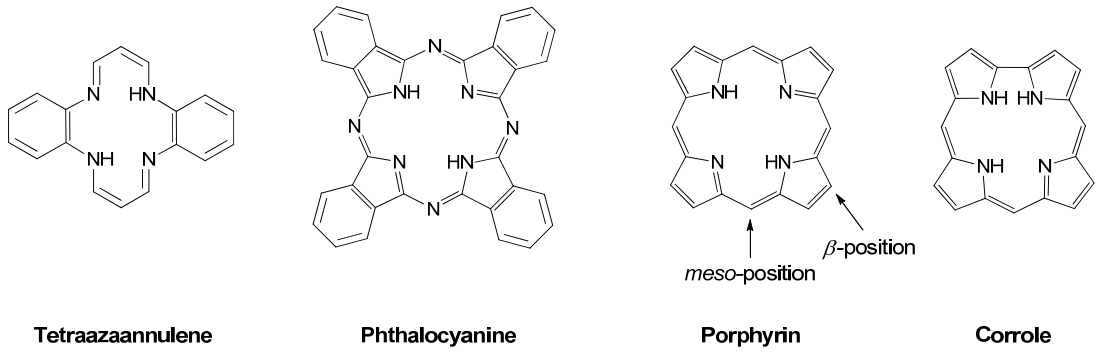

Figure 1.3: Nitrogen containing macrocycles supporting metal complexes with relevance to the catalysis of the oxygen reduction reaction

Nitrogen-containing macrocyclic complexes constitute a very promising class of ligands to generate ORR catalysts. Among their advantages are their low cost of production, their resistance to methanol and the promising catalytic activity of the complexes they support. However, and despite the intensive investigations carried out, most of these catalysts are still less stable and less active than platinum-based materials. Work on macrocyclic complexes was pioneered by Jasinski in the 1960s[31] and has received increasing attention ever since. Their use as ORR catalysts has also been widely reviewed recently[15, 17, 28, 29, 32] and only an overview of the main findings from this extensive work is given here. The most commonly-used macrocycles are tetraazaannulenes, phthalocyanines and porphyrins (**Figure 1.3**) bearing various substituents. Research has principally targeted iron and cobalt complexes because their $M^{(II)}/M^{(III)}$ standard potential (0.77 V and 1.92 V respectively)[33] is high enough to generate catalysts with the potential to work at low over-potential and yet the electron density on the metal remains large enough to activate oxygen. Manganese, iridium and rhodium-based macrocycles also exhibit catalytic activity but have been much less investigated due to limited activity or to cost of the metal.[34] As a general

rule, iron macrocycles tend to catalyse the four-electron reduction of oxygen to water while cobalt macrocycles often catalyse the two-electron reduction to produce hydrogen peroxide, which is less desirable. However, cobalt catalysts are more stable than their iron counter-parts, which is important for a durable catalyst. In order to increase the activity and the stability of the complexes, heat treatments are often carried out on supported catalysts. A compromise usually has to be made in that lower temperatures usually afford the most active catalysts but higher temperatures generate the most stable materials, with the optimal values lying around 600-800 ºC in most cases. A large number of other parameters also affect the catalyst activity, like the catalyst support (often carbon), the deposition method, and the gas under which the catalyst is heat treated. Two main breakthroughs in catalyst development were made in the past five years and deserve particular attention. In 2006, Bashyam and Zelenay described a cobalt-polypyrrole-carbon catalyst showing considerable activity without requiring any heat treatment.[35] This was the first non-noble metal catalyst showing activity and durability comparable to carbon supported platinum (Pt/C) without heat treatment and at low loading. In 2009, Dodelet also published a non-noble metal catalyst with properties comparable to (Pt/C).[36] This catalyst is based on the accommodation of iron cations on the surface of graphite sheets by coordination to pyridinic nitrogen atoms. After two heat treatments, the catalyst was less stable than the one of Bashyam and Zelenay but much higher current densities were produced from the start of testing and throughout the 100-hour period over which the experiment was carried out.

While major breakthroughs have been recently made towards achieving readily available, cheap ORR catalysts, little is known to date about the mechanism of this reaction. It is usually acknowledged that the active site probably contains a metal centre as well as carbon and nitrogen atoms as $MN_xC_y^+$ ions have been observed by time-of-flight secondary ion mass spec (ToF SIMS)[37] but little is known about the key features of an efficient catalyst. A better understanding of the catalytic cycle can be gained by generating catalytic intermediates or carrying out the reaction in solution phase as more characterisation techniques are available. Coordination

complexes have been developed to serve as model compounds and catalysts with this aim in mind.

1.4 Catalyst design

1.4.1 *Cytochrome c oxidase*

The biological energy production process, "Nature's fuel cell", is respiration, during which foodstuffs are oxidised to carbon dioxide while oxygen is reduced to water. This generates a proton gradient which leads to the biosynthesis of adenosine triphosphate (ATP), the energy carrier in the body. The energy is then released when ATP is metabolised within the cell. As in a fuel cell, the different reactions need to be catalysed, in particular the reduction of oxygen to water which is thermodynamically favourable but kinetically slow. In the body, the "oxygen electrode" role is played by an enzyme: Cytochrome *c* Oxydase (C*c*O). A high resolution X-ray structure of C*c*O afforded a precise knowledge of the structure of the active site (**Figure 1.4**, (a)).[38, 39] It consists of a heme (heme a_3) in which the iron is penta-coordinate, with a histidine (His^{376}) residue occupying the proximal binding site and a vacant binding site on the distal side of the heme. A copper atom (Cu_B) is located about 4.7 Å from the iron centre on the distal face and is bound to three histidine ligands. The final key feature in the active site is a tyrosine (Tyr^{244}) bound directly to one of the histidine ligands of the copper, with the phenolic proton of this tyrosine located 5.6 Å away from the iron atom. In the reduced form, the metals are in their lowest oxidation state, Fe(II) and Cu(I), and the tyrosine is protonated. Upon O_2 binding, the heme a_3 is oxidized to Fe(III) as the first electron is transferred to the oxygen to generate an end-on bound iron superoxide ligand on the distal face. The transfer of a proton from Tyr^{244} is accompanied by three more electron transfers: one from the oxidation of the tyrosine, yielding a tyrosine radical, one from the oxidation of Cu_B and one from the oxidation of a_3. This process results in oxygen bond cleavage and the formation of a ferryl oxide heme Fe(IV)=O and a cupric hydroxide Cu(II)-OH. Other parts of the enzyme ensure the delivery of protons and electrons to the active site, and a succession of proton and electron transfers liberates two molecules of water and regenerates the initial Fe(II), Cu(I) and reduced tyrosine moieties.[40]

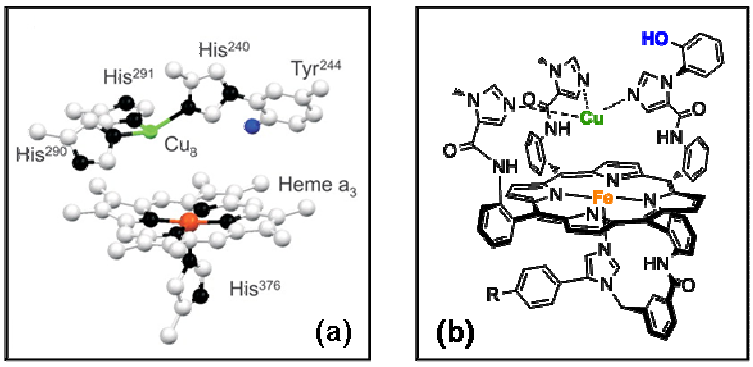

Figure 1.4: (a) active site of C*c*O from the bovine heart, from **[41]**, reprinted with permission from AAAS, and **(b)** structural and functional model reproducing its key elements. R= H, CF_3, C≡CH

In summary, the four-electron reduction of oxygen to water by C*c*O happens within a very well defined active site within which the four electrons which are required for this process are stored in two metal centres and organic residues. The reaction requires the concerted action of pre-organised elements: a heme, a copper centre and a redox active tyrosine.

1.4.2 ORR catalyst models: designs inspired by enzymes

Model complexes that mimic C*c*O have been engineered for two main purposes. First, structural and functional analogues help understand the C*c*O reaction mechanism by reproducing the key features of the enzyme. Second, the full reduction of oxygen is interesting for renewable energies and the use of fuel cells as explained earlier (see section 1.2).

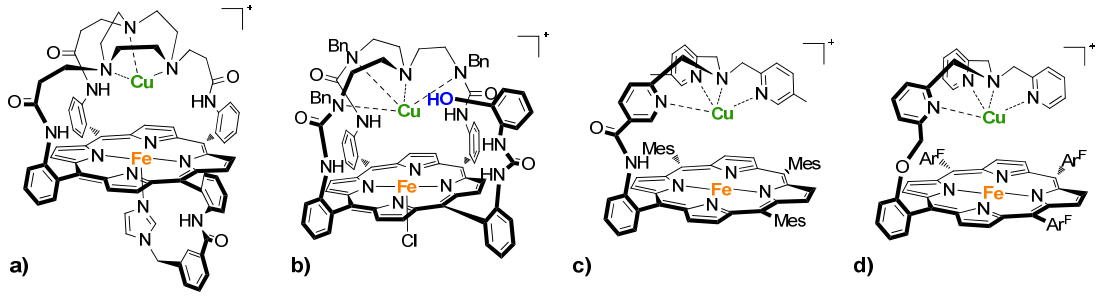

Figure 1.5: Examples of synthetic CcO analogues developed by a) the Collman group[42] (early model, a more recent example is presented on **Figure 1.4**), b) the Boitrel group,[43] c) the Naruta group[44] and d) the Karlin group.[45]

Intensive work has been carried out to synthesise chemical complexes that model the active site of C*c*O. Historically, the models were based on the fully oxidised Cu(II) Fe(III) resting state and the initial synthesis of a copper-iron complex which is active towards oxygen was carried out by the Gunter and Murray groups in the 1980s.[46] Most of the following work on the subject was carried out by the Collman, Karlin, Naruta and Boitrel groups, and slightly different models were developed which all evolved similarly with successive addition of crucial features (**Figure 1.5**).[41-45, 47]

The intense study of C*c*O and its synthetic structural and functional models helped in understanding the structural prerequisites for a catalyst to be active towards the reduction of oxygen; in particular the features favouring the four-electron reduction to water over the two-electron reduction to hydrogen peroxide were identified. The creation of a well defined molecular cavity was meticulously addressed and the activity of the resulting compounds toward oxygen reduction was studied. Most of this work has been based on systems comprising the combined action of two cofacially held metallo-porphyrins and complexes analogous to these bearing corrole macrocycles and/or acid/base groups.

1.5 Control of the second coordination sphere: porphyrin-based catalysts

Due to the bimetallic character of C*c*O, it was suggested that cooperativity between two metal centres could be a feature which promotes the four-electron reduction of oxygen. It was reasoned that a reaction carried out within the intermetallic space, in a well defined environment, should avoid the unproductive one- and two-electron pathways. A predefined inter-metallic distance, suitable for small molecules only, should also prevent the undesired binding of bigger competitive ligands. The pK_a of the activated molecule also plays an important role in a PCET reaction and the coordination of the substrate to a second metal centre should allow for adjustment of this parameter. Finally, and most importantly, the metal centres can act as very practical electron reservoirs: they can quickly deliver electrons to the substrate when required due to their facile oxidation and be later reduced to regenerate the catalyst.

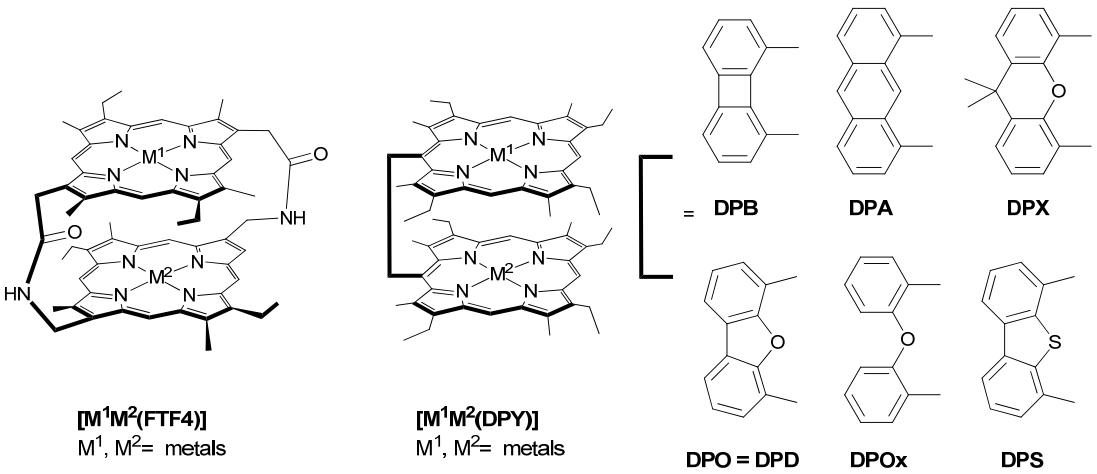

Figure 1.6: [M_2(FTF4)], an example of a binuclear complex of a "face-to-face" strapped diporphyrin (left, the number corresponds to length of the strap, here: a four-atom strap separates the two porphyrins) and binuclear Pacman cofacial diporphyrins with the most common linkers (right, the third letter refers to the backbone: DPY is a generic Pacman diporphyrin, DPA is diporphyrin anthracene, DPB is diporphyrin bibenzene, DPO = DPD is diporphyrin dibenzofurane, DPOx is diporphyrin diphenylether and DPS is diporphyrin dibenzothiophenyl).

1.5.1 *Initial work, "face-to-face" porphyrin catalysts*

Single cobalt porphyrins have been shown to catalyse principally the two-electron reduction of oxygen and their limited activity towards the four-electron reduction was attributed to self-assembly of dimers on the electrode surface.[48] As a result, macromolecules with two porphyrins held in a cofacial arrangement on top of one another were developed. Work in the field of covalently-linked porphyrins was initiated by Schwartz and co-workers[49] in order to study energy transfer between chromophores in the early 1970s and the first cofacial diporphyrins appeared in 1977 in publications by Collman,[50] Ogishi,[51] Chang,[52] Kagan[53] and their co-workers. (Sanders[54] and others[55] also developed similar system but the focus will be kept here on catalysts active toward oxygen activation). In this first class of dimeric ligands, two porphyrins were strapped together by two to four covalent links between either the *meso*- or the β-positions of the porphyrins. Their binuclear metal complexes showed overall poor selectivity for the four-electron reduction of oxygen. Only [Co_2(FTF4)] (FTF = "face-to-face", 4 = number of atoms in the main chain of the strap, **Figure 1.6**, left) was found to catalyse the four-electron reaction,[56] highlighting the importance of the relative position of the porphyrin units and of the intermetallic distance. Most strapped porphyrins adopt a split conformation and are

separated by ca. 3.5 Å to maximize π-π interaction between the two macrocyclic units which (1) prevents the metals from laying "on-top" of one another and (2) separates the two metals (for example, in [Cu_2(FTF6)] Cu···Cu = 6.33 Å). The shorter spacer of FTF4 constrains the porphyrins in a non-slipped conformation with closer metal centres sitting above one another (for example, in [Co_2(FTF4)] Co···Co = 3.42 Å, **Table 1.1**). The catalytic activity is measured in most of the examples cited here (and unless otherwise stated) by rotating disk electrode (RDE) or rotating ring-disk electrode (RRDE) experiments with the catalyst absorbed on a carbon electrode, often edge-plain graphite (EPG). For [Co_2(FTF4)], the half wave potential was observed at a remarkably high potential of $E_{1/2}$ = 0.72 V *vs.* NHE but the production of water occurs only at potentials higher than 0.55 V, when the catalyst is singly oxidised; below this threshold H_2O_2 is produced.[56-58] It was therefore suggested that, in contrast to initial beliefs, the second metal centre does not act as a redox site but as a Lewis acid to stabilise the partially reduced oxygen intermediate. This hypothesis was further supported by the activity observed for related complexes. [Co(H_2FTF4)], which presents only one cobalt centre and [AlCo(FTF4)], which bears a redox-inactive Lewis acidic centre, both present a mixed mechanism where both water and hydrogen peroxide are electrocatalytically produced whereas [CuCo(FTF4)], which bears a redox-inactive metal with no affinity for axial ligands, catalyses the reduction to hydrogen peroxide only.[59]

1.5.2 *Pacman porphyrin catalysts*

1.5.2.1 Pacman porphyrin catalysts: structural aspects

Initial understanding of the ORR gained from the first generation, "face-to-face" porphyrins triggered the design of a second generation of catalysts; the Pacman porphyrins in which the two macrocycles are hold by a single aromatic linker (**Figure 1.6**, right, in the rest of the document, the term "cofacial diporphyrin" will refer to these single pillared designs). This new feature constrains the two units to remain superimposed and limits the lateral twist. As a result, the two metal centres are vertically aligned and the distance between them can be adjusted by variation of the size of the spacer. Furthermore, the single linker introduces more vertical

flexibility and the two porphyrins can deviate from co-planarity by clamping down or springing open; these molecules are able to "chew on a substrate" in a motion called the "Pacman effect".[60, 61] This distortion is desirable to accommodate the different intermediates during the catalytic cycle.

This work was pioneered in the early 1980s by Collman and Chang with the introduction of anthracene (DPA)[62, 63] and biphenyl (DPB)[62, 64, 65] *meso*-linked cofacial diporphyrins and their mono- and binuclear complexes (**Figure 1.6**), with a later contribution on heterobimetallic catalysts by Guilard.[58, 66] In 2000, Nocera developed two analogues bearing a xanthene (DPX)[67] and a dibenzofuran (DPD = DPO)[60] spacer in order to access a wider range of cavity sizes. Optimised synthetic routes were also developed[68] to afford the ligands in about 15 steps and 3% overall yield. Ligands with other variations of the spacer (dibenzothiophenyl, DPS,[69] and diphenylether, DPOx[70]) have also been synthesised and were mainly used for purposes other than the catalytic reduction of oxygen. DPY is a generic notation referring to any cofacial diporphyrin, *i.e.* Y = A, B, D or X.

Complexes of H_4DPA and H_4DPB were investigated concomitantly.[61] For reasons previously cited, the investigation focused on iron and cobalt complexes. The presence of an iron centre in [Fe(H_2DPA)] initially promotes two-electron reduction to H_2O_2, and further reduction of H_2O_2 to H_2O follows in a second step.[71] With [Fe_2(DPA)], the second iron centre facilitates the one-step four-electron reduction of oxygen.[71] However, with ligands other than DPA, the bimetallic iron complexes irreversibly form an oxo-bridge between the two metals which makes them unsuited for the four electron reduction of oxygen. Instead, [Fe_2(μ-O)(DPX)] and [Fe_2(μ-O)(DPD)] were found to be active catalysts for oxygen atom transfer reactions.[72] Intensive studies have also been carried out on the catalase-like activity (reduction of hydrogen peroxide to water) and oxygen atom transfer activity of monometallic complexes bearing a metalloporphyrin with an acid/base group "hanging" above it - these are called "Hangman" systems.[58, 68, 73] The mixed metal complex [FeCo(DPA)] also catalyses the reduction of oxygen but this was found to proceed via complicated pathways consistent with a Co(II)-based redox-active site at

lower potentials, followed by a mixed two- and four-electron reaction catalysed by the Fe(III)-based redox-active site at higher potential, with the four-electron pathway largely dominant.[71] Despite the higher potential at which the reduction of oxygen was observed with the heterobimetallic complex compared to iron-free analogues, iron was discarded from the study which focused on cobalt-containing complexes in the hope of gaining a better insight into the mechanism of the ORR. A methodology similar to the one previously used for "face-to-face" porphyrins was applied and the activity of [Co_2(DPY)] (Y = A, B)[64] was compared to results obtained with [Co(H_2DPA)] where one of the cobalt atoms is missing,[74] with [CoM^2(DPY)] (M^2 = AlOR, TiO, GaOAc, GaOH, InCl, LuAcac, ScOH; Y = A, B) where the second metal is a redox-inactive Lewis acid[58, 66] and [CoCu(DPY)] where the second metal is redox-inactive and has no affinity for axial ligands.[71] The overall behaviour of the Pacman complexes is in good agreement with the rational established for the "face-to-face" complexes. In contrast to isolated cobalt porphyrins, Pacman complexes containing at least one cobalt centre catalyse (at least partially) the 4-electron reduction of oxygen provided that they are associated with an appropriate Lewis or Brønsted acidic centre (M^2 = H_2, LuAcac, ScOH). In contrast with the FTF4 analogues, [Co(AlOR)(DPY)] complexes do not promote the desired mechanism, and neither do the other complexes bearing a cobalt centre and a group 13 metal due to their poorer Lewis acid character compared to lutetium and scandium. [CoCu(DPY)] also catalyses the two-electron reduction only. In comparison to their DPB analogues, DPA complexes generated a larger amount of water and the best selectivity was achieved by [Co_2(DPA)] in which the larger intermetallic distance (4.53 Å)[75] is better suited to accommodate the catalytic intermediates. One cobalt atom is initially in the +2 oxidation state and acts as the redox-active centre, whereas the second centre, at potentials where it is in the +3 oxidation state, acts as a Lewis acid platform and stabilises the partially reduced oxygen species.

The crucial role of the intermetallic distance was addressed by Nocera with the development of [Co_2(DPX)] and [Co_2(DPD)] (**Figure 1.6**) for which the ligand synthesis is more straightforward and the intermetallic distance is 4.53 and 8.62 Å.[76]

Interestingly, both compounds catalyse the four-electron reduction almost exclusively, as measured by RRDE (**Table 1.1**), regardless of the large difference in intermetallic distance. This is due to the exceptionally large vertical flexibility of the DPD derived complexes, as illustrated in the solid state structures of $[Zn_2(DPD)]$ (Zn···Zn = 7.78 Å) and $[Fe_2(\mu\text{-}O)(DPD)]$ (Fe···Fe = 3.50 Å) which provide a direct observation of the Pacman effect.[60] The "clamping" ability of DPD enables the accommodation of varied intermediates.

	M···M (Å)	**CV** (V *vs.* NHE)	**RRDE** $E_{1/2}$ (V *vs.* NHE)	**RRDE** % H_2O	**UV-vis** %H_2O[a]
$[Co_2(FTF4)]$[61]	3.42	+0.86 / +0.51	+0.71	97	-
$[Co_2(DPA)]$[61]	4.53	+0.87 / +0.57	+0.67	94	80
$[Co_2(DPB)]$[61]	3.73	+0.88 / +0.54	+0.7	94	80
$[Co_2(DPX)]$[68, 77]	4.53	+0.17 +0.26[b]	+0.38[b]	72	99
$[Co_2(DPD)]$[68, 77]	8.62[c]	+0.33[b]	+0.37[b]	80	70
$[Co_2(DPXM)]$[77]	5.91	+0.14 / +0.33[b]	+0.24[b]	52	54
$[Co_2(DPDM)]$[77]	-	+0.33[b]	+0.25[b]	46	58

Table 1.1: Characteristic data of some binuclear cobalt diporphyrins. [a] in benzonitrile, $[O_2]$ = 1.7 mM, [Fc] = 0.1 M , $[HClO_4]$ = 0.02 M and [catalyst] = 0.02 mM, [b] *vs.* Ag/AgCl ($E_{Ag/AgCl}$ ~ +0.197 V *vs.* NHE), [c] 2 MeOH solvent molecules accommodated within the cleft.

Methoxyaryl substituents were introduced at the porphyrin *meso*-position opposite the linker in an attempt to tune the size of the molecular cavity further and the resulting complexes, $[Co_2(DPXM)]$ and $[Co_2(DPDM)]$, show significantly reduced selectivity for the four-electron reduction mechanism.[78] A DFT study suggested, however, that subtle electronic effects were responsible for this change, not steric effects. The electron density of the HOMO in $[Co_2(O_2)DPX)]^+$ has mainly π* Co-O and π* O-O character whilst the HOMO in $[Co_2(O_2)(DPXM)]^+$ is mainly located on the porphyrin rings, making the oxygen species less reactive towards protonation. This was attributed to distortion of the porphyrins (induced by the clash between the sterically demanding substituents) which are believed to prevent the transfer of the electron density from the porphyrin to the cobalt and therefore the following cobalt to oxygen electron transfer. This hypothesis of electronic effects prevailing over steric effect is also supported by the solid state structures of $[Zn_2(DPXM)]$ (Zn···Zn = 5.91 Å) and $[Fe_2(\mu\text{-}O)(DPXM)]$ (Fe···Fe = 3.49 Å) which confirm that even though the unbridged complexes exhibit large intermetallic separations compared to the ones

supported by DPX, the steric hindrance generated by the methoxyaryl groups does not prevent the "clamping" effect and the size of the cavity is not greatly affected.

1.5.2.2 Pacman porphyrin catalysts: mechanistic aspects

As mentioned earlier, the potential at which the ORR is catalysed is also a vital parameter to take into account when evaluating the activity of a catalyst; the closer to 1.23 V *vs.* NHE, the standard reduction potential of O_2 to water, the better. For the Pacman complexes [Co_2(DPY)] (Y = A, B, D, X) this potential is close to 0.6 V which is quite remarkable for non-noble metal catalysts but relatively poor in comparison to the 1.23 V goal or the *ca.* 0.9 V potential of platinum-based catalysts. Nevertheless these compounds are very good models to investigate the mechanistic aspects of the process.

Initially, their catalytic properties were investigated with the complex deposited on a carbon-based electrode and, even though the overall structure is believed to remain unchanged under these conditions, only limited information can be obtained from deposited catalysts. Complexes of cofacial diporphyrins were therefore studied in solution to gain further insight into the mechanism of the oxygen reduction reaction. Two main breakthrough investigations have been carried out: (1) the detailed electrochemistry and spectro-electrochemistry of [Co_2(DPA)], [Co_2(DPB)] and some "face-to-face" diporphyrin complexes were studied by Le Mest, both under nitrogen[79] and oxygen atmospheres,[80] to describe precisely the different intermediates of the reaction and (2) a spectroscopic method was developed by Fukuzumi and Guilard[81] to monitor the homogeneous catalytic reaction, four [Co_2(DPY)] complexes (Y = A, B, D, X) were studied and compared to their single porphyrin relative, Co(OEP), which catalyses the two-electron reduction only. The combination of these studies provides a good insight into the mechanism of the oxygen reduction reaction, which is very informative for the design of new, efficient catalysts.

Electrochemical study

The study by Le Mest revealed that, under a nitrogen atmosphere, the initial oxidation of cofacial diporphyrins occurs at the porphyrin ring in either a one-step two-electron process (for [Co_2(DPA)]) or in a two-step process, each step accounting for one electron, (for [Co_2(DPB)]).[79] Both metals therefore remain Co(II) at this stage and are oxidised at higher potentials. The reactivity of [Co_2(DPY)] (Y = A, B) in its different electro-chemically generated oxidation states was also studied under an oxygen atmosphere. While non-oxidised Co(II) cofacial diporphyrin do not react with oxygen, both one-electron oxidised and two-electron oxidised species reversibly bind oxygen to form a μ-superoxo (O_2^-) and a μ-peroxo (O_2^{2-}) intermediate respectively.[80] The peroxo and superoxo species were found to interconvert reversibly in a one-electron redox process. Upon addition of acid only the superoxo intermediate is protonated, suggesting that it is the key intermediate in the four-electron reduction of oxygen. This hypothesis is in agreement with the often proposed mechanism for the biological model in which an initial one-electron reduction of the O_2-complex is followed by protonation before the O-O bond cleavage occurs.[39, 82] Comparison of the EPR spectra of the product of oxygenation of [Co_2(FTF6)] (selective for the two-electron reduction) and of [Co_2(DPA)] (selective for the four-electron reduction) also supports the importance of the superoxo-intermediate: with the FTF6 supported complex, O_2 binds to one cobalt atom only and the protonation product is EPR silent (which is consistent with a peroxo-intermediate) whilst the DPA-based complex binds O_2 in a bridging fashion and EPR spectroscopy shows the protonation product to be consistent with a π-radical. This highlights once again the importance of the participation of the two metal centres in the binding and points towards the following relationship:

superoxo intermediate ↔ water production

peroxo intermediate ↔ hydrogen peroxide production

The study also establishes that complex π-ring ↔ cobalt ↔ oxygen intramolecular electron transfers are involved in the initial O_2 binding and protonation processes.

Work by Nocera also backs up the mechanism proposed by Le Mest. The DFT study previously mentioned[77] carried out on the superoxo-intermediates $[Co_2(\mu\text{-}O_2)(DPX)]^+$ and $[Co_2(\mu\text{-}O_2)(DPXM)]^+$ concluded that the HOMO of the DPX derivative has a much stronger cobalt-oxygen character and the negative charge on the oxygen moiety is larger than in the DPXM analogue. As $[Co_2(DPX)]$ is selective for the 4-electron reduction whereas $[Co_2(DPXM)]$ catalyses the reduction of oxygen through a mixed two- and four-electron mechanism, this suggests that a basic superoxo intermediate favours the four-electron pathway. This hypothesis is supported by homogenous catalysis experiments using various acids in which the pKa of the conjugate acid of $[Co_2(\mu\text{-}O_2)(DPX)]^+$ was estimated to be ~12.5.[68] Based on these results, Nocera suggested that a basic enough superoxo intermediate will be protonated and lead to O-O bond cleavage which results in the production of water. In contrast, a less basic superoxo intermediate will preferentially be reduced to peroxo and will result in the production of hydrogen peroxide (**Figure 1.7**). The differentiation between the two mechanisms would therefore depend on which step is quicker between electron transfer and proton transfer to the superoxo-species. This mechanism is in good agreement with the one proposed by Le Mest seven years earlier, and it also accounts for the proper three electron, one proton stoichiometry needed for bond cleavage as observed in C*c*o and for the strictly Lewis acid role of the second cobalt centre which remains Co(III) in the whole cycle.

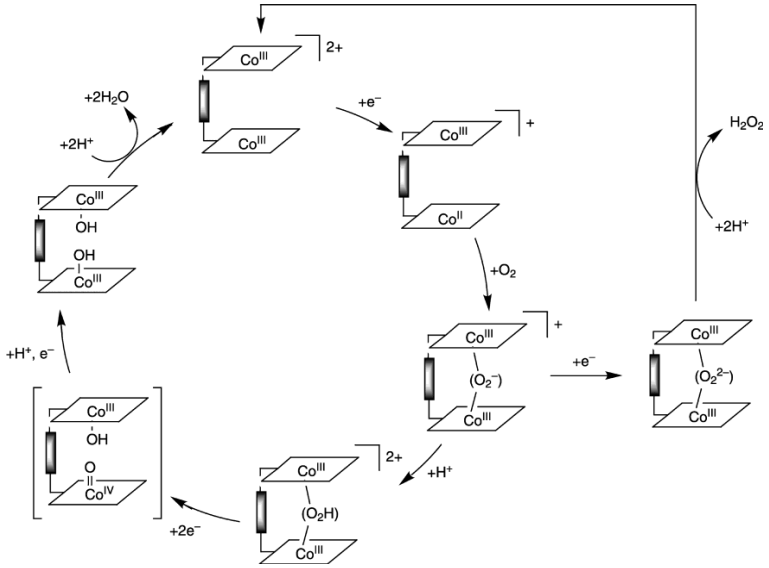

Figure 1.7: Catalytic cycles for the reduction of oxygen by a binuclear cobalt diporphyrin as proposed by Nocera and co-workers. Reprinted with permission from **[77]**. Copyright 2004 American Chemical Society.

Homogeneous catalysis, a spectroscopic study

A new method to study the homogeneous catalytic activity of cofacial diporphyrins was developed by Fukuzumi and Guilard.[81, 83] Ferrocene derivatives were used to mimic Cytochrome *c*, the one-electron donor which delivers electrons to C*c*O, and the colour change which occurs upon oxidation of these derivatives was monitored by UV-visible spectroscopy. Alteration of the concentration of the different components of the reaction (oxygen, acid, electron donor, catalyst) allows the analysis of the kinetics of the reaction.

From an early stage, the intermetallic distance in cofacial diporphyrin complexes has been seen as a crucial parameter in catalysis. Amongst [Co_2(DPY)] complexes (Y = A, B, D, X), [Co_2(DPX)] is the only one to be fully selective for the four-electron pathway under homogeneous conditions (**Table 1.1**). This is in contrast with the heterogeneous measurements for which [Co_2(DPA)] and [Co_2(DPD)] exhibited very high selectivity as well. It was reasoned that the DPB and DPD spacers have too small and too large intermetallic distances respectively. The higher selectivity of [Co_2(DPX)] compared to [Co_2(DPA)] was attributed to a higher flexibility conferred by the DPX linker, as observed in the solid state for the binuclear cobalt complexes.[61, 77] These results also suggest that the structure of the catalyst is, to some extent, different in solution and when adsorbed on a carbon electrode.

The kinetic study carried out using the single porphyrin [Co(OEP)], which is selective for the two electron process, showed that the turn-over determining step (t.d.s.) was the electron transfer from the ferrocene derivative to the Co(III) centre to regenerate the Co(II) catalyst. In contrast, the t.d.s in the reaction catalysed by [Co_2(DPX)] was either the initial oxygen binding/PCET step (with [$Fe(C_5H_5)_2$] or [$Fe(C_5H_4Me)_2$] as the electron donor) or the O-O bond cleavage (with the more reducing electron donor [$Fe(C_5Me_5)_2$], **Figure 1.8**). This highlights the importance of the O-O bond cleavage step and the authors proposed a slightly different mechanism (**Figure 1.8**) to those proposed by Le Mest and Nocera. In this second mechanism, the initial superoxo is first reduced to a peroxo intermediate and the differentiation

between the two- and four-electron mechanisms depends on which step is quicker between the protonation of the peroxo and the O-O bond cleavage. In this mechanism, only two electrons are transferred to the oxygen before the O-O bond is cleaved (against one proton and three electrons in the other proposed mechanism) and both of the two metal centres are redox-active.

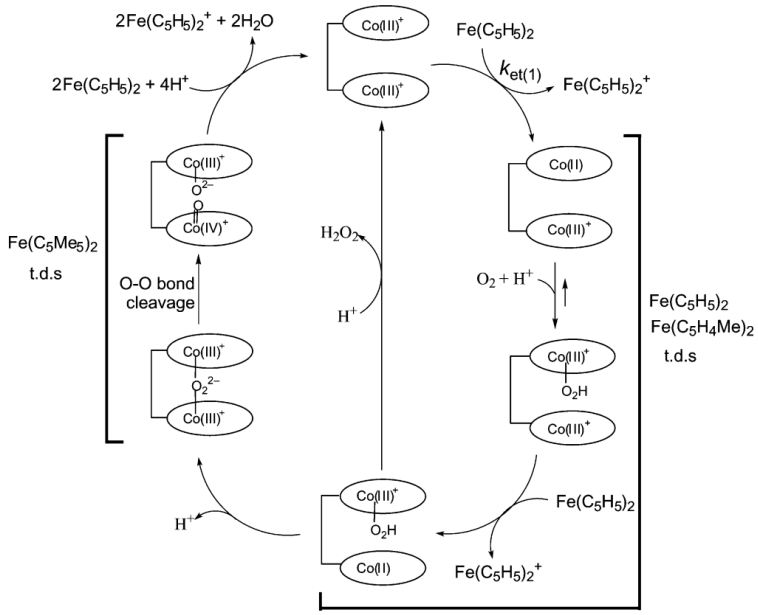

Figure 1.8: Catalytic cycle for the reduction of oxygen by a binuclear cobalt diporphyrin as proposed by Guilard, Fukuzumi and co-workers. Reprinted with permission from **[81]**. Copyright 2004 American Chemical Society.

Neither of the two mechanisms proposed have been fully proved or disproved to date and the exact stage of differentiation between the two-electron and the four-electron mechanism remains uncertain. However, both mechanisms agree on a number of points: (1) a mixed valence Co(II)/Co(III) complex is required for the initial oxygen binding and the formation of a superoxo intermediate, (2) the stability of the partially-reduced oxygen intermediate(s) is a crucial factor for the selectivity, (3) the liberation of hydrogen peroxide arises from the early protonation of a peroxo or hydroperoxo intermediate, (4) the O-O bond cleavage results in a high oxidation state Co(IV) oxo intermediate, and (5) the second cobalt atom stabilises the partially reduced oxygen complex and adjusts the pK_a of the intermediates.

1.5.3 Cofacial porphyrin-corrole and biscorrole catalysts

The knowledge gained on cofacial diporphyrins led to the introduction of variations of the ligand core. One or two of the porphyrin macrocycles were replaced by a corrole, whilst keeping the Pacman arrangement and the backbones used for cofacial diporphyrins (**Figure 1.9**). The work on porphyrin-corroles and bis-corroles was carried out as a collaboration between the Kadish group and the Guilard group.[84]

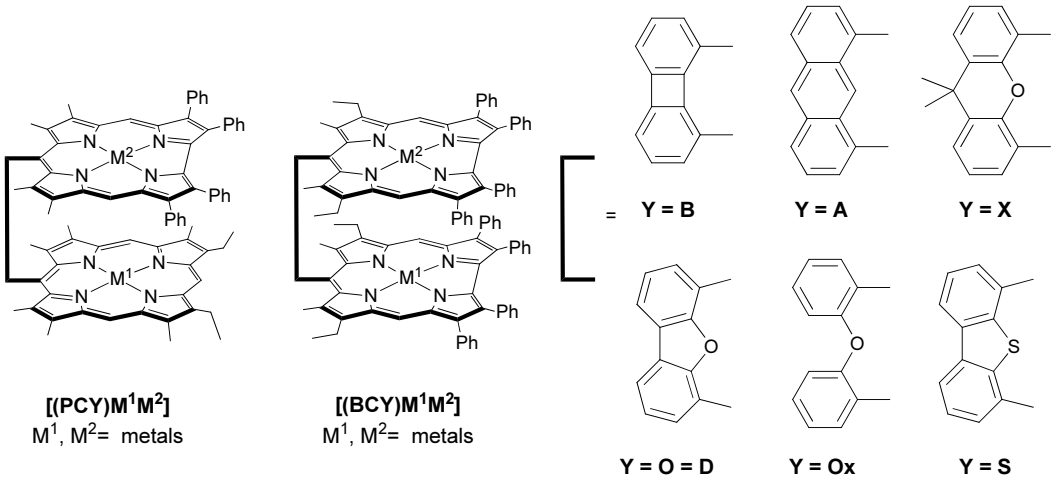

Figure 1.9: Porphyrin-corrole (PCY) and bis-corroles (BCY) based cofacial binuclear complexes and the possible linkers. The most common ring substituants are shown.

Once again, a methodology similar to the one used to study "face-to-face" diporphyrin was used. Overall, the results obtained with porphyrin-corrole catalysts closely relate to the cofacial diporphyrin catalysts. In both cases, the selective reduction of oxygen to water requires the catalytic action of a redox-active cobalt(II) porphyrin and the stabilising action of a Lewis acidic centre, best played by a cobalt(III) centre stabilised within the second N_4-macrocycle. In both cases also, the catalyst exhibits the best selectivity and efficiency when the two macrocyclic units are held cofacial by a rigid backbone of a specific size, best suited by an anthracene or a xanthene linker, and the introduction of sterically demanding groups generates a decline both in activity and selectivity. Steric hindrance is therefore believed to induce subtle geometrical changes which in turn drastically affect the electronic properties of the complex.

1.6 Pacman catalysts based on Schiff-base pyrrole macrocycles: towards more accessible catalysts

Porphyrin and corrole-based cofacial and Hangman ligands proved to be very useful model compounds to understanding the mechanistic aspects of the reduction of oxygen and, even though parts of it remain uncertain and debated, the overall process has been quite well decrypted and studies on different systems support the same hypothesis. These catalysts are quite selective for the four-electron pathway provided they bear the appropriate features and the reaction is catalysed at a reasonably high potential. However, this reaction still proceeds with a large 0.5 V over-potential compared to the 0.3 V over-potential for platinum-based catalysts currently in use in fuel cells. In addition, no catalyst has shown 100% selectivity for the reduction of O_2 to water, meaning that undesired hydrogen peroxide is always produced at least in small quantities. Also, the nature of the key intermediates remains uncertain as the debate between peroxo and superoxo complexes subsists. Most importantly, the synthesis of the cofacial ligands used in these studies are long-winded and low yielding; an improved cofacial diporphyrin synthesis described by Nocera still consists of 15 steps and the ligand is obtained in 3% overall yield.[68] As a result it is highly desirable to develop readily available analogues to cofacial diporphyrins and porphyrin-corroles but with similar properties.

In 2003, the Love[85] and Sessler groups[86] independently developed a new class of Schiff-base pyrrole macrocycles (**Chart 1.1**). This family of compounds proved to be very versatile as Sessler initially reported its anion recognition properties, taking advantage of hydrogen binding within the macrocyclic cavity, whilst Love reported its ability to act as a L^{4-} ligand with two N_4-donor pockets accommodating a metal atom each.

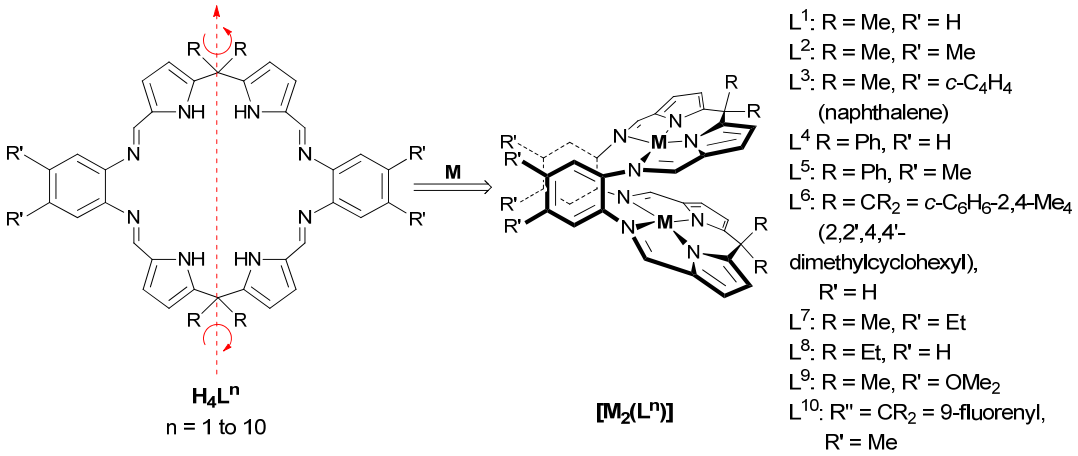

Chart 1.1 : Schiff base pyrrole macrocycles developed by Love and Sessler and their Pacman binuclear complexes.

Remarkably, on metallation these ligands fold around the *meso*-position, between the pyrroles, and at the aryl-hinge to imine bond, so that the two aryl hinges come together in a face-to-face arrangement and interact by π-stacking. As a result, the macrocycle accommodates two square planar metals within a wedge-shape Pacman geometry with a well-defined cavity located between the two metal centres (**Chart 1.1**). This feature makes the binuclear complexes structural analogues to diporphyrin complexes, with two linkers in the former instead of one for the latter.

Most importantly, the ligands are synthesised from inexpensive, readily-available starting materials (acetone, pyrrole, DMF and 1,2-diaminobenzene for H_4L^1) in only three high yielding steps (35% overall yield for H_4L^1) and the procedure can easily be carried out on multi-gram scales. As illustrated in **Chart 1.1**, the substitution on the macrocycle is easy to modulate, in particular at the *meso*-position, where the R groups correspond to the substituents on the ketone starting material, and at the aryl hinge, which corresponds to the diamine starting material. In addition, the macrocycle is a very versatile ligand able to accommodate numerous transition metals[85, 87-90] as well as actinides and lanthanides[88, 91] in the Pacman arrangement. The size of the binding pocket can be tuned to accommodate sterically more demanding guests by increasing the separation between the aryl hinges (which do not necessarily π-stack any more). Bowl shaped complexes, where the Schiff-base pyrrole macrocycle acts as a neutral ligand to transition metals, have also been isolated.[90, 92]

In the interest of ORR catalysis, $[Co_2(L^1)]$ was synthesised and its ability to activate oxygen was evaluated.[93] $[Co_2(L^1)]$ and its pyridine adduct $[Co_2(py)_2(L^1)]$ were isolated in the solid state and showed intermetallic separations of 4.12 and 4.30 Å, which are slightly shorter than the 4.53 Å separation observed for both $[Co_2(DPA)]$ and $[Co_2(DPX)]$. When exposed to air in the presence of pyridine, $[Co_2(L^1)]$ spontaneously binds oxygen and the peroxo complex formed was the first oxygen adduct of a Pacman complex to be characterised structurally in the solid state. The oxygen is bound in a μ^2-η^1:η^1, "zig-zag" bridging mode called the Pauling mode (as opposed to the μ^2-η^2:η^2, side-on, Griffith binding mode) and the complex is best assigned as $[Co^{(III)}_2(\mu\text{-}O_2^{2-})(L^1)]$. An X-ray study showed that very little rearrangement has occurred upon oxygen binding and the intermetallic distance (4.15 Å) remains virtually unchanged compared to the oxygen-free complexes. In solution however, a 15-line EPR spectrum was observed that is characteristic of the superoxo complex $[Co^{(III)}_2(\mu\text{-}O_2^{-})(L^1)]^+$, which was estimated to constitute around 10% of the oxygenated sample with the peroxo complex the remaining 90%. It is important to note that, in contrast to cobalt diporphyrins, $[Co_2(L^1)]$ binds oxygen spontaneously and irreversibly. In particular, the peroxo intermediate appears very stable and is not oxidised to the superoxo complex with common oxidants such as iodine.

The activity of $[Co_2(L^1)]$ as an ORR catalyst was investigated under heterogeneous (by RRDE experiment) and homogeneous (by UV-visible spectroscopy) conditions. While the complex catalysed the reduction of oxygen, it was found to be a relatively poor catalyst with a half wave potential of $E_{1/2}$ ~ 0.2 V vs. Ag/AgCl (*ca.* 0.4 *vs.* NHE) and only 0.4 electrons were exchanged (by UV-visible spectroscopy) in conditions similar to those that favour four-electron chemistry using cofacial diporphyrins. As such, the catalyst appeared to be readily inactivated. However, no hydrogen peroxide was detected by iodate titration or by RRDE, suggesting that the catalyst is selective for the four-electron pathway and that only a small portion of the oxygen available is actually consumed over the time scale of the experiment. It was therefore proposed that the superoxo-product was the active form of the catalyst and the peroxo-complex was unable to catalyse the reaction. If, as suggested by the initial

oxygenation experiments, the oxygen-free catalyst binds oxygen to form a 10:90 mixture of superoxo/peroxo-adducts and these two species are not interconvertible, then at the beginning of each catalytic cycle only 10% of the remaining catalyst is regenerated to its superoxo active form and 90% is transformed into the inactive peroxo (**Figure 1.10**). This results in a diminishing amount of the catalytically-active species and would account for the low turnover numbers.

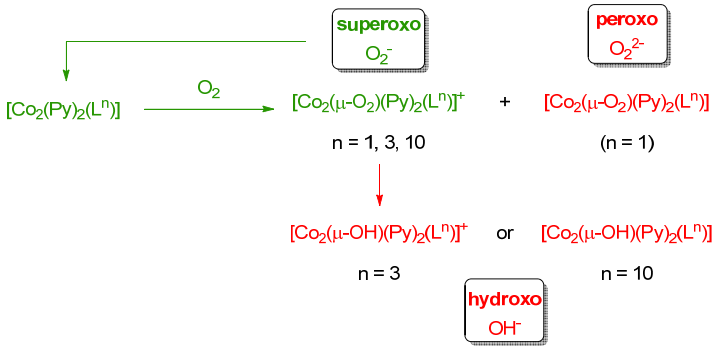

Figure 1.10: Proposed mechanism of degradation for wedge-shape Schiff-base pyrrole binuclear cobalt catalysts $[Co_2(L^n)]$.

Further investigation using the naphthyl-hinged macrocycle L^3 also permitted the isolation of another catalytically-inactive oxygenated intermediate, the hydroxyl-bridged $[Co^{(III)}_2(\mu\text{-}OH)(L^3)]^+$. In the solid state, the hydroxide bridges symmetrically the two Co(III) atoms with a shortened intermetallic distance of 3.61 Å and an unusually obtuse Co-O-Co angle of 138.4º. The bite angle between the two N_4-donor mean planes was significantly smaller (54º) than in the other binuclear cobalt complexes (62-65º), which illustrates a clamping effect reminiscent of the Pacman effect observed for cofacial diporphyrins.

These insights into the deactivation pathways of the binuclear cobalt catalysts encouraged further modifications to the ligand in order to favour the formation of superoxo complexes on oxygenation and to limit the stability of peroxo and single-atom-bridged complexes. It was reasoned that the introduction of sterically-demanding groups at the *meso*-positions should prevent any twisting or clamping action that brings the metal centres close together and should thereby promote the formation of diatomic bridges over monoatomic ones. In addition, subtle electronic effects should favour superoxo over peroxo complexes. A ligand was

developed that fulfils these criteria with the introduction of a fluorenyl substituent at the *meso*-position and the binuclear cobalt complex [$Co_2(L^{10})$] was synthesised.[89] In the solid state, [$Co_2(L^{10})$] and its pyridine adduct [$Co_2(py)_2(L^{10})$] actually exhibit significantly shorter intermetallic distances (3.64 and 4.12 Å respectively) than their *meso*-methyl substituted analogues. Oxygenation of these complexes in the presence of pyridine yielded a paramagnetic complex only, excluding the formation of a peroxo-complex and EPR confirmed the formation of the superoxo-intermediate which was isolated in the solid state.[94] The solid state structure of the zwitterion [$Co^{(III)}_2(\mu\text{-}O_2^-)(OH)(L^1)$] showed a hydrogen-bonding interaction between the superoxo group and the hydroxide anion. This could potentially indicate a strong basic character for the superoxo group, a characteristic highly desirable for the catalytic activity. In chloroform solution, the dioxygen ligand appeared to be readily displaced by hydroxide and [$Co^{(II/III)}_2(\mu\text{-}OH)(L^{10})$], an unusual mixed valence hydroxo bridged complex, was formed and structurally characterised. The Co(II) atom is displaced away from the N_4-donor plane towards the cavity by 0.59 Å to accommodate the hydroxide within the geometrically constrained cavity.

In terms of catalytic activity, [$Co_2(L^{10})$] represented a large improvement compared to the initial system as about twice as many electrons were consumed under the same conditions and under optimum conditions: with a strong electron donor and high concentration of acid, transformations involving almost four electrons were observed. Once again the catalyst is selective for the four-electron reduction of oxygen to water and the improved activity was attributed to the preferential formation of a superoxo-intermediate on exposure to oxygen (and therefore exclusion of the inactive peroxo-complex). The formation of a singly bridged species was not completely prevented and may account for the relatively poor activity compared to cofacial diporphyrins under similar conditions.

It appears clear from these results that subtle electronic modifications alter catalytic activity quite drastically, preventing the formation of the catalytically inactive peroxo-species. The introduction of sterically demanding substituents, however, was not enough to prevent single-atom bridged species and a different approach is

required to separate the metal centres. Major structural changes in the ligand core, like the replacement of the aryl hinges by larger ones, might provide more robust catalytic intermediates. The development of such a ligand and the study of its binuclear complexes constitute the aim of this thesis.

1.7 Bibliography

1 M. I. Hoffert, K. Caldeira, A. K. Jain, E. F. Haites, L. D. D. Harvey, S. D. Potter, M. E. Schlesinger, S. H. Schneider, R. G. Watts, T. M. L. Wigley, and D. J. Wuebbles, *Nature*, 1998, **395**, 881.

2 P. Moriarty and D. Honnery, *Int. J. Hydrogen Energy*, 2010, **35**, 12374.

3 S. B. Benson and F. M. J. Orr, *Mat. Res. Soc. Bull.*, 2008, **33**, 297 and references within.

4 *Energy Information Administration. Annual Energy Outlook (US Dept of Energy, Washington, DC)*, 2005; *United Nations Development Program. World Energy Assessment Report: Energy and the Challenge of Sustainability (United Nations, New York)*, 2003; G. J. Kramer and M. Haigh, *Nature*, 2009, **462**, 568; *IEA. World Energy Outlook 2004, Paris, France*, 2004; W. Zittel and J. Schindler, in 'Alternative World Energy Outlook 2006: a possible path towards a sustainable future', ed. D. Y. Goswami, 2007; *IEA. World Energy Outlook 2006, Paris, France*, 2006.

5 P. Wender, C. C. Cummins, L. Kiessling, E. W. 'Bert' Meijer, P. Alivisatos, K. Wooley, D. King, J. Aizenberg, G. Fleming, *Nature*, 2011, **469**, 23.

6 N. S. Lewis and D. G. Nocera, *Proc. Natl. Acad. Sci.*, 2006, **103**, 15729.

7 W. D. Grossmann, I. Grossmann, and K. Steininger, *Environ. Sci. Technol.*, 2010, **44**, 4849.

8 R. E. Smalley, *Mat. Matt.*, 2005, 412.

9 M. Zerta, P. R. Schmidt, C. Stiller, and H. Landinger, *Int. J. Hydrogen Energy*, 2008, **33**, 3021.

10 M. Momirlan and T. N. Veziroglu, *Int. J. Hydrogen Energy*, 2005, **30**, 795.

11 D. G. Nocera, *Inorg. Chem.*, 2009, **48**, 10001.

12 O. Erdinc and M. Uzunoglu, *Renew. Sust. Energ. Rev.*, 2010, **14**, 2874.

13 D. G. Nocera, *ChemSusChem*, 2009, **2**, 387.

14 M. Dresselhaus, G. Crabtree, and M. Buchanan, 'Basic Research Needs for the Hydrogen Economy', 2003.

15 A. A. Gewirth and M. S. Thorum, *Inorg. Chem.*, 2010, **49**, 3557.

16 C. M. Johnston, P. Piela, and P. Zelenay, 'Transition metal/polymer catalysts for O_2 reduction', Handbook of Fuel Cells, John Wiley & Sons, Ltd, 2010.

17 P. H. Matter, E. J. Biddinger, and U. S. Ozkan, in 'Non-precious metal oxygen reduction catalysts for PEM fuel cells', 2007.

18 N. M. Marković, T. J. Schmidt, V. Stamenković, and P. N. Ross, *Fuel Cells*, 2001, **1**, 105.

19 *Johnson and Matthey Platinum Today*, http://www.platinum.matthey.com.

20 *London Metal Exchange*, http://www.lme.com/home.asp.

21 *MetalPrices.com, quotation on 24th Septembre 2010*, http://www.metalprices.com/.
22 H. A. Gasteiger, S. S. Kocha, B. Sompalli, and F. T. Wagner, *Appl. Catal. B*, 2005, **56**, 9.
23 D. R. Lide, 'CRC Handbook of Chemistry and Physics, 84th edition', CCR Press, 2003-2004.
24 'Anglo Platinum Inc.' Ore Reserves and Mineral Resources, 2005.
25 H. A. Gasteiger, J. E. Panels, and S. G. Yan, *J. Power Sources*, 2004, **127**, 162.
26 M. Z. Jacobson, W. G. Colella, and D. M. Golden, *Science*, 2005, **308**, 1901.
27 R. Jiang and D. Chu, *J. Electrochem. Soc.*, 2000, **147**, 4605.
28 D. A. Scherson, A. Palencsár, Y. Tolmachev, and I. Stefan, 'Transition Metal Macrocycles as Electrocatalysts for Dioxygen Reduction', Electrochemical Surface Modification, Wiley-VCH Verlag GmbH & Co. KGaA, 2008.
29 Y. Feng and N. Alonso-Vante, *Phys. Status Solidi B*, 2008, **245**, 1792; C. W. B. Bezerra, L. Zhang, K. Lee, H. Liu, A. L. B. Marques, E. P. Marques, H. Wang, and J. Zhang, *Electrochim. Acta*, 2008, **53**, 4937; B. Wang, *J. Power Sources*, 2005, **152**, 1; J. Zhang, K. Lee, L. Zhang, and J. Zhang, in 'Non-noble Electrocatalysts for the PEM Fuel Cell Oxygen Reduction Reaction', 2008.
30 B. R. Viswanathan, Ch. Venkateswara; Varadaraju, U. V, in 'On the search for non-noble metal based electrodes for oxygen reduction reaction', 2006; J. Zhang, C. Song, and J. Zhang, in 'Electrocatalytic Oxygen Reduction Reaction', 2008.
31 R. Jasinski, *Nature*, 1964, **201**, 1212; R. Jasinski, *J. Electrochem. Soc.*, 1965, **112**, 526.
32 H.-J. Zhang, Q.-Z. Jiang, L. Sun, X. Yuan, Z. Shao, and Z.-F. Ma, *Int. J. Hydrogen Energy*, 2010, **35**, 8295.
33 C. M. A. Brett and A. M. O. Brett, 'Electrochemistry Principles, Methods, and Application', Oxford University Press, 1993.
34 J. A. R. van Veen, J. F. van Baar, and K. J. Kroese, *J. Chem. Soc., Faraday Trans. I*, 1981, **77**, 2827.
35 R. Bashyam and P. Zelenay, *Nature*, 2006, **443**, 63.
36 M. Lefèvre, E. Proietti, F. Jaouen, and J.-P. Dodelet, *Science*, 2009, **324**, 71.
37 M. Lefèvre, J. P. Dodelet, and P. Bertrand, *J. Phys. Chem. B*, 2005, **109**, 16718; M. Lefèvre, J. P. Dodelet, and P. Bertrand, *J. Phys. Chem. B*, 2000, **104**, 11238.
38 H. Michel, J. Behr, A. Harrenga, and A. Kannt, *Annu. Rev. Biophys. Biomol. Structure*, 1998, **27**, 329; T. Tsukihara, H. Aoyama, E. Yamashita, T. Tomizaki, H. Yamaguchi, K. Shinzawa-Itoh, R. Nakashima, R. Yaono, and S. Yoshikawa, *Science*, 1996, **272**, 1136; S. Iwata, C. Ostermeier, B. Ludwig, and H. Michel, *Nature*, 1995, **376**, 660.
39 T. Tsukihara, H. Aoyama, E. Yamashita, T. Tomizaki, H. Yamaguchi, K. Shinzawa-Itoh, R. Nakashima, R. Yaono, and S. Yoshikawa, *Science*, 1995, **269**, 1069.
40 P. R. Rich and M. Iwaki, *Biochemistry (Moscow)*, 2007, **72**, 1047; C. W. Hoganson, M. A. Pressler, D. A. Proshlyakov, and G. T. Babcock, *Biochim. Biophys. Acta - Bioenergetics*, 1998, **1365**, 170.

41 J. P. Collman, N. K. Devaraj, R. A. Decréau, Y. Yang, Y.-L. Yan, W. Ebina, T. A. Eberspacher, and C. E. D. Chidsey, *Science*, 2007, **315**, 1565.
42 J. P. Collman, R. Schwenninger, M. Rapta, M. Broring, and L. Fu, *Chem. Commun.*, 1999, 137.
43 G. Charalambidis, K. Ladomenou, B. Boitrel, and A. G. Coutsolelos, *Eur. J. Org. Chem.*, 2009, **2009**, 1263.
44 T. Chishiro, Y. Shimazaki, F. Tani, Y. Tachi, Y. Naruta, S. Karasawa, S. Hayami, and Y. Maeda, *Angew. Chem., Int. Ed. Engl.*, 2003, **42**, 2788.
45 H. Shin, D.-H. Lee, C. Kang, and K. D. Karlin, *Electrochim. Acta*, 2003, **48**, 4077.
46 M. J. Gunter, L. N. Mander, and K. S. Murray, *J. Chem. Soc., Chem. Commun.*, 1981, 799.
47 J. P. Collman and S. Ghosh, *Inorg. Chem.*, 2010, **49**, 5798; F. Liu, J. J. Concepcion, J. W. Jurss, T. Cardolaccia, J. L. Templeton, and T. J. Meyer, *Inorg. Chem.*, 2008, **47**, 1727; J. P. Collman, I. M. Shiryaeva, and R. Boulatov, *Inorg. Chem.*, 2003, **42**, 4807; J. P. Collman, S. Ghosh, A. Dey, R. A. Decréau, and Y. Yang, *J. Am. Chem. Soc.*, 2009, **131**, 5034; J. P. Collman, M. Rapta, M. Bröring, L. Raptova, R. Schwenninger, B. Boitrel, L. Fu, and M. L'Her, *J. Am. Chem. Soc.*, 1999, **121**, 1387; B. S. Lim and R. H. Holm, *Inorg. Chem.*, 1998, **37**, 4898; J. P. Collman and R. A. Decréau, *Chem. Commun.*, 2008, 5065; J. P. Collman, R. A. Decréau, Y. Yan, J. Yoon, and E. I. Solomon, *J. Am. Chem. Soc.*, 2007, **129**, 5794; J. P. Collman, R. A. Decréau, and C. J. Sunderland, *Chem. Commun.*, 2006, 3894; K. Ladomenou, G. Charalambidis, and A. G. Coutsolelos, *Inorg. Chim. Acta*, 2010, **363**, 2201; D. Ricard, B. Andrioletti, B. Boitrel, and M. L'Her, *Chem. Commun.*, 1999, 1523; D. Ricard, A. Didier, M. L'Her, and B. Boitrel, *ChemBioChem*, 2001, **2**, 144; D. Ricard, M. L'Her, P. Richard, and B. Boitrel, *Chem.-Eur. J.*, 2001, **7**, 3291; D. Ricard, A. Didier, M. L'Her, and B. Boitrel, *Comptes Rendus Chimie*, 2002, **5**, 33; A. Didier, M. L'Her, and B. Boitrel, *Org. Biomol. Chem.*, 2003, **1**, 1274; J.-G. Liu, Y. Naruta, and F. Tani, *Angew. Chem., Int. Ed. Engl.*, 2005, **44**, 1836; E. E. Chufán, S. C. Puiu, and K. D. Karlin, *Acc. Chem. Res.*, 2007, **40**, 563; J.-G. Liu, Y. Naruta, and F. Tani, *Chem.-Eur. J.*, 2007, **13**, 6365; Y. Naruta, T. Sasaki, F. Tani, Y. Tachi, N. Kawato, and N. Nakamura, *J. Inorg. Biochem.*, 2001, **83**, 239; K. D. Karlin, D.-H. Lee, O. H. V., and K. J. Humphreys, *Pure Appl. Chem.*, 1998, **70**, 855; E. Kim, E. E. Chufán, K. Kamaraj, and K. D. Karlin, *Chem. Rev.*, 2004, **104**, 1077.
48 F. D'Souza, Y.-Y. Hsieh, and G. R. Deviprasad, *Chem. Commun.*, 1998, 1027.
49 F. P. Schwarz, M. Gouterman, Z. Muljiani, and D. H. Dolphin, *Bioinorg. Chem.*, 1972, **2**, 1.
50 J. P. Collman, C. M. Elliott, T. R. Halbert, and B. S. Tovrog, *Proc. Natl. Acad. Sci. U. S. A.*, 1977, **74**, 18.
51 H. Ogoshi, H. Sugimoto, and Z.-I. Yoshida, *Tetrahedron Lett.*, 1977, **18**, 169.
52 C. K. Chang, M.-S. Kuo, and C.-B. Wang, *J. Heterocycl. Chem.*, 1977, **14**, 943.
53 N. E. Kagan, D. Mauzerall, and R. B. Merrifield, *J. Am. Chem. Soc.*, 1977, **99**, 5484.

54 H. L. Anderson, C. A. Hunter, M. N. Meah, and J. K. M. Sanders, *J. Am. Chem. Soc.*, 1990, **112**, 5780.
55 Y. P. Myer and A. Pande, in 'The Porphyrins', ed. D. Dolphin, New York, 1978.
56 J. P. Collman, M. Marrocco, P. Denisevich, C. Koval, and F. C. Anson, *J. Electroanal. Chem. Interfac. Electrochem.*, 1979, **101**, 117; J. P. Collman, P. Denisevich, Y. Konai, M. Marrocco, C. Koval, and F. C. Anson, *J. Am. Chem. Soc.*, 1980, **102**, 6027.
57 J. P. Collman, F. C. Anson, C. E. Barnes, C. S. Bencosme, T. Geiger, E. R. Evitt, R. P. Kreh, K. Meier, and R. B. Pettman, *J. Am. Chem. Soc.*, 1983, **105**, 2694; R. R. Durand, C. S. Bencosme, J. P. Collman, and F. C. Anson, *J. Am. Chem. Soc.*, 1983, **105**, 2710.
58 R. Guilard, S. Brandes, C. Tardieux, A. Tabard, M. L'Her, C. Miry, P. Gouerec, Y. Knop, and J. P. Collman, *J. Am. Chem. Soc.*, 1995, **117**, 11721.
59 J. P. Collman, N. H. Hendricks, K. Kim, and C. S. Bencosme, *J. Chem. Soc., Chem. Commun.*, 1987, 1537.
60 Y. Deng, C. J. Chang, and D. G. Nocera, *J. Am. Chem. Soc.*, 2000, **122**, 410.
61 J. P. Collman, P. S. Wagenknecht, and J. E. Hutchison, *Angew. Chem., Int. Ed. Engl.*, 1994, **33**, 1537 and references within.
62 J. P. Collman, D. A. Tyvoll, L. L. Chng, and H. T. Fish, *J. Org. Chem.*, 1995, **60**, 1926.
63 C. K. Chang and I. Abdalmuhdi, *J. Org. Chem.*, 1983, **48**, 5388.
64 C. K. Chang, H. Y. Liu, and I. Abdalmuhdi, *J. Am. Chem. Soc.*, 1984, **106**, 2725.
65 C. K. Chang and I. Abdalmuhdi, *Angew. Chem. Int. Ed.*, 1984, **23**, 164.
66 R. Guilard, M. A. Lopez, A. Tabard, P. Richard, C. Lecomte, S. Brandes, J. E. Hutchison, and J. P. Collman, *J. Am. Chem. Soc.*, 1992, **114**, 9877.
67 C. J. Chang, Y. Deng, A. F. Heyduk, C. K. Chang, and D. G. Nocera, *Inorg. Chem.*, 2000, **39**, 959.
68 J. Rosenthal and D. G. Nocera, *Acc. Chem. Res.* , 2007, **40**, 543.
69 S. Faure, C. Stern, R. Guilard, and P. D. Harvey, *J. Am. Chem. Soc.* , 2004, **126**, 1253.
70 M. Tanaka, K. Ohkubo, C. P. Gros, R. Guilard, and S. Fukuzumi, *J. Am. Chem. Soc.* , 2006, **128**, 14625.
71 C. L. Ni, I. Abdalmuhdi, C. K. Chang, and F. C. Anson, *J. Phys. Chem.*, 1987, **91**, 1158.
72 B. J. Pistorio, C. J. Chang, and D. G. Nocera, *J. Am. Chem. Soc.* , 2002, **124**, 7884; J. M. Hodgkiss, C. J. Chang, B. J. Pistorio, and D. G. Nocera, *Inorg. Chem.*, 2003, **42**, 8270; J. Rosenthal, B. J. Pistorio, L. L. Chng, and D. G. Nocera, *J. Org. Chem.* , 2005, **70**, 1885; J. Rosenthal, T. D. Luckett, J. M. Hodgkiss, and D. G. Nocera, *J. Am. Chem. Soc.* , 2006, **128**, 6546.
73 J. Rosenthal, L. L. Chng, S. D. Fried, and D. G. Nocera, *Chem. Commun.*, 2007, 2642; J. D. Soper, S. V. Kryatov, E. V. Rybak-Akimova, and D. G. Nocera, *J. Am. Chem. Soc.*, 2007, **129**, 5069; C.-Y. Yeh, C. J. Chang, and D. G. Nocera, *J. Am. Chem. Soc.*, 2001, **123**, 1513; L. L. Chng, C. J. Chang, and D. G. Nocera, *Org. Lett.*, 2003, **5**, 2421; J. Y. Yang, J. Bachmann, and D. G. Nocera, *J. Org. Chem.*, 2006, **71**, 8706; M. Schwalbe, D. K. Dogutan, S. A. Stoian, T. S. Teets, and D. G. Nocera, *Inorg. Chem.*, 2011, **50**, 1368; D. K.

Dogutan, S. A. Stoian, R. McGuire, M. Schwalbe, T. S. Teets, and D. G. Nocera, *J. Am. Chem. Soc.*, 2011, **133**, 131; V. G. Organo, A. S. Filatov, J. S. Quartararo, Z. M. Friedman, and E. V. Rybak-Akimova, *Inorg. Chem.*, 2009, **48**, 8456; J. Y. Yang, S.-Y. Liu, I. V. Korendovych, E. V. Rybak-Akimova, and D. G. Nocera, *ChemSusChem*, 2008, **1**, 941; J. Y. Yang and D. G. Nocera, *J. Am. Chem. Soc.*, 2007, **129**, 8192; S.-Y. Liu, J. D. Soper, J. Y. Yang, E. V. Rybak-Akimova, and D. G. Nocera, *Inorg. Chem.*, 2006, **45**, 7572; Y. Watanabe, A. Namba, N. Umezawa, M. Kawahata, K. Yamaguchi, and T. Higuchi, *Chem. Commun.*, 2006, 4958; J.-G. Liu, Y. Shimizu, T. Ohta, and Y. Naruta, *J. Am. Chem. Soc.*, 2010, **132**, 3672.

74 H. Y. Liu, I. Abdalmuhdi, C. K. Chang, and F. C. Anson, *J. Phys. Chem.*, 1985, **89**, 665.

75 F. Bolze, M. Drouin, P. D. Harvey, C. P. Gros, E. Espinosa, and R. Guilard, *J. Porphyrins Phthalocyanines* 2003, **7**, 474.

76 C. J. Chang, Y. Deng, C. Shi, C. K. Chang, F. C. Anson, and D. G. Nocera, *Chem. Commun.*, 2000, 1355.

77 C. J. Chang, Z.-H. Loh, C. Shi, F. C. Anson, and D. G. Nocera, *J. Am. Chem. Soc.*, 2004, **126**, 10013.

78 C. J. Chang, Y. Deng, S.-M. Peng, G.-H. Lee, C.-Y. Yeh, and D. G. Nocera, *Inorg. Chem.* , 2002, **41**, 3008.

79 Y. Le Mest, M. L'Her, and J. Y. Saillard, *Inorg. Chim. Acta*, 1996, **248**, 181.

80 Y. Le Mest, C. Inisan, A. Laouénan, M. L'Her, J. Talarmin, M. El Khalifa, and J.-Y. Saillard, *J. Am. Chem. Soc.*, 1997, **119**, 6095.

81 S. Fukuzumi, K. Okamoto, C. P. Gros, and R. Guilard, *J. Am. Chem. Soc.*, 2004, **126**, 10441.

82 B. G. Malmstroem, *Acc. Chem. Res.*, 1993, **26**, 332; B. G. Malmstroem, *Chem. Rev.*, 1990, **90**, 1247; G. T. Babcock and M. Wikstrom, *Nature*, 1992, **356**, 301; C. Varotsis, Y. Zhang, E. H. Appelman, and G. T. Babcock, *Proc. Natl. Acad. Sci.*, 1993, **90**, 237; S. I. Chan and P. M. Li, *Biochemistry*, 1990, **29**, 1; L. Que and Y. Dong, *Acc. Chem. Res.*, 1996, **29**, 190; A. L. Feig and S. J. Lippard, *Chem. Rev.*, 1994, **94**, 759; K. Yoshizawa and R. Hoffmann, *Inorg. Chem.*, 1996, **35**, 2409; A. Ghosh, J. Almlöf, and L. Que, *Angew. Chem., Int. Ed. Engl.*, 1996, **35**, 770; E. I. Solomon, M. J. Baldwin, and M. D. Lowery, *Chem. Rev.*, 1992, **92**, 521; T. N. Sorrell, *Tetrahedron*, 1989, **45**, 3.

83 S. Fukuzumi, *Chem. Lett.*, 2008, **37**, 808.

84 F. Jérôme, C. P. Gros, C. Tardieux, J.-M. Barbe, and R. Guilard, *New J. Chem.* , 1998, **22**, 1327; F. Jérôme, C. P. Gros, C. Tardieux, J.-M. Barbe, and R. Guilard, *Chem. Commun.* , 1998, 2007; R. Guilard, F. Jérôme, J.-M. Barbe, C. P. Gros, Z. Ou, J. Shao, J. Fischer, R. Weiss, and K. M. Kadish, *Inorg. Chem.* , 2001, **40**, 4856; R. Guilard, F. Burdet, J.-M. Barbe, C. P. Gros, E. Espinosa, J. Shao, Z. Ou, R. Zhan, and K. M. Kadish, *Inorg. Chem.*, 2005, **44**, 3972; K. M. Kadish, L. Frémond, Z. Ou, J. Shao, C. Shi, F. C. Anson, F. Burdet, C. P. Gros, J.-M. Barbe, and R. Guilard, *J. Am. Chem. Soc.*, 2005, **127**, 5625; K. M. Kadish, J. Shao, Z. Ou, L. Frémond, R. Zhan, F. Burdet, J.-M. Barbe, C. P. Gros, and R. Guilard, *Inorg. Chem.*, 2005, **44**, 6744; K. M. Kadish, L. Frémond, J. Shen, P. Chen, K. Ohkubo, S. Fukuzumi, M. El Ojaimi, C. P. Gros, J.-M. Barbe, and R. Guilard, *Inorg. Chem.*, 2009, **48**, 2571; R. Guilard, F. Jérôme, C. P. Gros, J.-M. Barbe, Z. Ou, J. Shao, and K.

M. Kadish, *C. R. Acad. Sci. Paris, Chimie*, 2001, **4**, 245; J.-M. Barbe, F. Burdet, E. Espinosa, C. P. Gros, and R. Guilard, *J. Porphorph. Phthalocyanines*, 2003, **7**, 365; K. M. Kadish, Z. Ou, J. Shao, C. P. Gros, J.-M. Barbe, F. Jérôme, F. Bolze, F. Burdet, and R. Guilard, *Inorg. Chem.*, 2002, **41**, 3990.

85 G. Givaja, A. J. Blake, C. Wilson, M. Schroder, and J. B. Love, *Chem. Commun.*, 2003, 2508.

86 J. L. Sessler, W.-S. Cho, S. P. Dudek, L. Hicks, V. Lynch, and T. Huggins, *J. Porphyrins Phthalocyanines*, 2003, **7**, 97.

87 G. Givaja, A. J. Blake, C. Wilson, M. Schroder, and J. B. Love, *Chem. Commun.*, 2005, 4423; G. Givaja, M. Volpe, J. W. Leeland, M. A. Edwards, T. K. Young, S. B. Darby, S. D. Reid, A. J. Blake, C. Wilson, J. Wolowska, E. J. L. McInnes, M. Schröder, and J. B. Love, *Chem. - Eur. J.*, 2007, **13**, 3707; M. Volpe, S. D. Reid, A. J. Blake, C. Wilson, and J. B. Love, *Inorg. Chim. Acta*, 2007, **360**, 273; J. W. Leeland, A. M. Z. Slawin, and J. B. Love, *Organometallics*, **29**, 714.

88 J. B. Love, *Chem. Commun.*, 2009, 3154.

89 E. Askarizadeh, A. M. J. Devoille, D. M. Boghaei, A. M. Z. Slawin, and J. B. Love, *Inorg. Chem.*, 2009, **48**, 7491.

90 J. M. Veauthier, W. S. Cho, V. M. Lynch, and J. L. Sessler, *Inorg. Chem.*, 2004, **43**, 1220; J. Sessler and E. Tomat, *Acc. Chem. Res.*, 2007, **40**, 371.

91 P. L. Arnold, A. J. Blake, C. Wilson, and J. B. Love, *Inorg. Chem.*, 2004, **43**, 8206; P. L. Arnold, D. Patel, A. J. Blake, C. Wilson, and J. B. Love, *J. Am. Chem. Soc.*, 2006, **128**, 9610; P. L. Arnold, D. Patel, C. Wilson, and J. B. Love, *Nature*, 2008, **451**, 315; P. L. Arnold, N. A. Potter, C. D. Carmichael, A. M. Z. Slawin, P. Roussel, and J. B. Love, *Chem. Commun.*, **46**, 1833; P. L. Arnold, N. A. Potter, N. Magnani, C. Apostolidis, J.-C. Griveau, E. Colineau, A. Morgenstern, R. Caciuffo, and J. B. Love, *Inorg. Chem.*, **49**, 5341; A. Yahia, P. L. Arnold, J. B. Love, and L. Maron, *Chem.-Eur. J.*, **16**, 4881; P. L. Arnold, D. Patel, A.-F. Pecharman, C. Wilson, and J. B. Love, *Dalton Trans.*, **39**, 3501; J. J. Berard, G. Schreckenbach, P. L. Arnold, D. Patel, and J. B. Love, *Inorg. Chem.*, 2008, **47**, 11583; A. Yahia, P. L. Arnold, J. B. Love, and L. Maron, *Chem. Commun.*, 2009, 2402.

92 J. L. Sessler, E. Tomat, T. D. Mody, V. M. Lynch, J. M. Veauthier, U. Mirsaidov, and J. T. Markert, *Inorg. Chem.*, 2005, **44**, 2125; J. M. Veauthier, E. Tomat, V. M. Lynch, J. L. Sessler, U. Mirsaidov, and J. T. Markert, *Inorg. Chem.*, 2005, **44**, 6736; E. Tomat, L. Cuesta, V. M. Lynch, and J. L. Sessler, *Inorg. Chem.*, 2007, **46**, 6224; L. Cuesta, V. M. Lynch, and J. L. Sessler, *J. Porphyrins and Phtalocyanines*, 2010, **14**, 41.

93 G. Givaja, M. Volpe, M. A. Edwards, A. J. Blake, C. Wilson, M. Schröder, and J. B. Love, *Angew. Chem. Int. Ed.*, 2007, **46**, 584; M. Volpe, H. Hartnett, J. W. Leeland, K. Wills, M. Ogunshun, B. J. Duncombe, C. Wilson, A. J. Blake, J. McMaster, and J. B. Love, *Inorg. Chem.*, 2009, **48**, 5195.

94 E. Askarizadeh, S. B. Yaghoob, D. M. Boghaei, A. M. Z. Slawin, and J. B. Love, *Chem. Commun.*, 2010, **46**, 710.

Chapter 2 – Ligand design, synthesis and metallation.

Part of the content of this Chapter, including the synthesis and characterisation of the ligand L, its tetranuclear potassium salt [K_4(L)] and its binuclear palladium complex [Pd_2(L)] was published in the article:

Ligand modifications for tailoring the binuclear microenvironment in Schiff-base calixpyrrole Pacman complexes**

E. Askarizadeh, A. M. J. Devoille, D. M. Boghaei, A. M. Z. Slawin, and J. B. Love,* *Inorg. Chem.*, 2009, **48**, 7491.

** E. Askarizadeh and A. M. J. Devoille contributed equally to this work

2.1 Ligand design

Numerous studies have been carried out on binuclear complexes of cofacial and Pacman diporphyrins and their corrole relatives as they have been shown to manage the multiple electron and proton inventory for a variety of redox reactions of small molecules including O_2, H_2O, N_2, and CO_2.[1-4] However, the multi-step synthetic routes to these compounds are c

hallenging, and, as an alternative, the Love and Sessler groups optimised synthetic procedures to a series of easily-prepared, binucleating Schiff-base calixpyrrole macrocycles (H_4L^n, n = 1 to 9, **Chart 1.1** in **Chapter 1**). Significantly, on metallation, these macrocycles adopt wedge-shaped, "double-pillared" Pacman geometries.[5] The binuclear cobalt Pacman complexes were shown to selectively catalyse the four-electron, four-proton reduction of dioxygen and, furthermore, the mechanism of this reaction is thought to be similar to that for the cobalt diporphyrin

analogues.[3, 6] In order to enhance the catalytic activity, it appears important that the design of the bimetallic microenvironment should favour the formation of diatom-bridged intermediates over single-atom-bridged species. This rationale has been used to good effect in binuclear diporphyrin chemistry, in particular that related to oxo-atom transfer and oxygen evolution, where the use of bulky *meso*-mesityl substituents on the porphyrin rings causes the two metalloporphyrin units to 'spring' apart and disfavour the formation of inhibitory oxo- and hydroxo-bridges.[7-9] In the case of the double-hinged ligands presented here, it was reasoned that two complementary ligand design approaches could be used to overcome the problems associated with mono-atom bridged complexes and to favour the formation of diatom-bridged complexes: (1) the incorporation of more sterically-hindering *meso*-substitutents that would promote both a lateral twist and open the mouth of the cleft, and (2) the use of elongated aryl hinges between the two N_4-donor compartments (**Chart 2.1**). These approaches make use of the intrinsic modularity of the ligand synthesis in that it is straightforward to modify the *meso*-substituents and aryl backbone as these components are derived from readily-available ketones and aromatic diamines.

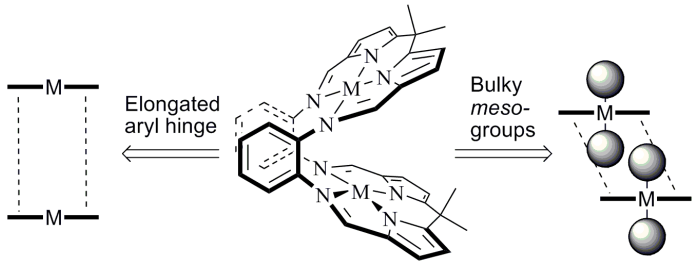

Chart 2.1: Ligand design strategies to disfavour single-atom-bridged binuclear complexes.

These two approaches have been tackled simultaneously within the Love group and the present work describes the enlargement of the aryl hinge. The sterically-hindering *meso*-substituent approach was developed by other students and was described in **Chapter 1**.[10] However, reference to this second approach will be made recurrently as it is closely linked to the work presented here.

On top of the enhanced intermetallic separation, the new ligand was designed to yield cofacial (as opposed to wedged shaped) complexes as the combination of these two parameters proved efficient in the case of cofacial diporphyrins.

With these considerations in mind, several possible backbones, often inspired from the design of related cofacial diporphyrins, were investigated along with their combination with an appropriate *meso*-substituent. The two features can be developed separately as the ligand results from the condensation of the diformyl-dipyrromethane which contains the *meso*-substituant and the backbone-based diamine. Therefore, the following sections focus on the synthesis of (1) the diamines used as the backbone (section 2.2), (2) the diformyl-dipyrromethane counterparts (section 2.3) and (3) their condensation reaction to form the ligand (section 2.4). Finally, (4) the most successful ligand, H_4L is investigated further and several of its bimetallic complexes are described in an attempt to evaluate its success (sections 2.5-2.8).

2.2 Diamine synthesis

2.2.1 Synthesis of 1,8-diaminoanthracene

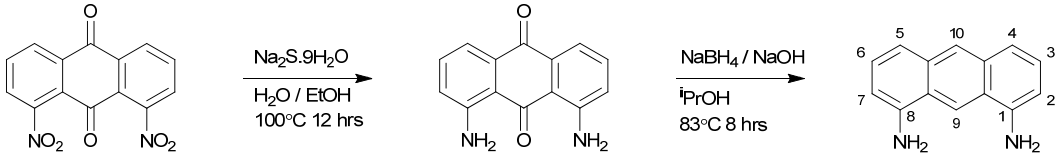

Scheme 2.1: Synthesis of 1,8-diaminoanthracene by reduction of 1,8-dinitroanthraquinone with numbering scheme of the product.

1,8-diaminoanthracene was synthesised as described in the literature[11] by the two step reduction of 1,8-dinitroquinone (**Scheme 2.1**). The first reduction carried out with sodium sulfide affords 1,8-diaminoquinone in high yield. The reduction of the quinone groups with sodium borohydride was also high yielding but the purity of the product was poor, which affected the following condensation step. However, conducting both the synthesis and recrystallisation steps in the dark afforded the pure diamine as pale yellow crystals in good yield.

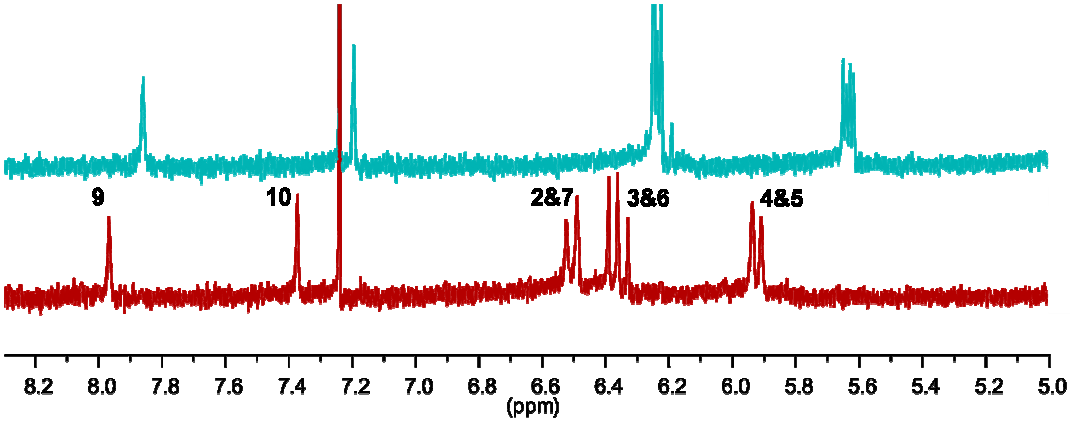

Figure 2.1: ^{1}H NMR spectra of 1,8-diaminoanthracene kept in the dark (bottom, red line with assignment according to the numbering scheme presented in **Scheme 2.1**) and its light decomposition product (top, blue line) in d-chloroform/d_6-DMSO.

When the Sessler group first reported the synthesis of this diamine, mention was made of a yellow compound in solution yielding a green solid upon evaporation and the return to a clean yellow material upon crystallisation. Exposure of a solution of 1,8-diaminoanthracene to UV radiation or daylight confirmed its sensitivity to light as decomposition was observed as illustrated in **Figure 2.1.** The decomposition products were found to be solvent dependant and were attemptively attributed to photo-triggered radical formation[12] followed by coupling or electron transfer reactions.[13]

2.2.2 Attempted synthesis of 1,8-diamino-9,10-dihydroanthracene

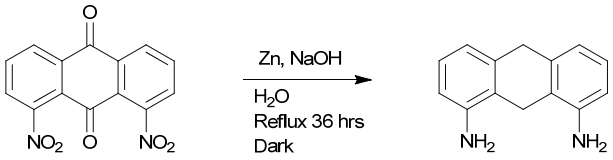

Scheme 2.2 : Attempted synthesis of 1,8-diamino-9,10-dihydroanthracene by reduction of 1,8-dinitroanthraquinone.

An attempt to synthesise 1,8-diamino-9,10-dihydroanthracene by the one step 18 electron reduction of 1,8-dinitroanthraquinone reported in the literature[14] (**Scheme 2.2**) afforded a mixture of partially reduced products, and the desired product could not be isolated. No further attempts were carried out, but a stepwise process with a final two electron reduction of 1,8-diaminoanthracene would probably be a better

approach as 1,8-diaminoanthracene is believed to be an intermediate in the 18 electron process.[14]

2.2.3 Synthesis of 4,5-diamino-xanthene derivatives

2.2.3.1 *Synthesis of 2,7,9,9-tetramethylxanthene and 2,7-di-tert-butyl-9,9-dimethylxanthene*

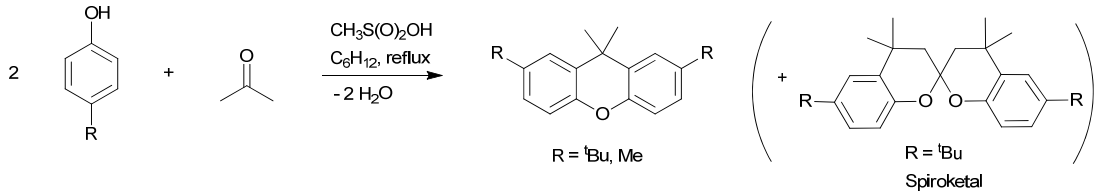

Scheme 2.3 : Synthesis of 2,7,9,9-tetramethylxanthene and 2,7-di-*tert*-butyl-9,9-dimethylxanthene from the corresponding cresol by condensation with acetone in the presence of methanesulfonic acid.

The synthesis of both the di-*tert*-butyl- and the dimethyl- substituted 9,9-dimethylxanthenes presented on **Scheme 2.3** were attempted by reaction of the corresponding cresol with acetone in the presence of methane sulfonic acid as repoted in the literature.[15] While the best results for 2,7,9,9-tetramethylxanthene were obtained from a reflux in toluene solution,[16] a reaction carried out in cyclohexane solution with extraction of the water formed using a Dean-Stark apparatus afforded a cleaner isolated mixture in the case of 2,7-di-*tert*-butyl-9,9-dimethylxanthene.[15] In both cases, a brown oil containing mainly unreacted cresol was isolated as a crude product and isolation of the desired xanthene by recrystallisation was quite difficult. 2,7,9,9-tetramethylxanthene was isolated as a pure product after recrystallisation from methanol. The synthesis from para-*tert*-butylphenol yielded a 50:50 mixture of the desired xanthene product and the corresponding spiroketal (**Scheme 2.3**), which is consistent with the by-product previously reported as this route is also used in the synthesis of the spiroketal.[16, 17] Concentration of the crystallisation liquors followed by crystallisation afforded a second crop which contained the spiroketal only.

2.2.3.2 *Synthesis of 4,5-diamino-2,7,9,9-tetramethylxanthene and 4,5-diamino-2,7-di-tert-butyl-9,9-dimethylxanthene*

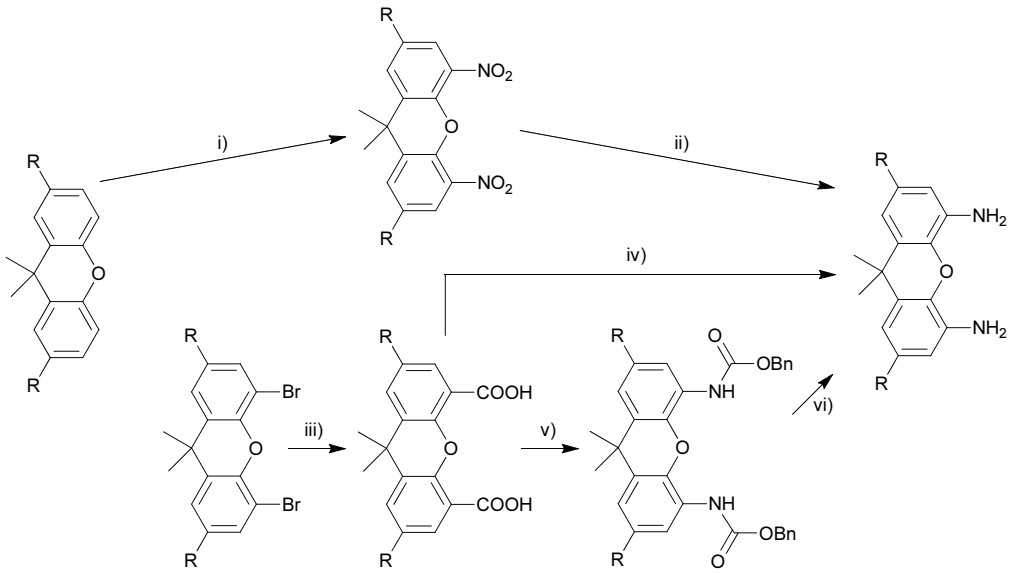

Scheme 2.4 : Synthetic routes to 4,5-diamino-2,7,9,9-tetramethylxanthene (R = Me) and 4,5-diamino 2,7-di-*tert*-butyl-9,9-dimethylxanthene (R = ^{t}Bu). i) fuming HNO_3/CH_3COOH,[17] ii) Sn/HCl, EtOH,[17] iii) 1. ^{t}BuLi, THF, 2. CO_2, 3. conc. HCl, iv) NaN_3, H_2SO_4, $CHCl_3$, v) diphenylphosphorazide, BnOH, TEA, toluene, vi) KOH, EtOH.

All the synthetic routes to the 4,5-diamino-xanthene presented in **Scheme 2.4** were attempted using the 2,7-di-*tert*-butyl-9,9-dimethylxanthene and while the initial experiments published by Jeong proved difficult to reproduce, alternative reaction conditions[17] afforded the expected diamine. The most experimentally and economically viable route was found to be nitration of the xanthene followed by a nitro-reduction (**Scheme 2.4**, i) and ii)) as described for the related spiroketones.[17] This route was used to synthesise both 4,5-diamino-2,7,9,9-tetramethylxanthene and 4,5-diamino-2,7-di-*tert*-butyl-9,9-dimethylxanthene in moderate yields from the corresponding xanthene (about 10% over two steps).

2.3 Dialdehyde synthesis

2.3.1 Synthesis of *meso*-diethyl-5,5′-diformyl-2,2′dipyrromethane

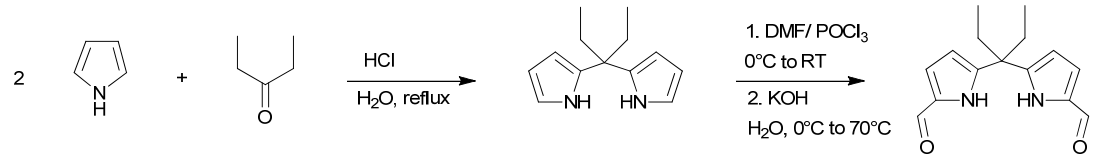

Scheme 2.5 : Synthesis of *meso*-diethyl-5,5′-diformyl-2,2′dipyrromethane by a condensation reaction between acetone and pyrrole followed by Vielsmeier-Haack formylation.

The synthesis of *meso*-diethyl-5,5′-diformyl-2,2′-dipyrromethane was previously developed in the Love group (**Scheme 2.5**): the condensation of pyrrole and pentane-3-ol in the presence of hydrochloric acid affords 2,2′-dipyrromethane[18] and a following Vielsmeier-Haack formylation of the 5 and 5′ positions yields the desired diformyl-dipyrromethane as an off-white solid in 45% overall yield.[10]

2.3.2 Synthesis of *meso*-fluorene -5,5′-diformyl-2,2′dipyrromethane

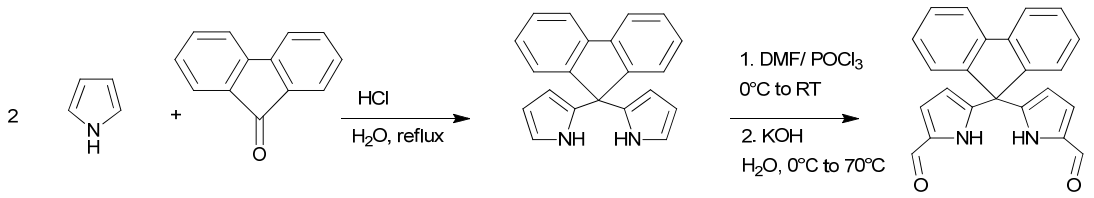

Scheme 2.6 : Synthesis of *meso*-fluorene-5,5′-diformyl-2,2′-dipyrromethane by condensation reaction between fluorenone and pyrrole followed by Vielsmeier-Haack formylation.

A synthetic route similar to the one previously described for *meso*-diethyl-5,5′-diformyl-2,2′-dipyrromethane was also developed within the Love group[19] and affords *meso*-fluorene-5,5′-diformyl-2,2′-dipyrromethane (**Scheme 2.6**). The condensation between fluorenone and pyrrole carried out at 0 °C instead of room temperature resulted in a dramatic increase in yield from 45% to 71%. After a standard $POCl_3$/DMF Vielsmeier-Haack procedure,[10] the desired diformyl-dipyrromethane was obtained in a 60% yield over two steps as a very pale pink solid.

2.4 Synthesis and characterisation of [2+2] Schiff base pyrrole macrocycles

2.4.1 Strategies in the condensation of a diamine backbone and a diformyl-dipyrromethane

While the condensation of any of the diamines previously described with any of the diformyl-dipyrromethanes are theoretically possible, some choices were made in the combinations attempted. Most of the diamines available do not feature any solubilising groups; their combination with alkyl-substituted diformyl-dipyrromethanes ensures the solubility of the resulting macrocycle and its metal complexes. The xanthene-based diamines, however, already possess solubilising alkyl groups and cyclisation was attempted with both the *meso*-diethyl and the *meso*-fluorenyl diformyl-dipyrromethane. The last combination features both the enlarged xanthene hinge and the sterically-hindered fluorenyl substituents, so combining the two approaches previously cited to favour di-atomic bridged over mono-atomic bridged compounds. The corresponding condensation reactions as well as the reduction of one of the macrocyles are described below.

2.4.2 Synthesis of H_4L

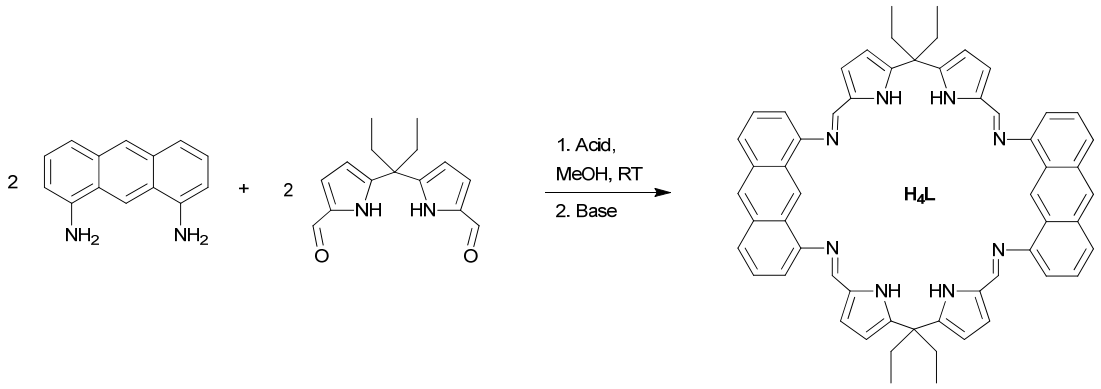

Scheme 2.7 : Synthesis of H_4L by condensation reaction between *meso*-diethyl-5,5′-diformyl-2,2′-dipyrromethane and 1,8-diaminoanthracene in the presence of an acid.

Meso-diethyl-5,5′-diformyl-2,2′-dipyrromethane reacts with 1,8-diaminoanthracene in methanol in the presence of acid, in this case generated from trifluoroacetic anhydride, to form the [2+2] macrocyclic orange acid salt H_4L.nTFA, which was

neutralised with triethylamine to yield H_4L as an analytically pure bright yellow solid (**Scheme 2.7**). Due to the reversibility of the imine bond formation in a wet environment, the synthesis of H_4L was carried out in the dark to prevent the formation of 1,8-diaminoanthracene and the subsequent light-induced decomposition (see section 2.2.1 and **Figure 2.1**). However, once dry, the ligand can be stored indefinitely under a dry nitrogen atmosphere in the presence of light.

The ^1H NMR spectrum of H_4L supports the formation of a single, symmetric macrocycle and displays a single resonance at 8.34 ppm characteristic of imine bond formation and a broad resonance at 9.28 ppm integrating to the four pyrrolic N-H groups (**Appendix 1**). In particular, the complete disappearance of the aldehyde resonance (at δ = 9.07 ppm) confirms that no oligomeric or polymeric products are formed. In the electrospray mass spectrum of H_4L, a parent ion was seen at m/z = 861 and also a half-mass fragmentation peak at m/z = 430; these data support the sole formation of the [2+2] macrocycle, and not any lower or higher order macrocyclic products (the crystals used for the X-ray diffraction study afforded a spectrum identical to the one of the bulk sample). The infra-red spectrum of H_4L shows an NH stretch at 3250 cm^{-1} and a C=N stretch at 1613 cm^{-1}. Elemental analysis is consistent with the expected composition.

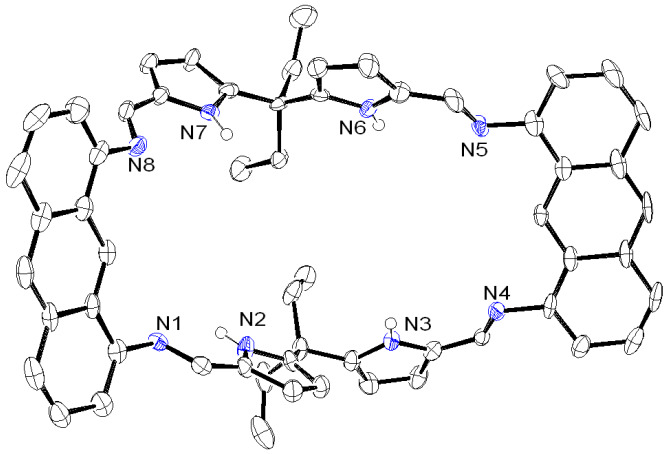

Figure 2.2 : X-ray crystal structure of $H_4L \cdot CH_2Cl_2 \cdot 6.5(MeOH)$ (displacement ellipsoids are drawn at 50 % probability). For clarity, all hydrogen atoms are omitted. (The disordered solvents of crystallisation were accounted for using the SQUEEZE routine of PLATON).

	$H_4L^3 \cdot 2EtOH$	$H_4L^6 \cdot H_2O$	$H_4L^{10} \cdot CH_2Cl_2 \cdot (MeOH)_{6.5}$	$H_4L \cdot CH_2Cl_2 \cdot 6.5MeOH$
N1-C1	1.2827(17)	1.289(3)	1.280(8)	1.270(6)
N1-C46	1.4091(17)	-	-	-
N1-C26A	-	1.413(3)	-	-
N1-C62	-	-	1.416(7)-	-
N1-C55	-	-	-	1.422(6)
C1-C2	1.4313(19)	1.433(3)	1.427(8)	1.427(7)
C2-C3	1.3729(19)	1.371(3)	1.392(8)	1.380(6)
N2-C2	1.3752.17	1.375(3)	1.376(7)	1.380(5)
N2-C5	1.3602(16)	1.370(3)	1.362(7)	1.361(6)
C3-C4	1.405(2)	1.400(3)	1.413(8)	1.406(7)
C4-C5	1.3739(19)	1.383(3)	1.377(8)	1.370(6)
C1-N1-C46	120.66(13)	-		-
N1-C1-C26A	-	121.0(3)	-	-
N1-C1-C62	-	-	119.7(5)-	-
N1-C1-C58	-	-	-	115.9(4)

Table 2.1 : Selected bond lengths [Å] and angles [°] for $H_4L^3 \cdot 2EtOH$, $H_4L^6 \cdot H2O$, $H_4L^{10} \cdot 2EtOH$ and $H_4L \cdot DCM \cdot 6.5MeOH$.

Crystals suitable for an X-ray diffraction study of H_4L were grown by diffusion of methanol into chloroform and the crystal structure determined (**Figure 2.2**). Crystal data are displayed in **Appendix 2** and selected bond lengths and angles are detailed in **Table 2.1** and **Appendix 3**. The solid-state structure of H_4L supports the formation of the [2+2] macrocycle. The molecule adopts a wedge-shape in the solid state with solvent molecules in the cleft consistent with the hydrogen bond donor and acceptor character of this type of ligand, as seen previously.[20] All the distances and angles are similar to those observed in related ligands previously reported[20] (**Table 2.1**). Only the angle around the imine is slightly smaller than in previous structures (C1-N1-C58 115.9(4)° compared to 121° in previous structures).

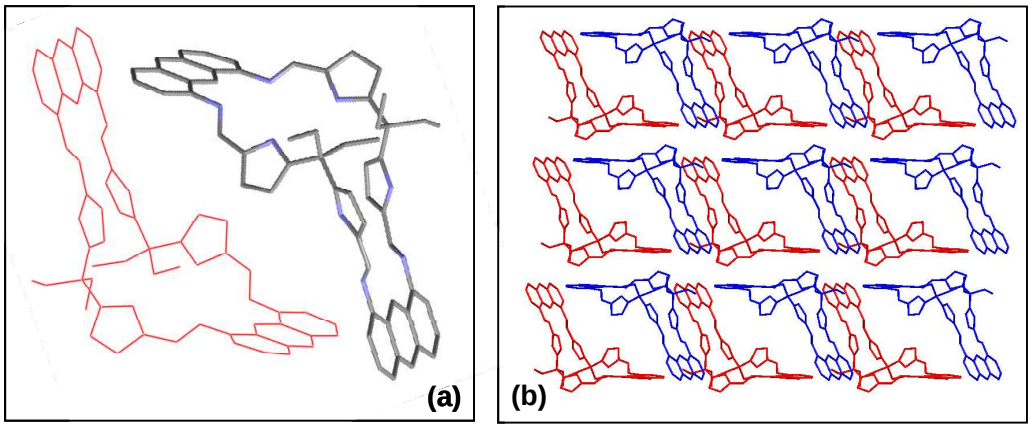

Figure 2.3 : Supramolecular assembly within the X-ray crystal structure of H_4L·DCM·6.5 MeOH (the disordered solvents of crystallisation were accounted for using a SQUEEZE routine of PLATON and are not displayed). (a) Representation of main building block of the motif, made of two superimposed wedge shaped molecules, side view, (b) overall network.

On a supramolecular level, the macrocyclic molecules assemble into dimeric units (**Figure 2.3**, (a)). The assembly results in a cavity that accommodates the solvent of crystallisation by hydrogen bonding No obvious interactions were observed between two adjacent units (**Figure 2.3**, (d)).

2.4.3 Reduction of H_4L

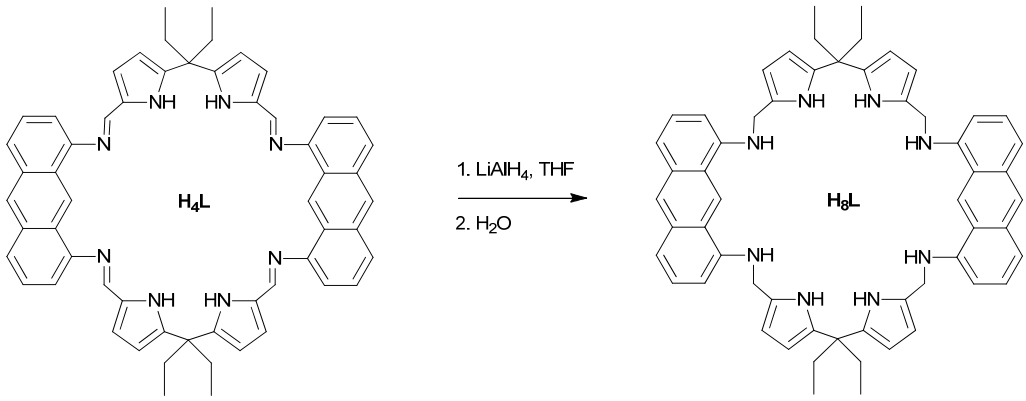

Scheme 2.8 : Synthesis of H_8L by reduction of H_4L.

No reduction of H_4L was observed using sodium borohydride. However, the reaction between H_4L and lithium aluminium hydride in THF followed by quenching with water afforded the tetraamino-tetrapyrrolic macrocycle H_8L (**Scheme 2.8**). The product was characterised by ^1H NMR spectroscopy only. In the ^1H NMR spectrum, the absence of the imine resonance at 8.30 ppm and the appearance of two singlets at

4.34 ppm (4H, N*H*) and 4.26 ppm (8H, CH_2) are consistent with the reduction of the imine bonds. The full characterisation of H_8L would require a scale up of the reduction reaction and a proper aqueous work up to be carried out. Upon deprotonation H_8L would potentially generate an L^{8-} ligand and stabilise either four metal(II) cations or two metal cations of higher oxidation states, e.g. M(IV).

2.4.4 Attempted synthesis of H_4L'

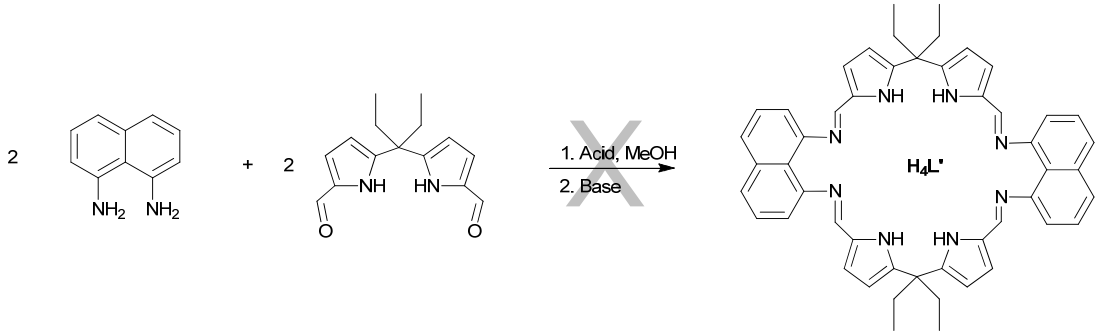

Scheme 2.9 : Attempted synthesis of H_4L by condensation reaction between *meso*-diethyl-5,5′-diformyl-2,2′-dipyrromethane and 1,8-diaminonaphthalene in the presence of an acid.

The condensation of 1,8-diaminonaphthalene with *meso*-diethyl-5,5′-diformyl-2,2′-dipyrromethane in methanol at 0 °C in the presence of hydrochloric acid followed by neutralisation with triethylamine yielded a green-yellow solid (**Scheme 2.9**). The ^{1}H NMR spectrum of this solid consisted of broad resonances and showed no imine-like resonances. Variation of the reaction conditions proved to be unsuccessful. The purification of 1,8-diaminonaphthalene by recrystallisation or sublimation did still not afford a high purity starting material and the quality of the starting materials was found to be crucial for this type of condensation reaction. No further investigation was carried out as the resulting ligand would lead to metallic complexes with very small metal-metal separations which are not of direct interest to small molecule activation.

2.4.5 Synthesis of H_4L" and H_4L"'

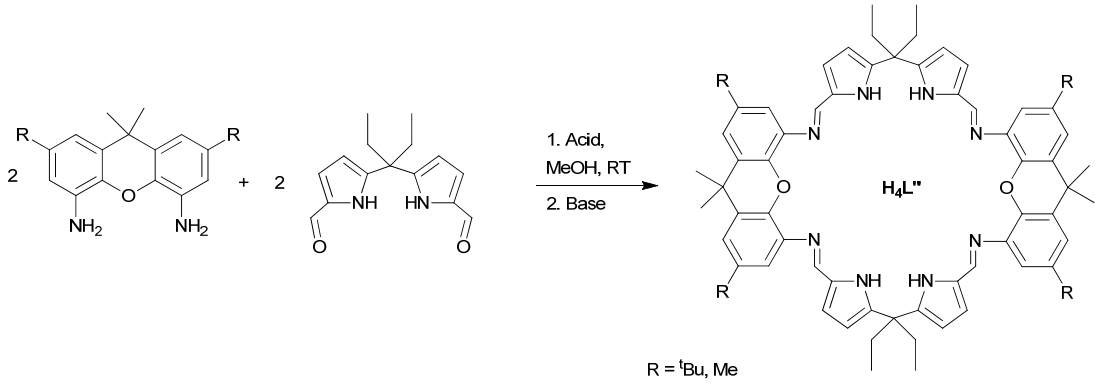

Scheme 2.10 : Synthesis of H_4L by condensation reaction between *meso*-diethyl-5,5′-diformyl-2,2′-dipyrromethane and 4,5-diamino-2,7-di-*tert*-butyl-9,9-dimethylxanthene (R = ^{t}Bu) or 4,5-diamino-2,7,9,9-tetramethylxanthene (R = Me) in the presence of an acid.

The reaction between 4,5-diamino-2,7-di-*tert*-butyl-9,9-dimethylxanthene and *meso*-diethyl-5,5′-diformyl-2,2′-dipyrromethane in the presence of TFA afforded an orange solution from which a yellow solid precipitated upon neutralisation with potassium hydroxide (**Scheme 2.10**); potassium hydroxide was chosen over triethylamine to facilitate the precipitation of the product. The ^{1}H NMR spectrum of this yellow solid exhibited a large number of resonances in the range 0 to 9.5 ppm amongst which characteristic resonances could be identified: three resonances at 9.42 ppm, 9.34 ppm and 9.24 ppm indicate that aldehyde groups remain whilst resonances at 8.38 ppm and 8.27 ppm support the formation of imine bonds. In the aliphatic region, at least two different environments could be identified for the ethyl groups (quartets at 2.23 and 2.09 ppm and triplets at 0.60 and 0.44 ppm) as well as *tert*-butyl signals (singlets at 1.40, 1.35 and 1.24 ppm) and the methyl signals (singlets at 1.65, 1.62 and 1.59 ppm). This suggests that Schiff-base condensation is occurring but the reaction is not complete; longer reaction times and heating might be required to drive the condensation to completion. Nevertheless, the ESI-mass spectrum exhibits the parent peak for the [2+2] macrocycle H_4L expected at m/z = 1149, as well as a peak at m/z = 575 corresponding to the mass of a [1+1] adduct. These observations are similar to the data obtained for H_4L, and the [1+1] adduct is believed to form from fragmentation of the [2+2] macrocycle. Weaker ion peaks at m/z = 277 and m/z = 353 confirmed the presence of starting material (diformyl-dipyrromethane + H_3O^+

and diamine respectively) and confirmed that the reaction had not reached completion.

Condensation reactions catalysed with tetrafluoroboric acid and *para*-toluenesulfonic acid were attempted under similar conditions and yielded similar material by ^{1}H NMR spectroscopy and optimisation of the reaction conditions would be required to yield H_4L as a pure compound.

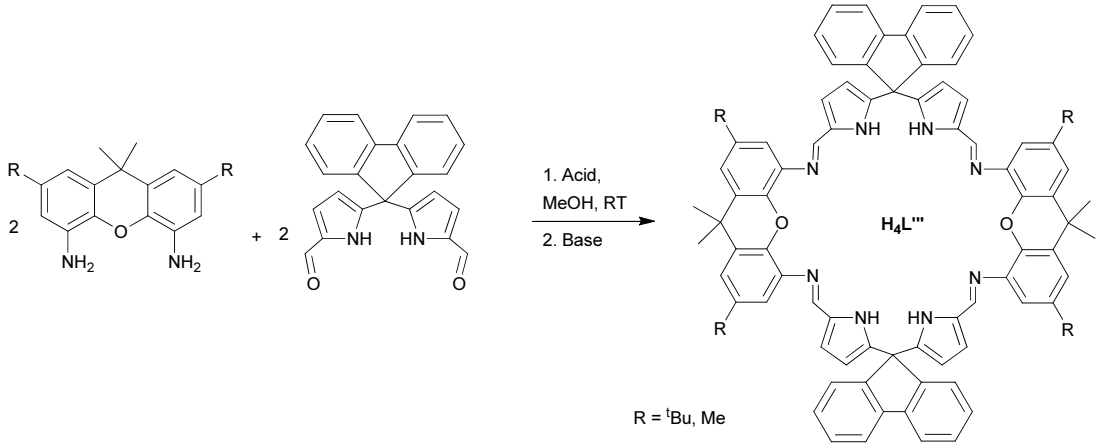

Scheme 2.11 : Synthesis of H_4L by condensation reaction between *meso*-fluorene-5,5′-diformyl-2,2′-dipyrromethane and 4,5-diamino-2,7-di-*tert*-butyl-9,9-dimethylxanthene in the presence of a Lewis acid.

A condensation reaction was carried out between *meso*-fluorene-5,5′-diformyl-2,2′-dipyrromethane and 4,5-diamino-2,7-di-*tert*-butyl-9,9-dimethylxanthene (R = ^{t}Bu on **Scheme 2.11**); the reaction time was increased to 45 minutes, the liquors were concentrated under reduced pressure and the resulting mixture was neutralised with triethylamine. Trituration with hexane, then ether afforded a pale yellow solid in a 23% yield. The product obtained has high solubility in organic solvents due to the *tert*-butyl groups on the xanthene backbone and the replacement of triethylamine by potassium hydroxide for the neutralisation of the acid salt is expected to dramatically improve the yield. The ^{1}H NMR spectrum exhibits the expected resonances for the formation of a [2+2] macrocycle. The proton resonance for the imine C*H* is broad and is observed at 8.16 ppm which is quite unusual as this signal is usually a sharp signal between 8.30 ppm and 8.40 ppm. The resonances for the pyrrolic protons are also surprisingly broad and one of these two signals is observed at 5.58 ppm, which is quite a shielded signal for this type of protons (pyrrolic protons usually appear as

well resolved doublets between 6 ppm and 7 ppm). The broadness of the signals could be indicative of a more rigid macrocycle or higher cyclisation products.

The same condensation reaction was carried out with 4,5-diamino-2,7,9,9-tetramethylxanthene (R = Me on **Scheme 2.11**) and *meso*-fluorene-5,5′-diformyl-2,2′-dipyrromethane. Again, the presence of imine resonances and remaining dialdehyde resonances were observed, suggesting that an increase of the reaction time is necessary.

2.4.6 Conclusion

The new macrocycle based on the anthracene backbone, H_4L, was generated from readily available materials and the synthesis was found to be quite straightforward, high yielding and easily achievable on a large scale. The poor solubility of the anthracenyl backbone is counter-balanced by the *meso*-ethyl groups which provide sufficient solubility to carry out reactions and yet eases the isolation of most complexes as solids as described in the following sections. Considering the advantages of H_4L, the present work was focused on studying the complexation abilities of this ligand (see the following section of this Chapter) and on investigating the properties of the complexes generated as catalyst for the reduction of oxygen (see **Chapter 3**) or as an anion receptor (see **Chapter 4**).
Synthetic routes to a few enlarged hinge macrocycles have also been investigated and promising results were obtained using xanthene diamines. The synthesis of these macrocyclic ligands requires optimisation of the reaction conditions to obtain clean compounds in good yields and on a large scale. These ligands would provide a desired intermetallic separation as well as enhanced solubility properties. Furthermore, their cofacial diporphyrin counterpart, H_4DPX, supports the most effective cobalt-diporphyrin catalyst for the ORR and it would be very interesting to investigate the properties of the double-pillared equivalent.

2.5 Possible geometries adopted on metallation of H_4L

H_4L is a tetraimino-tetrapyrrolic ligand and proved to be very versatile. Ligands of the same type developed within the Love group and the Sessler group proved to have two main types of reactivity.

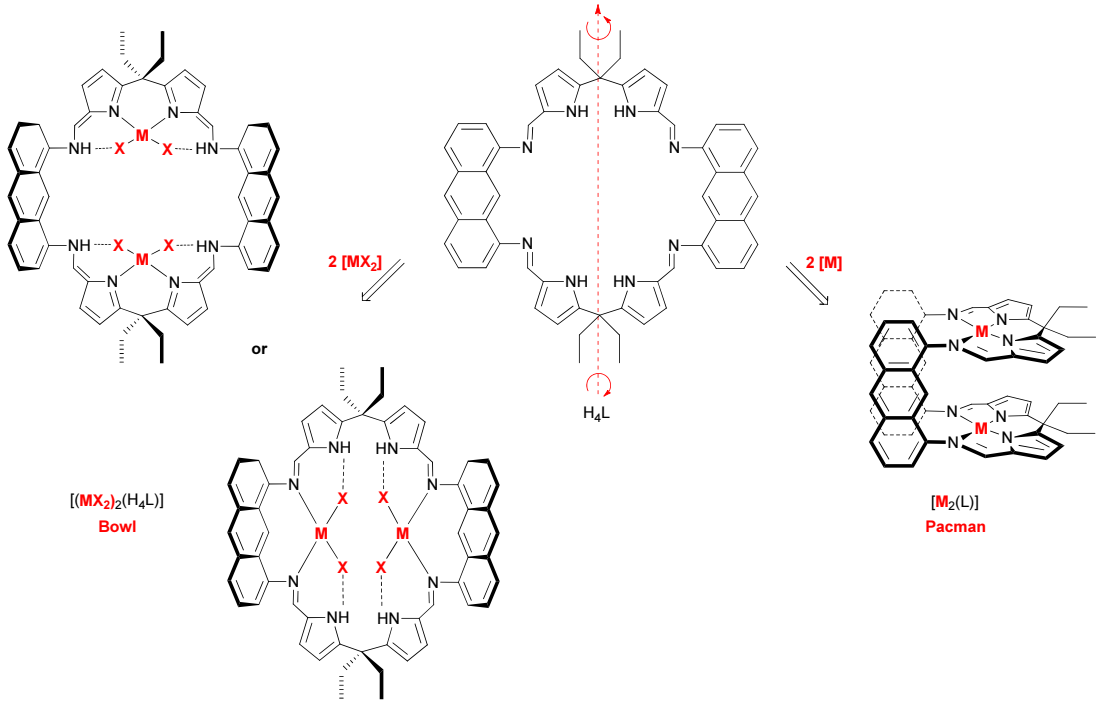

Chart 2.2 : Possible complex geometries generated by metallation of L.

Macrocycles related to H_4L were shown to act as a neutral ligand and accommodate two metal centres. Two coordination modes, both resulting in bowl shaped complexes, can then be expected: the metal can coordinates either to the two imine nitrogen atoms of one anthracene hinge, with the other ligands hydrogen binding to the pyrrolic N*H* (**Chart 2.2**, bottom left), or to the pyrrolic nitrogen atoms with an imine-pyrrole to amine-azafulvene tautomerisation of the macrocycle and the other ligands can hydrogen bond to the resulting amine NH. (**Chart 2.2**, top left).

Alternatively, the deprotonation of the pyrrolic N*H*s affords L^{4-} and the accommodation of two di-cationic metals or four mono-cationic metals is possible. The accommodation of one or two M^{2+} cations triggers the folding of the macrocycle around the metal centres affords a Pacman cofacial arrangement (**Chart 2.2**, right).[5, 7, 20-24] The two metals are held at a well tuned distance and in a very precise

environment pre-organised by the ligand design. As the relative position of the metallic centres is crucial for the activation of small molecules, this coordination mode is the main focus of the work presented here. The principal features of these complexes are presented in **Figure 2.4**.

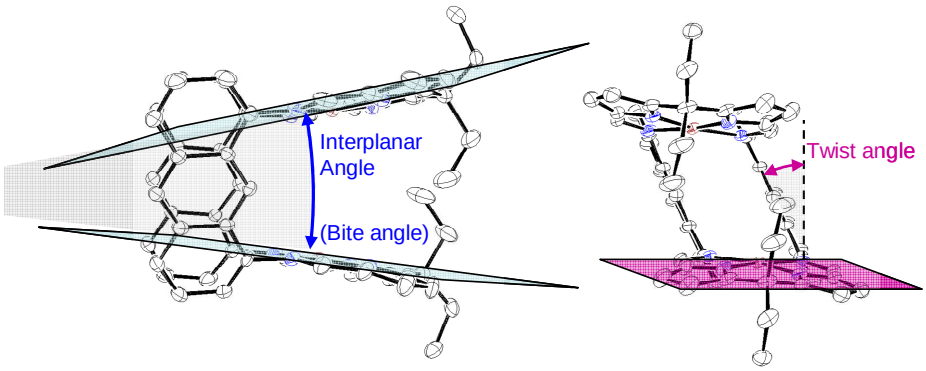

Figure 2.4 : Typical X-ray crystal structure of $[M_2(L)]$ showing the definitions of the important geometric parameters. Interplanar angle: angle between the two N_4-mean planes, twist angle: mean angle between the N_4-mean plane and the mean plane defined by the 14 carbon atoms of the anthracenyl backbone.

The reactivity of H_4L towards deprotonation and metallation was investigated through several synthetic routes and with reactants ranging from group 1 and group 2 metals to transition metals and even actinides.

2.6 Synthesis and characterisation of group 1 and group 2 metal complexes of L

2.6.1 Synthesis of $[K_4(L)]$

$$H_4L \xrightarrow[-\,2\,H_2]{4\,KH,\ THF} [K_4(L)]$$

Equation 2.1 : Synthesis of $[K_4(L)]$ by acid-base reaction.

The reaction of 5 equivalents of potassium hydride with H_4L in THF solution under nitrogen resulted in the evolution of hydrogen and the formation of $[K_4(L)]$ (**Equation 2.1**). After filtration to remove the excess potassium hydride and solvent removal under reduced pressure, the potassium salt was isolated as its THF adduct as

a red-orange solid in good yield. The solubility of $[K_4(L)]$ in THF is limited and its ^{1}H NMR spectrum is consistent with an aggregated product. The spectrum recorded in d_5-pyridine is better resolved and highlights the disappearance of the pyrrolic N*H* resonance as well as the presence of 2.65 molecules of THF per macrocycle (coordinated solvent displaced by pyridine). Furthermore, the broadness and multiplicity of resonances suggest a completely de-symmetrised macrocycle: the four resonances observed for the *meso*-ethyl CH_2 protons at 3.49, 3.14, 2.79 and 2.73 ppm are indicative of (1) a cleft shaped molecule with the ethyl groups *endo*- and *exo*- to the cavity and (2) different environments between the two binding pockets. Unfortunately, no crystal suitable for X-ray diffraction was obtained to gain extra insight but a cleft shaped potassium salt was observed for the previously developed ligand L^1 and appears as the most probable arrangement.[7] The IR spectrum no longer displays an NH stretch (seen at 3250 cm^{-1} in the IR spectrum of H_4L) and the shift of the imine bond stretch to lower frequencies, from 1613 cm^{-1} in H_4L to 1583 cm^{-1} in the potassium salt, confirms the potassium coordination. Finally, elemental analysis is consistent with the expected composition for $[K_4(L)]\cdot 2.65THF$. Although $[K_4(L)]$ can be isolated, it was usually generated *in situ* to react immediately with metal halides.

2.6.2 Synthesis of $[Li_4(L)]$

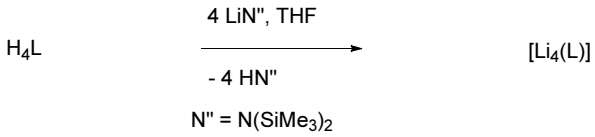

Equation 2.2 : Synthesis of $[Li_4(L)]$ by transamination reaction.

In contrast to potassium hydride, lithium hydride does not react with H_4L. Nevertheless, the transamination reaction with four equivalents of lithium bis(trimethylsilylamide) (LiN″) in THF solution yields the lithium salt $[Li_4(L)]$ as a deep orange solution in 95% yield by ^{1}H NMR spectroscopy (**Equation 2.2**). Solvent removal under reduced pressure affords a yellow solid in high yield, and $[Li_4(L)]$ was studied *in situ* only due to its high reactivity. In the ^{1}H NMR spectrum of $[Li_4(L)]$, no pyrrolic N*H* resonances were observed and the presence of a single doublet of

doublets and a single triplet for the *meso*-ethyl groups suggests that the salt is highly symmetric in solution (similar to the shape of H_4L in the solid state). This symmetry is also apparent in the $^{13}C\{^1H\}$ NMR spectrum although the ^7Li NMR spectrum revealed three inequivalent lithium environments. $[Li_4(L)]$ was usually generated *in situ* due to its high reactivity.

2.6.3 Synthesis of $[Mg_2(L)]$

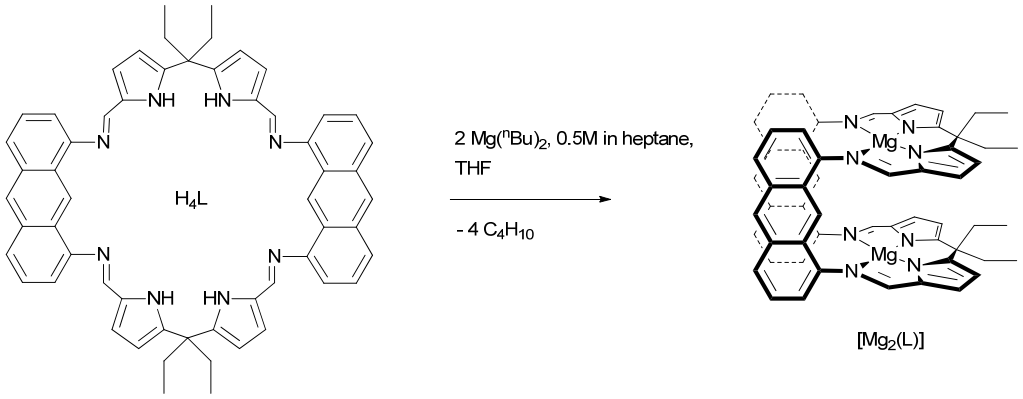

Scheme 2.12 : Synthesis of $[Mg_2(L)]$ by reaction of H_4L with an alkyl-metal.

The protonolysis reaction of H_4L with di-butylmagnesium in THF, followed by layering with hexane affords $[Mg_2(L)]\cdot 2THF$ as a microcrystalline solid (**Scheme 2.12**). In the ^1H NMR spectrum in THF/d_6-benzene, only one quartet is observed at 2.05 ppm, the second one is not observed due to the signal overlapping with one of THF (the resonance gets suppressed with the solvent signal). Yet, the presence of two triplets at 0.85 ppm and 0.60 ppm corresponding to the terminal -C*H*$_3$ of the *meso*-ethyl groups confirm the presence of an *endo*- and an *exo*-environment for these groups, so suggesting that a Pacman structure is adopted in solution. Furthermore, the $^{13}C\{^1H\}$ NMR spectrum shows two *C*H$_2$ carbon resonances at 40.51 ppm and 30.35 ppm as well as *C*H$_3$ carbon resonances at 9.99 ppm and 9.24 ppm, confirming the Pacman arrangement. The ^1H NMR spectrum recorded in d_5-pyridine revealed the missing resonance; as expected two multiplets (at 2.03 ppm and 1.48 ppm) and two triplets (at 0.68 ppm and 0.07 ppm) were observed. Integration of the displaced THF resonances showed that there were two per bimetallic complex. Furthermore, the IR spectrum of the compound does not display an N-H stretch and the shift of the C=N stretch to

1572 cm^{-1} from 1613 cm^{-1} in H_4L confirms metal coordination. Dissolution of $[Mg_2(L)]$ in pyridine requires heating and the complex crystallises in bulk upon cooling as orange blocks suitable for an X-ray diffraction study. The structure of $[Mg_2(\textit{endo}\text{-py})(\textit{exo}\text{-py})_2(L)]\cdot 5py$ was determined and is displayed in **Figure 2.5** with crystal data and selected bound length and angles in **Appendix 2** and **Appendix 3**.

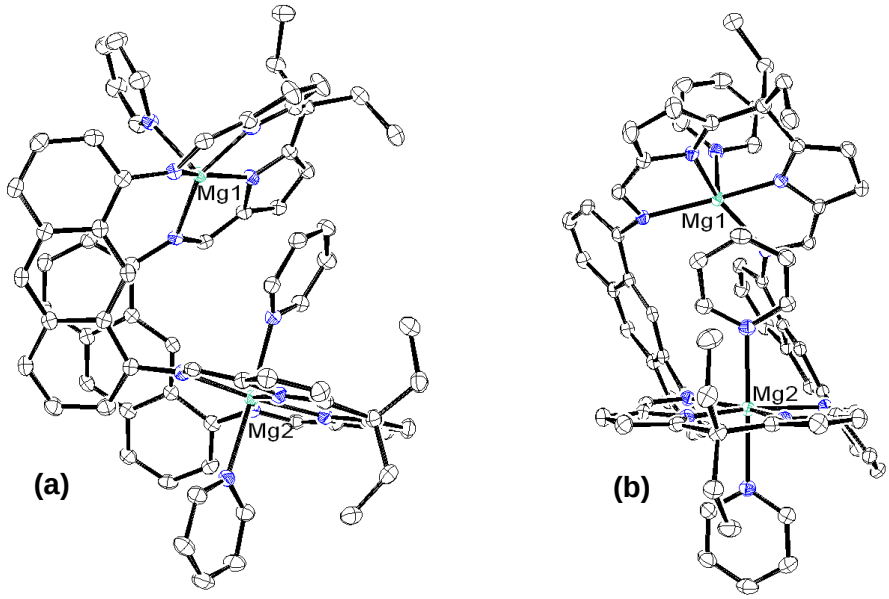

Figure 2.5: X-ray crystal structure of $[Mg_2(\textit{exo}\text{-py})_2(\textit{endo}\text{-py})(L)]\cdot 5py$ (displacement ellipsoids are drawn at 50 % probability), (a) side view, (b) face view. For clarity, the toluene solvent of crystallisation and all hydrogen atoms are omitted.

As suggested by the ^1H NMR spectroscopic data, the bis-magnesium complex, $[Mg_2(\textit{exo}\text{-py})_2(\textit{endo}\text{-py})(L)]$, adopts a double-pillared Pacman geometry in the solid state, featuring two *exo*-ethyl (pointing away from the molecular cavity) and two *endo*-ethyl substituents (pointing towards the molecular cavity). The asymmetric unit contains one molecule of $[Mg_2(\textit{exo}\text{-py})_2(\textit{endo}\text{-py})(L)]$ in which Mg1 is bound to an *exo*-pyridine and Mg2 is bound both to an *exo*- and an *endo*-pyridine. The accommodation of an end-on *endo*-pyridine molecule within the cavity was unexpected: it prevents the cofacial arrangment and generates a very distorted molecule. In contrast to crystal structures obtained with the related ligands L^n (n = 1 to 10) where the two hinges are superimposed in a face-to-face manner, the anthracenyl backbones in $[Mg_2(\textit{exo}\text{-py})_2(\textit{endo}\text{-py})(L)]$ are staggered but still exhibit some face-to-face π-stacking with a 3.481(3) Å shortest contact and a deviation from

coplanarity of 13.76°. The distortion of the molecule also generates a remarkably large bite angle of 54.84° which is in contrast to the initial design as the two anthracenyl moieties were chosen to favour a cofacial arrangement (i.e. a bite angle close to 0°). Another consequence of the unusual arrangement is the 6.272(1) Å intermetallic separation between Mg1 and Mg2. By design of H_4L, this separation in a cofacial complex would be largely imposed by the size of the hinge and approximate 5 Å (H_4L presents a 4.998(7) Å N1···N8 separation and a 5.063(8) Å N4···N5 separation in the solid state). Interestingly, the 28.14° twist angle is within the range observed for related wedge shaped complexes. Mg1 is bound to an *exo*-pyridine ligand and is accommodated with a pseudo square-based pyramidal geometry. The metal is located 0.340 Å away from the N_4-basal plane, towards the pyridine ligand. The second metal, Mg2, is accommodated within a pseudo-octahedral geometry, with the *exo*-pyridine in trans-position to the *endo*-pyridine, and Mg2 lays within the diimino-dipyrrolic plane (Mg2···N_4-donor plane: 0.004 Å). No supramolecular interaction was observed within the extended structure. This is the first bis-magnesium complex of either this type of Pacman ligands or the cofacial diporphirin/dicorrole family to be structurally characterised by an X-ray diffraction study, the M···N distances will therefore be compared to those observed in salen and porphyrin complexes for the M···N(imine) and M···N(pyrrole) distances respectively. For [Mg_2(*exo*-py)$_2$(*endo*-py)(L)], the 2.21 Å average M···N(imine) is larger than the 2.14 Å distance observed in the only structurally characterised magnesium salen complex while the 2.06 Å M···N(pyrrole) is slightly smaller than the average observed in magnesium porphyrins (CCDC: 28 examples –mean 2.24 Å, range 1.97 Å to 2.95 Å).[25] These observations are most likely attributable to the distorted nature of the complex which forces the imino-nitrogen atoms away from the metallic centre and the pyrrolic-nitrogen atoms are slightly closer to the metallic centre as a result.

2.7 Synthesis and characterisation of transition metal complexes of L

2.7.1 Synthesis of $[Pd_2(L)]$

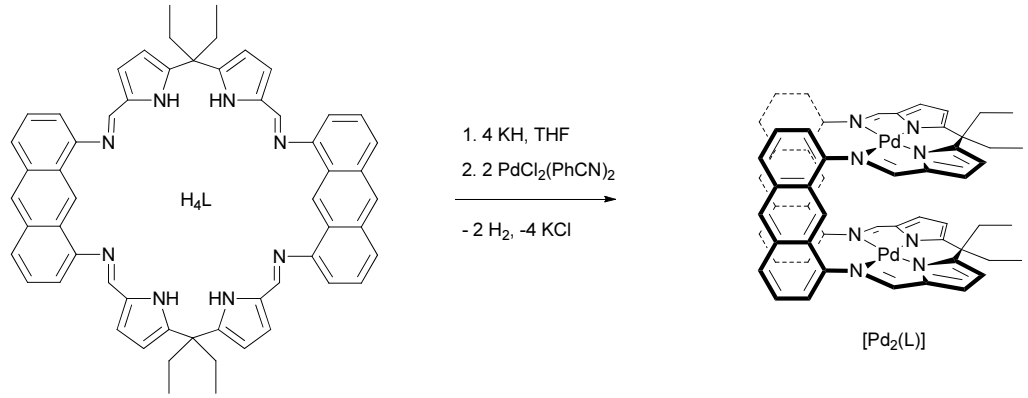

Scheme 2.13: Synthesis of $[Pd_2(L)]$ by salt elimination reaction.

The reaction between $[Pd_2Cl_2(PhCN)_2]$ and $[K_4(L)]$, prepared *in situ* in THF, was carried out for 20 days in the dark (**Scheme 2.13**) and was the most straightforward route to the binuclear palladium complex $[Pd_2(L)]$ which crystallised from THF as a poorly soluble yellow solid in low yield. Reactions for shorter time periods gave lower yields of the desired product. The ^1H NMR spectrum of $[Pd_2(L)]$ shows two sets of *meso*-ethyl-substituent resonances: two quartets at 2.15 and 1.89 ppm (CH_2) and two triplets at 0.51 and 0.27 ppm (CH_3) (**Appendix 1**) and is characteristic of a cofacial ligand geometry in solution. This feature is corroborated in the $^{13}C\{^1H\}$ NMR spectrum which displays two secondary carbon resonances at 40.0 and 36.6 ppm (CH_2) and two primary carbon resonances at 11.2 and 10.4 ppm (CH_3); the quaternary *meso*-carbon could not be located in the $^{13}C\{^1H\}$ NMR spectrum due to the poor solubility of the compound. In the IR spectrum of $[Pd_2(L)]$, the disappearance of the N-H stretch (υ = 3250 cm^{-1} in H_4L) and a shift of the C=N stretch to lower energies (from 1613 in H_4L to 1570 cm^{-1}) supports the coordination of the metal by the macrocycle. The electrospray mass spectrum of $[Pd_2(L)]$ showed a molecular ion $[Pd_2(L)]^+$ at m/z = 1070 and its sodium adduct $[NaPd_2(L)]^+$ at m/z = 1093 with the expected isotopic pattern, and elemental analysis further supported the proposed molecular formula.

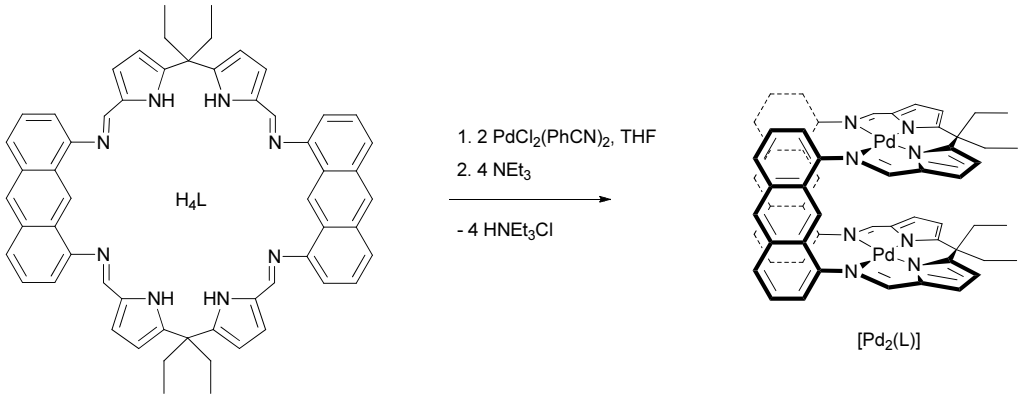

Scheme 2.14: Synthesis of $[Pd_2(L)]$ by reaction of a metal chloride in the presence of a base.

As an alternative synthetic procedure, $[Pd_2(L)]$ can also be accessed by the reaction between H_4L and $[PdCl_2(PhCN)_2]$ in the presence of triethylamine (**Scheme 2.14**), although yields from this route were generally lower. However, the ^1H NMR spectrum of the product from this route is identical to that described above, and yellow crystals suitable for an X-ray diffraction study were isolated by solvent evaporation from a d-chloroform solution. The structure of $[Pd_2(L)].NEt_3.CDCl_3$ was determined and is shown in **Figure 2.6** with crystal data and selected bond length and angles in **Appendix 2** and **Appendix 3**.

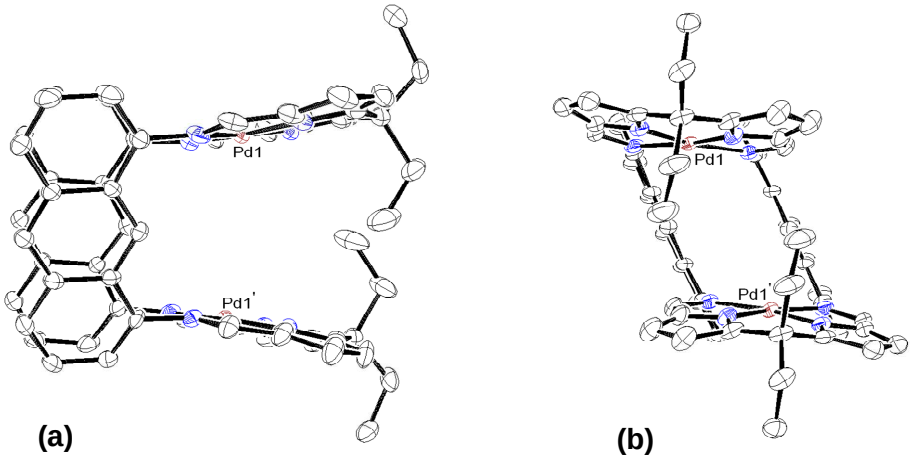

Figure 2.6: X-ray crystal structure of $[Pd_2(L)]\cdot NEt_3\cdot CDCl_3$ (displacement ellipsoids are drawn at 50% probability), (a) side view, (b) face view. For clarity, the chloroform solvent of crystallisation and all hydrogen atoms are omitted. (The triethylamine molecule of crystallisation was accounted for using the SQUEEZE routine of PLATON)

As for $[Mg_2(L)]$ and other binuclear-palladium complexes previously characterised within the Love group, the macrocyclic ligand folds at the

meso-position to accommodate the metal centres. This has resulted in the formation of a double-pillared cofacial complex in which the two anthracenyl moieties π-stack in a face-to-face manner with a shortest contact of 3.620(8) Å and are coplanar (interplanar angle 7.6°). In contrast to the structure of $[Mg_2(L)]$, the aromatic backbones are superimposed and the overall geometry exhibits much smaller distortions. The two metal coordination planes are almost planar and show a slight divergence away from co-planarity (interplanar angle 15.3°); this deviation from co-planarity is likely attributable to a steric clash between the ethyl *meso*-substituents. Overall, the complex adopts a lateral twist of 29.4°, again possibly due to the steric hindrance provided by the ethyl *meso*-substituents. Each N_4-donor compartment offers a *pseudo*-square-planar environment to the metal (sum of angles at Pd1 359.4°) and the palladium is located 0.122 Å out of the N_4-mean plane. The triethylamine molecule was disordered and was accounted for using the SQUEEZE routine of PLATON. No particular supramolecular assembly pattern was observed within the packing diagram of $[Pd_2(L)]\cdot NEt_3\cdot CDCl_3$.

The introduction of the anthracenyl backbone results in a Pd···Pd separation which is longer by *ca*. 1.3 Å than those seen in the 1, 2-aryl-hinged complexes and similar to those observed for the related anthracenyl porphyrinic complexes (**Table 2.2**). The average Pd-N(imine) and Pd-N(pyrrole) distances are however very similar to those observed in the 1,2-aryl-hinged complexes (2.08 and 1.93 Å respectively, 1,2-aryl-hinged complexes: 6 examples, Pd-N(imine): mean 2.07 Å, range 2.04 Å to 3.0 Å, Pd-N(pyrrole): mean 1.93 Å, range 1.92 Å to 1.95 Å). This ligand proffers a geometric arrangement very similar to the diporphyrin DPA and dicorrole DCA ligands,[30] and $[Pd_2(L)]$ can be viewed as a double-pillared analogue of the series of well-known single-pillared complexes $[M_2(DPA)]$.[1, 9, 26, 31, 32] As the solid state structures of $[Pd_2(DPA)]$ and $[Pd_2(DCA)]$ are unknown, the structurally-characterised cofacial diporphyrin H_4DPA[26] and its metal complexes $[Co_2(DPA)]$[26] and $[Ni_2(DPA)]$[27] are used for comparison (**Table 2.2**), along with the related dicorrole complexes $[Cu_2(DCA)]$[33] and $[Ni_2(DCA)]$.[34] While the twist angle for $[Pd_2(L)]$ is similar to those seen in the structures of $H_4(DPA)$,

[Co_2(DPA)], and [Ni_2(DPA)], the interplanar angle is larger for [Pd_2(L)] than for the diporphyrin analogues which suggests that the mouth of the cleft can expand vertically, as observed in the solid state structure of [Mg_2(L)].

Compound	M···M [Å]	Twist [°]	Interplanar Angle [°]
[Pd_2(L)][10]	5.377(1)	29.4	15.3
[Pd_2(L^1)][21]	3.7618(5)	19.35	53.07
[Pd_2(L^2)][20]	4.11/4.12[a, b]	11.1	62.1
[Pd_2(L^3)][20]	3.5440(4)	23.91	46.87
[Pd_2(L^4)][21]	3.8274(6)	28.5	59.7
[Pd_2(L^5)][20]	3.94[a]	28.5	59.7
[Pd_2(L^{10})][10]	3.720(1)	27.8	56.4
[Co_2(DPA)][26]	4.53	36.6	3.0
[Ni_2(DPA)][27]	4.57	31.7	3.1
H_4(DPA)[26]	4.52[c]	22.1	-10.2
[Cu_2(DCA)][d, 28]	6.35	19.9	18.9
[Ni_2(DCA)][29]	4.68	22.4	9.4

Table 2.2: Comparison between the X-ray structural data of [Pd_2(L)], other bis-palladium complexes isolated in the Love group, the anthracenyl-based cofacial diporphyrin H_4(DPA) and its Co and Ni complexes, and the Co and Ni complexes of the anthracenyl-based cofacial dicorrole H_4(DCA). [a]Estimated standard deviation (esd) not published; [b]two molecules in the asymmetric units; [c]distance between the centroids of the two N_4-binding sites; [d]a molecule of toluene is sandwiched within the bimetallic cleft.

Various binuclear DPA and DCA compounds have been characterised structurally, and the M···M separations (range: DPA 3.49 to 6.17 Å; DCA 4.68 to 7.46 Å)[25] show that these ligands allow considerable vertical flexibility. The presence of endogenous solvent or ligands (*e.g.* methanol) is found to cause vertical expansion whereas single-atom bridging ligands (*e.g.* O or OH) promote closer interaction of the metallo-porphyrinic compartments. It is anticipated that the combination of the longer M···M separations and the presence of the very rigid double-anthracenyl pillars in [M_2(L)] complexes would limit the stability of singly-atom bridged complexes when the metallic centre is preferably

accommodated in a square planar or octahedral environment; this would favour diatomic bridges over monoatomic ones.

2.7.2 Synthesis of $[(FeCl)_2(L)]$, $[Fe_2(L)]$ and $[Fe_2(\mu\text{-}O)(L)]$

2.7.2.1 *Synthesis of $[(FeCl)_2(L)]$*

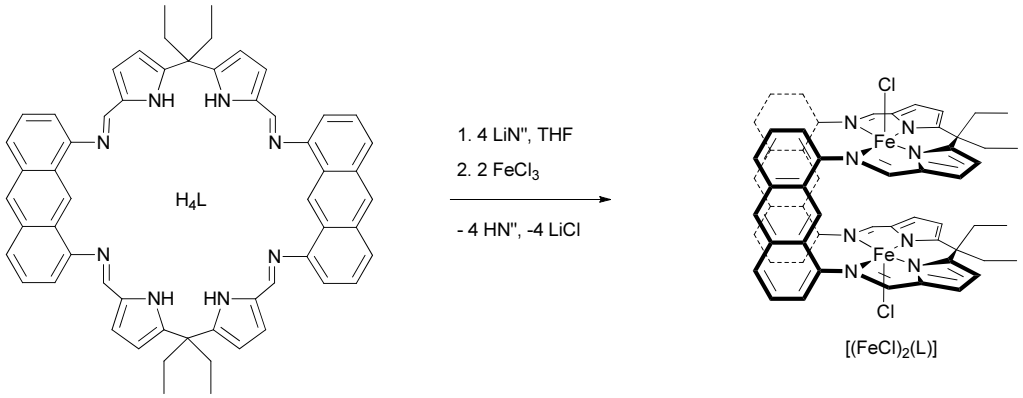

Scheme 2.15: Synthesis of $[(FeCl)_2(L)]$ by salt elimination reaction.

The *in situ* synthesis of the lithium salt $[Li_4(L)]$ followed by reaction with two equivalents of iron trichloride in THF solution, and concentration of the solution under reduced pressure, afforded the binuclear iron complex $[(FeCl)_2(L)]$ as a black solid (**Scheme 2.15**). The ^1H NMR spectrum exhibits 11 resonances between 40 and -65 ppm (a resonance could not be assigned with certainty due to overlapping with the THF suppressed signals) and is consistent with the formation of the symmetrically-disposed cofacial complex $[(FeCl)_2(L)]$ in which the metal atoms adopt square-based pyramidal geometries. As with the palladium complex $[Pd_2(L)]$, the absence of N-H vibration and the C=N stretch at 1575 cm^{-1} in the IR spectrum support the formation of the desired compound, and elemental analyses are consistent with the expected composition. Unfortunately, crystals suitable for X-ray diffraction could not be obtained, but the chemical reduction of the complex (see the next section) further supports its nature.

2.7.2.2 *Synthesis of [Fe_2(L)]*

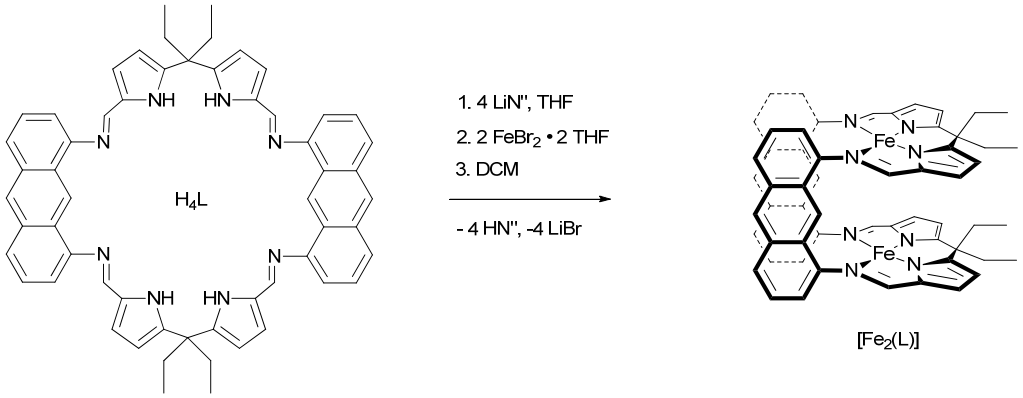

Scheme 2.16: Synthesis of [Fe_2(L)] by salt elimination reaction.

The salt elimination reaction between [K_4(L)], generated *in situ*, and iron dibromide in THF followed by filtration of the salt by-product affords [Fe_2(L)] as a deep red solid (**Scheme 2.16**). While the silent ^{1}H NMR spectrum is consistent with the formation of a high spin square planar or square pyramidal Fe(II) complex, the high reactivity of the product towards oxygenation prevented its isolation as a pure solid sample. Alternatively, [Fe_2(L)] could be synthesised from the lithium salt [Li_4(L)] under similar conditions. The ^{1}H NMR spectrum of the crude product of this reaction exhibits 9 resonances between -70 and 60 ppm (extra resonances could be hidden by the THF suppressed signals or are simply not observed due to the paramagnetic nature of the complex). The complex obtained after extraction in dichloromethane and filtration was NMR silent which is consistent with a change in geometry caused by the extraction and the isolation of [Fe_2(L)]; although its high reactivity towards oxygen prevented the isolation of an analytically pure solid sample.

Even though no further characterisation data could be gained on this compound, comparison to the anion recognition ability observed for the binuclear zinc complexes of L (see C**hapter 4**) and analogy to other complexes described in the literature,[35] lead us to propose that that the reaction initially formed then "-ate" complex [Li(THF)$_4$][Fe_2(μ-Br)(L)], and the loss of lithium bromide upon extraction of the complex in dichloromethane would be consistent with observation made during isolation attempts of [K][Zn_2(μ-Cl)(L)].

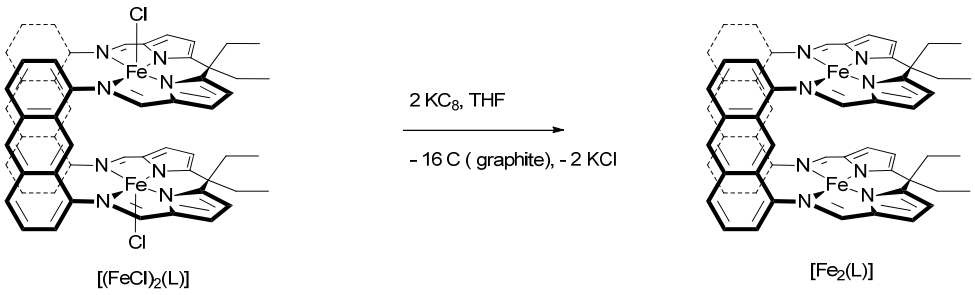

Scheme 2.17: Synthesis of $[Fe_2(L)]$ by reduction of $[(FeCl)_2(L)]$.

Alternatively, $[Fe_2(L)]$ can also be synthesised by the reduction of $[(FeCl)_2(L)]$. As such, $[(FeCl)_2(L)]$ was generated in-situ as described above and the deep brown suspension obtained was reacted with C_8K in THF (**Scheme 2.17**). This caused the dissolution of the solids, a subtle colour change to a deep red and the formation of a black solid which is consistent with the generation of graphite. After filtration, the THF-supressed ^1H NMR spectrum was mainly silent (weak paramagnetic resonances were observed and attributed to impurities) which is consistent with the formation of $[Fe_2(L)]$. The full characterisation of $[Fe_2(L)]$ synthesised by this route would require a scale-up of the reaction and further investigation.

2.7.2.3 *Synthesis and structure of $[Fe_2(\mu\text{-}O)(L)]$*

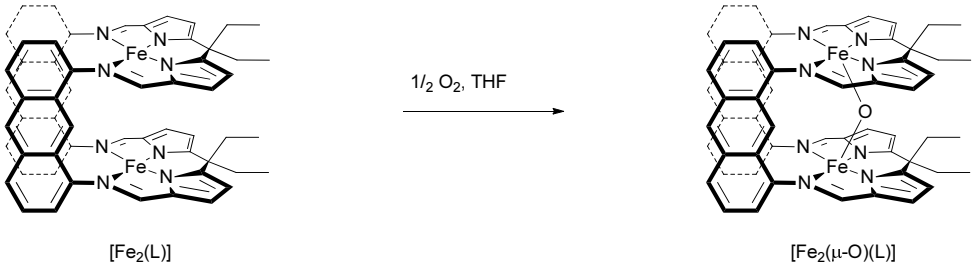

Scheme 2.18: Synthesis of $[Fe_2(\mu\text{-}O)(L)]$ by oxidation of $[Fe_2(L)]$.

In an attempt to further characterise by inference, $[Fe_2(L)]$ was generated *in-situ* from the potassium salt as described above and the resulting THF solution was exposed to air (**Scheme 2.18**). The solution turned black instantly and an analytically pure sample of $[Fe_2(\mu\text{-}O)(L)]$ was isolated. The ^1H NMR spectrum exhibits 9 resonances between 45 and -5 ppm, most of which are located in the diamagnetic region of the spectrum. For this reason, the full assignment of the spectrum was not possible due to the overlapping of the resonances with the

suppressed broad signals of the THF solvent; the best resolved resonances are two singlets observed at 44.15 ppm and 23.46 ppm. The paramagnetic spectrum is consistent with a binuclear iron(III) complex. The absence of an NH stretch in the IR spectrum confirms metallation and the multiplicity of the C=N stretch confirms the change in geometry. Upon diffusion of hexane into a THF solution, crystals suitable for X-ray diffraction were isolated and the structure of $[Fe_2(\mu\text{-}O)(L)]\cdot 0.5\ C_6H_{14}$ was determined and is displayed in **Figure 2.1** with crystal data and bond length and angles in **Appendix 2** and **Appendix 3**.

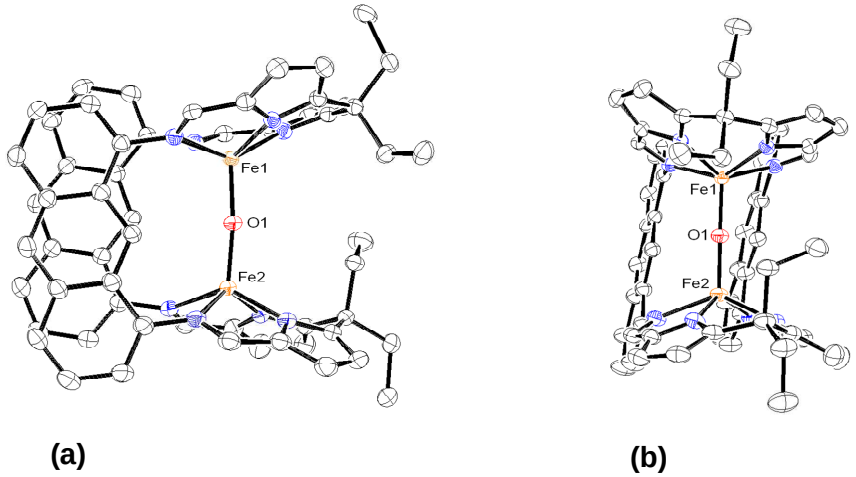

Figure 2.7: X-ray crystal structure of $[Fe_2(\mu\text{-}O)(L)]\cdot 0.5C_6H_{14}$ (displacement ellipsoids are drawn at 50% probability), (a) side view, (b) face view. For clarity, all hydrogen atoms are omitted. (Distorted hexane of crystallisation was located on the 3-fold axis and was accounted for using the SQUEEZE routine of PLATON).

In the solid state, $[Fe_2(\mu\text{-}O)(L)]$ adopts the cofacial, double pillared structure expected with an oxygen atom bridging the two iron atoms. The two anthracenyl groups are slightly slipped and interact through face-to-face π-stacking with a 3.295(2) Å shortest contact; the two backbones deviate from co-planarity by 3.5°. The structure exhibits an 11° interplanar angle and an unusually small 8.8° twist angle. The accommodation of the Fe-O-Fe unit induces a rotation of the pyrrolic units towards the molecular cavity, so enabling the iron atoms to adopt pseudo-square-based pyramidal geometries. This results in displacement from the N_4-basal plane into the cavity of 0.70 and 0.77 Å for Fe1 and Fe2, respectively. The Fe1-O1 and Fe2-O2 bond distances are 1.799(2) and 1.795(1) Å, respectively, with a 173.32(8)° Fe-O-Fe angle and a 3.295(2) Å Fe1···Fe2 intermetallic separation.

Disordered molecules of hexane were located on the 3-fold axis and were accounted for using the SQUEEZE routine of PLATON.

Binuclear iron oxo-complexes are very common and the features observed in [Fe_2(μ-O)(L)] are within the range usually expected (CCDC: 1656 examples – including 38 oxo-bridged haems, with Fe···Fe: mean 3.25 Å, range 2.46 Å to 4.51 Å; Fe-O: mean 1.99 Å, range 1.70 Å to 2.39 Å and Fe-O-Fe: mean 113 °, range 77 ° to 180 °).[25] The M···M distance in [Fe_2(μ-O)(L)] is the shortest observed for all solid-state structures of bimetallic complexes of L. Binuclear iron oxo-complexes of related wedge-shaped Pacman ligands and of DPA were isolated by the Sessler [24] and Lee groups[36] respectively and selected geometric parameters are presented in **Table 2.3** for comparison with [Fe_2(μ-O)(L)]. Compared to the other Pacman complexes, [Fe_2(μ-O)(L)] exhibits a significantly longer intermetallic distance (3.14 Å for the wedge-shape complexes vs. 3.4913(9) Å), the Fe-O bonds of [Fe_2(μ-O)(L)] are on the high side of the 1.67-1.79 Å range observed for the wedge-shaped complexes, the iron is further away from the diimino-dipyrrolic plane (0.59-0.68 Å range compared to 0.70-0.77 Å) and the Fe-O-Fe angle is remarkably obtuse (124-141° range compared to 173° for [Fe_2(μ-O)(L)]). These features are all a result of the separation induced by the anthracene backbones and are a sign of a more strained structure. As such, it is anticipated that the 3.3 Å intermetallic separation is amongst the lowest accessible by complexes of L. The average Fe-N(imine) and Fe-N(pyrrole) distances are once again very similar to those observed in the 1,2-aryl-hinged complexes, with the Fe-N(imine) being slightly larger (2.16 and 2.04 Å respectively, 1,2-aryl-hinged complexes: 3 examples, Fe-N(imine): range 2.10 Å to 2.18 Å, Fe-N(pyrrole): range 2.01 Å to 2.03 Å). The Fe-N(pyrrole) distances are also comparable to those observed in [Fe_2(μ-O)(DPA)] (average 2.08 Å)

The cofacial diporphyrin structural equivalent of [Fe_2(μ-O)(L)], [Fe_2(μ-O)(DPA)], exhibits an even longer 3.4913(9) Å intermetallic separation than the one observed in the double pillared structure and an obtuse angle at the oxygen (165.7(3)°. This is a

direct consequence of the limited flexibility of the porphyrinic rings, which, in contrast to the N_4-donor set of L, are constrained in a flat, aromatic porphyrin.

Compound	M⋯M [Å]	Twist [°]	Interplanar Angle[a] [°]	M⋯O [Å]	M⋯O⋯M [°]	M⋯N4 [Å]
$[Fe_2(\mu\text{-}O)(L)]$	3.295(2)	8.8	11.69	1.795(2)/ 1.799(2)	173.32(8)	0.700/ 0.769
$[Fe_2(\mu\text{-}O)(L^1)]$ [a, 24]	3.145(1)	3.52	67.47	1.780(2)/ 1.67(2)	124(3)/ 141(4)	0.664
$[Fe_2(\mu\text{-}O)(L^8)]$[24]	3.143(2)	2.76	67.95	1.772(4)/ 1.774(5)	124.8(3)	0.587/ 0.678
$[Fe_2(\mu\text{-}O)(L^9)]$[24]	3.143(1)	3.2	68.07	1.777(4)/ 1.794(5)	123.3(3)	0.653/ 0.654
$[Fe_2(\mu\text{-}O)(DPA)]$[36]	3.4913(9)	1.92	-11.52	1.579(1)/ 1.5793(6)	165.7(3)	0.183

Table 2.3: Comparison between the X-ray structural data of $[Fe_2(\mu\text{-}O)(L)]$, wedge-shaped binuclear iron oxo-complexes and the anthracenyl-based cofacial diporphyrin complex [Fe2(μ-O)(DPA)]. [a]Half a molecule in the asymmetric unit, oxygen atom refined over two positions with partial occupancies.

Extended solid state structure of $[Fe_2(\mu\text{-}O)(L)]\cdot 0.5C_6H_{14}$

The di-iron oxo complex $[Fe_2(\mu\text{-}O)(L)]$ crystallises in the space group R-3 and contains 3-fold axes. In this structure, neighbouring Pacman molecules interact by head-to-face π-stacking between the anthracenyl units of one molecule and the pyrrolic moieties of the next one (**Figure 2.8**, (a)) with a shortest intermolecular C-C distance of 3.541(5) Å. This assembly generates a "star-like" pattern and large solvent accessible channels along the c axis (**Figure 2.8**, (b) and (c)). During refinement of the structure, disordered hexane molecules were found to be located in the 3-fold axes but modelling was not successful, so they were accounted for using the SQUEEZE routine of PLATON. This procedure highlighted electron density corresponding to 8.5 molecules of hexane per unit cell, which corresponds to about 0.5 solvent molecules per $[Fe_2(\mu\text{-}O)(L)]$ unit (Z = 18).

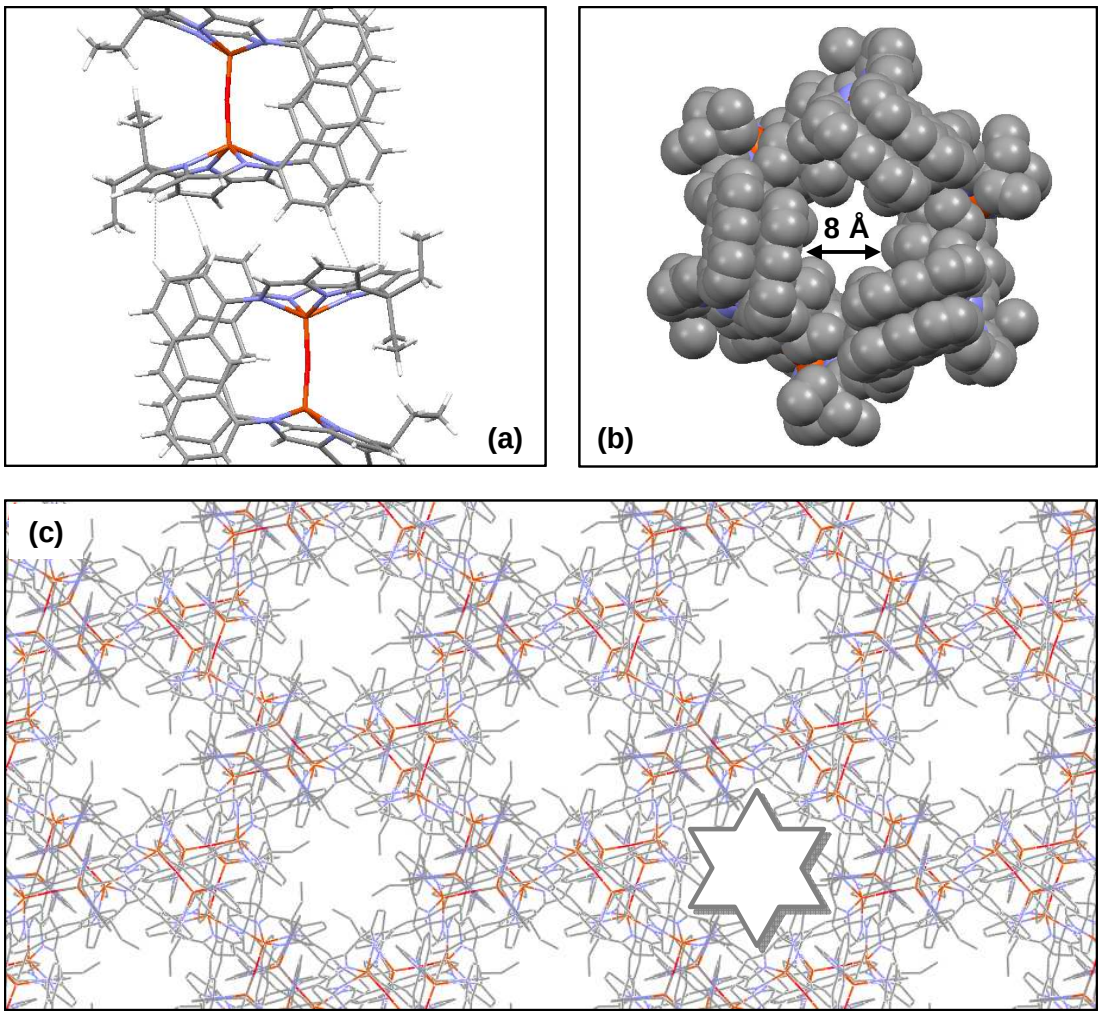

Figure 2.8: Supramolecular assembly within the X-ray crystal structure of [Fe2(μ-O)(L)]·0.5 C_6H_{14}. (a) Detail of the supramolecular assembly: stick representation of the extra-molecular interactions between the anthracene units and the pyrrolic units, the thin grey lines show close contacts, (b) space fill representation of a channel along the c axis, (c) overall network, view along the c axis.

The presence of channels within the solid-state structure is an interesting feature due to the increasing interest of microporous materials. Indeed, materials such as zeolites, carbon nanotubes, metal-organic frameworks (MOFs) or covalent organic frameworks have recently been intensely investigated for their potential applications in gas separation, purification and storage, ion exchange or even as drug delivery agents.[37] More interestingly for our study, porous materials have high potential as catalytic materials.[38] As the dimension and regularity of the pores size is crucial for the material to have potential applications, a crystalline material is of particular interest. However, materials are considered to be more useful when the pores are 1 nm (10 Å) or more in size which limits the interest in this crystalline form of

[Fe_2(μ-O)(L)]. Other related compounds isolated within the Love group show interesting supramolecular assembly in the solid state and form channels of 7-8 Å diameter, usually occupied by diffuse solvent molecules (see [$Co_2(O_2H_3)$(L)] in **Chapter 3** and work by James Leeland)[39] and these characteristics are potentially relevant to their catalytic activity. The assembly of discrete metal complexes to form large, cyclic structures in which the catalytic potential of the metallic complex is retained is rare. Macro- and nano-ring assemblies have been engineered by making use of the Zn···N interaction between zinc prophyrin units and nitrogen donor ligands.[40, 41] Some of these assemblies were characterised in the solid state and present solvent accessible channels along the axis passing through the centre of the superimposed rings.[41] In vanadyl salen complex, a V=O···V=O interaction was also found to generate 5.3 Å diameter channels in the solid state.[42]

2.8 Structure of [$(UO_2)_2$(L)]

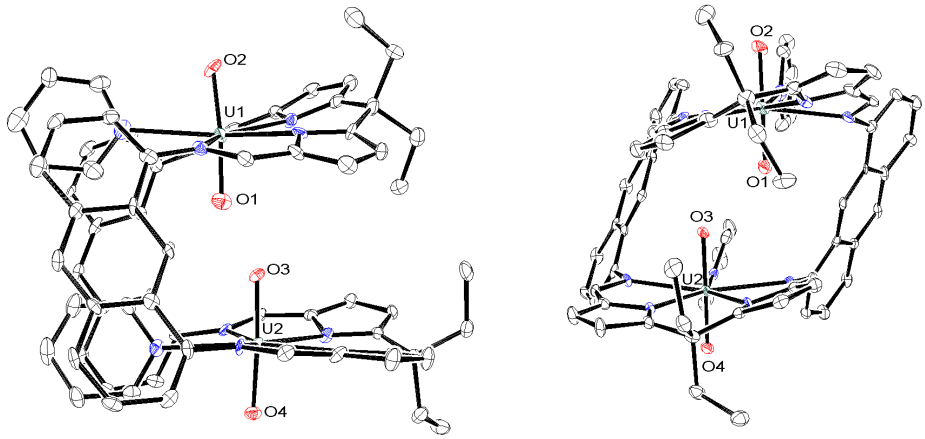

Figure 2.9: X-ray crystal structure of [$(UO_2)_2$(L)] (displacement ellipsoids are drawn at 50 % probability), (a) side view, (b) face view. For clarity, all hydrogen atoms are omitted.

The binuclear uranyl complex [$(UO_2)_2(py)_2$(L)] was synthesised and crystallised by Guy Jones as part of a collaboration between the Love and Arnold groups. While the synthesis will not be described within this work, the solid state structure is presented here to give a complete overview of binding abilities of the newly-designed ligand L.

As observed for the *d*-block metals, the complex $[(UO_2)_2(py)_2(L)]$, formed upon metallation with two equivalents of the uranyl dication, adopts a cofacial structure (**Figure 2.9**). In the present case however, the diimino-dipyrrolic cavities are expanded and the two anthracenyl moieties do not interact *via* face-to-face π-stacking, instead deviating from coplanarity by 42.49° and exhibiting a shortest C-C distance of 5.83(1) Å. Each uranium centre is pentagonal bypyramidal with a pyridine as the fifth ligand in the equatorial plane, sandwiched between the two anthracenyl backbones. The two uranium atoms are separated by 5.6994(3) Å and the molecule exhibits a 16.77° bite angle, a 22.6° twist angle.

Apart from the cavity expansion leading to a pentacoordinate trans-uranyl ion and the absence of π-stacking between the anthracenyl aromatic hinges, the geometrical features of $[(UO_2)_2(py)_2(L)]$ are surprisingly close to those observed in the structure of transition metal and alkaline earth metal complexes supported by L. For example, the intermetallic separation (5.6994(3) Å), the twist angle (22.6°) and the interplanar angle (16.77°) are very close to those observed in the structure of $[Pd_2(L)]$ (5.377(1) Å, 29.4°, 15.3° respectively). While the coordination mode of each uranyl cation is similar to the one observed in the wedge-shape complex $[(UO_2)(py)(H_2L^1)]$.[22] However, the accommodation of two uranyl dications in a Pacman geometry is extremely unusual and contrasts to that seen with other Schiff-base polypyrrolic ligands. As such, the enlarged anthracenyl hinges of L generate a cavity wide enough to accommodate the two oxo-moieties with limited steric hindrance, with the two *endo*-oxygen atoms separated by 2.709(6) Å only.

No uranyl complexes of porphyrins or cofacial diporphyrins are known as the acvity size of the porphyrin is too small to accommodate the trans-uranyl. Uranyl complexes of donor-expanded macrocycles,[43] including expanded porphyrins,[44] and calixarenes[45] can be prepared. The formation of the unusual bis(uranyl) complex of L illustrates how this new macrocycle can not only stabilise complexes that are alternatives to their cofacial diporphyrin counterparts, but can also allow access to new complexes of which the porphyrinic analogue is not available.

2.9 Conclusion: the Pacman effect

The isolation of several complexes of the new generation ligand H_4L has enabled the investigation of their properties in terms of geometrical parameters. Initially, the ligand was designed to enlarge the intermetallic separation in order to prevent the formation of undesired mono-atomic bridges. The binuclear-palladium complex $[Pd_2(L)]$ is a good model for the estimation of the intermetallic distance. The observed Pd···Pd separation of 5.377(1) Å is not only significantly elongated compared those in $[Pd_2(L^n)]$ (n = 1-5, 10), but is also *ca*. 0.8 Å longer than in the related cobalt diporphyrins $[Co_2(DPA)]$[26] and $[Co_2(DPX)]$[4]. The features observed in $[Pd_2(L)]$ makes the ligand a good candidate to support an efficient cobalt catalyst for the reduction of oxygen and this will be fully discussed in **Chapter 3**.

The complexes presented in this chapter also illustrate the versatility and the adaptability of the ligand studied. Indeed, the anthracenyl ligand was found to be able to accommodate a wide range of metals including alkali metals in $[Li_4(L)]$ and $[K_4(L)]$, alkaline earth metals illustrated by $[Mg_2(py)_3(L)]$, transition metals in $[Pd_2(L)]$ and $[Fe_2(\mu\text{-}O)(L)]$ as well as actinides in $[(UO_2)_2(py)_2(L)]$. This extra flexibility is in contrast with the properties of cofacial diporphyrins, which are less flexible, and is mainly conferred by the double pillared nature of the Pacman complexes of L. On top of these features, the complexes supported by L also exhibit the same flexibility as cofacial diporphyrins in terms of bite angle and twist angle. The flexibility of the ligand engenders an enhanced Pacman effect with accessible metal separations ranging from 3.3 Å to 6.3 Å and bite angles comprised between 11º and 55 º. This effect was shown to have an important impact on the catalytic activity, in particular in the case of dicobalt diporphyrin catalysed reduction of oxygen.[1, 3, 32]

2.10 Bibliography

1 J. P. Collman, P. S. Wagenknech, and J. E. Hutchison, *Angew. Chem. Int. Ed.*, 1994, **33**, 1537.

2 P. D. Harvey, C. Stern, C. P. Gros, and R. Guilard, *Coord. Chem. Rev.*, 2007, **251**, 401.

[3] J. Rosenthal and D. G. Nocera, *Prog. Inorg. Chem.*, 2007, **55**, 483.
[4] C. J. Chang, Y. Deng, D. G. Nocera, C. Shi, F. C. Anson, and C. K. Chang, *Chem. Commun.*, 2000, 1355.
[5] J. B. Love, *Chem. Commun.*, 2009, 3154.
[6] S. Fukuzumi, K. Okamoto, C. P. Gros, and R. Guilard, *J. Am. Chem. Soc.*, 2004, **126**, 10441; C. J. Chang, Z.-H. Loh, C. Shi, F. C. Anson, and D. G. Nocera, *J. Am. Chem. Soc.*, 2004, **126**, 10013.
[7] M. Volpe, S. D. Reid, A. J. Blake, C. Wilson, and J. B. Love, *Inorg. Chim. Acta*, 2007, **360**, 273.
[8] C. J. Chang, Z.-H. Loh, Y. Deng, and D. G. Nocera, *Inorg. Chem.*, 2003, **42**, 8262; J. Rosenthal, B. J. Pistorio, L. L. Chng, and D. G. Nocera, *J. Org. Chem.*, 2005, **70**, 1885; J. Rosenthal, T. D. Luckett, J. M. Hodgkiss, and D. G. Nocera, *J. Am. Chem. Soc.* , 2006, **128**, 6546; Y. Naruta, M.-a. Sasayama, and T. Sasaki, *Angew. Chem., Int. Ed. Engl.*, 1994, **33**, 1839; Y. Shimazaki, T. Nagano, H. Takesue, B.-H. Ye, F. Tani, and Y. Naruta, *Angew. Chem., Int. Ed. Engl.*, 2004, **43**, 98.
[9] Y. Naruta and K. Maruyama, *J. Am. Chem. Soc.*, 1991, **113**, 3595.
[10] E. Askarizadeh, A. M. J. Devoille, D. M. Boghaei, A. M. Z. Slawin, and J. B. Love, *Inorg. Chem.*, 2009, **48**, 7491.
[11] J. L. Sessler, T. D. Mody, D. A. Ford, and V. Lynch, *Angew. Chem., Int. Ed. Engl.*, 1992, **31**, 452; A. Dahan, T. Ashkenazi, V. Kuznetsov, S. Makievski, E. Drug, L. Fadeev, M. Bramson, S. Schokoroy, E. Rozenshine-Kemelmakher, and M. Gozin, *J. Org. Chem.*, 2007, **72**, 2289.
[12] P. Wuelfing, E. A. Fitzgerald, and H. H. Richtol, *Anal. Chem.*, 1970, **42**, 299; H. H. Richtol, E. A. Fitzgerald, and P. Wuelfing, *The Journal of Physical Chemistry*, 1971, **75**, 2737.
[13] S. G. Cohen, A. Parola, and G. H. Parsons, *Chem. Rev.*, 1973, **73**, 141.
[14] H. Y. D.-L. W. G.-Y. L. Chao-Zhi Zhang, *Chinese Journal of Chemistry*, 2007, **25**, 653.
[15] J. Herwig, H. Bohnen, P. Skutta, S. Sturm, P. W. N. M. Van Leeuwen, and R. Bronger, in 'Novel diphosphines and method for their production', 2002.
[16] A. J. Caruso and J. L. Lee, *J. Org. Chem.*, 1997, **62**, 1058.
[17] S. Xavier, J. G. S. Eduardo, F. Zoraida, B.-B. Jordi, and W. N. M. v. L. Piet, *Eur. J. Org. Chem.*, 2008, **2008**, 6197.
[18] A. J. F. N. Sobral, N. G. C. L. Rebanda, M. da Silva, S. H. Lampreia, M. Ramos Silva, A. M. Beja, J. A. Paixão, and A. M. D. A. Rocha Gonsalves, *Tetrahedron Lett.*, 2003, **44**, 3971.
[19] M.-Y. Song, H.-K. Na, E.-Y. Kim, S.-J. Lee, K. I. Kim, E.-M. Baek, H.-S. Kim, D. K. An, and C.-H. Lee, *Tetrahedron Lett.*, 2004, **45**, 299.
[20] G. Givaja, M. Volpe, James W. Leeland, Michael A. Edwards, Thomas K. Young, S. B. Darby, Stuart D. Reid, Alexander J. Blake, C. Wilson, J. Wolowska, Eric J. L. McInnes, M. Schröder, and Jason B. Love, *Chem.-Eur. J.*, 2007, **13**, 3707.
[21] G. Givaja, A. J. Blake, C. Wilson, M. Schroder, and J. B. Love, *Chem. Commun.*, 2003, 2508.
[22] P. L. Arnold, A. J. Blake, C. Wilson, and J. B. Love, *Inorg. Chem.*, 2004, **43**, 8206.

[23] P. L. Arnold, D. Patel, A. J. Blake, C. Wilson, and J. B. Love, *J. Am. Chem. Soc.*, 2006, **128**, 9610; G. Givaja, M. Volpe, Michael A. Edwards, Alexander J. Blake, C. Wilson, M. Schröder, and Jason B. Love, *Angew. Chem. Int. Ed.*, 2007, **46**, 584; P. L. Arnold, D. Patel, C. Wilson, and J. B. Love, *Nature*, 2008, **451**, 315; E. Askarizadeh, S. B. Yaghoob, D. M. Boghaei, A. M. Z. Slawin, and J. B. Love, *Chem. Commun.*, 2010, **46**, 710; P. L. Arnold, N. A. Potter, N. Magnani, C. Apostolidis, J.-C. Griveau, E. Colineau, A. Morgenstern, R. Caciuffo, and J. B. Love, *Inorg. Chem.*, **49**, 5341; J. W. Leeland, A. M. Z. Slawin, and J. B. Love, *Organometallics*, **29**, 714; J. L. Sessler, E. Tomat, T. D. Mody, V. M. Lynch, J. M. Veauthier, U. Mirsaidov, and J. T. Markert, *Inorg. Chem.*, 2005, **44**, 2125.

[24] J. M. Veauthier, W. S. Cho, V. M. Lynch, and J. L. Sessler, *Inorg. Chem.*, 2004, **43**, 1220.

[25] F. Allen, *Acta Crystallogr., Sect. B*, 2002, **58**, 380.

[26] F. Bolze, M. Drouin, P. D. Harvey, C. P. Gros, E. Espinosa, and R. Guilard, *J. Porphyrins Phthalocyanines*, 2003, **7**, 474.

[27] J. P. Fillers, K. G. Ravichandran, I. Abdalmuhdi, A. Tulinsky, and C. K. Chang, *J. Am. Chem. Soc.*, 1986, **108**, 417.

[28] R. Guilard, C. P. Gros, J.-M. Barbe, E. Espinosa, F. Jerome, A. Tabard, J.-M. Latour, J. Shao, Z. Ou, and K. M. Kadish, *Inorg. Chem.*, 2004, **43**, 7441.

[29] F. Jerome, J.-M. Barbe, C. P. Gros, R. Guilard, J. Fischer, and R. Weiss, *New J. Chem.*, 2001, **25**, 93.

[30] M. El Ojaimi, C. P. Gros, and J.-M. Barbe, *Eur. J. Org. Chem.*, 2008, **2008**, 1181.

[31] C. L. Ni, I. Abdalmuhdi, C. K. Chang, and F. C. Anson, *The Journal of Physical Chemistry*, 1987, **91**, 1158; Y. Naruta, N. Sawada, and M. Tadokoro, *Chem. Lett.*, 1994, **23**, 1713; M.-a. Sasayama and Y. Naruta, *Chem. Lett.*, 1995, **24**, 63; L. M. Proniewicz, J. Odo, J. Goral, C. K. Chang, and K. Nakamoto, *J. Am. Chem. Soc.*, 1989, **111**, 2105; A. Osuka, K. Maruyama, I. Yamazaki, and N. Tamai, *Chem. Phys. Lett.*, 1990, **165**, 392; Y. Naruta, M.-a. Sasayama, and K. Ichihara, *Journal of Molecular Catalysis A: Chemical*, 1997, **117**, 115; H. Y. Liu, I. Abdalmuhdi, C. K. Chang, and F. C. Anson, *The Journal of Physical Chemistry*, 1985, **89**, 665; R. Guilard, M. A. Lopez, A. Tabard, P. Richard, C. Lecomte, S. Brandes, J. E. Hutchison, and J. P. Collman, *J. Am. Chem. Soc.*, 1992, **114**, 9877; R. Guilard, S. Brandes, C. Tardieux, A. Tabard, M. L'Her, C. Miry, P. Gouerec, Y. Knop, and J. P. Collman, *J. Am. Chem. Soc.*, 1995, **117**, 11721; P. H. Rieger, I. Bernal, W. H. Reinmuth, and G. K. Fraenkel, *J. Am. Chem. Soc.*, 1963, **85**, 683; T. Fujihara, K. Tsuge, Y. Sasaki, Y. Kaminaga, and T. Imamura, *Inorg. Chem.*, 2002, **41**, 1170; Y. Le Mest, C. Inisan, A. Laouénan, M. L'Her, J. Talarmin, M. El Khalifa, and J.-Y. Saillard, *J. Am. Chem. Soc.*, 1997, **119**, 6095; J. P. Collman, H. T. Fish, P. S. Wagenknecht, D. A. Tyvoll, L.-L. Chng, T. A. Eberspacher, J. I. Brauman, J. W. Bacon, and L. H. Pignolet, *Inorg. Chem.*, 1996, **35**, 6746; J. P. Collman, L. L. Chng, and D. A. Tyvoll, *Inorg. Chem.*, 1995, **34**, 1311.

[32] C. K. Chang, H. Y. Liu, and I. Abdalmuhdi, *J. Am. Chem. Soc.*, 1984, **106**, 2725.

[33] R. Guilard, C. P. Gros, J.-M. Barbe, E. Espinosa, F. Jerome, A. Tabard, J.-M. Latour, J. Shao, Z. Ou, and K. M. Kadish, *Inorg. Chem.*, 2004, **43**, 7441.

[34] F. Jerome, J.-M. Barbe, C. P. Gros, R. Guilard, J. Fischer, and R. Weiss, *New J. Chem.*, 2001, **25**, 93.

[35] J.-M. Chen, X.-M. Zhuang, L.-Z. Yang, L. Jiang, X.-L. Feng, and T.-B. Lu, *Inorg. Chem.*, 2008, **47**, 3158; V. Amendola, E. Bastianello, L. Fabbrizzi, C. Mangano, P. Pallavicini, A. Perotti, A. M. Lanfredi, and F. Ugozzoli, *Angew. Chem., Int. Ed. Engl.*, 2000, **39**, 2917.

[36] G.-H. Lee, *Pirvate communication*, 2003, **CCDC 115142**.

[37] *Chem. Soc. Rev.*, 2009, **38**, 1201; M. E. Davis, *Nature*, 2002, **417**, 813; S. M. Cohen, *Curr. Opin. Chem Biol.*, 2007, **11**, 115.

[38] J. Perez-Ramirez, C. H. Christensen, K. Egeblad, C. H. Christensen, and J. C. Groen, *Chem. Soc. Rev.*, 2008, **37**, 2530; X. S. Zhao, X. Y. Bao, W. Guo, and F. Y. Lee, *Materials Today*, 2006, **9**, 32; J. Lee, O. K. Farha, J. Roberts, K. A. Scheidt, S. T. Nguyen, and J. T. Hupp, *Chem. Soc. Rev.*, 2009, **38**, 1450; Z. Xie, Z. Liu, Y. Wang, Q. Yang, L. Xu, and W. Ding, *Int. J. Mol. Sci.*, 2010, **11**, 2152.

[39] J. W. Leeland, F. J. White, and J. B. Love, *Chem. Commun.*, 2011, DOI:10.1039/c0cc04883f.

[40] Y. Kuramochi, A. Satake, and Y. Kobuke, *J. Am. Chem. Soc.*, 2004, **126**, 8668; M. Hoffmann, J. Kärnbratt, M.-H. Chang, L. M. Herz, B. Albinsson, and H. L. Anderson, *Angew. Chem., Int. Ed. Engl.*, 2008, **47**, 4993 and references therein; K. Fujisawa, A. Satake, S. Hirota, and Y. Kobuke, *Chem.-Eur. J.*, 2008, **14**, 10735.

[41] E. Kuhn, V. Bulach, and M. W. Hosseini, *Chem. Commun.*, 2008, 5104.

[42] K. Oyaizu and E. Tsuchida, *J. Am. Chem. Soc.*, 2003, **125**, 5630.

[43] M. E. Amato, F. P. Ballistreri, S. Gentile, A. Pappalardo, G. A. Tomaselli, and R. M. Toscano, *The Journal of Organic Chemistry*, **75**, 1437; P. Zanello, R. Seeber, and A. Cinquantini, *Inorg. Chim. Acta*, 1982, **65**, L43.

[44] J. L. Sessler, P. J. Melfi, and G. D. Pantos, *Coord. Chem. Rev.*, 2006, **250**, 816; J. L. Sessler, A. E. Vivian, D. Seidel, A. K. Burrell, M. Hoehner, T. D. Mody, A. Gebauer, S. J. Weghorn, and V. Lynch, *Coord. Chem. Rev.*, 2001, **216-217**, 411; J. L. Sessler, D. Seidel, A. E. Vivian, V. Lynch, B. L. Scott, and D. W. Keogh, *Angew. Chem., Int. Ed. Engl.*, 2001, **40**, 591.

[45] P. Thuéry, M. Nierlich, J. Vicens, B. Masci, and H. Takemura, *Eur. J. Inorg. Chem.*, 2001, **2001**, 637; P. Thuery and H. Takemura, *Acta Crystallographica Section C*, 2003, **59**, m384; P. C. Leverd, M. Nierlich, I. Dumazet-Bonnamour, and R. Lamartine, *Chem. Commun.*, 2000, 493; B. Masci and P. Thuery, *New J. Chem.*, 2005, **29**, 493.

Chapter 3 – Binuclear cobalt complexes and reduction of oxygen to water.

The major part of the content of this Chapter is the subject of the following full paper, manuscript submitted:

Double-pillared cobalt Pacman complexes: synthesis, structures and four-electron oxygen reduction catalysis

A. M. J. Devoille, F. White and J. B. Love,* *Manuscript submitted.*, 2011.

The binuclear cobalt complex [Co_2(L)] is a potential candidate for the full reduction of oxygen to water. The catalytic reaction targeted is a PCET and it is therefore crucial to understand the behaviour of the catalyst towards electron transfer. As the binding of oxygen to the complex is a prerequisite for its reduction, the oxygen affinity is also a crucial parameter to consider in order to gain an insight into the mechanism of the catalytic reaction. Thus the binuclear cobalt complex was synthesised, characterised and its redox properties and affinity for oxygen were studied. Finally, its catalytic activity towards oxygen in the presence of protons and an electron source was investigated.

3.1 Synthesis and characterisation of $[Co_2(L)]$

3.1.1 Synthesis of $[Co_2(L)]$

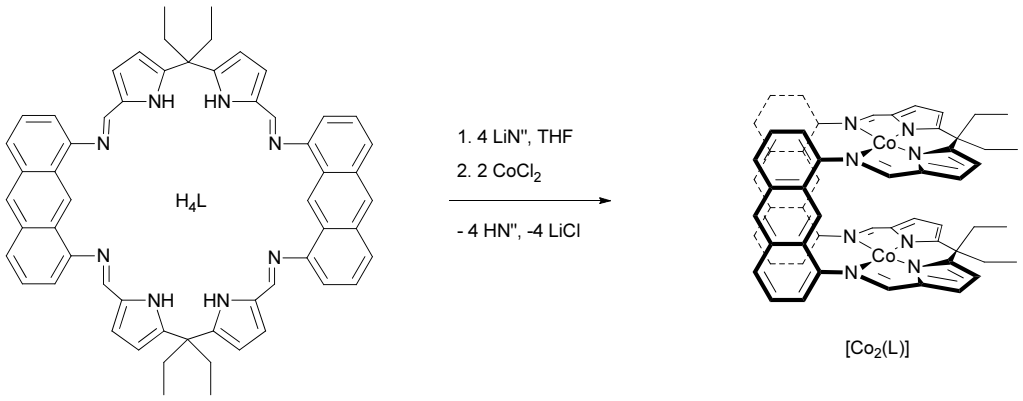

Scheme 3.1 : Synthesis of $[Co_2(L)]$ by salt elimination reaction.

In-situ synthesis of the lithium salt $[Li_4(L)]$ (synthesis discussed in **Chapter 2**) followed by reaction with two equivalents of cobalt dichloride in THF and concentration of the solution under reduced pressure afforded the binuclear cobalt complex $[Co_2(L)]$ as a red solid in 51% isolated yield (**Scheme 3.1**). The ^1H NMR spectrum recorded in THF/d_6-benzene exhibits twelve resonances spread between 40 ppm and -60 ppm, as expected for the paramagnetic cofacial complex. The formation of $[Co_2(L)]$ is further supported by the absence of N-H vibration in the infra red spectrum (observed at 3250 cm^{-1} for the free ligand) and the decrease in wave number of the C=N vibration to 1580 cm^{-1} (C=N vibration observed at 1616 and 1570 cm^{-1} for H_4L and $[Pd_2(L)]$ respectively). This observation is consistent with the binding of a metal to the imino-nitrogen as seen for other binuclear metal complexes. In the positive ionisation mode, the ESI mass spectrum obtained from a THF/acetonitrile solution exhibits the molecular ion at m/z = 974 as well as a very intense peak at m/z = 991, corresponding to the loss of a water molecule from the hydroxo-hydrate $[Co_2(O_2H_3)(L)]^-$ observed in the solid-state structure of a sample exposed to air (structure discussed in section 3.3.5). For each of these two masses, peaks corresponding to the loss of one and two of the *meso*-ethyl groups of the ligand were also observed at 962 and 933 for $[Co_2(O_2H_3)(L)]^+$ and 945 and 916 for $[Co_2(L)]^+$ respectively (the deviation from the M+1 mass peak expected at

(m+z)/z = 975 was attributed to miscalibration of the spectrometer). Elemental analyses were also consistent with the composition of [Co_2(L)].

3.1.2 Magnetic properties of [Co_2(L)]

The magnetic properties of [Co_2(L)] in solution were investigated further by the Evans' method.[1] This experiment takes advantage of the dependence of the NMR chemical shift of a given species on the magnetic susceptibility of the medium in which it is immersed. In a THF/d_6-benzene, [Co_2(L)] exhibits a calculated effective magnetic moment of μ_{eff} = 3.5 B.M., which is consisten with the paramagnetic nature of the complex. However, due to the binuclear nature of the complex a simple spin only interpretation cannot account for the magnetic behaviour of the complex ($\mu_s = 2\sqrt{s(s+1)}$ = 2.83 B.M. for a molecule of spin s = 1). The value is similar to the ones obtained forth the wedge shaped analogue.[2] The full description of the magnetic properties of [Co_2(L)] would require further investigation such as a SQUID experiment. The Evans' method measurements were also carried out in benzonitrile due to the relevance of this solvent to the oxygen reduction catalytic activity of [Co_2(L)]. These results are described and discussed within the oxygen activation study in section **Error! Reference source not found.**.

3.1.3 Solid state structures under inert atmosphere

3.1.3.1 [Co_2(*exo*-THF)$_2$(L)][Co_2(L)]

Diffusion of toluene into a THF solution of [Co_2(L)] yielded crystals suitable for X-ray diffraction and the solid state structure of [Co_2(*exo*-THF)$_2$(L)][Co_2(L)] was determined. The molecular structure is displayed on **Figure 3.1** with crystal data and selected bound length and angles in **Appendixes 2** and **3**. As suggested by the number of resonances observed in the ^{1}H NMR spectrum, [Co_2(L)] adopts the double-pillared cofacial arrangement already observed in other bi-metallic complexes of L, with a cobalt cation accommodated in each of the two diimino-dipyrrolic compartments. The asymmetric unit contains two different molecules: [Co_2(*exo*-THF)$_2$(L)], where one molecule of THF is bound to the each of

the metal centres (**Figure 3.1** (a) and (b)), and [Co_2(L)], where the cobalt centres are complexed to the macrocyclic ligand only (**Figure 3.1** (c) and (d)). In both molecules, the anthracenyl backbones are face-to-face π-stacked with the shortest contact between the backbone of 3.505(7) Å and 3.368(7) Å and a deviation from co-planarity of 14.3° and 9.8° respectively (for the definition of the geometric parameters, see the bookmark). No obvious supramolecular interactions were observed within the packing diagram.

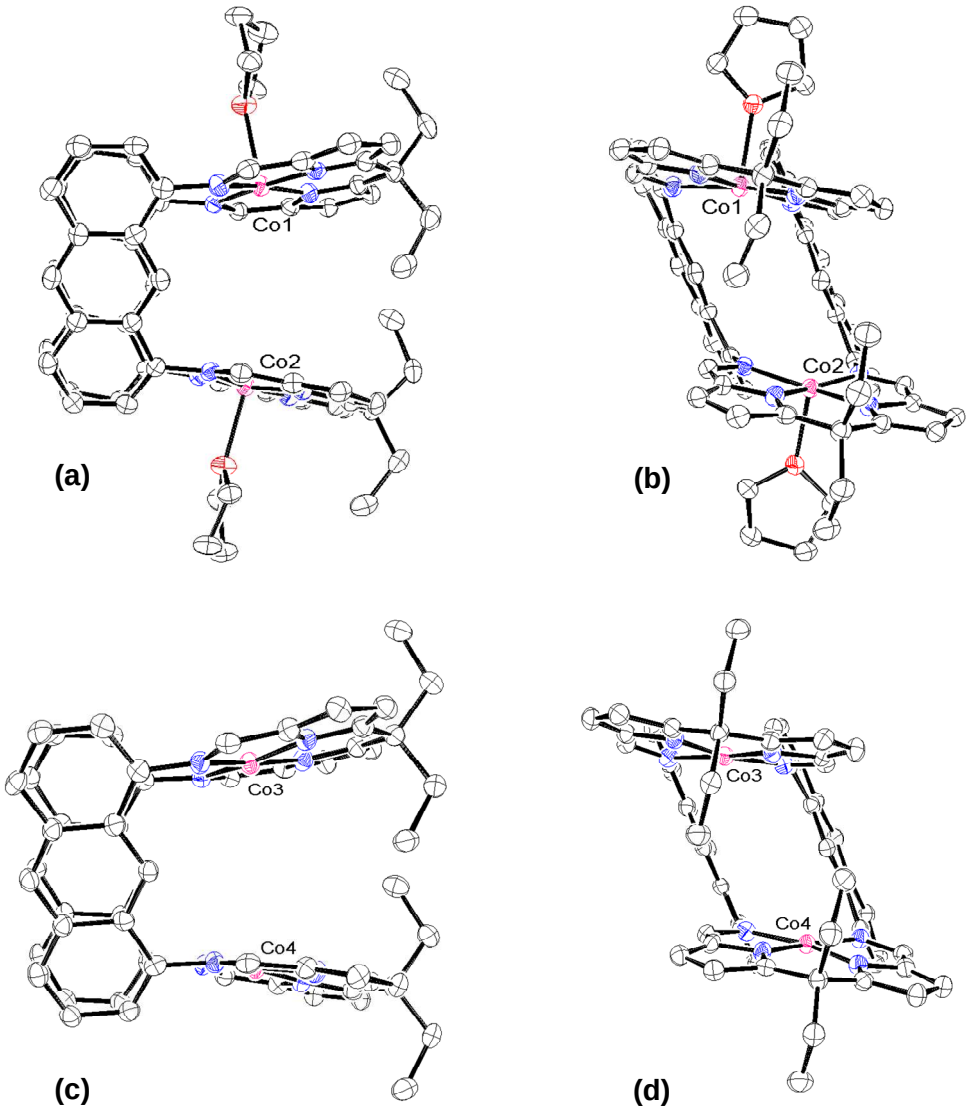

Figure 3.1 : X-ray crystal structure of [Co_2(*exo*-THF)$_2$(L)][Co_2(L)]·3Tol (displacement ellipsoids are drawn at 50 % probability). (a) Side view of the [Co_2(*exo*-THF)$_2$(L)] moiety, (b) face view of the [Co_2(*exo*-THF)$_2$(L)] moiety, (c) side view of the [Co_2(L)] moiety, (d) face view of the [Co_2(L)] moiety. For clarity, the toluene solvent of crystallisation and all hydrogen atoms are omitted; the two moieties are represented separately and their relative position is arbitrary.

Compound	M···M [Å]	Twist [°]	Interplanar Angle[a]	Ref
$[Co_2(exo\text{-}THF)_2(L)][Co_2(L)]$	5.710(2)/ 5.471(2)[b]	30.7/ 28.8	19.8/18.1	This work
$[Co_2(exo\text{-}py)_2(L)]$ [c]	5.8374(9)	28.6	16.2	This work
$[Co_2(exo\text{-}py)_2(L)]$ [d]	5.8139(2)	33.3	18.3	This work
$[Co_2(L^{10})]$	3.639(1)/ 3.635(1)[b]	34.2	54.7	[3]
$[Co_2(exo\text{-}py)_2(L^{10})]$	4.120(1)	25.9	62.3	[3]
$[Co_2(L^1)]$	4.083(1)/ 4.1199(9)[b]	31.3	62.6	[4]
$[Co_2(endo\text{-}py)(exo\text{-}py)(L^1)]$	4.300(2)/ 4.325(2)[b]	2.9	64.8	[4]
$[Co_2(DPA)]$	4.533(3)	36.6	3.0	[5]
$[Co_2(DPX)]$	4.583(2)	20.8	2.5	[6]

Table 3.1 : Comparison of geometric parameters derived from the X-ray crystal structures of $[Co_2(L)]$ and related compounds. [a] Also called bite angle, [b] two molecules in the asymmetric unit, [c] $[Co_2(exo\text{-}py)_2(L)]\cdot 1.8py$ crystalline form, [d] cited as an indication only, the poor quality of the data allowed a solution for connectivity only.

In $[Co_2(exo\text{-}THF)_2(L)]$, the two N_4-donor planes deviate from co-planarity by 19.8° and the mean C_2-twist angle between the metal-coordination plane and the anthracenyl backbone is 30.7°. The two cobalt cations lay 5.710(2) Å apart, each of them being in a pseudo square-pyramidal environment with the metallic centre in the N_4-plane (Co1 and Co2 sit 0.07 Å and 0.10 Å above the corresponding N_4-donor plane respectively, towards the solvent molecule) and the oxygen of the THF molecule occupies the apical site. Both THF molecules are located outside the molecular cavity. In the THF free molecule, the two N_4-donor planes form an 18.1° bite angle and display a mean twist angle of 28.8°. The two pseudo square-planar cobalt cations are located 0.05 Å from their respective N_4-donor plane towards the intramolecular cavity, leading to a Co3···Co4 separation of 5.471(2) Å. The presence of coordinated THF molecules in every other molecule is considered to be a packing effect as supported by the relatively long Co-O distance of 2.233(4) Å and

2.243(3) Å for Co1 and Co2 respectively (CCDC: 68 examples, mean 2.11 Å, range 1.88 Å to 2.45 Å).[7]

All the dimensions observed in this solid state structure are comparable to the ones in [Pd_2(L)](see **Chapter 2**). The average Co-N(imine) and Co-N(pyrrole) distances (1.98 and 1.86 Å respectively) are also very similar to those observed in the 1,2-aryl-hinged binuclear cobalt complexes [$Co_2(L^1)$] and [$Co_2(L^{10})$] (1.96 and 1.85 Å respectively for both complexes). [Co_2(DPA)],[5] the cofacial diporphyrin analogue of [Co_2(L)], and the closely related [Co_2(DPX)][8] complexes both exhibit significantly smaller metal-metal separations than [Co_2(L)] in the solid state (4.5 Å and 4.6 Å respectively *vs.* 5.5 Å for [Co_2(L)]). The doubly pillared system also manages an 18.1° deviation from coplanarity while the porphyrinic analogues are held more strictly cofacial and exhibit only a 2° to 3° bite angle. As mentioned for [Pd_2(L)], these differences can be attributed to a clash between the two *meso*-ethyl substituents of L.

3.1.3.2 [Co_2(*exo*-py)$_2$(L)]·4THF

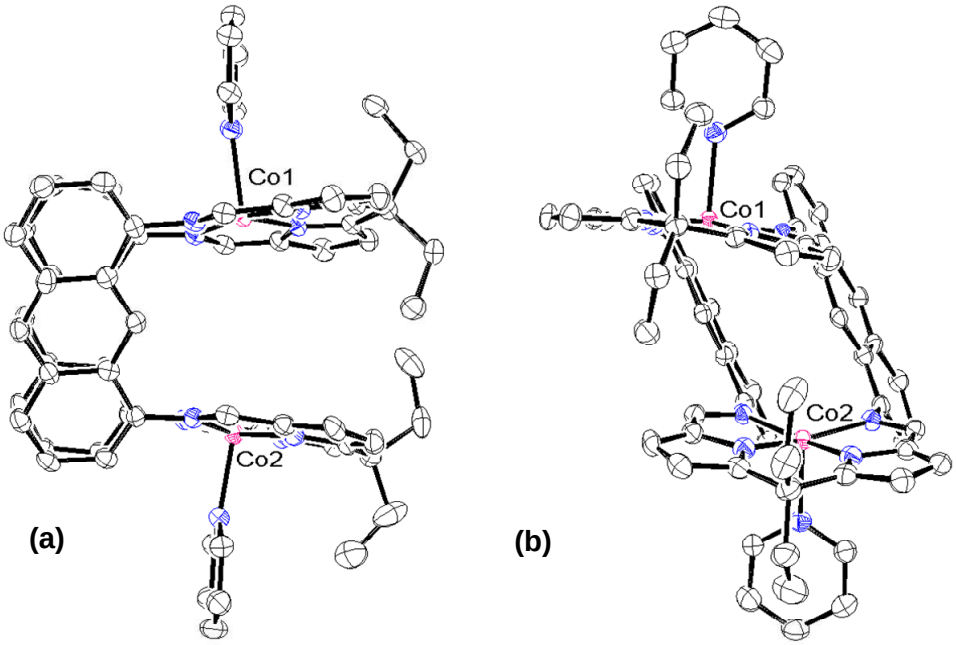

Figure 3.2 : X-ray crystal structure of [Co_2(*exo*-py)$_2$(L)]·4THF (displacement ellipsoids are drawn at 50 % probability), (a) Side view, (b) face view. For clarity, the THF solvent of crystallisation and all hydrogen atoms are omitted.

The diffusion of hexane in a pyridine/THF mixture caused the crystallisation of $[Co_2(exo\text{-}py)_2(L)]\cdot 4THF$ and the structure was determined by X-ray crystallography (**Figure 3.2**). Crystal data and selected bound length and angles are presented in **Appendixes 2** and **3**. The overall molecular arrangement is very similar to that observed in $[Co_2(exo\text{-}THF)_2(L)]$ and no particular supramolecular arrangement was observed. Once again, the two anthracenyl backbones exhibit face-to-face π-stacking with an angle between the two aromatic units of 11.8° and a shortest carbon-carbon distance of 3.212(7) Å. The two metals are separated by 5.8374(9) Å and the two cobalt cations are located 0.18 Å away from their respective N_4-coordination plane outside the molecular cavity and towards their respective pyridine ligand. The distance between the metal atom and the nitrogen of the apical pyridine is 2.145(3) Å and 2.142(3) Å for Co1 and Co2 respectively. These two last features testify to the better donor character of pyridine compared to THF (when the apical ligand is THF, Co1 and Co2 are located 0.07 Å and 0.10 Å away from their respective donor plane and the cobalt to oxygen distance is 2.233(4) Å and 2.243(3) Å for Co1 and Co2 respectively). The Co-N(py) distance, used in the past to help determine the oxidation state of the cobalt centre, is typical of a Co(II) centre as previously observed in $[Co_2(endo\text{-}py)(exo\text{-}py)(L^1)]$ and $[Co_2(exo\text{-}py)_2(L^{10})]$[2, 3] in which the Co(II)-N(py) bonds were observed in the range 2.071(8)-2.181(9) Å, and Co(III)-N(py) bonds in the range 1.971(8)-2.085(3) Å.

3.1.3.3 $[Co_2(exo\text{-}py)_2(L)]$

Upon addition of pyridine to the THF/Toluene crystallisation system, small red needles grew in good yield and an X-ray diffraction study afforded the structure of $[Co_2(exo\text{-}py)_2(L)]$ (**Figure 3.3**, crystal data and selected bound length and angles are presented in **Appendixes 2** and **3**) with a crystalline form slightly different from the one of $[Co_2(exo\text{-}py)_2(L)]\cdot 4THF$ discussed above (the latter structure including some solvent of crystallisation that is absent in the former).The geometry of the new complex is very similar to the one of $[Co_2(exo\text{-}py)_2(L)]\cdot 4THF$. Due to very weak diffraction, the structure could be refined for connectivity only and all elements were refined isotropically to sustain a stable refinement. As a result, the geometric parameters of $[Co_2(exo\text{-}py)_2(L)]$ cannot be precisely determined.

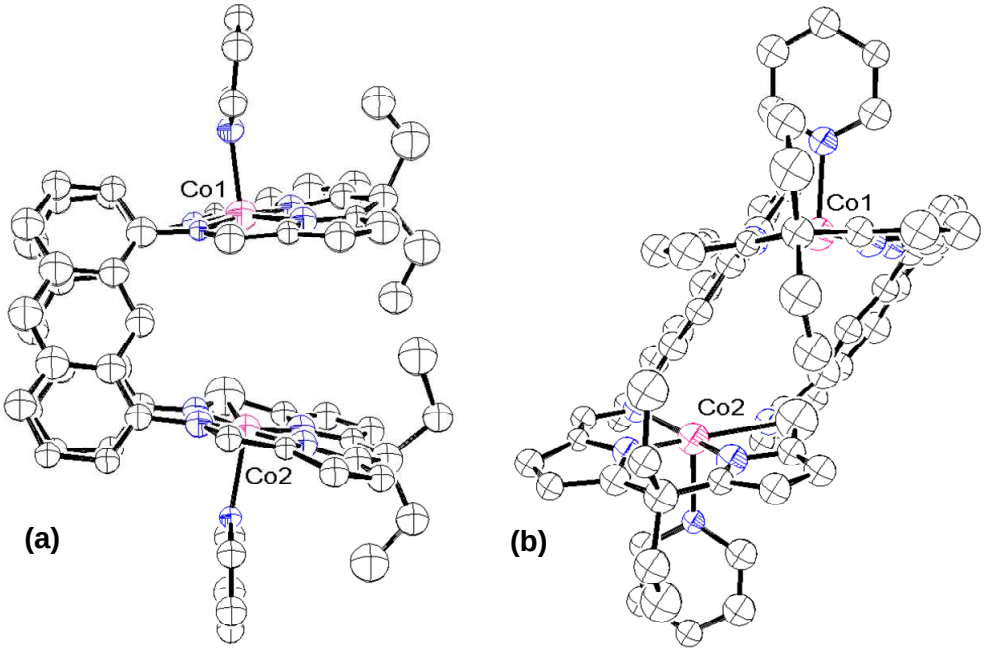

Figure 3.3 : X-ray crystal structure of $[Co_2(exo\text{-}py)_2(L)]$ (all atoms were refined isotropically, connectivity purposes only), (a) Side view, (b) face view. For clarity, all hydrogen atoms are omitted.

3.2 Redox properties of $[Co_2(L)]$

3.2.1 Electrochemical study

3.2.1.1 Comparison of the electrochemistry of $[Zn_2(L)]$ and $[Co_2(L)]$ under nitrogen

An insight into the redox properties of $[Co_2(L)]$ was gained by cyclic voltametry (CV) experiments. CVs were recorded in dry, distilled benzonitrile under nitrogen atmosphere using a platinum working electrode (WE), a platinum foil counter electrode (CE) and a silver wire reference electrode (RE). All voltamograms were referenced to the ferrocene/ferrocenium couple (Fc^+/Fc, $E_0(Fc^+/Fc)$ was recorded at 0.82V *vs.* Ag/Ag^+). The distinction between ligand-based and metal-based features was deduced from the comparison of the voltamograms of $[Zn_2(L)]$ and $[Co_2(L)]$ (**Figure 3.4**).

The electrochemistry of $[Zn_2(L)]$ is dominated by irreversible processes: two oxidation features around 0.30 V and 0.60 V as well as a reduction feature around -2.0 V, associated with the oxidation processes. These three ligand-based features were also observed in the voltamogram of $[Co_2(L)]$ at 0.38 V, 0.57 V and -2.11 V and the formation of the corresponding oxidised species leads to electrode coating and fundamental alteration of the electrochemical behaviour of the system (**Figure 3.6** (a)). Therefore, the study was focused on the metal based oxidations and reductions; and voltamograms were recorded between -2.40 V and 0.00 V.

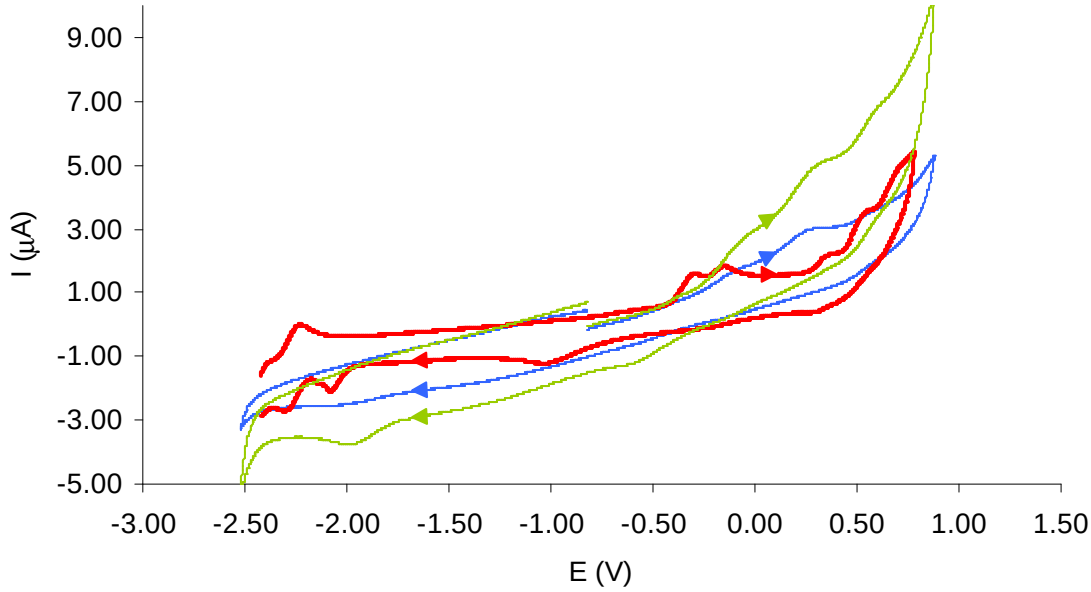

Figure 3.4 : CV under nitrogen of $[Co_2(L)]$ recorded at 100 $mV.s^{-1}$ (bold red trace); $[Zn_2(L)]$ recorded at 200 $mV.s^{-1}$ (blue trace) and 1000 $mV.s^{-1}$ (green trace) in the range -2.52 V to +0.88 V. Conditions: 1mM of $[Co_2(L)]$ or 0.45 mM $[Zn_2(L)]$ in dried and distilled benzonitrile, 0.2 M $^{n}Bu_4NBF_4$ *vs.* Fc^{+}/Fc (Reference electrode: silver wire, counter electrode: platinum wire, working electrode: platinum). The arrows indicate the direction of scanning.

3.2.1.2 Electrochemistry of $[Co_2(L)]$ under nitrgen

Cyclic voltamograms of $[Co_2(L)]$ under nitrogen at different scan rates are presented in **Figure 3.5** and details of the electrochemistry recorded at 100 $mV.s^{-1}$ are presented in **Figure 3.6**. The most important features consist of two successive oxidation waves at E_{p2}^{a} = -0.32 V and E_{p3}^{a} = -0.17 V. Each of these oxidations is associated with a return reduction wave around E_{p2}^{c} = -0.41 V and E_{p3}^{c} = -0.23 V (**Figure 3.6** (b)). These features were attributed to the successive oxidation of the two metallic centres of $[Co_2(L)]$ from the +2 to the +3 oxidation state followed by

two successive one electron reductions to recover the binuclear cobalt(II) complex. This corresponds to an EE mechanism (*i.e.* two successive charge transfer process). Testing for reversibility highlighted that the current intensity I_{p1}^{a} and I_{p2}^{a} are almost directly proportional to the square root of the scan rate, $\nu^{1/2}$ (**Figure 3.7**, green and blue lines respectively) and the potentials E_{p2}^{a}, E_{p3}^{a}, E_{p2}^{c} and E_{p3}^{c} are independent of the scan rate as expected for reversible processes.

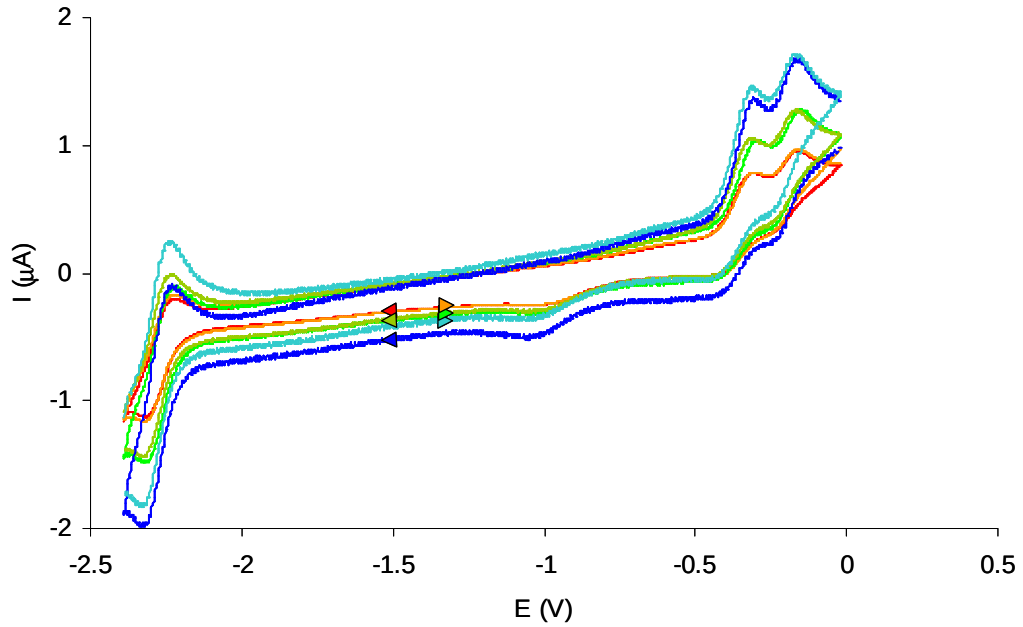

Figure 3.5: Cyclic voltamogram of $[Co_2(L)]$ under nitrogen recorded at 25 $mV.s^{-1}$ (red and orange traces trace), 50 $mV.s^{-1}$ (dark and light green traces) and 100 $mV.s^{-1}$ (dark and light blue trace) in the range -2.40 V to +0.00 V. Conditions: 1mM of $[Co_2(L)]$ in dried and distilled benzonitrile, 0.2 M $^{n}Bu_4NBF_4$ *vs.* Fc^{+}/Fc (Reference electrode: silver wire, counter electrode: platinum wire, working electrode: platinum). The arrows indicate the direction of scanning.

In contrast, further tests revealed a difference between the anodic and the cathodic potential of 90 mV and 60 mV for the first and second process respectively when the reversible value is expected to be 57 mV. Furthermore, the reduction waves are less intense than for a reversible process ($-I_p^{a}/ I_p^{c} \geq 1$) and the reduction wave with the highest potential is better resolved at higher scan rates. This is indicative of a chemical reaction of $[Co^{(III/III)}{}_2(L)]$ to form an unknown product P. This hypothesis is also supported by the irreversible reduction occurring around $E_{p4}^{c} \sim -1.00$ V. Reducing the scanning window to [-1.31 V – 0.00 V] and [-1.31 V – -0.28 V] confirmed the association of this reduction feature with the second oxidation wave (**Figure 3.6** (c)) which is consistent with the reduction of the unknown product P to P^{-n}. The extra process involving the degradation of $[Co^{(III/III)}{}_2(L)]$ to P and the

reduction to P^{-n} constitutes a CE mechanism (*i.e.* a charge transfer followed by a chemical reaction). Thus, the electrochemistry of [Co_2(L)] results from the competition between a pseudo-reversible EE mechanism and a CE mechanism.

Finally, an irreversible reduction (**Figure 3.7**, red line) is observed at E_{p1}^{c} ~ -2.32 V and is associated with an oxidation wave at E_{p1}^{a} = -2.24V (**Figure 3.6**, (d)) and these were attributed to the Co(I)/Co(II) redox couple.

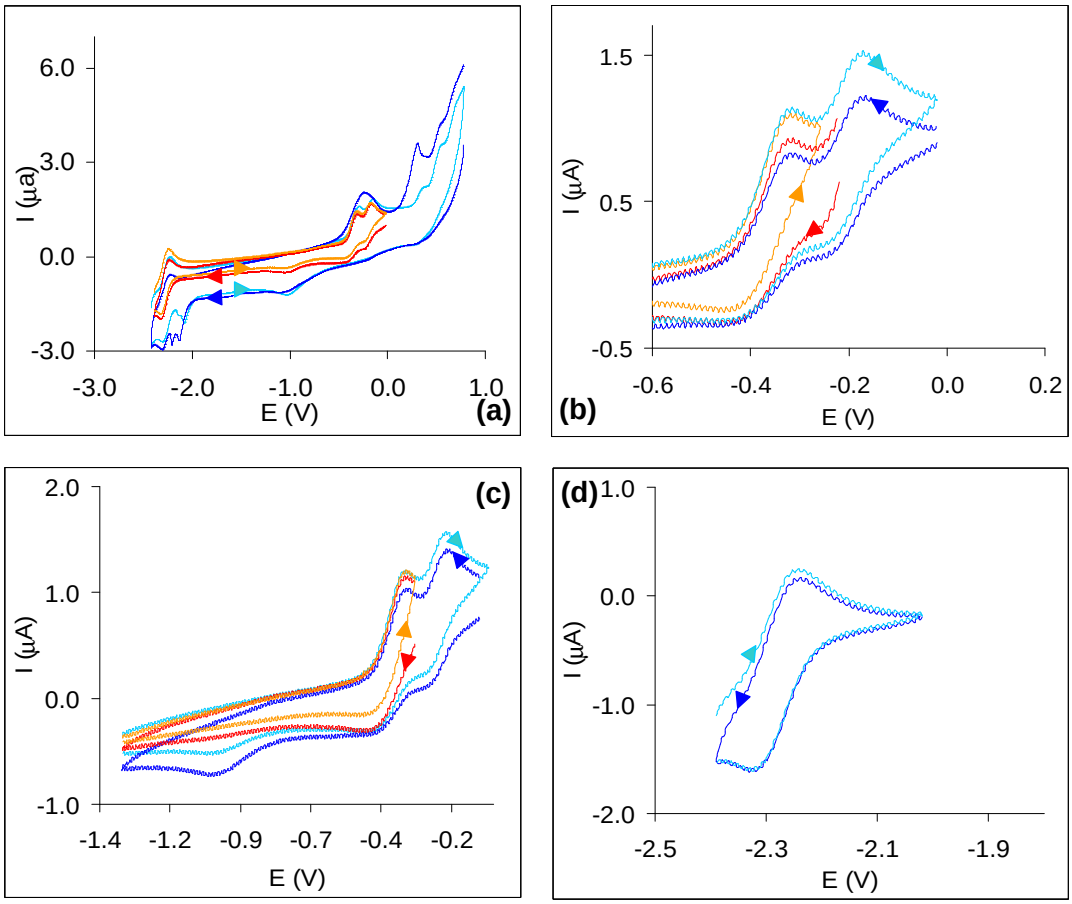

Figure 3.6 : Cyclic voltamogram under nitrogen of [Co_2(L)] recorded at 100 mV.s^{-1} (a) in the range -2.40 V to +0.80 V (dark and light blue traces) and -2.40 to +0.00 V (red and orange traces), (b) in the range -0.6 V to +0.00 V (dark and light blue traces) and -0.6 V to -0.26 V (red and orange traces), (c) in the range -1.31 V to +0.00 V (dark and light blue traces) and -1.31 V to -0.28 V (red and orange traces), and (d) in the range -2.42 V to -2 V (dark and light blue traces).Conditions: 1mM of [Co_2(L)] in dried and distilled benzonitrile, 0.2 M $^{n}Bu_4NBF_4$ *vs.* Fc^{+}/Fc (Reference electrode: silver wire, counter electrode: platinum wire, working electrode: platinum). The arrows indicate the direction of scanning.

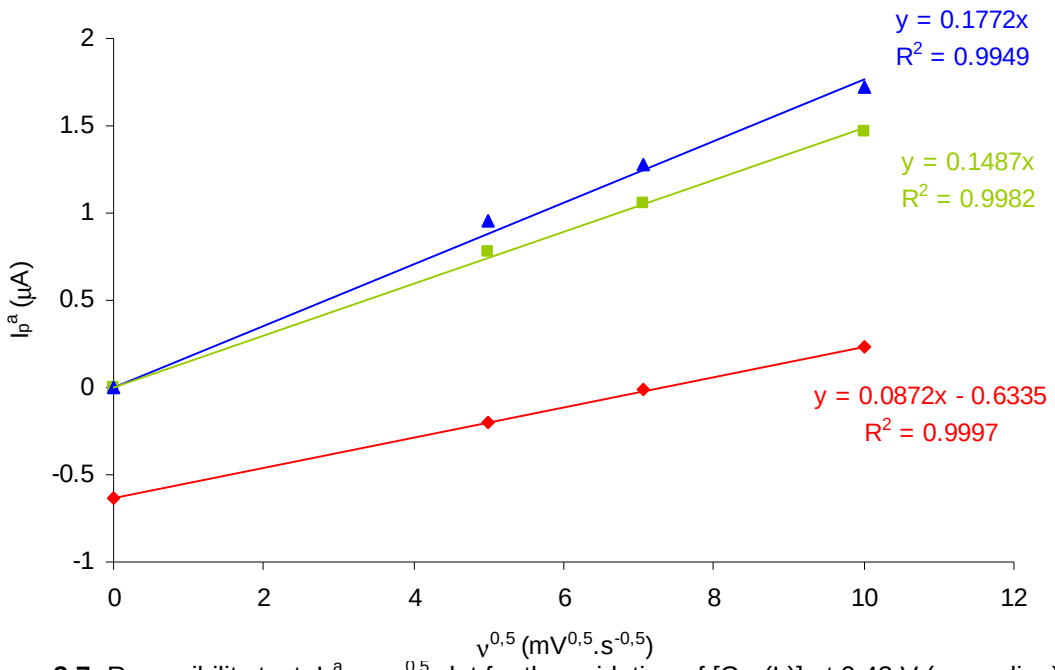

Figure 3.7: Reversibility test: I_p^a vs. $v^{0.5}$ plot for the oxidation of [Co_2(L)] at 0.43 V (green line) and 0.57 V (blue line) and the reduction at -1.57 V (red line).

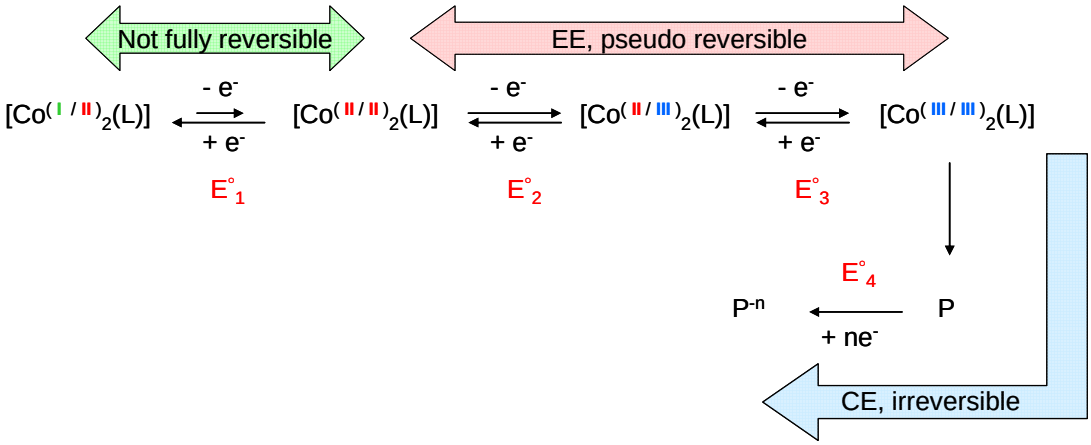

Scheme 3.2: Electrochemical and chemical reactions occurring during cyclic voltametry of [Co_2(L)] under nitrogen.

The electrochemistry of the apparented cofacial diporphyrin [Co_2(DPX)] and [Co_2(DPD)], as well as their *meso*-trans-aryl substituted counter parts [Co_2(DPXM)] and [Co_2(DPDM)] was published by the Nocera group and only the initial oxidation process was studied.[8, 9] While the *trans*-substitution did not affect the overall electrochemistry, the complexes with a xanthene spacer exhibit a two-step process, each corresponding to a one-electron step while those with a dibenzofuran spacer exhibit a one-step, two-electron process (**Table 3.2**). The Le Mest group studied the

electrochemistry of [Co_2(DPA)] and [Co_2(DPB)] on the full electrochemical window of benzonitrile and observed extra features. The first process was observed as well and consisted in a one-step, two-electron process for the anthracene based complex and two separated one-electron steps for the biphenylene one. In this case, the intensive EPR and UV-visible spectrochemistry study and the comparison with complexes of several other metals localised the redox site for this first process on the π-rings. A second process consisting in a one-step two-electron reduction was also present at higher potenciel (0.59 V and 0.65 V for [Co_2(DPA)] and [Co_2(DPB)] respectively) and was attriduted to a metal-centre based oxidation. A third process accounting for a one-step, two-electron oxidation was identified and attributed to a π-ring located redox centre.

Compound	1st process E° (V)[a]	2nd process E° (V)	3rd process E° (V)	Ref
[Co_2(L)]	-0.37 / -0.22	0.38 / 0.57	N/A	This work
[Co_2(DPX)]	0.17 / 0.28[a]	N/P	N/P	8
[Co_2(DPD)]	0.33 [a]	N/P	N/P	8
[Co_2(DPA)]	0.05[b]	0.59	0.77	10
[Co_2(DPB)]	0.00 / 0.17[b]	0.65	0.88	10

Table 3.2: Electrochemical data for the oxidation of [Co_2(L)] and related compounds, obtained from cyclivoltametry in PhCN + $^nBu_4NBF_4$ under N_2 unless otherwise stated. For the cobalt diporphyrins, all processes are reversible, [a] recorded in nitrobenzene, *vs.* Ag/AgCl; [b] electrolyte: $^nBu_4NPF_6$, N/P: not published.

In comparison, the first oxidation process observed in [Co_2(L)] was a two-step process and is believed to correspond to the successive one electron reduction of the two metallic centres, which indicates a communication between the two cobalt atoms. The initial oxidation of the Schiff-base complex occurs at slightly lower potentials than in the corresponding diporphyrin based complexes. A second oxidation process was also observed and consisted in two steps; it is believed to be ligand based (but probably correspond to a process quite different from the π-ring-based one observed in the cobalt diporpyrin systems as the two types of ligands are fundamentally different). This later process was considered to be of too high potential to be involved in any ORR.

The location of the redox centres for the different processes in [Co_2(L)] is based only on the comparison of the CVs with the ones where the cobalt metallic centres were replaced by non-electroactive zinc metallic centres. This statement was not confirmed by a spectroelectrochemistry study but the EC character of the Co(II)/Co(III) redox process is similar to that was observed cobalt porphyrins and supports the theory of a metal based process. Furthermore, the two step process observed supports an effective communication between the two cobalt atoms. The reduction of the cobalt(II) centres was also observed in cofacial diporphyrins and, as for [Co_2(L)], this process was not investigated in detail because it does not contribute to the reaction with oxygen.

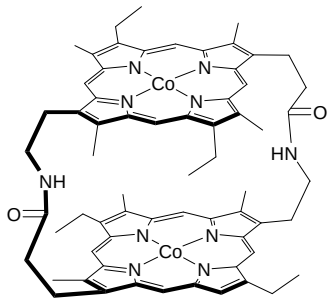

Chart 3.1: Representation of [Co_2(FTF6)]

Despite some differences, the electrochemistry of [Co_2(L)] is quite similar to that of cofacial diporphyrins and similar catalytic behaviours can be expected. Nevertheless, complexes with similar electrochemistry under N_2 and under O_2 were shown to have very different catalytic activity towards the reduction of oxygen. For example, [Co_2(DPA)] catalyses the reduction of oxygen to water and [Co_2(FTF6)] (Error! Reference source not found.) does not; this is believed to be due to the clamping ability of [Co_2(DPA)] (Pacman effect) whereas [Co_2(FTF6)] is more rigid.[10] This demonstrates that the geometry-activity relationship is more relevant than the electrochemistry-activity relationship, and the clamping ability of [Co_2(L)] makes it a good candidate for oxygen reduction reactions (ORR).

3.2.2 Chemical reactivity

3.2.2.1 Chemical oxidation of [Co_2(L)]

$$\left[Co_2^{(II)}(L)\right] \rightarrow \left[Co_2^{(II/III)}(L)\right]^{+} + e^{-} \rightarrow \left[Co_2^{(III)}(L)\right]^{2+} + 2e^{-} \quad \textbf{(3.1)}$$

The chemical oxidation of [Co_2(L)] as described by (**3.1**) was attempted using both the single electron oxidant $AgBF_4$ and oxygen transfer oxidising agents such as trimethylamine N-oxide and pyridine N-oxide. Using the latter reagents, no reactions were observed in THF (at room temperature or at 66 °C) and only crystals of the starting material were isolated. In contrast, the reaction between [Co_2(L)] and [$AgBF_4$] in benzonitrile resulted in the oxidation of both cobalt centres.

In-situ reactions between [Co_2(L)] and $AgBF_4$ in benzonitrile were carried out and ^{1}H NMR spectra were recorded with double solvent suppression of benzonitrile resonances. An excess of silver tetrafluoroborate leads predominantly to a diamagnetic ^{1}H NMR spectrum, consistent with the double oxidation of [Co_2(L)] to the binuclear cobalt(III) complex, [Co_2(L)][BF_4]$_2$ (**Figure 3.8**), the weak paramagnetic resonances around -1.3 ppm and -2.5 ppm almost disappear when the sample is filtered and were attributed to small impurities). The relatively poor quality of the spectrum in the diamagnetic region prevented a full interpretation. As expected for a fully oxidised species, no reaction was observed upon freeze-pump-thaw degassing the sample followed by exposure of the sample to oxygen. The same reaction carried out with only one equivalent of [$AgBF_4$] afforded a new paramagnetic compound with a smaller magnetic moment than [Co_2(L)] under the same conditions (1.25 B.M for the singly oxidised complex compared to 1.7 B.M for [Co_2(L)] in benzonitrile under nitrogen). The measurement of a smaller magnetic moment is consistent with the formation of the mixed valence cobalt(II)/cobalt(III) complex [Co_2(L)][BF_4]. However, solution magnetic moments measured by the Evans' method proved to give quite confusing results and their full interpretation in terms of number of unpaired electrons was not possible (see section 3.1.1).

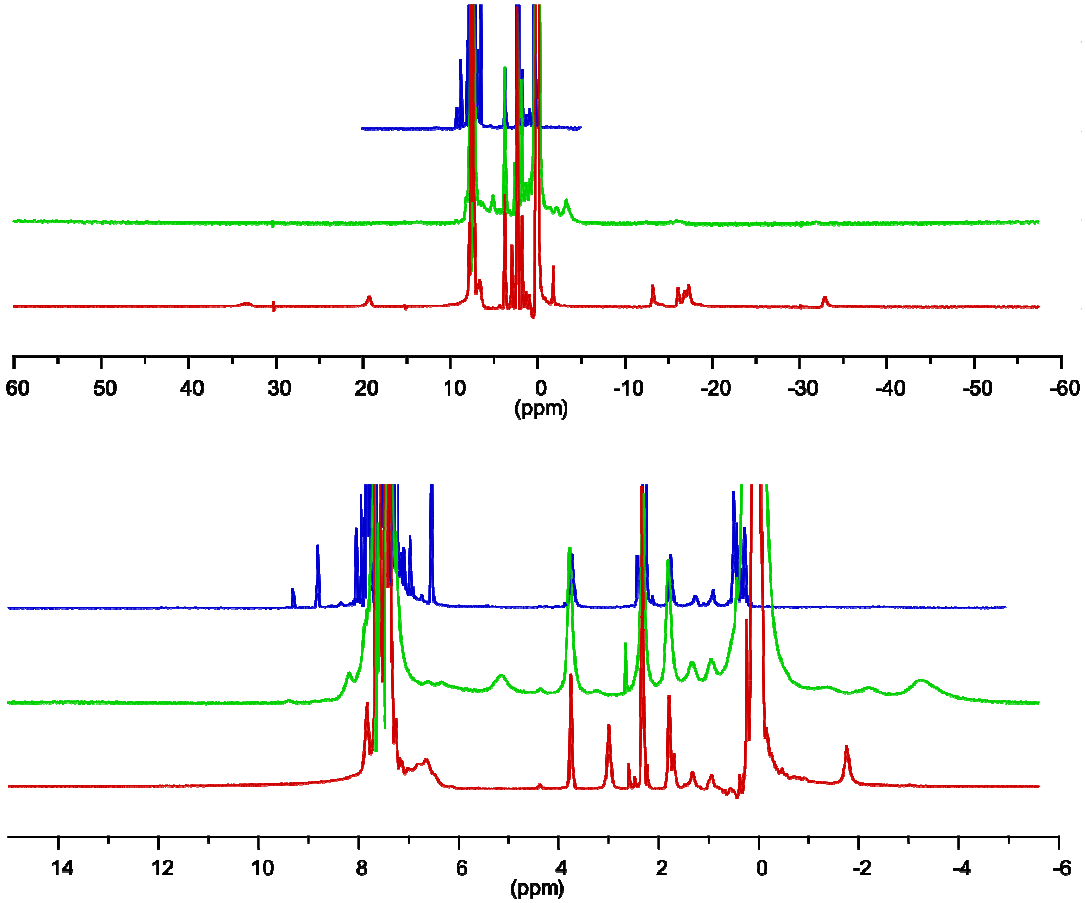

Figure 3.8: ^{1}H NMR spectra in PhCN of [Co_2(L)] in different oxidation state: [Co_2(L)] (bottom, red spectrum), [Co_2(L)][BF_4] (middle, green spectrum) and [Co_2(L)][BF_4]$_2$ (top, blue spectrum). Top figure: full paramagnetic spectra (60 to -60 ppm), bottom figure: expansion of the diamagnetic region (15 to -6 ppm).

3.2.2.2 Chemical reduction of [Co_2(L)]

$$\left[Co_2^{(II)}L\right] + 2e^- \rightarrow \left[Co_2^{(I/II)}L\right]^- + e^- \rightarrow \left[Co_2^{(I)}L\right]^{2-} \qquad \textbf{(3.2)}$$

Upon addition of potassium graphite to a solution of [Co_2(L)] in THF, the formation of a large amount of brown solid was observed. The addition of pyridine solubilised the reduced product and an insoluble black powder, consistent with graphite, remained in the reaction mixture. The ^{1}H NMR spectrum in THF/d_5-pyridine was silent (**Figure 3.9**, top spectrum, only the resonances for the solvent and small impurities are observed), which is consistent with the reduction of the two cobalt cations to Co(I) to form [K]$_2$[Co_2(L)] as described by (**3.2**). A paramagnetic minor product was also observed. The same reaction carried out with only one equivalent of potassium graphite yielded exclusively the paramagnetic product previously

observed (**Figure 3.9**, middle spectrum) which is consistent with the formation of the Co(I)/Co(II) mixed valence complex [K][Co_2(L)].

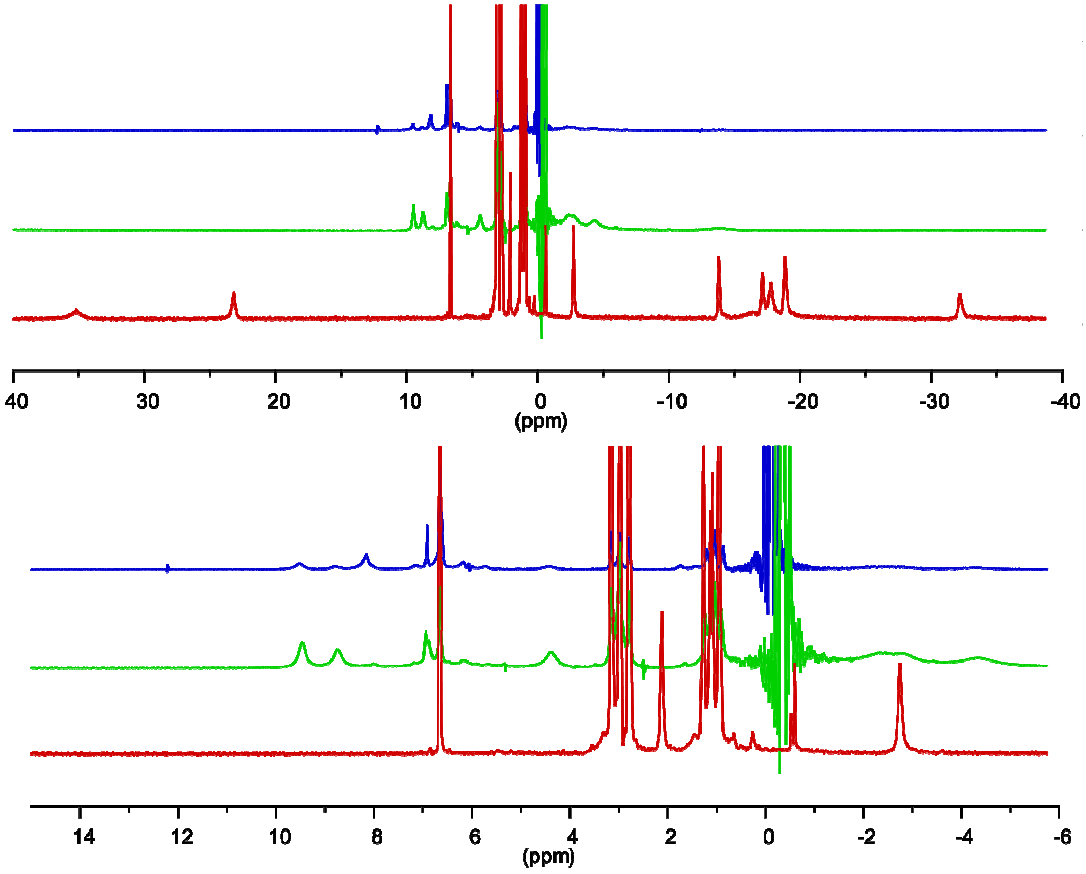

Figure 3.9: ^{1}H NMR spectra in THF of [Co_2(L)] in different oxidation state: [Co_2(L)] (bottom, red spectrum), [Co_2(L)][K] (middle, green spectrum), [Co_2(L)][K] and [Co_2(L)][K]$_2$ mixture (top, blue spectrum). Top figure: full paramagnetic spectra (60 to -60 ppm), bottom figure: expansion on the diamagnetic region (15 to -6 ppm).

When the reduced complexes were exposed to air, re-oxidation occurred and resonances were observed both in the paramagnetic and diamagnetic regions of the ^{1}H NMR spectra (**Figure 3.10**). The singly reduced complex oxidised to a single compound and the ^{1}H NMR spectrum exhibits 12 resonances spread between -10 and 65 ppm; this observation is consistent with the possible formation of a single Co(II)/Co(III) cofacial complex. The other sample oxidizes to the same complex and another product; a paramagnetic complex for which only 5 resonances are observed and which could be a Co(I)/Co(II) species. In both cases, the spectrum of the aerated samples still contained the paramagnetic resonances attributed to [K][Co_2(L)], a sign of incomplete oxidation. A more detailed study would be required to determine with certainty the nature of the different complexes formed.

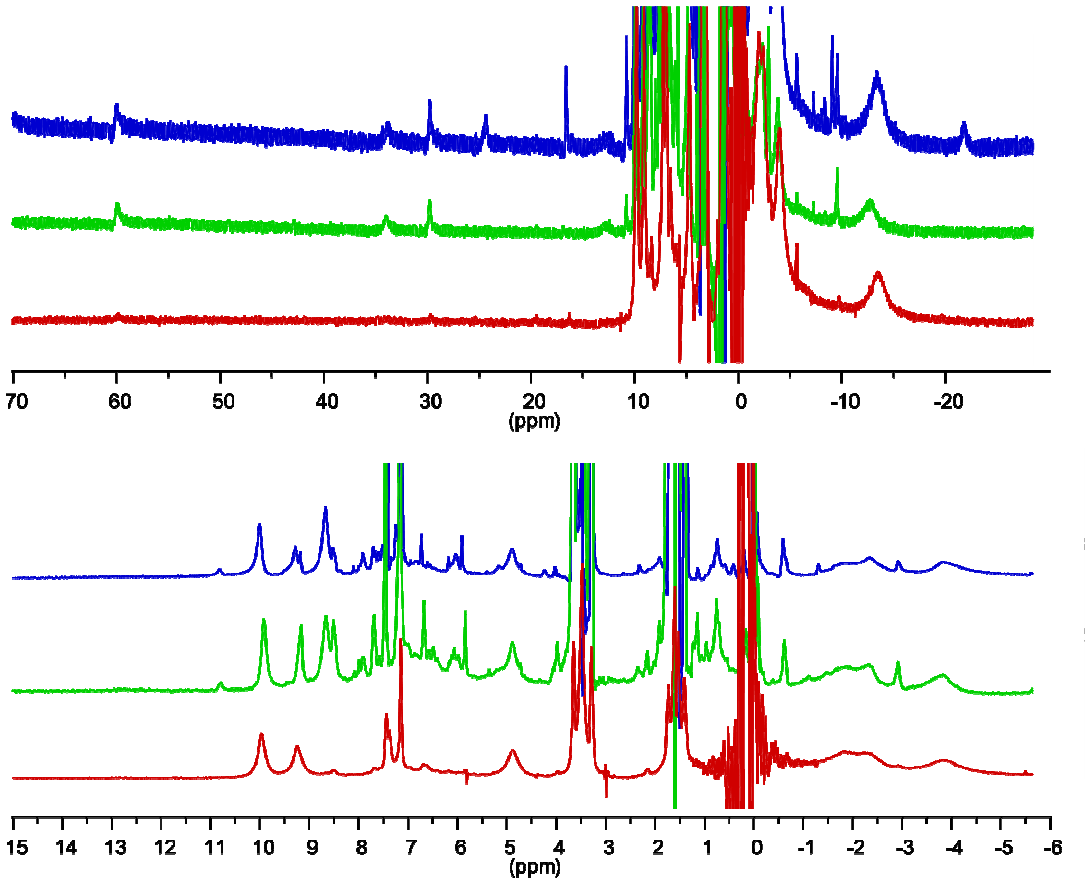

Figure 3.10: ^{1}H NMR spectra in THF of the products of the reaction between the reduced forms of [Co_2(L)] and air: [K][Co_2(L)] (bottom, red spectrum), [K][Co_2(L)] + air (middle, green spectrum), [K][Co_2(L)] and [K]$_2$[Co_2(L)] mixture + air (top, blue spectrum). Top figure: full paramagnetic spectra (70 to -30 ppm), bottom figure: expansion on the diamagnetic region (15 to - 6ppm).

The initial redox studies show that both the Co(III) and the Co(I) oxidation states are chemically and electrochemically available. Upon oxidation and reduction, the communication between the two cobalt centres in [Co_2(L)] allows stepwise redox processes with reaction of one cobalt at a time. The Co(I)/Co(I) oxidation state seems difficult to access but many other oxidation states - Co(I)/Co(II), Co(II)/Co(III) and Co(III)/Co(III) - appear to be readily available from [Co_2(L)]. The mixed valence complexes are of particular catalytic interest and further investigation would be required to fully characterise these different complexes and study their properties in more details.

3.3 Reactivity of $[Co_2(L)]$ towards molecular oxygen

The binuclear cobalt complexes of the wedge-shaped ligands previously studied in the Love group spontaneously bind dioxygen in THF, especially in the presence of small amounts of pyridine which affords the di-pyridine adducts of the oxygen compound.[2, 4, 11] The oxygen reaction product generally consists of a mixture of: (1) the superoxo (O_2^-) cobalt(III) complex $[Co_2(O_2)(py)_2(L^n)]^+$ (n = 1, 10) and (2) either the peroxide (O_2^{2-}) cobalt(III) complex $[Co_2(O_2)(py)_2(L^1)]^4$ or the hydroxide (OH^-) mixed valence cobalt(II/III) complex $[Co_2(OH)(py)_2(L^{10})]$.[11] With respect to full oxygen reduction to water, the peroxide and the hydroxide species are not desirable as the former can lead to hydrogen peroxide production and the latter is catalytically inactive. Furthermore, the superoxo complex was shown to be the active species in the catalytic cycle of the full reduction of oxygen by cofacial diporphyrins[9] and is therefore the only desired oxygenation product. In contrast to complexes previously synthesised in the Love group, binuclear cobalt(II) cofacial diporphyrins do not react spontaneously with dioxygen and chemical oxidation is a prerequisite to the entrance in a catalytic cycle.

Quite surprisingly, it was found that $[Co_2(L)]$ does not spontaneously react with oxygen in THF or upon addition of pyridine. Even a solution in neat pyridine under aerobic conditions does not afford an oxygenation product of the complex. In benzonitrile, however, the reversible binding of oxygen by $[Co_2(L)]$ was observed under atmosphere of dioxygen, causing the red solution of $[Co_2(L)]$ to turn dark brown. The higher potency to uptake oxygen in benzonitrile is in agreement with observations made on a related cofacial diporphyrin $[Co_2(DPB)]$.[12] The resulting complex of L, as well as the reversibility of the oxidation, were studied by ^1H NMR spectroscopy, EPR, and UV-visible spectroscopies as well as by cyclic voltametry.

The same solution of $[Co_2(L)]$ in benzonitrile was used for both EPR and ^1H NMR spectroscopy. The sample, initially prepared under N_2, was freeze-pump-thaw degassed and placed alternatively under O_2 then N_2 and the spectra obtained after a few cycles are presented in **Figure 3.11** and **Figure 3.12**.

3.3.1 Oxygen binding observed by ^{1}H NMR spectroscopy

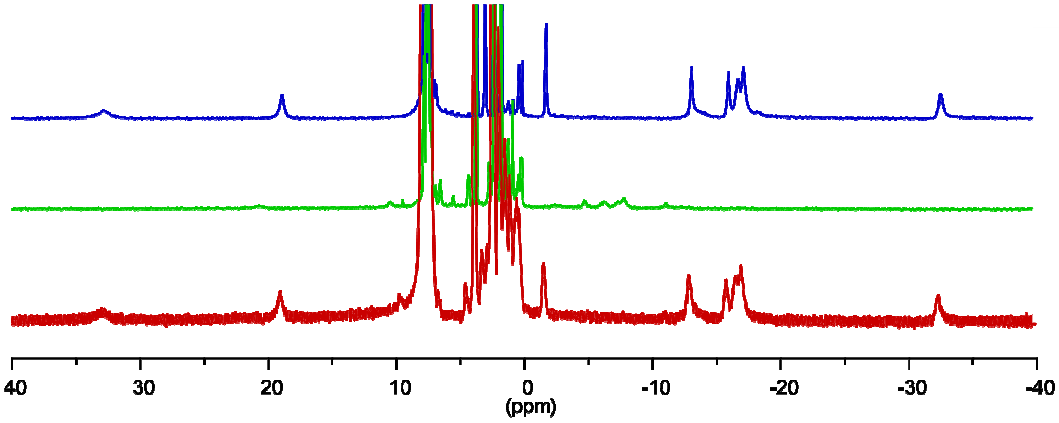

Figure 3.11: ^{1}H NMR spectra in benzonitrile of [Co_2(L)] under nitrogen (top, blue spectrum), degassed and placed under oxygen (middle, green spectrum), and degassed again and placed back under nitrogen (bottom, red spectrum). Intensities were referenced to a residual signal of PhCN for the spectra to be on a comparable scale.

The poor quality of the solvent-suppressed ^{1}H NMR spectra, especially in the aliphatic region, prevented complete assignment; however, many features are still clear. Under a nitrogen atmosphere, only 8 paramagnetically shifted resonances out of the 12 resonances expected were clearly identified between -40 ppm and 40 ppm. Nevertheless, the comparison of the different spectra as well as magnetic moment measurements using the Evans' method could be achieved. When the sample was placed under an oxygen atmosphere, 6 resonances of very weak intensity were identified between -15 ppm and 25 ppm and the original spectrum was recovered when the sample was placed under nitrogen again (**Figure 3.11**). The weak signals observed under O_2 suggest the formation of a major, NMR silent product and an observed minor paramagnetic product. Comparative integration comparative to a residual resonance of the solvent (around 4 ppm) quantified the minor product of oxidation as less than 10% of the sample and both products reversibly return to the original [$Co^{(II)/(II)}_2$(L)] complex when placed back under an inert atmosphere. The by-product could not be identified with certainty, but a number of formulations can be ruled out by comparison to some of the compounds observed for other Pacman ligands;[3, 4] the peroxo-complex [$Co^{(III/III)}_2(O_2^{2-})$(L)] would be diamagnetic and the hydroxyl-complex is geometrically very unlikely due to the large metal separation. The hydroxide salt of the superoxo cation, [$Co^{(III/III)}_2(O_2^{-})$(L)][OH], remains one possibility, although in the related system this was found to be NMR silent.

Interestingly, when the sample is exposed to air (from the ambient atmosphere) most paramagnetic resonances vanish, even the ones corresponding to the minor oxidation product. This difference implies the formation of yet another compound which could be $[Co_2(\mu\text{-}O_2H_3)(L)]^+$, the product of an oxidation reaction in the presence of atmospheric water (see section 3.3.5).

The paramagnetic nature of the main oxidation product and the full reversibility of the oxygen binding were confirmed by *in situ* measurement of the solution magnetic moment (**Table 3.3**). A larger magnetic moment was observed under oxygen and the initial value was restored on return to inert atmosphere.

	μ_{eff} (B.M.)	Unpaired electrons Calculated[a]	Expected
Initial sample under N_2	1.693	0.966	2 [b]
Sample under O_2	1.969	1.209	1[c]
Sample placed back under N_2	1.672	0.948	2 [b]
Sample under air	1.566	0.8585	0 or 1[d]

Table 3.3: Evans' method on $[Co_2(L)]$ in benzonitrile under different atmospheres, average over 3 samples. [a]spin only value, [b]for $[Co_2(L)]$, [c]for $[Co_2(\mu\text{-}O_2)(L)]^+$ and [d]for $[Co_2(\mu\text{-}O_2H_3)(L)]^+$ or $[Co_2(\mu\text{-}O_2)(L)]^+$ respectively.

The full interpretation in terms of number of unpaired electrons was not straightforward as the value observed for $[Co_2(L)]$ in benzonitrile is much lower than the 2.83 B.M. expected for a Co(II)-Co(II), s = 1 species and actually much closer to the spin-only value of 1.73 B.M. expected for a Co(II)-Co(III) complex. These confusing results are consistent with observations made in the chemical oxidation of $[Co_2(L)]$ (see 3.2.1.1) and the extra contribution to the magnetic moment was not fully understood.

3.3.2 Oxygen binding observed by EPR spectroscopy

No signal was observed in fluid solution by EPR spectroscopy under N_2 or under O_2 and so the spectra were recorded on frozen samples at 100K. [10] The initial EPR spectrum under N_2 shows a very weak, featureless resonance at g ~ 2.0.

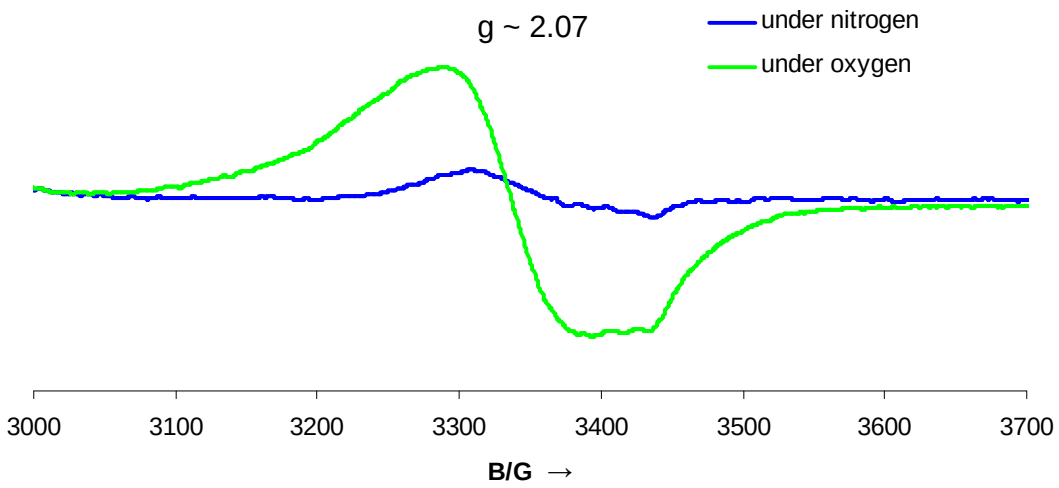

Figure 3.12: EPR spectrum of [Co_2(L)] under nitrogen (blue line) and under oxygen (green line).

Under O_2, the axial EPR spectrum exhibits an intense resonance at g ~ 2.07 showing only weak hyperfine. This contrasts with the 15 line spectrum expected for a superoxo radical coupling with both of the cobalt nuclear spins (^{59}Co, 100% natural abundance, I = 7/2, multiplicity = 2nI+1 = 15 lines). Even though no coupling is observed, the g value is consistent with a ligand-based single electron which may suggest the superoxo complex $[Co^{(III/III)}_2(O_2^{-})(L)]^{+}$ has formed, as suggested by the NMR data; the peroxo complex $[Co^{(III/III)}_2(O_2^{2-})(L)]$ would be EPR silent. Returning to a nitrogen atmosphere affords the initial featureless signal (the weak feature present on **Figure 3.12** is due to residual traces of oxygen in the sample after a few cycles).

3.3.3 Oxygen binding observed by UV-Visible spectroscopy

The UV-visible spectrum of [Co_2(L)] under nitrogen consists of two broad signals at 430 (ln ε = 10.69) and 355 nm (ln ε = 11.04) (**Figure 3.13**). Degassing the sample and exposure to oxygen increases the intensity of the signal, resulting in a broad band at 449 nm (ln ε = 10.79) and a sharp band at 358 nm (ln ε = 11.36). Once again the return of the original spectrum was observed when the sample was placed back under an inert atmosphere, confirming the reversibility of the oxygen binding.

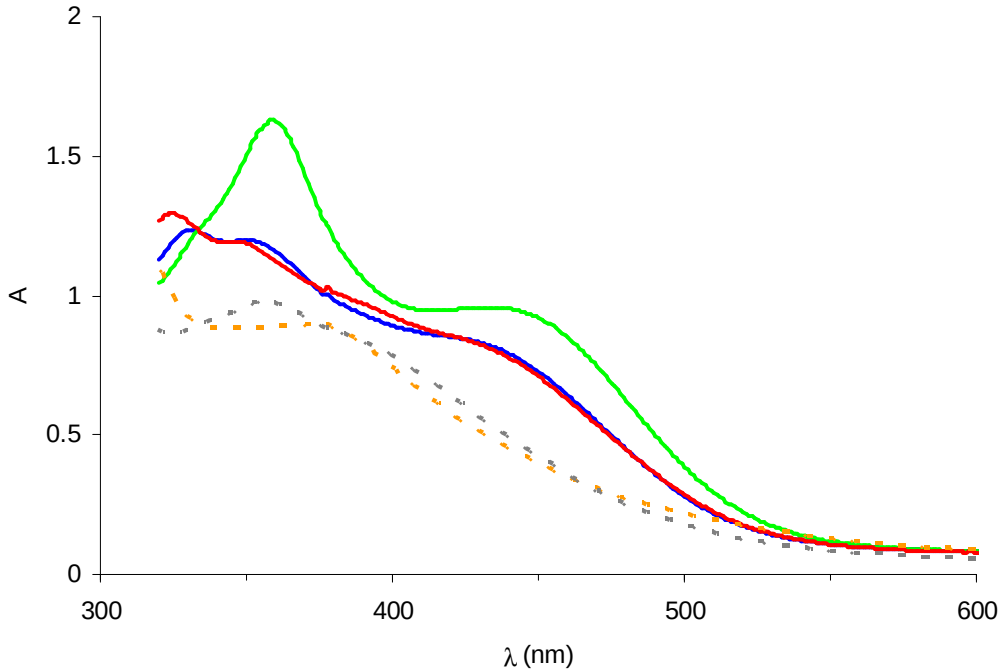

Figure 3.13: UV-visible spectrum of a 20 μM solution of [Co_2(L)] in benzonitrile under nitrogen (blue spectrum), degassed and placed under oxygen (green spectrum), degassed again and placed back under nitrogen (red spectrum), in air (orange dashed spectrum) and in a 20:80 O_2/N_2 mixture with 2 mM TFA.

The changes in shape and intensity indicates a behaviour consistent with the same experiment carried out on $[Co_2(DPA)]^+$ and $[Co_2(DPB)]^+$.[12] In the case of the cofacial diporphyrins, a one electron π-ring based oxidation is a prerequisite to the oxygen uptake. The spectra recorded under oxygen exhibits sharper, red shifted Soret band and Q-band compared to the corresponding spectrum recorded under nitrogen. Bubbling nitrogen through the sample regenerated the initial spectrum which is indicative of a reversible binding of oxygen.

Stirring the sample in air afforded a new spectrum with a single, very broad feature around 380 nm (ln ε = 10.75), supporting the formation a different product which arises from a reaction with water (see section 3.3.5). The addition of a small amount of water to a sample under nitrogen led to a partially opaque sample as the solubility of water in benzonitrile is very limited. However, the poor quality spectrum exhibited the same shape as the sample exposed to ambient atmosphere.

The addition of a 100 fold excess of TFA to a sample of $[Co_2(L)]$ under dry air (made from a 20:80 mixture of O_2 and N_2) afforded yet another spectrum which consisted of a broad peak at 356 nm (ln ε =10.80). The quenching of the shoulder above 450 mn observed in the absence of an acid suggests the formation of a new compound arising from the protonation of the oxygenated compound. In the light of the EPR spectroscopy experiment which suggested that the electron in $[Co_2(O_2)(L)]^+$ is located on the dioxygen ligand, the most sensible product of protonation is $[Co_2(HO_2)(L)]^{2+}$.

3.3.4 Oxygen binding observed by cyclic voltametry

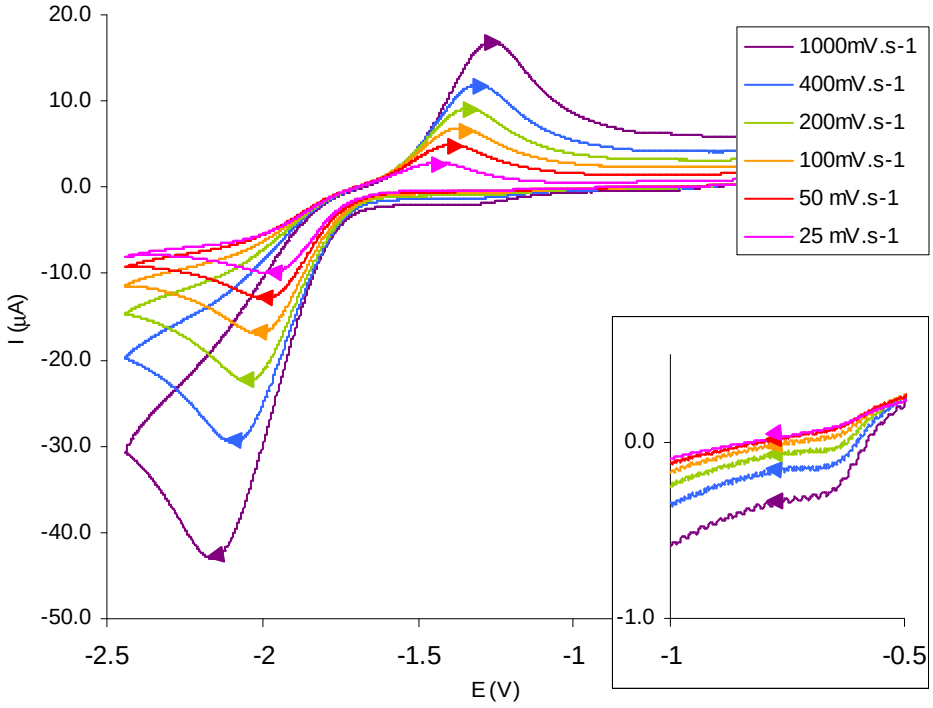

Figure 3.14 : Cyclic voltamogram of $[Co_2(L)]$ under oxygen recorded at 25 $mV.s^{-1}$ (pink trace), 50 $mV.s^{-1}$ (red trace), 100 $mV.s^{-1}$ (orange trace), 200 $mV.s^{-1}$ (green trace), 400 $mV.s^{-1}$ (blue trace), 1000 $mV.s^{-1}$ (purple trace) in the range -2.5 V to -0.5 V. Conditions: 1mM of $[Co_2(L)]$ in dried and distilled benzonitrile, 0.2 M $^nBu_4NBF_4$ *vs.* Fc^+/Fc (Reference electrode: silver wire, counter electrode: platinum wire, working electrode: platinum). The arrows indicate the direction of scanning.

In an attempt to establish the behaviour of the oxygenated complex towards redox reactions, the samples previously studied by CV under nitrogen in benzonitrile solution were oxidized by bubbling oxygen through the solution for 15 minutes. The CVs were recorded at various scan rates and are presented in **Figure 3.14**. The

reduction wave observed at -2.2 V and the oxidation wave observed at -1.25 V correspond to the ORR occurring at the platinum electrode and dominates the spectra; even focusing on the positive potentials did not afford good quality data (**Figure 3.14**, insert), only a weak reduction was observed around -0.4 V and could correspond to the $[Co_2(L)]$ catalysed reduction of oxygen. This is in contrast with experiments carried out on $[Co_2(L^1)]$ where the different solvent and electrode system allowed the observation of two reversible oxidations waves. A less intense reduction wave, at -0.19 V (vs Fc/Fc^+ in chloroform) was also observed[4] and could be reminiscent of the weak reduction observed here at -0.4 V here. Returning to an inert atmosphere by bubbling N_2 through the solution afforded the original voltamograms as expected from the reversible nature of the oxygen binding.

3.3.5 Solid state structure obtained under aerobic conditions

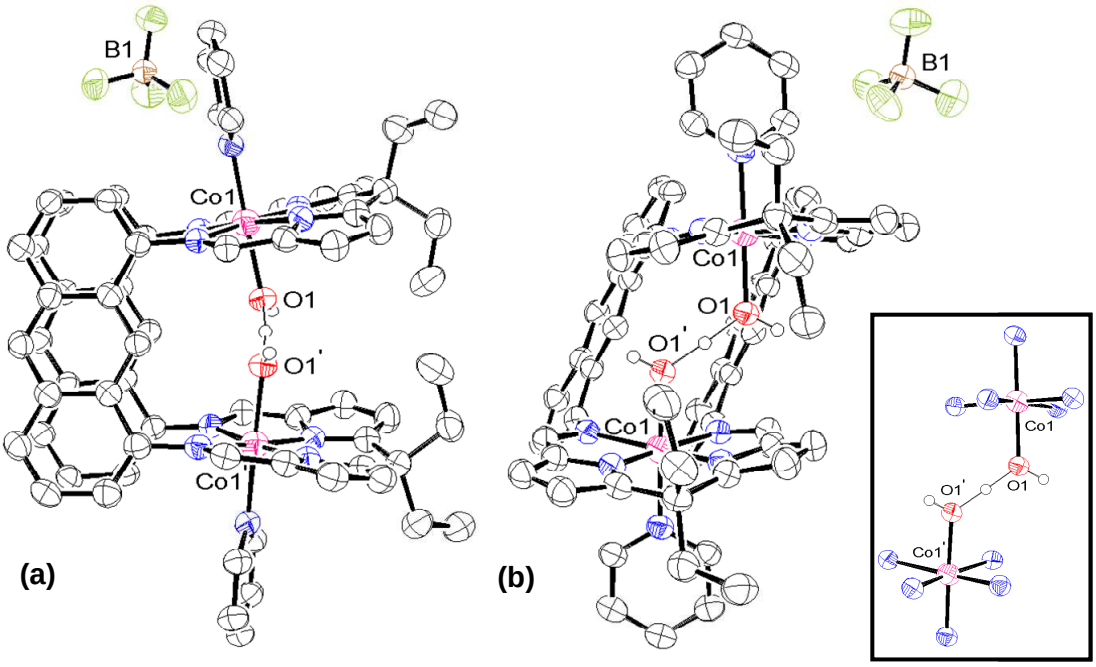

Figure 3.15: X-ray crystal structure of $[Co_2(O_2H_3)(exo\text{-}py)_2(L)][BF_4]\cdot 1.8py$ (displacement ellipsoids are drawn at 50 % probability). (a) Side view, (b) face view. For clarity, the pyridine solvent of crystallisation and all hydrogen atoms are omitted.

Slow diffusion of hexane into a THF solution of $[Co_2(L)]$ containing $^nBu_4NBF_4$ and pyridine under aerobic conditions afforded brown crystals suitable for an X-ray

diffraction study. The solid-state structure of $[Co_2(\mu\text{-}O_2H_3)(exo\text{-}py)_2(L)][BF_4]\cdot 1.8py$ was determined and confirmed that $[Co_2(L)]$ reacted with water under oxidising conditions. The complex adopts the usual cofacial arrangement with each N_4-coordination plane containing a cobalt centre. A hydroxo-hydrate anion is bridging the two metal centres and an *exo*-pyridine ligand is also coordinated to each of the cobalt centres (**Figure 3.15**). The molecule contains a C_2 axis passing between the two backbones, parallel to the two N_4-donor plans and passing through the central hydrogen of the $(O_2H_3)^-$ unit which relates the two N_4-coordination planes by symmetry.

The face-to-face π-stacked anthracene units deviate from co-planarity by 7° and display a shortest carbon-to-carbon contact of 3.443(6) Å. The two N_4-donor mean planes form a bite angle of 18.45° and the mean twist angle is of 24.3°. The two cobalt centres are 5.575(1) Å apart. All the general geometrical parameters of $[Co_2(\mu\text{-}O_2H_3)(exo\text{-}py)_2(L)]^+$ are very similar to those observed in the oxygen-free binuclear cobalt complexes of the same ligand (see section 3.1.3). In the present case, the cobalt atoms are very close to octahedral and are located only 0.06 Å above the N_4-donor plane towards the pyridine ligand.

The fundamental difference between $[Co_2(\mu\text{-}O_2H_3)(exo\text{-}py)_2(L)]^+$ and the previously described $[Co_2(exo\text{-}S)_2(L)]$ (S = -, THF or py) is the change in the oxidation state of the metal centres. While crystals grown under an inert atmosphere lead to Co^{II}-Co^{II} complexes, the present structure exhibits two Co^{III} centres. The presence of a high electronic density peak between the two cobalt-bounded oxygen atoms pointed towards the hydroxo-hydrate anion and was assigned to a bridging hydrogen atom. The hydroxo-hydrate anion hypothesis is further supported by the 2.444(4) Å distance between the two oxygen atoms and the metal to oxygen distance of 1.932(3) Å, parameters in agreement with those reported in the literature for similar moieties (hydroxo-hydrate bridging between any two transition metals: 11 examples reported; O-O range: 2.41 Å to 2.52 Å, average: 2.45 Å; M-O range: 1.87 Å to 2.06 Å, average: 1.93 Å. Hydroxo-hydrate anion bridging between two cobalt atoms: 1 example reported, O-O: 2.41 Å, M-O: 1.91 Å).[7, 13] With the presence of a BF_4^-

counter anion, charge balance assigns the +3 oxidation state to both metal centres. Furthermore, the Co-N(py) distance was shown to be the best indicator of the metal oxidation state for previous Pacman and cofacial diporphyrin complexes[2, 3] and the very short 1.973(3) Å Co-N(py) distance also supports the assignment of the +3 oxidation state. In each unit cell, two BF_4^- molecules could not be located and the structure exhibits large diameter channels (see discussion on nano-scale structure below). The use of the SQUEEZE routine contained within the PLATON software package was required to account for the missing anions and revealed voids with a total solvent accessible volume of 1432 $Å^3$ and a density of 422 electrons per unit cell. This was attributed to two BF_4^- units (requires 41 electrons each) and 8 diffuse molecules of pyridine (requires 42 electrons each).

Compound	M⋯M [Å]	Twist [°]	Interplanar Angle[a]	Co-O [Å]	O⋯O [Å]	Ref
$[Co_2(\mu\text{-}O_2H_3)(exo\text{-}py)_2(L)]$	5.575(1)	24.3	18.5	1.932(3)	2.444(4)	This work
$[Co_2(\mu\text{-}O_2)L^{10}](OH)$	4.150(1)	14.5	65.5	1.908(3)/ 1.942(4)	1.389(4)	3
$[Co_2(\mu\text{-}OH)L^{10}]$	3.531(2)	6.6	58.6	1.988(6)/ 1.916(6)	N/A	3
$[Co_2(\mu\text{-}OH)L^3]$	3.61	5.1	53.8	1.930	N/A	4
$[Co_2(\mu\text{-}O_2)(L^1)]$	4.1511(6)	19.6	62.7	1.936(2)/ 1.932(2)	1.361(3)	4
$[\{Co(OH)\}_2(DPD)]$	8.625(1)	11.2	56.7	2.290(5)/ 2.268(2)	4.597(8)	8

Table 3.4: Comparison of geometric parameters derived from the X-ray crystal structures of $[Co_2(O_2H_3)(exo\text{-}py)_2(L)]$ and related compounds. [a] Also called bite angle.

As a result, the formation of $[Co^{(III/III)}{}_2(\mu\text{-}O_2H_3)^-(exo\text{-}py)_2(L)]^+$ was established and this compound could represent an unknown intermediate in mechanism of the four-electron reduction of oxygen to water by binuclear cobalt cofacial complexes. The addition of a proton and an electron followed by the elimination of two water molecules would afford the di-cobalt(III) oxygen free complex, widely

acknowledged as a crucial step of the catalytic cycle.[9, 14] As this is the first example of a cofacial binuclear cobalt hydroxyo-hydrate, no relevant comparison can be made but geometrical parameters for other oxygen-containing binuclear cobalt complexes are listed in **Table 3.4** as a reminder of the different structurally characterised compound involved in the catalytic process.

The formation of a hydroxo-hydrate can be seen as a result from the larger intermatellic separation compared to the related wedge shaped complexes which, instead, generate hydroxo bridges. A similar behaviour was observed for some binuclear zinc complexes which formed more reactive $(O_2H_3)^-$ bridges, instead of inert OH bridges, when the ligand design induced a larger intermetallic separation (4.3 *vs.* 3.6 Å in the hydroxo-bridged complex).[15]

As mentioned above, it is quite remarkable that the double oxidation from $Co^{(II)}$-$Co^{(II)}$ to $Co^{(III)}$-$Co^{(III)}$ occurs with such a subtle geometrical rearrangement. The change in oxidation state with minimal rearrangement together with the precise positioning of two metals held at a specific distance generates a very well tuned reactive centre as seen in enzymes, Nature's catalysts. In $[Co_2(L)]$ these characteristics are achieved with only 66 carbon and nitrogen core atoms and give the new complex good potential as a catalyst.

Extended solid state structure of $[Co_2(\mu\text{-}O_2H_3)(exo\text{-}py)_2(L)][BF_4]\cdot 1.8py$

The complex $[Co_2(\mu\text{-}O_2H_3)(exo\text{-}py)_2(L)]$ crystallised in the hexagonal space group, P3*C*1. On the nanometer scale, the Pacman molecules $[Co_2(\mu\text{-}O_2H_3)(exo\text{-}py)_2(L)]^+$ assemble into a honeycomb pattern forming large solvent-accessible channels along the *c* axis of the structure (**Figure 3.16**, (a) and (c)). The building block unit for the assembly is made up by two Pacman molecules superimposed as shown on **Figure 3.16** (a), insert. These units assemble in a hexagonal shape, forming the wall of a 12 Å diameter channel (**Figure 3.16**, (b)). Two superimposed BF_4^- anion are located at each vertex of the hexagons, accounting for one third of the counter anions. The channels accommodate the rest of the anions as well as eight diffuse molecules of pyridine as established by the SQUEEZE routine. The assembly occurs via weak

interactions between the electronegative fluorine atoms of the BF_4^- anions and the π-orbitals of the cobalt-bound pyridines (**Figure 3.17**).

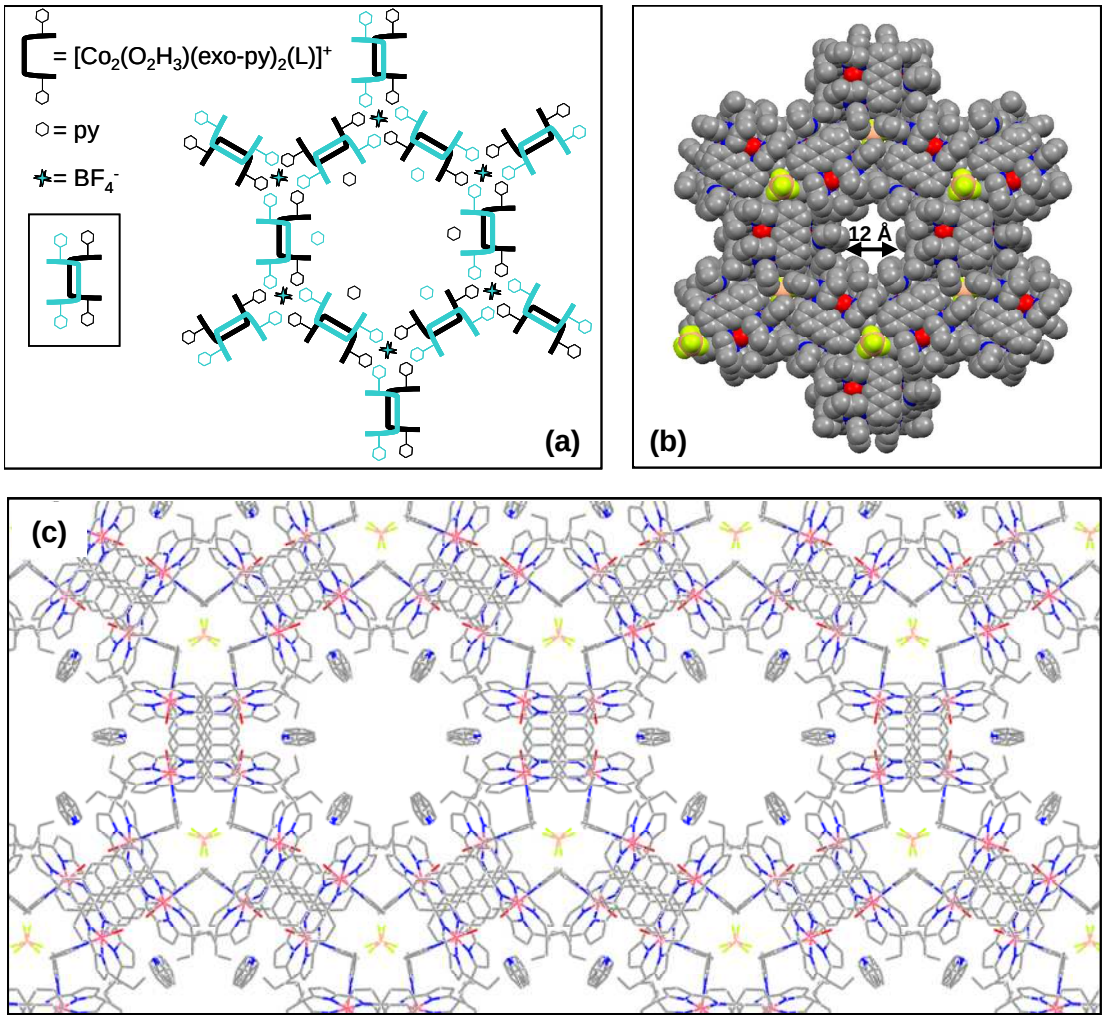

Figure 3.16: Supramolecular assembly within the X-ray crystal structure of $[Co_2(\mu\text{-}O_2H_3)(exo\text{-}py)_2(L)][BF_4]\cdot 1.8py$, view along the *c* axis. **(a)** Schematic representation of the assembly pattern, blue elements are above the mean plane of the represented unit, black elements are below, insert: main building block of the motif made of two superimposed Pacman molecules, **(b)** space fill representation of a channel, **(c)** overall network.

The interaction between the tetrafluoroborate anion and the pyridine corresponds to a weak hydrogen bond where the bond donor in a halogen atom and the acceptor is an aromatic ring. Several examples of this type of bound have been reported and the interaction is involved in the assembly of supramolecular networks,[16, 17] the accommodation of a molecular host in a supramolecular basket[18] or anion recognition.[19] In particular, the interaction of a tetrafluoroborate anion with aromatic C-H bonds is quite unusual and was reported by Brewer and co-workers[17] as

contributing to the supramolecular assembly of an iron(II) complex, tetrafluoroborate and an alkali metal cation (Na, K, Rb or Cs). The carbon-fluorine bonds were found to be ranging between 2.91 and 3.53 Å with an average of 3.14 Å. The Wan group also reported the importance of the B-F···H-C interaction in the assembly of bis-2,2'-difluoro-1,2,3-dioxaborine and the carbon-fluorine distance in the solid state is between 3.11 Å and 3.45 Å.[20] In the assembly pattern of $[Co_2(O_2H_3)(exo\text{-}py)_2(L)]$, the carbon-fluorine bonds are 2.84 to 3.29 Å with an average of 3.02 Å, which is similar to the bond length observed by the Brewer group.

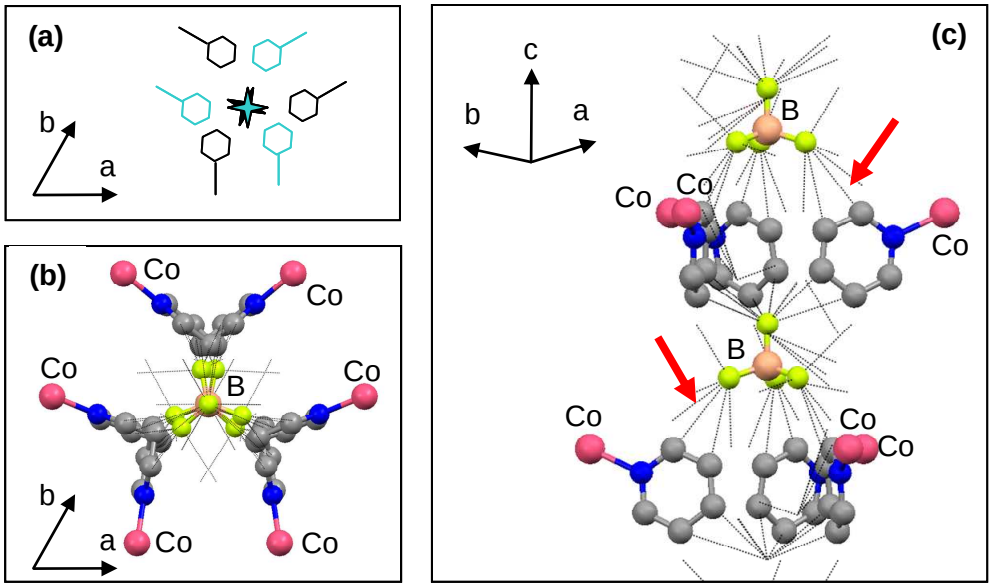

Figure 3.17: Detail of the supramolecular assembly of $[Co_2(\mu\text{-}O_2H_3)(exo\text{-}py)_2(L)][BF_4]\cdot 1.8py$. Only the BF_4^- anions, the exogenous pyridine ligand and the cobalt atom are represented. (a) Schematic representation of the unit along the *c* axis (same colour coding as **Figure 3.16**, (a)), (b) ball and stick view of the same part along the c axis, the thin black lines show close contacts, (c) balls and sticks view of the same part along the *a** axis, the thin black lines show close contacts, the red arrows point to interactions representative the main fluorine-pyridine interaction.

3.4 Catalytic activity study

So far, the study of $[Co_2L]$ revealed its ability to react reversibly with oxygen to afford $[Co_2(O_2)(L)]^+$, best described as a binuclear cobalt(III) superoxo complex, and UV-visible spectroscopy supported the formation of $[Co_2(O_2H)(L)]^{2+}$ upon acidification. Furthermore, $[Co_2(O_2H_3)(L)]^+$ was also identified as a potential intermediate for the reduction of oxygen. However, the ability of $[Co_2(L)]$ to manage the full proton and electron inventory required for the ORR had still to be

demonstrated and the selectivity for water *vs.* hydrogen peroxide needed to be established. This investigation is the subject of the following section.

For [Co_2(L)] to be a catalyst for the reduction of oxygen, it needs to be able to manage the right proton-electron inventory.

$$H_2O_2 \xleftarrow{n=2} O_2 + n\,H^+ + n\,e^- \xrightarrow{n=4} 2\,H_2O \qquad \textbf{(3.3)}$$

The oxygen reduction reaction can happen by two different pathways as depicted in (3.3**)**, resulting in the production of water, hydrogen peroxide, or mixtures of both. For practical reasons discussed in **Chapter 1**, high selectivity towards water production is needed for a viable catalyst. Thus, more than the reduction of oxygen as such, the nature of the reduced products needs to be investigated.

3.4.1 Rotating ring disk electrode experiment

The identification of the oxygen reduction product is of critical importance as the efficiency and durability of the catalyst is directly affected by this selectivity. This was evaluated by a RRDE experiment with the glassy carbon disk drop-coated with the catalyst and the reduction carried out in air-saturated acidic solution. The rotation of the electrode creates a vortex and ensures that the reactants arrive at the disk where the initial oxygen reduction occurs. The reduction products are subsequently directed to the platinum ring by the vortex where the detection of hydrogen peroxide occurs. In the experiments presented here, the glassy carbon disk electrode was drop coated with [Co_2(L)] and the platinum ring electrode was held at +1.00 V *vs.* Ag/AgCl, a potential at which any hydrogen peroxide is oxidised to oxygen. The reaction was carried out in air-saturated 1.0 M TFA.

On **Figure 3.18** to **Figure 3.20**, the bottom (black) line shows the disk current which is an indication of the reduction of oxygen. The top line (red) shows the ring current. As the products of the reduction at the disk are directed to the ring, the presence of an oxidation current at the ring corresponds to the production of H_2O_2 at the disk. When the glassy carbon disk electrode was coated with [Co_2(L)], the reduction of oxygen was observed at 0.13 V *vs.* Ag/AgCl with a disk current of approximately

60 µA **(Figure 3.18**). The absence of a current at the ring electrode is indicative of the absence of hydrogen peroxide and therefore supports the production of water only at the [Co_2(L)] coated disk electrode. After the initial cycle, the reduction wave became significantly less intense and was almost unobservable in the third cycle (**Figure 3.19**). This can be indicative of different phenomena; either the catalyst becomes inactive after the first cycle or the adherence of the catalyst to the disk is poor. As the presence of the red complex could still be visually assessed at the end of the experiment the degradation hypothesis was favoured. Similar observations were also made in the case of the first generation catalyst [$Co_2(L^1)$] within the Love group[4] and in that of face-to-face dicobalt diporphyrins.[21]

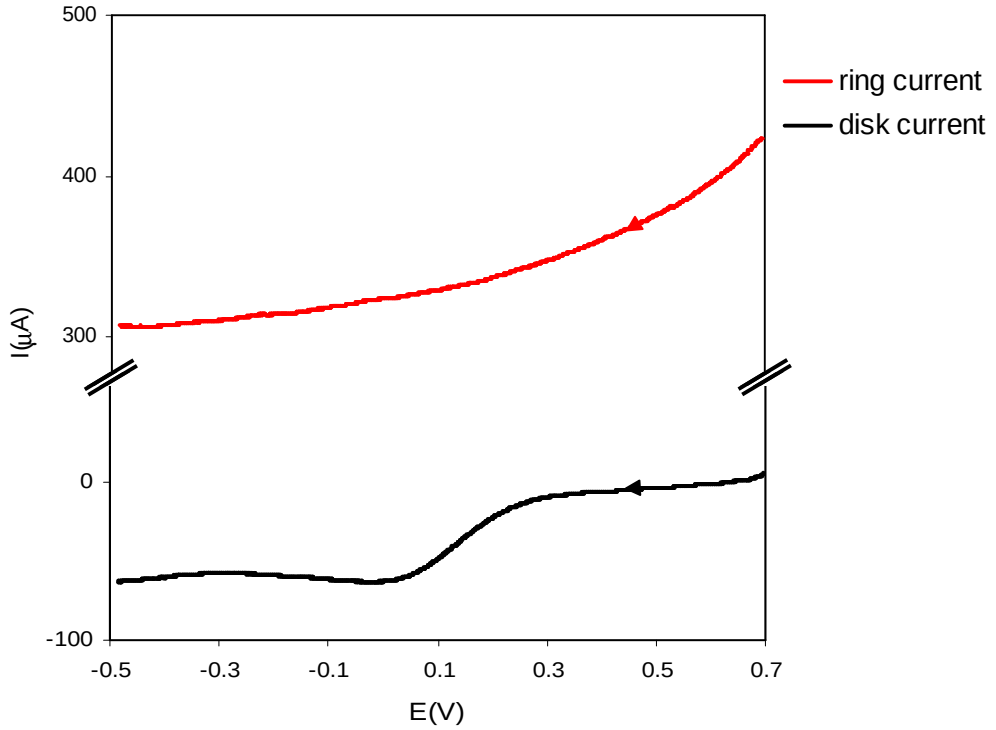

Figure 3.18: Rotating ring disk voltamogram for the reduction of O_2 with [Co_2(L)] coated on a glassy carbon electrode in air-saturated 1.0 M aqueous TFA. The platinum ring was held at +1.00 V *vs.* Ag/AgCl. Rotation rate: 100 rpm (23 % collection efficiency correction factor was applied to the ring current).[4]

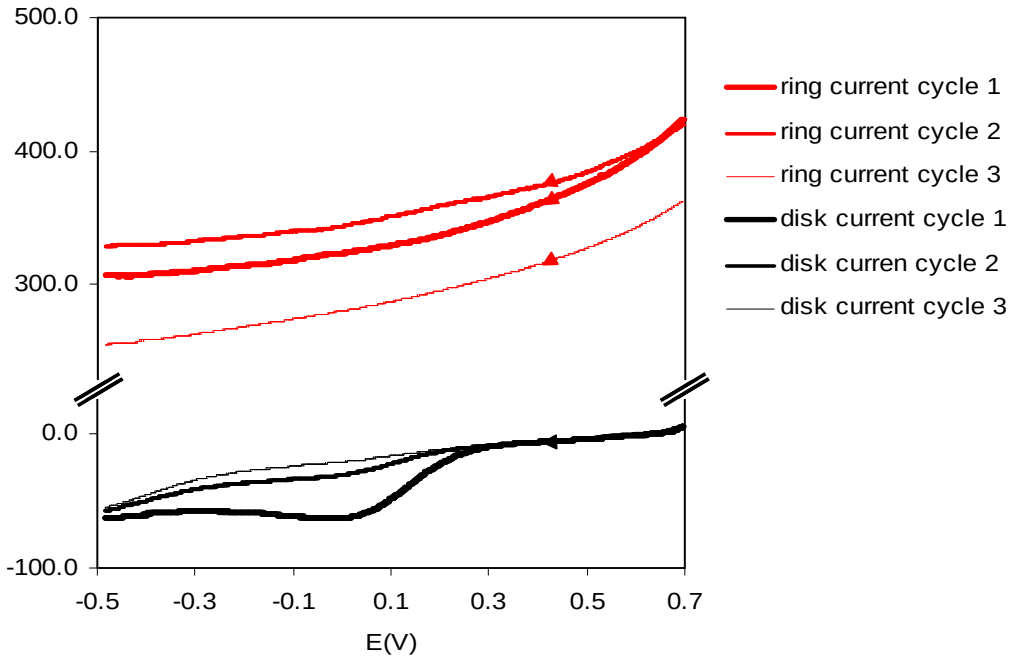

Figure 3.19: Rotating ring disk voltamogram for successive reduction cycles. All other conditions are identical to **Figure 3.18**.

The study of the electrocatalytic activity of $[Co_2(L)]$ would normally require conducting the same experiment (without re-coating the disk electrode) at different rotation rates to access Levich and Koutecky-Levich plots in order to gain an insight on the mechanism and the number of electrons involved. In an attempt to overcome the degradation mentioned above, the disk was cleaned and polished between the experiments and for each rotating rate, the disk was recoated with fresh catalyst. The voltamograms recorded did not show dependency on the rotation rate expected for a catalytic process (**Figure 3.20**) and no conclusions could be reached concerning the electrocatalytic mechanism.

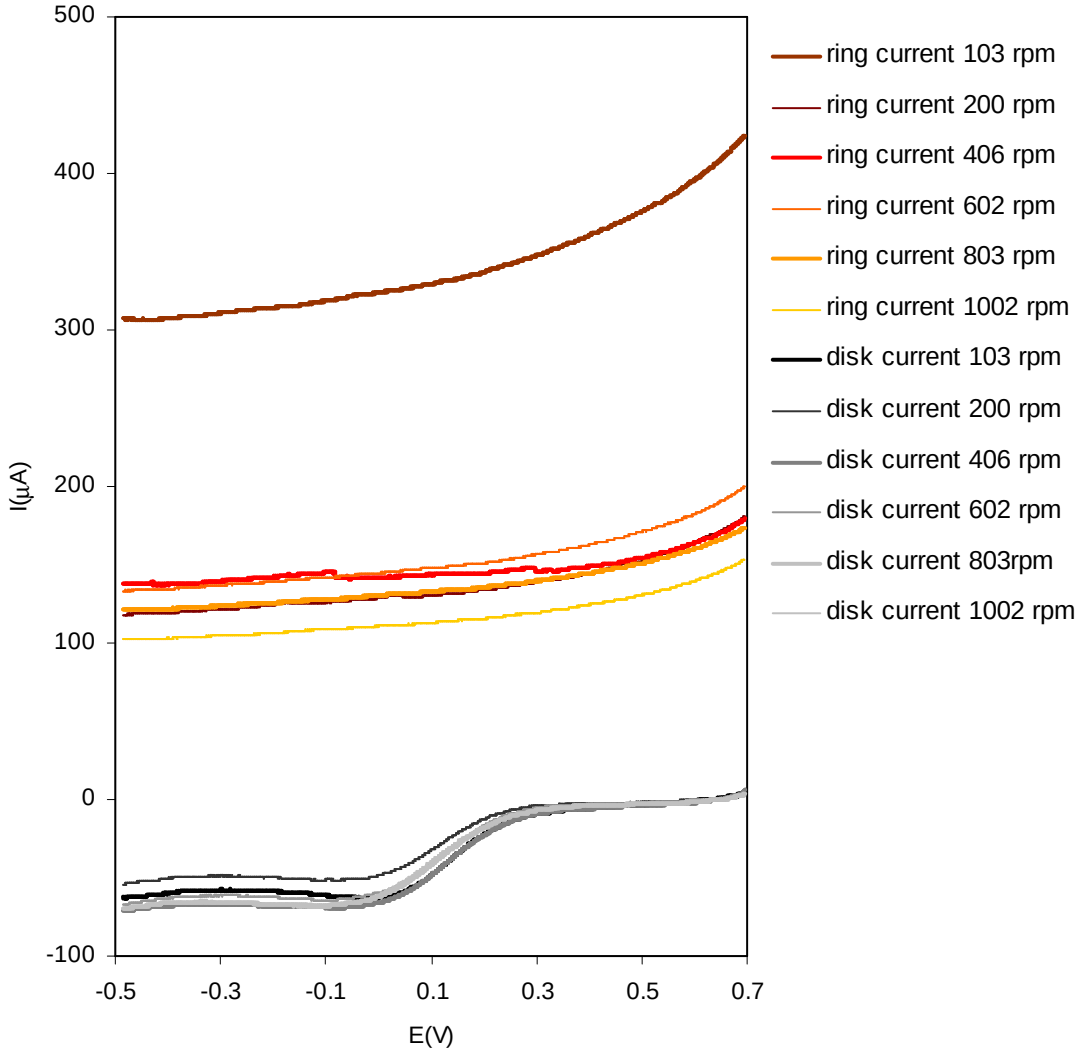

Figure 3.20: Rotating ring disk voltamogram recorded at differend rotation rates. All other conditions are identical to **Figure 3.18**

The RRDE of [Co_2(L)] is similar to the one of [$Co_2(L^1)$] in terms of on-set potencial and current amplitude but an intensity plateau is observed for [Co_2(L)] which was not the case in [$Co_2(L^1)$]. Compared to cofacial diporphyrins, [Co_2(L)] is more selective for the four electron reduction of oxygen as no hydrogen peroxide is detected but the reaction proceeds at larger over-potencials (0.13V *vs.* 0.38 V for [Co_2(DPX)] and 0.37 V for [Co_2(DPD)]), making [Co_2(L)] a slightly less efficient catalyst.[8]

3.4.2 UV-visible spectroscopy experiment

3.4.2.1 Principle of the experiment

The UV-visible method first developed by Fukuzumi and Guilard[14] was used to evaluate the catalytic activity of [Co_2(L)]. In this method, the catalyst is placed in an acidic solution of known oxygen content, and the electron source is provided by the oxidation of a ferrocene derivative to the corresponding ferrocenium ion. The formation of the blue ferrocenium ion is monitored by UV-visible spectroscopy and gives an indication of the number of electrons involved in the reaction and allows identification of the products formed (Error! Reference source not found.). In practice, the experiment is carried out in an air tight cell containing a solution of the catalyst and the ferrocene derivative, a solution of protic acid is added at the starting time of the experiment and the formation of ferrocenium is recorded over time. Under these conditions, the ferrocenium concentration can be determined by the Beer-Lambert law (**3.4**).

$$A = \varepsilon \, l \, C \qquad \textbf{(3.4)}$$

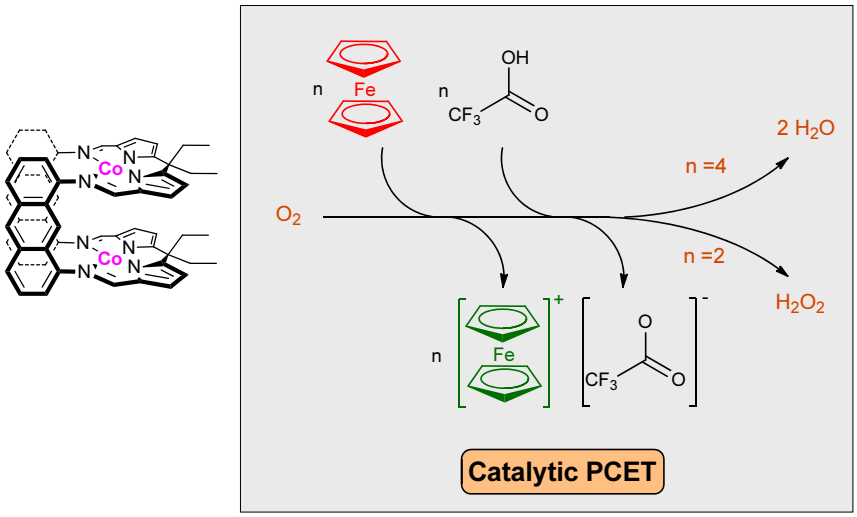

Scheme 3.3: Possible PCET for the reduction of oxygen catalysed by [Co_2(L)] in presence the of ferrocene and TFA.

3.4.2.2 Application to the study of the catalytic activity of [Co_2(L)]

In contrast to the reactions catalysed by [Co_2(DPX)], oxygen reduction carried out with Pacman catalysts in the Love group were found to require higher acid concentration and higher catalyst loading. In particular, the rate of the reaction is

dramatically dependant on the acid concentration.[3, 4] For this reason, the catalytic experiments with $[Co_2(L)]$ were repeated using low concentrations of acid and either high loading of catalyst (**Figure 3.21**, blue line) or low loading of catalyst (**Figure 3.21**, red line). Experiments were carried out in benzonitrile saturated with a 20:80 O_2/N_2 gas mixture so that the initial dioxygen concentration was 1.7 mM. The proton source, TFA, and the electron source, $[Fe(C_5H_5)_2]$, were introduced in a 10 to 60 fold excess making O_2 the limiting reagent. The formation of $[Fe(C_5H_5)_2]^+$ was monitored over time by the absorption at λ_{max} = 620 nm (ε_{max} = 330 $M^{-1}.cm^{-1}$). Under these conditions, the total reduction of oxygen by the two-electron pathway generates 3.4 mM of ferrocenium (A = 1.122), while the four-electron pathway produces 6.8 mM ferrocenium (A = 2.224).

Background reactions

In addition to the ORR, a number of background reactions can affect the observed absorbance at 620 nm. These include the spontaneous (non-catalysed) oxygen reduction by $[Fe(C_5H_5)_2]$ in acidic medium and the absorption due to the catalytic intermediates. For example, at 620 nm, $[Co_2(O_2)(L)]^+$ has a molar extinction of $\ln \varepsilon = 8.26$ (measured under an O_2 atmosphere) and $[Co_2(O_2H)(L)]$ of $\ln \varepsilon = 8.24$ (measured under 20:80 O_2:N_2 atmosphere in the presence of TFA). In an attempt to correct the absorption, background experiments were carried out; the first in the absence of catalyst (**Figure 3.21**, blue dotted line) to account for the spontaneous ORR and the second in the absence of an electron donor (**Figure 3.21**, blue dashed line) to mimic the formation of $[Co_2(O_2H)(L)]$ and to approximate the contribution from the catalytic intermediates (a precise correction would require the knowledge of the absorbances and actual concentrations of all the catalytic intermediates). The two phenomena contributed an absorbance of up to 0.37 and the profiles obtained for the catalytic runs were corrected accordingly.

Results

Initially, the catalyst was studied under the conditions used typically for catalysts previously synthesised within the Love group (**Figure 3.21**, green line) and the formation of four equivalents of ferrocenium were observed, indicative of the full

four-electron four-proton reduction of oxygen and therefore the production of water only. To corroborate the total selectivity for the four-electron reduction, the presence of hydrogen peroxide assessed by iodometric titrationand no I_3^- was detected by UV-vis spectrophotometry.

As stated before, the catalytic experiments with $[Co_2(L)]$ were repeated using lower concentrations of acid and either high loading of catalyst (**Figure 3.21**, blue line) or low loading of catalyst (**Figure 3.21**, red line) to compare the new catalyst with wedge-shaped catalyst synthesised within the group in the past and also with cofacial diporphyrins. In the first case, the reaction reaches completion with three minutes and in the second case it reaches 94% completion (100% completion was reached within six minutes, the full profile is shown on **Figure 3.22**, red line).

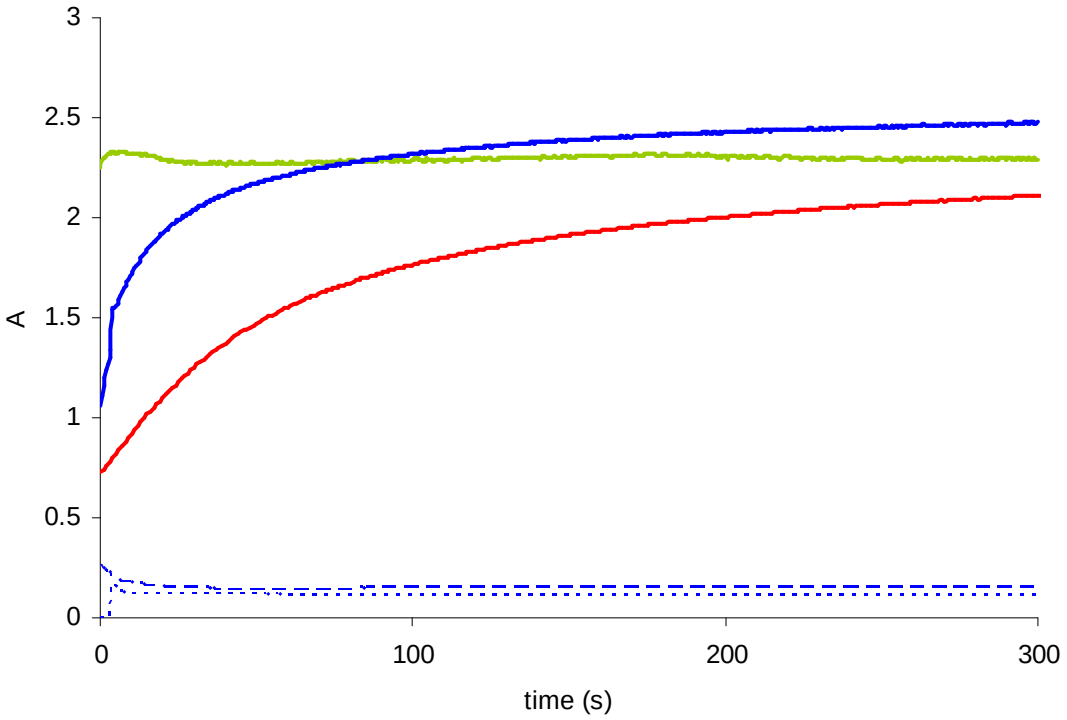

Figure 3.21: Profile of formation of $[Fe(C_5H_5)_2]^+$ monitored at 620 nm in the electron transfer oxidation of $[Fe(C_5H_5)_2]$ by O_2 catalysed by $[Co_2(L)]$ in the presence of TFA in benzonitrile at 298K.
Blue plain line: $[Co_2(L)]$ = 0.2 mM, $[Fe(C_5H_5)_2]$ = 0.1 M, [TFA] = 0.02 M and $[O_2]$ = 1.7 mM.
Blue dotted line: background, [Co2(L)] = 0 mM, $[Fe(C_5H_5)_2]$ = 0.1 M, [TFA] = 0.02 M and $[O_2]$ = 1.7 mM.
Blue dashed line: no ferrocene, $[Co_2(L)]$ = 0.2 mM, $[Fe(C_5H_5)_2]$ = 0 M, [TFA] = 0.02 M and $[O_2]$ = 1.7 mM.
Green plain line: $[Co_2(L)]$ = 0.2 mM, $[Fe(C_5H_5)_2]$ = 0.1 M, [TFA] = 0.1 M and $[O_2]$ = 1.7 mM.
Red plain line: $[Co_2(L)]$ = 0.02 mM, $[Fe(C_5H_5)_2]$ = 0.1 M, [TFA] = 0.02 M and $[O_2]$ = 1.7 mM.

In order to compare results with the literature, the experiments were carried out with stronger acids in the same concentration (0.02 M). When perchloric acid (pKa ~ 2 in acetonitrile compared to pKa ~ 12 for TFA)[22] was used, the full conversion of oxygen to water was observed with high catalyst loading (0.2 mM) but lower catalyst loading (0.02 mM) afforded only 40% conversion. Higher acid concentration (0.1M) led to a full conversion of oxygen to water even without catalyst and this experiment will therefore not be discussed further.

Under the low catalyst loading conditions, the use of methanesulfonic acid (pKa ~ 8 in acetonitrile)[22] afforded 50% conversion only. This suggest that under these experimental conditions, either the catalyst reacts with the acid to form a catalytically inactive species or the reaction follows a different pathway and hydrogen peroxide is formed instead of water; this latter pathway would be at odds with that seen in cofacial diporphyrins as the rate was shown to be dependant on the rate of an electron transfer.[9] The results obtained with stronger acids are not yet fully understood and further investigation would be required to fully elucidate these reactions.

Kinetic experiments were attempted under pseudo-first-order conditions (i.e. using ferrocene as the limiting reagent with all other reagents in excess) to investigate the mechanism of the [Co_2(L)] catalysed reduction of oxygen. Unfortunately, the reaction was too fast to be monitored using the equipment available to us, with typically, full conversion reached within a few seconds, and would require stopped-flow analysis.

Discussion

As expected, the rate of the reaction is directly dependant on the relative concentration of reaction components. When all other parameters are kept constant:

- a much quicker reaction was observed for experiments carried out in a solution more concentrated in TFA (0.1 M) (green line, **Figure 3.21**),

- a much slower reaction was observed for experiments carried out with only 0.02 mM catalyst (instead of 0.2 mM), but the full conversion was still observed after six minutes of reaction (**Figure 3.21**, red line).

In an attempt to prevent undesired intermediates such as the hydroxyl-bridge complex, the fluorenyl substituted catalyst [$Co_2(L^{10})$] has been investigated within the Love group and showed a 4-fold improvement of the conversion of the reaction over 6 minutes compared to the initial catalyst, [$Co_2(L^1)$], under highly acidic conditions (**Table 3.5**, entries 2 and 3 and **Figure 3.22**). Under much less acidic conditions (0.02M instead of 0.4M of TFA and with concentration of other species similar), [$Co_2(L)$] produced 10 times more ferrocenium than the initial catalyst [$Co_2(L^1)$] in the conversion of oxygen to water; [$Co_2(L)$] is a dramatically more active catalyst under milder conditions, a major breakthrough towards a viable catalyst.

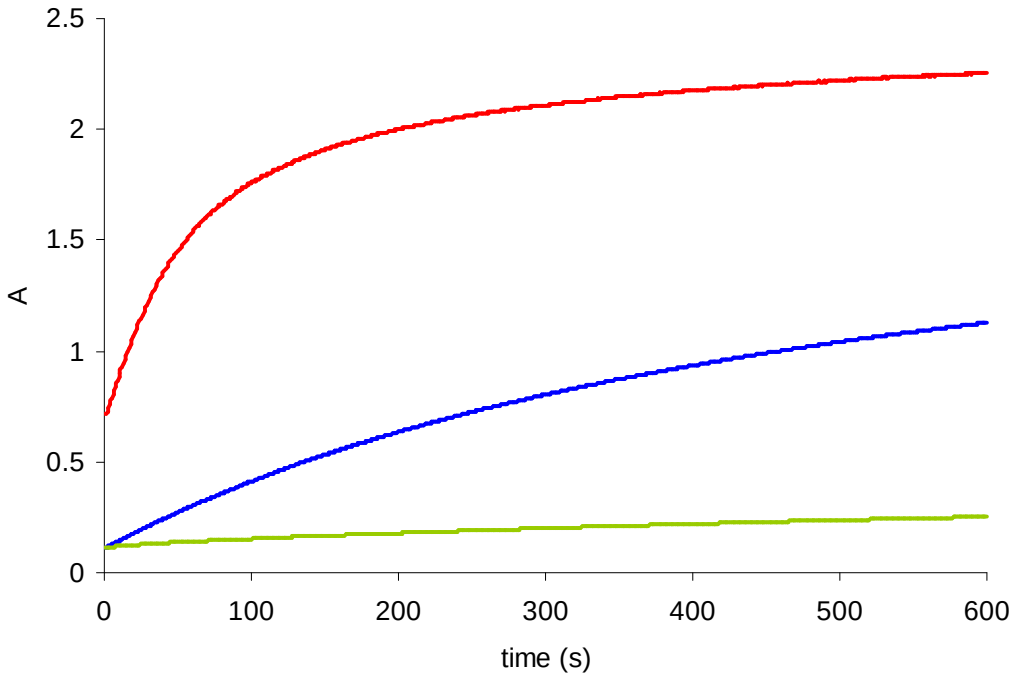

Figure 3.22: Profile of formation of $[Fe(C_5H_5)_2]^+$ monitored at 620 nm in the electron transfer oxidation of $[Fe(C_5H_5)]$ by O_2 catalysed by [$Co_2(L)$] (red line), [$Co_2(L^{10})$] (blue line), [$Co_2(L^1)$] (green line) in the presence of TFA in benzonitrile at 298K.
Red plain line: [$Co_2(L)$] = 0.02 mM, $[Fe(C_5H_5)_2]$ = 0.1 M, [TFA] = 0.02 M and $[O_2]$ = 1.7 mM
Blue plain line: [$Co_2(L^{10})$] = 0.024 mM, $[Fe(C_5H_5)_2]$ = 0.1 M, [TFA] = 0.4 M and $[O_2]$ = 1.7 mM.
Green plain line: [$Co_2(L^1)$] = 0.024 mM, $[Fe(C_5H_5)_2]$ = 0.1 M, [TFA] = 0.4 M and $[O_2]$ = 1.7 mM.

The related cobalt diporphyrins were initially studied by Fukuzumi and Guilard with $HClO_4$ (**Table 3.5,** entry 5), and [Co_2(DPX)] was the only catalyst to convert oxygen to water quantitatively and selectively.[14] As such this complex was taken as a comparison point for [Co_2(L)]. Following up on this work, Nocera studied the behaviour of [Co_2(DPX)] toward weaker acids including TFA (**Table 3.5,** entry 4),[6, 22] which highlighted the importance of the basicity of the superoxo unit to the mechanism and water production. Significantly, full conversion of oxygen to water occurs using [Co_2(L)] as a catalyst in the presence of TFA whereas the use of [Co_2(DPX)] as a catalyst under similar conditions leads to 20% conversion only. This suggests that in [$Co_2(O_2)$(L)]$^+$ the superoxo unit is more basic than in [$Co_2(O_2)$(DPX)]$^+$, a characteristic that is widely acknowledged to determine the selectivity towards the four-electron pathway. Achieving full conversion with a weaker acid also represents a big improvement on the cofacial diporphyrin catalysts.

Compound	[cat] (mM)	[O_2] (mM)	[H^+] (mM)	[$Fe(C_5H_5)_2$] (mM)	conversion [b]	entry
[Co_2(L)]	0.02	1.7	20	100	100%	**1**
[$Co_2(L^{10})$]	0.024	1.7	400	100	36%	**2**[3]
[$Co_2(L^1)$]	0.02	1.7	400	100	9%	**3**[3]
[Co_2(DPX)]	0.022	1.7	20	80	~ 20%	**4**[22]
[Co_2(DPX)]	0.026	1.7	20[c]	100	100%	**5**[14]

Table 3.5: Catalytic performances of [Co_2(L)] and related compounds under selected reaction conditions. Limiting reagent: O_2, reaction time: 600s, under air. [a] limited by [O_2], [b] at 300 seconds,[c] $HClO_4$

In the catalytic experiment carried out with $HClO_4$ and $MeSO_3H$, the quantity of ferrocenium produced decreases with the strength of the acid but the full conversion was observed when the acid concentration was increased. This phenomenon may be due to a catalyst decomposition process in acidic medium.

3.5 Conclusion: proposed catalytic cycle

The results of the present study, combined with evidence gained from the cobalt diporphyrins and other Pacman complexes studied in the Love group, allow a catalytic cycle to be proposed (Error! Reference source not found.).

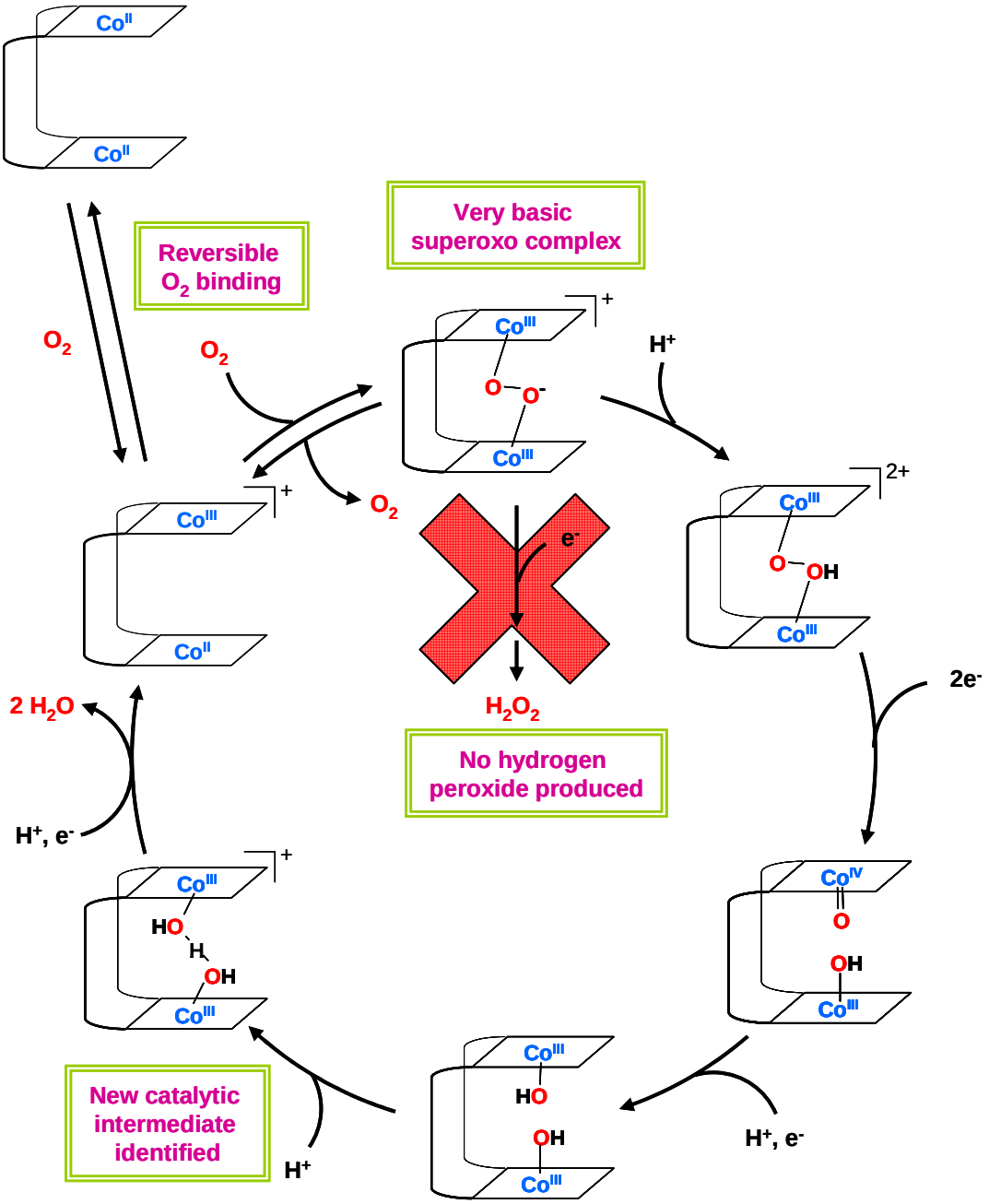

Figure 3.23: Proposed catalytic cycle for the selective reduction of oxygen to water by [Co_2(L)].

The entrance to the catalytic cycle occurs via spontaneous and reversible binding of oxygen to form a superoxo complex, as evidenced by the oxygen based radical observed in EPR spectroscopy. The reversible formation of this speices was probed by NMR, EPR and UV-visible spectroscopy as well as electrochemistry; and after 4 or 5 cycles, the reversibility was still total and no degradation of the complex was observed. The second step of the process consists in the protonation of the superoxo radical and the basicity of this unit is known have a dramatic impact on the selectivity for the four-electron reduction *versus* the two electron reduction.[9] Evidence for the high basicity of the oxo-speices formed upon oxidation of [Co_2(L)] includes (1) EPR spectroscopy showing an oxygen located electron, with no coupling to the cobalt atoms and (2) the reactivity toward fairly weak acid such as TFA (pKa = 12 in acetonitrile)[22]: for the reduction of oxygen to be catalysed by [Co_2(DPX)], a stronger acid (such as perchloric acid, pKa = 2 in acetonitrile, or methanesulfonic acid, pKa = 8 in acetonitrile)[22] is required to protonate the superoxo anion, while the [Co_2(L)] catalysed reaction reaches completion when TFA is used as a proton source.

Rapid proton transfer to the superoxo should result in high selectivity for the water formation process as demonstrated electrochemically by the RRDE experiment and in solution by UV-visible spectroscopy. If the electron transfer was quicker than the proton transfer, the peroxo complex would be formed and hydrogen peroxide would be produced.[9] After the initial protonation, a putative double electron transfer drives the O_2 bond cleavage and is believed to generate a very reactive Co(IV)-oxo complex. Another proton and electron are transferred and a binuclear cobalt(III) dihydroxo complex is formed. In our case, X-ray diffraction allowed the characterisation of a fairly stable hydroxo-hydrate anion which suggests the occurrence of a stepwise protonation at this stage of the catalysis. After a final PCET event, water is eliminated and the Co(II)/Co(III) cation regenerated can bind to oxygen and regenerate the initial superoxo complex. While the initial oxygen binding and first protonation are supported by experimental evidence, the following catalytic steps are analogous to suggestions made in studies of binuclear cobalt cofacial diporphyrins.[9, 14] The hydroxo-hydrate complex was characterised by X-Ray crystal

structure and the elimination of water followed by oxygen binding seems the most logical path to close the catalytic cycle.

In conclusion, [Co_2(L)] proved to be a promising catalyst for the reduction of oxygen to water. The high basicity of its superoxo complex can be attributed to the large distance between the metals which generates weaker Co-O bonds, this is believed to promote the retention of the electrondensity on the superoxo unit and to render it more basic. This favours protonation rather than electron transfer and makes the catalyst fully selective towards water production both in solution and electrocatalytically. The new hydroxo-hydrate intermediate isolated suggests a stepwise process with protons being transferred one at a time; the stable hydroxo-hydrate would be the resting state of the catalyst.

The catalyst studied can be synthesised by a short synthetic route and from readily available starting materials which contrasts with the synthesis of related cofacial diporphyrins. Cobalt is a cheap, non-noble metal and the catalyst showed not only a complete selectivity towards the full reduction of oxygen to water but also a largely enhanced catalytic activity in a fairly weakly acidic medium compared to the best related complexes of cofacial diporphirins. Even though the manufacture of an electrode containing [Co_2(L)] - in order to test the compound in a real hydrogen fuel cell - has not been realised to date, the present results are very promising and may prove to be a big step forward in the use of non-noble metals for the full reduction of oxygen.[22]

3.6 Bibliography

1 E. M. Schubert, *J. Chem. Educ.*, 1992, **69**, 62; T. H. Crawford and J. Swanson, *J. Chem. Educ.*, 1971, **48**, 382.

2 G. Givaja, M. Volpe, Michael A. Edwards, Alexander J. Blake, C. Wilson, M. Schröder, and Jason B. Love, *Angew. Chem. Int. Ed.*, 2007, **46**, 584.

3 E. Askarizadeh, S. B. Yaghoob, D. M. Boghaei, A. M. Z. Slawin, and J. B. Love, *Chem. Commun.*, 2010, **46**, 710.

4 M. Volpe, H. Hartnett, J. W. Leeland, K. Wills, M. Ogunshun, B. J. Duncombe, C. Wilson, A. J. Blake, J. McMaster, and J. B. Love, *Inorg. Chem.*, 2009, **48**, 5195.
5 F. Bolze, M. Drouin, P. D. Harvey, C. P. Gros, E. Espinosa, and R. Guilard, *J. Porphyrins Phthalocyanines*, 2003, **7**, 474.
6 J. Rosenthal and D. G. Nocera, *Acc. Chem. Res.* , 2007, **40**, 543.
7 F. Allen, *Acta Crystallogr., Sect. B*, 2002, **58**, 380.
8 C. J. Chang, Y. Deng, D. G. Nocera, C. Shi, F. C. Anson, and C. K. Chang, *Chem. Commun.*, 2000, 1355.
9 C. J. Chang, Z.-H. Loh, C. Shi, F. C. Anson, and D. G. Nocera, *J. Am. Chem. Soc.*, 2004, **126**, 10013.
10 Y. Le Mest, M. L'Her, and J. Y. Saillard, *Inorg. Chim. Acta*, 1996, **248**, 181.
11 E. Askarizadeh, A. M. J. Devoille, D. M. Boghaei, A. M. Z. Slawin, and J. B. Love, *Inorg. Chem.*, 2009, **48**, 7491.
12 J. P. Collman, J. E. Hutchison, M. A. Lopez, A. Tabard, R. Guilard, W. K. Seok, J. A. Ibers, and M. L'Her, *J. Am. Chem. Soc.*, 1992, **114**, 9869.
13 A. Bino and D. Gibson, *J. Am. Chem. Soc.*, 1981, **103**, 6741; M. Ardon and A. Bino, *Inorg. Chem.*, 1985, **24**, 1343; M. Ghiladi, J. T. Gomez, A. Hazell, P. Kofod, J. Lumtscher, and C. J. McKenzie, *Dalton Trans.*, 2003, 1320; M. Ardon and A. Bino, in 'A new aspect of hydrolysis of metal ions: The hydrogen-oxide bridging ligand', 1987; M. Ardon, A. Bino, and W. G. Jackson, *Polyhedron*, 1987, **6**, 181.
14 S. Fukuzumi, K. Okamoto, C. P. Gros, and R. Guilard, *J. Am. Chem. Soc.*, 2004, **126**, 10441.
15 F. Meyer and P. Rutsch, *Chem. Commun.*, 1998, 1037.
16 G. Brewer, R. J. Butcher, C. Viragh, and G. White, *Dalton Trans.*, 2007, 4132.
17 L. Alvarado, C. Brewer, G. Brewer, R. J. Butcher, A. Straka, and C. Viragh, *CrystEngComm*, 2009, **11**, 2297.
18 C. L. D. Gibb, E. D. Stevens, and B. C. Gibb, *J. Am. Chem. Soc.*, 2001, **123**, 5849.
19 S. S. Zhu, H. Staats, K. Brandhorst, J. Grunenberg, F. Gruppi, E. Dalcanale, A. Lützen, K. Rissanen, and C. A. Schalley, *Angew. Chem., Int. Ed. Engl.*, 2008, **47**, 788; V. S. Bryantsev and B. P. Hay, *J. Am. Chem. Soc.*, 2005, **127**, 8282; C.-H. Lee, H.-K. Na, D.-W. Yoon, D.-H. Won, W.-S. Cho, V. M. Lynch, S. V. Shevchuk, and J. L. Sessler, *J. Am. Chem. Soc.*, 2003, **125**, 7301; K. J. Wallace, W. J. Belcher, D. R. Turner, K. F. Syed, and J. W. Steed, *J. Am. Chem. Soc.*, 2003, **125**, 9699; S. O. Kang, D. VanderVelde, D. Powell, and K. Bowman-James, *J. Am. Chem. Soc.*, 2004, **126**, 12272.
20 D. Rohde, C.-J. Yan, and L.-J. Wan, *Langmuir*, 2006, **22**, 4750.
21 J. P. Collman, P. Denisevich, Y. Konai, M. Marrocco, C. Koval, and F. C. Anson, *J. Am. Chem. Soc.*, 1980, **102**, 6027.
22 J. Rosenthal, *Proton-Coupled Electron Transfert: From Basic Principles to Small Molecule Activation (Thesis)*, 2007.

Chapter 4 – Binuclear zinc complexes and anion recognition.

The major part of the content of this Chapter was published in the article:

Selective Anion Binding by a Cofacial Binuclear Zinc Complex of a Schiff-Base Pyrrole Macrocycle

A. M. J. Devoille, P. Richardson, N. Bill, J. L. Sessler, and J B. Love*, *Inorg. Chem.*, 2011, **50**, 3116.

The recognition and binding of anions such as halides, phosphates, and sulfate are key features of many biological processes, including those associated with information transmission, whereas a breakdown in the normal regulation of anion transport is implicated in several disease states, including cystic fibrosis.[1] A critical role for anion recognition is either recognized or proposed in a number of industrial processes, such as nuclear waste extraction and remediation,[2] as well as base and precious metal extraction.[3] Special attention has been given to metal-containing anion receptors as the metal centre can play a crucial structural role in organizing anion-binding groups into a geometry appropriate for the recognition of a specific anion.[4-6] Furthermore, electrostatic interactions between the targeted anion and a Lewis acidic metal centre can promote a binding event.[7, 8] For example, in cascade complexes, first discovered by Lehn et al.,[9] a binucleating capsular ligand was used to accommodate two metallic centres within the cavity, typically in a pseudo-pyramidal geometry with a vacant site. These complexes, in which the two metallic centres are held at a well-defined distance from one another, can then recognize an anion of the appropriate size as the result of bridging coordination interactions involving the two metal centres. This principle has been further explored

by several groups; in particular, the Lu group found that dicobalt cryptates could be used to recognize selectively bromide and chloride over fluoride and iodide.[10] Separately, the Fabrizzi group showed that halides, cyanides, azide, and hydroxide were encapsulated by a binuclear copper bis(tren) complex,[6] while McKee and Nelson discovered that azide and cyanide could be accommodated within a binuclear copper cryptate.[11] Other binuclear complexes in which the two metals adopt pyramidal geometries have been synthesised and have been shown to be capable of accommodating anions such as phosphates and their derivatives in bridging modes while in certain cases also acting as sensors.[8, 12] Halide-bridged binuclear complexes of transition metals have been synthesised and isolated in the solid state but the anion recognition properties of the halide-free complex was not necessarily investigated. For example, compartemental pyrazolate ligands have been intensively studied and numerous structures of their polymetallic complexes feature metal brigded anions.[13] Homobinuclear nickel, copper and zinc complexes of a tetraazamacrocyclic ligand were also found to adopt a cofacial arrangement to accommodate a halide or a bicarbonate between the two metal centres.[14, 15] Similar behaviour was observed with related complexes based on a tetraazacyclotetradecane chore.[15, 16] Tirtrations were carried out to investigate the binding of bicarbonate and carbonate and the detection of carbon dioxide[15, 16] but the complexes were not considered as halide receptors; the influence of the halide bridge on the communication between the two metal centres were investigated instead; the electrochemistry and magnetic properties of the halide bridged binuclear copper or nickel complexes were considered.[14] While the detection of chloride using Lewis acidic late transition metal hosts remains relatively rare,[17] zinc porphyrins, species that are well-known to bind strong donor ligands,[18] have been shown to bind anions through electrostatic interactions.[5, 19]

Cofacial or Pacman diporphyrins combine the known coordinative properties of porphyrins with precise organisation of the two metal binding sites through the use of a rigid, covalent link, so as to provide a binuclear microenvironment that is particularly well suited for small molecule redox chemistry.[20] The unique binuclear environment provided by these and other molecules created through the assembly of two metalloporphyrins, has been exploited in some aspects of host-guest chemistry.

For example, using dimeric porphyrins, the recognition of molecules, such as DABCO,[21, 22] and other bifunctional nitrogen donors, such as bipyridines, azides, anilines and diamines, has been successfully achieved.[22, 23] Systems containing two zinc porphyrins have been designed to bind and signal the absolute configuration of diamines, aminoalcohols, and diols by exciton-coupled circular dichroism.[24] Also, increasing interest has been shown in the use of metallodiporphyrins to recognize larger molecules such as fullerenes.[25] Looking at the wide range of electron rich substrates that can be accommodated as guests, it is surprising that the anion-recognition ability of these systems remains largely unknown.

The binuclear complexes of L offer well-defined geometric environments with finely tuned distances between the two metallic centres and specific micro-environments within the molecular cleft and are, in this regard similar to cofacial diporphyrin complexes. In contrast with cage systems,[6, 10, 11] the Pacman design retains some flexibility through the modifications of the twist and bite angle, as well as the orientation of the pyrrolic units. This should allow fine tuning of the cavity to the guest. Zinc was thought to be a good candidate for the investigation of a wide range of anion host-guest interactions; it is the least electronegative of the late transition metals[26] which makes it a good potential acceptor and also a medium acid (in terms of HSAB)[27] which makes it a versatile acceptor, able to interact with both hard and soft anions. As a result of these characteristics, the binuclear zinc complex was thought to be a good candidate for anion encapsulation; as such, the synthesis of $[Zn_2(L)]$ and a few of its anionic host:guest "-ate" complexes are presented in this Chapter. The binuclear zinc complex was also found to aggregate and this phenomenon will also be addressed here. Finally, the selective anion recognition promoted by $[Zn_2(L)]$ is investigated using several analytical techniques, including ^{1}H NMR spectroscopy and isothermal microcalorimetry (ITC) and the experimental results appraised in light of DFT calculations.

4.1 Synthesis and characterisation of binuclear zinc complexes

4.1.1 Synthesis of $[Zn_2(L)]$

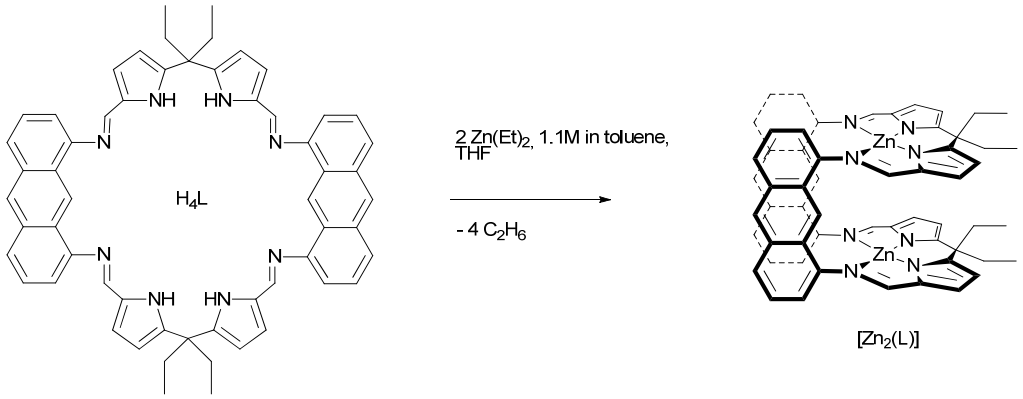

Scheme 4.1: Synthesis of $[Zn_2(L)]$ by transamination reaction.

The reaction between H_4L and $ZnEt_2$ in hot THF followed by the addition of diethyl ether affords the binuclear zinc complex $[Zn_2(L)]$ in good yield as an orange precipitate (**Scheme 4.1**). Even though the ^1H NMR spectrum of $[Zn_2(L)]$ is surprisingly complex and difficult to interpret, no obvious pyrrole N*H* resonances are seen, which is consistent with double-metallation of the macrocycle having occurred. This conclusion is supported further by the IR spectrum, in which the N-H stretch is absent (normally observed at 3250 cm^{-1} in H_4L) and a decrease in the C=N vibration from 1616 cm^{-1} (H_4L) to 1574 cm^{-1} upon metallation is seen. The nano-ESI mass spectrum in acetonitrile exhibits peaks with appropriate isotopic patterns at m/z = 1004 and 1068 for the water and bis-acetonitrile adducts $[Zn_2(L)]\cdot(H_2O)$ and $[Zn_2(L)]\cdot(CH_3CN)_2$ respectively; elemental analysis also supports the expected molecular composition. Unfortunately, and despite numerous attempts, crystals of $[Zn_2(L)]$ suitable for X-ray diffraction could not be grown and so the solid state structure remains undetermined. However, the numerous resonances observed in the ^1H NMR spectrum of $[Zn_2(L)]$ combined with its poor solubility suggests that aggregation is occurring (see section 4.2).

Even though the solid state structure of $[Zn_2(L)]$ could not be determined, an insight on its geometry in was obtained through DFT calculations. The X-ray structure of

[Pd_2(L)] was used as a starting point for the geometry optimisation calculations. The best balance between accuracy and computational cost was obtained at the M05-2X/LANL2DZ level of theory,[28, 29] with bulk THF solvent interactions accounted for *via* the self-consistent reaction field method (SCRF),[30] with the polarised continuum model (PCM), using the default parameters within Gaussian09. The calculations were carried out for [Zn_2(L)] and several anionic inclusion complexes. A good correlation was observed between calculated and experimental data (see section 4.3.5 for more details). The optimised structure of [Zn_2(L)] is presented in **Figure 4.1** with relevant parameters in **Table 4.1.**

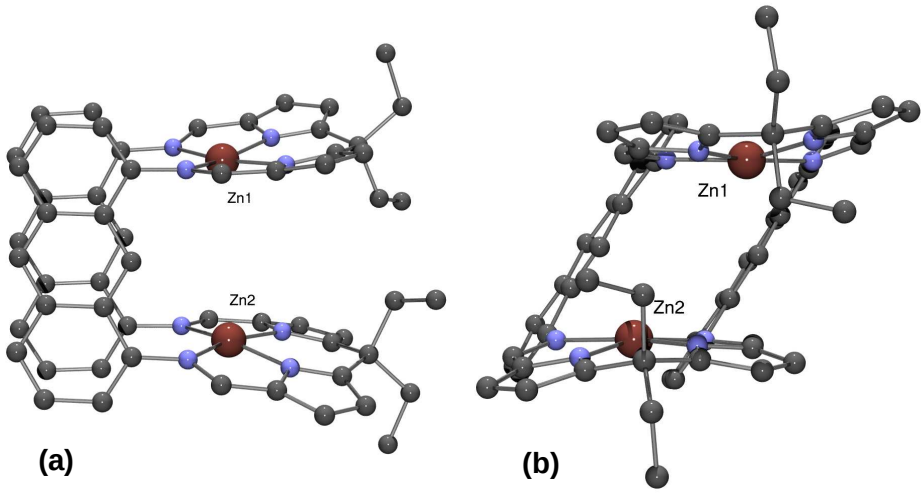

Figure 4.1 : M05-2X/LANL2DZ computed DFT structure of [Zn_2(L)], (a) Side view, (b) face view. Bulk solvent interactions were modelled via the self-consistent reaction field (SCRF) using the polarisable continuum model (PCM), employing the default parameters for THF within Gaussian 09.

The most stable structure presents [Zn_2(L)] as the expected cofacial complex with a zinc cation located in each of the diimino-dipyrrolic N_4-donor pockets. The overall structure is similar to the solid state structure of [Pd_2(L)] with significant distortion: a large 34° twist angle (*vs.* 29° in [Pd_2(L)]) and a surprisingly small 8° interplanar angle (*vs.* 15° in [Pd_2(L)]) makes [Zn_2(L)] the most twisted and also the most cofacial complex supported by L known to date. In terms of intermetallic distance, the two parameters compensate one another and the complex presents a standard 5.0 Å metal separation (*vs.* 5.4 Å in [Pd_2(L)]). The metal centres are in pseudo-square-planar environments, laying only 0.1 Å above the N_4-donor plane, towards the molecular cleft, a value almost identical to that observed in [Pd_2(L)]. The metal to ligand bond distances are predicted to be slightly longer in [Zn_2(L)] than in

[Pd_2(L)] with a 2.11 Å N(imine)-Zn distance (*vs.* 2.08 Å in [Pd_2(L)]) and a 2.01 Å N(pyrrole)-Zn (*vs.* 1.93 Å in [Pd_2(L)]). Considering the structure of [Pd_2(L)] was determined in the solid state and the one of [Zn_2(L)] was optimised as a gas phase structure, the first one is expected to be slightly more distorted and the bond length are expected to be slightly smaller as an effect of the packing forces. The two structures can therefore be considered as very similar. Furthermore, the N(imine)-Zn and N(pyrrole)-Zn distances in [Zn_2(L)] are also comparable to those observed in Zn salen complexes (84 examples: mean 2.050 Å, range 1.836 to 2.197 Å)[31] and in porphyrin complexes (722 examples: mean 2.055 Å, range 1.799 to 2.559 Å).[31]

Compound	M···M [Å]	Twist [°]	Interplanar Angle [°]	M···N_4-plane [Å]
[Zn_2(L)][a]	4.98	34.2	8.4	0.14
[Pd_2(L)]	5.377(1)	29.4	15.3	0.12
[Zn_2(DPX)]	3.709(1)	12.6	4.0	0.10/ 0.08
[Zn_2(*endo*-MeOH)(*endo*-H_2O)(*exo*-MeOH)(DPXM)]	5.9129(9)	11.5	33.6	0.21/ 0.11
[Zn_2(DPD)]	7.775(2)	23.7	30.1	0.11/ 0.11
[Zn_2(DPOx)][b]	6.1180(5)/ 6.1175(5)	27.0/ 27.4	6.8/ 6.8	0.03/ 0.03/ 0.04/ 0.02
[Zn_2(DPPh$_1$)]	3.853(7)	7.5	6.4	0.02/ 0.01
[Zn_2(*endo*-THF)$_2$(DPPh$_2$)]	7.021(1)	15.9	68.8	0.24/ 0.24
[Zn_2(*endo*-MeOH)(*exo*-MeOH)(DPPh$_3$)]	6.540(1)	20.4	56.4	0.45/ 0.05

Table 4.1 : Comparison between the calculated structure of [Zn_2(L)], the X-ray structural data of related binuclear zinc diporphyrin complexes. [a] calculated structure, [b] two molecules in the assymetric unit.

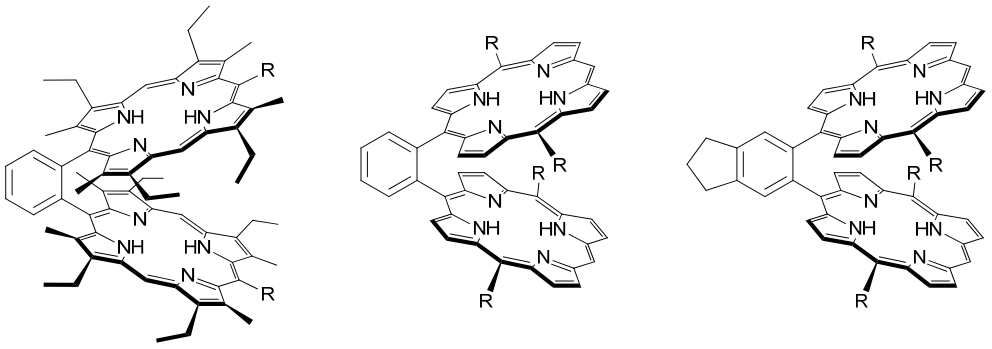

H_4DPPh_1
R = Cy-*p*-CH_3

H_4DPPh_2
R = Cy-*p*-$(C(CH_3)_3)$

H_4DPPh_3
R = $CH_2C(CH_3)_2(OCH_3)$

Chart 4.1: Wedge shape ligands supporting binuclear zinc complexes of diporphyrins.

Considering the unusual twist and bite angle and the non-favourable nature of the square-planar geometry around the zinc atoms, [Zn_2(L)] appears as a fairly unstable molecule. This observation suggests that a stabilising interaction is required in solution, resulting in aggregation when only [Zn_2(L)] is present in solution or the accommodation of an anion when one is available in solution (see sections 4.2 and 4.3).

Several binuclear zinc complexes of diporphyrins have been isolated in the solid state and their main geometric parameters are presented in **Table 4.1**. The ligands cited for the first time are presented in **Chart 4.1**. Each of these examples illustrates the instability of the square planar zinc which is compensated either of the two following interactions: (1) π-stacking interaction occurring between the porphyrinic units or (2) the binding of solvent molecule(s) at the metal centre. In the first case, stabilising face-to-face π-stacking between the porphyrinic rings can be intramolecular (e.g. [Zn_2(DPX)], [Zn_2(DPOx)] and [$Zn_2(DPPh_1)$]) or intermolecular (e.g. [Zn_2(DPD)] and [Zn_2(DPDx)]) and results in very small interplanar angles and intermetallic distances. For [$Zn_2(DPPh_1)$], these interactions even force the complex into a pseudo cofacial geometry (the 1,2-substituted phenyl aromatic backbone would normally promote a bite angle close to 60°). The calculated structure of [Zn_2(L)] exhibits an intermetallic distance and a bite angle slightly larger than those observed in the structure of closest related complex, [Zn_2(DPX)] (by 1.3 Å and 4.4° respectively), which further supports the accuracy of the computing model used and seems to indicate a slightly more constrained structure for [Zn_2(L)] than for its

cofacial diporphyrin analogue. It was reasoned that the stacking interactions observed in [Zn_2(DPX)] were prevented in [Zn_2(L)] by the steric hindrance generated by the *meso*-ethyl groups. In the other diporphyrin structures, when sterically-demanding substituents prevent the π-stacking interaction from occurring, the stabilisation is ensured by the binding of one or two solvent molecules to the electropositive zinc atom(s) within the molecular cleft (ex: [Zn_2(*endo*-MeOH)(*endo*-H_2O)(*exo*-MeOH)(DPXM)], [Zn_2(*endo*-THF)$_2$(DPPh_2) and [Zn_2(*endo*-MeOH)(*exo*-MeOH)(DPPh_3)]). With the ligand studied here, this phenomenon would lead to important distortion, as previously observed in [Mg_2(exo-py)$_2$(endo-py)(L)] (see **Chapter 2**). An exogenous solvent binding was, however, observed by mass spectroscopy in acetonitrile, a strongly binding solvent; but no experimental evidence support this hypothesis in less coordinating solvents such as THF. Instead the complicated nature of the ^{1}H NMR spectrum suggests a stabilisation by aggregation interactions.

4.1.2 Synthesis of [K(THF)$_6$][Zn_2(μ-Cl)(L)]

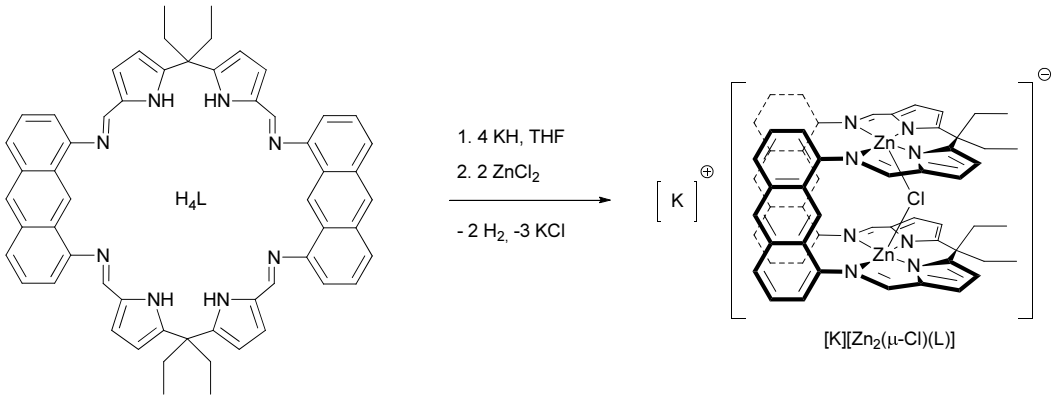

Scheme 4.2: Synthesis of [K][Zn_2(μ-Cl)(L)] by salt elimination reaction.

As an alternative synthetic route to [Zn_2(L)], the reaction between [K_4(L)] and $ZnCl_2$ was carried out in THF. It was found that only partial elimination of potassium chloride occurred and the cofacial "-ate" complex [K][Zn_2(μ-Cl)(L)] was isolated (**Scheme 4.2**). The ^{1}H NMR spectrum of [K][Zn_2(μ-Cl)(L)] displays the twelve expected resonances and the cofacial geometry of this complex was inferred from the non-equivalence of the *endo*- and *exo*-ethyl substituents forming two overlapped

quartets at 2.10 ppm and two triplets at 0.99 and 0.79 ppm. The non-equivalence of the ethyl groups was reinforced by appropriate resonances in the $^{13}C\{^{1}H\}$ NMR spectrum (at 47.31/39.19 and 10.72/9.90 ppm) and assignments were confirmed by 2D NMR experiments. Unfortunately, the bulk isolation of the product proved challenging due to the loss of THF solvent leading to apparent elimination of KCl. However, the slow evaporation of a THF solution of [K][Zn_2(μ-Cl)(L)] afforded a small quantity of crystals suitable for X-ray diffraction. The solid state structure of [K(THF)$_6$] [Zn_2(μ-Cl)(L)]·2THF was determined and is presented in **Figure 4.2**, with crystal data and selected bond lengths and angles detailed in **Appendix 2, Appendix 3** and **Table 4.2**. Selected geometric parameters are presented in **Table 4.3**.

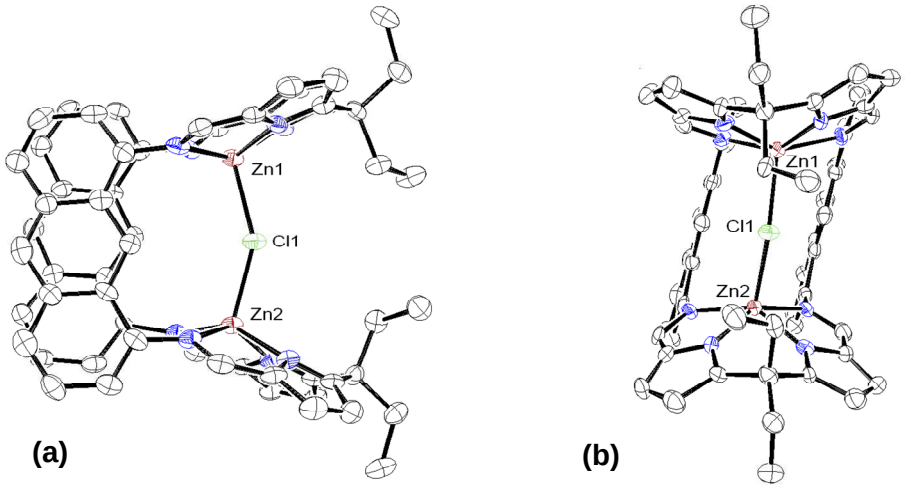

Figure 4.2 : X-ray crystal structure of [K(THF)$_6$][Zn(μ-Cl)(L)]·2THF (displacement ellipsoids are drawn at 50 % probability), (a) Side view, (b) face view. For clarity, the $[K(THF)_6]^+$ cation, THF solvent of crystallisation and all hydrogen atoms are omitted.

As expected from the solution NMR data, the complex adopts a double-pillared cofacial structure in the solid state, with a zinc cation coordinated in each of the two N_4-donor pockets of the ligand. A chloride anion bridges the two metal-centres and an octahedral potassium counter cation, surrounded by six THF molecules, is also present in the asymmetric unit. In a similar manner to that observed in the solid state structure of other binuclear complexes of L, the two anthracenyl backbones exhibit a face-to-face arrangement with the π-surfaces stacked against one another. In this case, the shortest C-C separation is 3.51(1) Å and the co-planarity of the aryl planes is high (3° deviation from the mean planes of the two anthracenes). The

accommodation of the chloride ion within the cleft forces the mouth to open and results in the two N_4-donor planes deviating from co-planarity by 26.6°. The molecule also presents an average twist angle of 13.8°. The two zinc atoms, Zn1 and Zn2, are five coordinate and adopt pseudo-square-base pyramidal geometries with the Zn1 and Zn2 cations displaced away from the basal N_4-plane towards the molecular cleft by 0.58 Å and 0.56 Å respectively. This results in a 4.532(1) Å Zn1···Zn2 separation, *ca*. 0.9 Å shorter than in $[Pd_2(L)]$. The chloride ion is symmetrically bridged between the two metal centres at distances of 2.340(2) Å and 2.346(2) Å from Zn1 and Zn2, respectively, and subtends a Zn1-Cl1-Zn2 angle of 150.54(9)°. The binding of the anion also causes the 2.17 Å mean N(imine)-Zn distance to be quite long compared to those usually observed in zinc salen complexes (84 examples: mean 2.050 Å, range 1.836 to 2.197 Å)[31]; the 2.02 Å mean N(pyrrole)-Zn is comparable to those observed in zinc porphyrin complexes (722 examples: mean 2.055 Å, range 1.799 to 2.559 Å).[31]

The bimetallic complexes of H_4L can be considered as structural, and in some cases, functional double-pillared analogues of cofacial diporphyrins.[32] In this case however, the structure of $[K(THF)_6][Zn_2(\mu\text{-}Cl)(L)]$ represents a unique example. Indeed, in all known binuclear zinc diporphyrin complexes the two square-planar metals are located within the porphyrin plane and to the best of our knowledge, $[K(THF)_6][Zn_2(\mu\text{-}Cl)(L)]$ is the first X-ray solid state structure of a cofacial binuclear zinc complex with an anion bridging the two metals.[33] This is due to the peculiar ability of the complex to allow distorted square-base pyramidal geometries at the metal centres so that a bridging anion is accommodated. This phenomenon is the result of the flexibility of the binding pocket: a twist of the pyrrolic groups at the *meso*-carbons orientates the nitrogen atoms towards the molecular cavity, as previously observed in the X-ray solid state structure of $[Fe_2(\mu\text{-}O)(L)]$ (see **Chapter 2**). This is in contrast with the rigidity of the binding pocket offered by an aromatic porphyrinic unit in which zinc atoms are forced to adopt a square planar geometry. Furthermore, the presence of a bridging chloride anion is quite unusual in polymetallic zinc chemistry and the Zn1-Cl1-Zn2 angle of $[K(THF)_6][Zn_2(\mu\text{-}Cl)(L)]$ is unusually obtuse, being among the largest found in the Chemical Structural

Database (105 examples: mean 96.21°, range 71.53 to 179.97°).[31] These structural data suggest that the interaction between the zinc cations and the chloride anion is relatively weak and likely a direct consequence of the pre-organisation of the binuclear cleft, an inference that is fully consistent with the difficulties encountered in isolating this fragile compound.

	$[K(THF)_6]$ $[Zn_2(\mu\text{-}Cl)(L)]$	$[Li(THF)_4]$ $[Zn_2(\mu\text{-}OH)(L)]$	$[^nBu_4N]$ $[Zn_2(\mu\text{-}OH)(L)]$
N1-C1	1.307 (8)	1.309 (3)	1.293 (7)
N1-C55	1.425 (8)	1.416 (3)	1.415 (8)
C1-C2	1.402 (9)	1.411 (4)	1.416 (8)
C2-C3	1.389 (9)	1.403 (4)	1.398 (8)
N2-C2	1.374 (8)	1.372 (3)	1.376 (7)
N2-C5	1.320 (8)	1.345 (3)	1.351 (7)
C3-C4	1.366 (9)	1.382 (4)	1.383 (9)
C4-C5	1.434 (9)	1.410 (4)	1.413 (8)
Zn1-N1	2.155 (6)	2.176 (2)	2.411 (5)
Zn1-N2	2.023 (5)	2.075 (2)	2.031 (5)
Zn1-N3	2.024 (5)	2.032 (2)	2.105 (5)
Zn1-N4	2.186 (5)	2.261 (2)	2.139 (4)
Zn2-N5	2.156 (5)	2.188 (2)	2.160 (5)
Zn2-N6	2.019 (5)	2.079 (2)	2.057 (5)
Zn2-N7	2.040 (5)	2.036 (2)	2.050 (5)
Zn2-N8	2.197 (5)	2.255 (2)	2.347 (5)
Zn1-X	2.3462 (18)	1.9625 (18)	1.978 (4)
Zn2-X	2.3398 (18)[a]	1.9620 (18)[b]	1.969 (4)[b]
Zn1···Zn2	4.532 (1)	3.9814 (5)	3.871 (1)
C1-N1-C55	117.9 (5)	116.7 (2)	115.3 (5)
N1-Zn1-N2	78.6 (2)	79.13 (8)	76.05 (18)
N2-Zn1-N3	81.9 (2)	80.81 (9)	81.78 (18)
N3-Zn1-N4	78.9 (2)	77.29 (9)	79.34 (19)
N4-Zn1-N1	103.8 (2)	97.47 (8)	95.66 (17)
Zn1-X-Zn2	150.54 (8)[a]	165.11 (12)[b]	157.4 (3)[b]

Table 4.2: Selected bond lengths [Å] and angles [°] for $[K(THF)_6][Zn_2(\mu\text{-}Cl)(L)]$, $[Li(THF)_4][Zn_2(\mu\text{-}OH)(L)]$ and $[^nBu_4N][Zn_2(\mu\text{-}OH)(L)]$, [a]X=Cl, [b]X=OH.

4.1.3 Synthesis of $[Li(THF)_4][Zn_2(\mu\text{-}OH)(L)]$

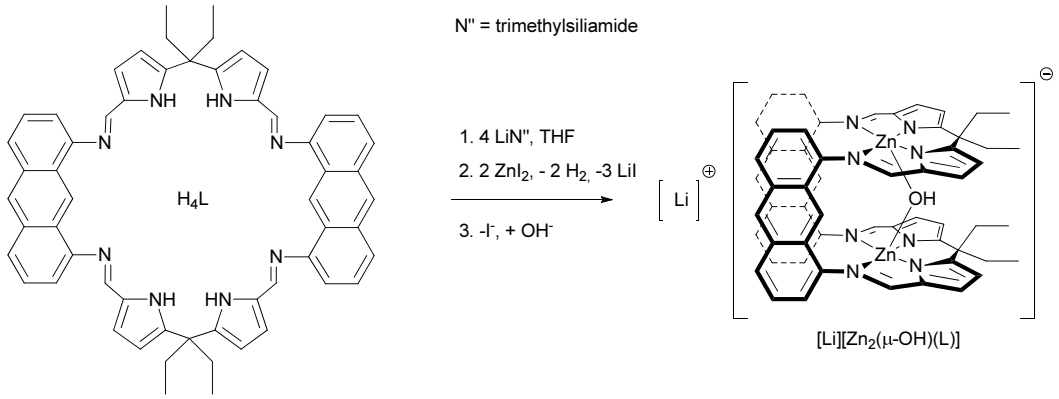

Scheme 4.3: Synthesis of $[Li][Zn_2(\mu\text{-}OH)(L)]$ by salt elimination reaction followed by anion exchange.

In an effort to prevent the incorporation of anion during the synthesis of $[Zn_2(L)]$ by salt elimination, the reaction between $[Li_4(L)]$ and ZnI_2 in THF was carried out (**Scheme 4.3**). It was reasoned that the large and soft iodide anion was less likely to bind strongly within the binuclear zinc cleft. The lithium salt of the ligand, $[Li_4(L)]$, was prepared in situ as previously described (see **Chapter 2**).The reaction between ZnI_2 and $[Li_4(L)]$ was monitored by ^1H NMR spectroscopy and showed at least three different species in solution, consistent with aggregated $[Zn_2(L)]$, *i.e.* no I^- is bound within the cleft. However, the isolation of the product did not yield any of the products initially expected ($[Zn_2(L)]$ or the iodide-bridged complex $[Li][Zn_2(\mu\text{-}I)(L)]$); but crystals of $[Li(THF)_4][Zn_2(\mu\text{-}OH)(L)]\cdot 2THF$ were instead obtained. On exposure of the reaction mixture to air, the uptake of atmospheric water (supported by the appearance of a resonance at 2.74 ppm in the ^1H NMR spectrum recorded in THF/d_6-benzene) results in the resolution of the spectrum that is again consistent with the formation of a single, symmetric and cofacial compound.

Crystals suitable for X-ray diffraction were grown from this reaction mixture and the solid state structure determined (**Figure 4.3**); selected bond lengths and angles are shown in **Table 4.2** and **Appendix 3** and crystal data in **Appendix 2**. Selected geometric parameters are presented in **Table 4.3**. Attempted refinements of the structure with the q-peak located in the molecular cavity assigned as an iodine atom led to much less satisfactory agreement between the density map and the model than

when it was assigned as an oxygen atom. The presence of a q-peak of density consistent with a hydrogen atom by O1 also suggested that a hydroxide anion was actually accommodated within the cleft.

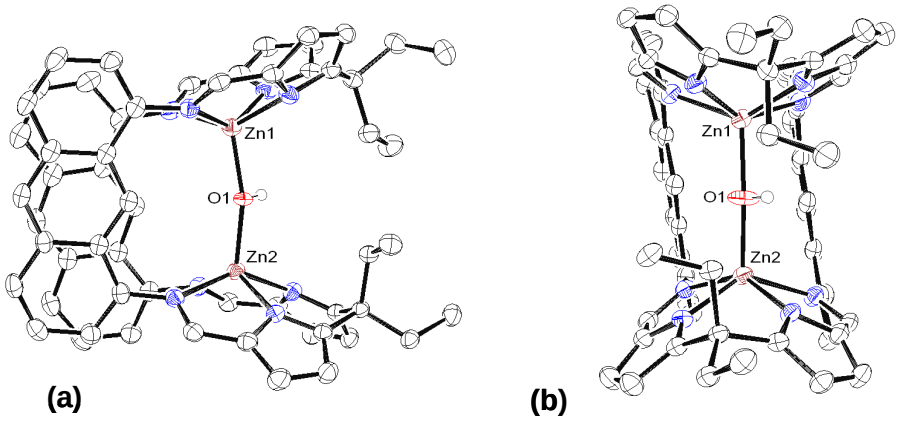

Figure 4.3 : X-ray crystal structure of $[Li(THF)_4][Zn_2(\mu\text{-}OH)(L)]$ (displacement ellipsoids are drawn at 50 % probability), (a) Side view, (b) face view. For clarity, the $[Li(THF)_4]^+$ cation and all hydrogen atoms except on the oxygen atom O1 are omitted.

The solid state structure of $[Li(THF)_4][Zn_2(\mu\text{-}OH)(L)]$ reveals a hydroxyl group bridging the two zinc cations that adopt a geometrical arrangement similar to that seen in $[K(THF)_6][Zn_2(\mu\text{-}Cl)(L)]$. The two N_4-donor planes are found to deviate from co-planarity by 14.6°, and the π-stacking anthracenyl backbones exhibit a shortest carbon atom separation of 3.456(4) Å with a deviation from co-planarity of 7.7°. The two zinc cations Zn1 and Zn2 are separated by 3.891(5) Å, *ca*. 0.5 Å shorter than in the chloride-bridged analogue. The zinc-hydroxide distances are 1.962(2) and 1.962(2) Å for Zn1-O1 and Zn2-O1, respectively. The bridge forms a Zn1-O1-Zn2 angle of 165.1(5)° which, as in the chloride analogue, is unusually obtuse, especially for a hydroxyl group bridged between two zinc cations. It is actually the largest found in literature (137 examples: mean 111.13°, range 82.81 to 147.19°).[31] This feature supports the hypothesis that the cofacial structure is unable to flex sufficiently to optimize further the interaction between the zinc cations and the hydroxide anion. This conclusion is reinforced by the observation that, compared to $[K(THF)_6][Zn_2(\mu\text{-}Cl)(L)]$, the two zinc cations are displaced even further into the cavity (N_4-plane···Zn of 0.71 Å and 0.72 Å for Zn1 and Zn2, respectively) and the twist angle is smaller by 5°. These features may be a consequence of the steric clash

between the *meso*-ethyl substituents and the fact that the two metals have to move within the cavity in order to obtain a small enough Zn···Zn separation and allow anion binding to occur. As observed for $[K(THF)_6][Zn_2(\mu\text{-}Cl)(L)]$, the 2.22 Å N(imine)-Zn bond is larger than usually observed in salen complexes and the 2.06 Å N(pyrrole)-Zn is comparable to a standard N(pyrrole)-Zn bond observed in porphyrin complexes. While all known binuclear zinc cofacial diporphyrins exhibit square planar geometries at the metal, the binuclear lutetium complex $[Lu_2(\mu\text{-}OH)_2(DPA)]$ was shown by X-ray crystallography to have two hydroxyl anions bridging the two metals within the cavity in a manner similar to the "-ate" complex $[Zn_2(\mu\text{-}OH)(L)]^-$.[34] In the former luthetium complex, however, the increased size of Lu^{3+} (ionic radius 85 pm) compared to Zn^{2+} (74 pm), and the inability of the porphyrin to expand its N_4-donor cavity presumably leads to the observed out-of-plane binding of the Lu metal centre and its corresponding propensity to stabilize bridging interactions with the co-bound anions. This structure nicely illustrates the lack of flexibility of the porphyrinic units: their overall flat character prevents the twist motion of the pyrrolic units causing the large metal cation to be displaced far away from the basal plane (by 1.05 and 1.09 Å for Lu1 and Lu2 respectively).

4.1.4 Synthesis of $[^nBu_4N][Zn_2(\mu\text{-}Cl)(L)]$

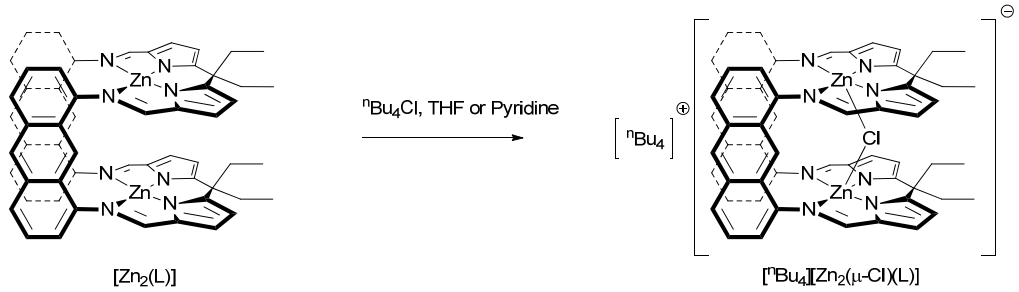

Scheme 4.4: Synthesis $[^nBu_4N][Zn_2(\mu\text{-}Cl)(L)]$ by host:guest interaction.

The reaction between $[Zn_2(L)]$ and one equivalent of $^nBu_4NCl$ in THF or pyridine generated the anion bound complex $[^nBu_4N][Zn_2(\mu\text{-}Cl)(L)]$. The ^1H NMR spectrum recorded *in situ* was consistent with the expected complex; in particular, the observation of two quartets and two triplets at 2.91/2.45 and 1.41/1.12 ppm were consistent with a cofacial, non-aggregated complex. Attempts to isolate this

compound as a solid were unsuccessful, probably because of partial elimination of $^{n}Bu_4NCl$, which suggest that the host:guest interaction is weak. Nevertheless, this simple reaction was used as a reliable purity test for $[Zn_2(L)]$ as the very good resolution of the NMR spectra obtained was in contrast with the complicated spectra obtained for $[Zn_2(L)]$ on its own.

4.1.5 Synthesis of $[^{n}Bu_4N][Zn_2(\mu\text{-}OH)(L)]$

4.1.5.1 From the reaction of $[^{n}Bu_4N][OH]\cdot 30H_2O$ and $[Zn_2(L)]$

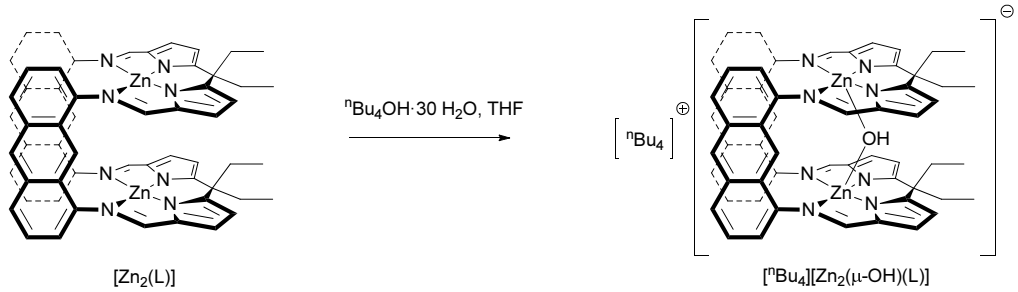

Scheme 4.5: Synthesis $[^{n}Bu_4N][Zn_2(\mu\text{-}OH)(L)]$ by host:guest interaction.

The reaction between $[Zn_2(L)]$ and one equivalent of $^{n}Bu_4NOH$ in THF to generate the anion bound complex $[^{n}Bu_4N][Zn_2(\mu\text{-}OH)(L)]$ (**Scheme 4.5**) proved to be quite challenging due to the hydrated and highly hygroscopic character of hydroxide source which, according to the appearance of resonances for the un-metallated H_4L in the ^{1}H NMR spectrum over time, acts to decompose the $[Zn_2(L)]$ host. Yet, the reaction with a fresh sample of $^{n}Bu_4NOH\cdot 30H_2O$ with $[Zn_2(L)]$ in dry THF and immediately analysed by ^{1}H NMR spectroscopy supports the formation of a product consistent with the initial formation of $[^{n}Bu_4N][Zn_2(\mu\text{-}OH)(L)]$. In particular, the observation of two quartets and two triplets at 2.49/2.25 and 1.26/1.09 ppm was consistent with a cofacial, non-aggregated complex. The rest of the spectrum is also consistent with the proposed product, even though the full assignment including signals integration was difficult, especially in the aliphatic region, due to the double-presaturation nature of the NMR experiment and the presence of some decomposition products.

4.1.5.2 From the reaction of $[^nBu_4N][F]\cdot 3H_2O$ and $[Zn_2(L)]$ in air

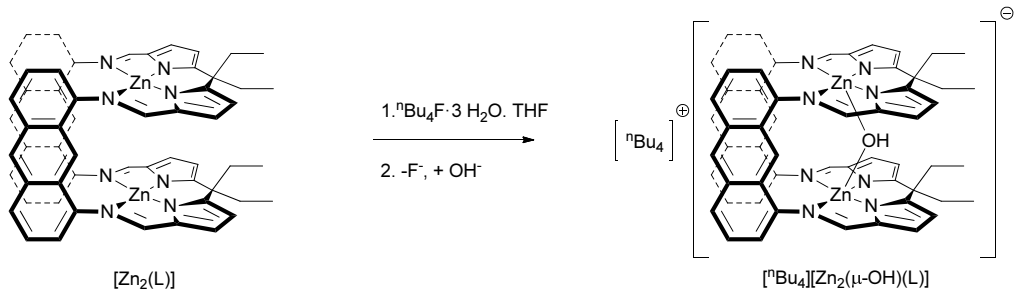

Scheme 4.6: Synthesis of $[^nBu_4N][Zn_2(\mu\text{-}OH)(L)]$ by host:guest interaction followed by anion exchange.

In an attempt to synthesise $[^nBu_4N][Zn_2(\mu\text{-}F)(L)]$, $^nBu_4NF$ was reacted with $[Zn_2(L)]$ in air and crystals were isolated (**Scheme 4.6**), these proved suitable for X-ray diffraction analysis. The solid state structure was determined (**Figure 4.4**) and selected bond lengths and angles are detailed in **Table 4.2** and **Appendix 3**, with crystal data in **Appendix 2**; selected geometric parameters are presented in **Table 4.3**. Refinement of the guest anion as fluoride led to a less satisfactory residual and the compound was assigned to $[^nBu_4N][Zn_2(\mu\text{-}OH)(L)]$. It is important to note that the differentiation between fluorine and hydroxide is very hard by X-ray diffraction due to the iso-electronic nature of the two anions (nine electrons in each case). By mass spectroscopy, the two possible complexes would appear very similar as well as their masses differ by two unit only (M_{OH}= 17 g.mol^{-1} and M_F=19 g.mol^{-1}). Only an element specific technique, such as ^{19}F NMR spectroscopy would unambiguously determine the nature of the guest, however the present assignment to a hydroxide is consistent with the high stability of $[Zn_2(\mu\text{-}OH)(L)]^+$ predicted by DFT calculations (see section 4.3.5).

The solid state structure of $[^nBu_4N][Zn_2(\mu\text{-}OH)(L)]$ reveals a hydroxyl group bridging the two zinc cations that adopt a geometrical arrangement similar to that seen in $[Li(THF)][Zn_2(\mu\text{-}OH)(L)]$. The two N_4-donor planes deviate from co-planarity by 16.8º, and the π-stacking anthracenyl backbones exhibit a shortest C-C separation of 3.322(8) Å with a displacement from co-planarity of 5.5°. The two zinc cations Zn1 and Zn2 are separated by 3.871(1) Å, *ca*. 0.5 Å shorter than in the chloride-bridged analogue. The Zn-bridging hydroxide distances are 1.978(4) and

1.969(4) Å for Zn1-O1 and Zn2-O1, respectively. The bridge forms a Zn1-O1-Zn2 angle of 157.4(3)° which, once again, is unusually obtuse. Interestingly, the angle around the hydroxyl anion is significantly smaller than in [Li(THF)][Zn_2(μ-OH)(L)] (by 8°) and even though the twist and bite angles are slightly larger in the structure of [^{n}Bu_4N][Zn_2(μ-OH)(L)], the Zn1-O1-Zn2 angle is the only parameter to be significantly affected by the counter-cation and packing forces. Once again, the 2.26 Å N(imine)-Zn bonds are larger than usually observed in salen complexes and the 2.06 Å N(pyrrole)-Zn bonds comparable to a standard N(pyrrole)-Zn bonds observed in porphyrin complexes.

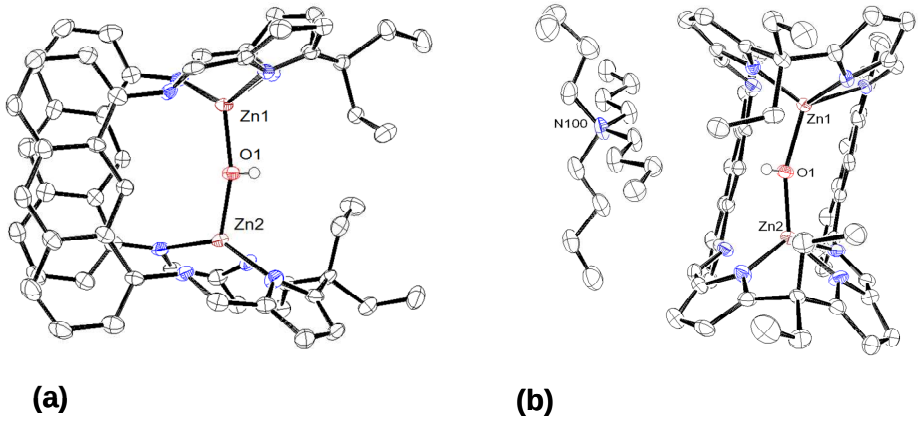

Figure 4.4 : X-ray crystal structure of [^{n}Bu_4N][Zn_2(μ-OH)(L)] (displacement ellipsoids are drawn at 50 % probability), (a) Side view, (b) face view. For clarity, the ^{n}Bu_4N^+ counterion is presented on the face view only and all hydrogen atoms except on the oxygen atom O1 are omitted.

At first glance, the anion bound "-ate" complexes [Zn_2(μ-X)(L)] might seem structurally similar to [Fe_2(μ-O)(L)] in which a single atom also bridges the two metal centres (see **Chapter 2**). However, the binuclear di-iron oxo complex presents a covalently bound central atom while the anion accommodation results from a weak Lewis acid-base interaction in the binuclear zincate complexes. In the solid state, this difference is revealed by the significantly shorter M-X distances observed in the iron complex (2.0 to 2.3 Å in the zinc complexes *vs.* 1.795(2) and 1.799(2) Å in the iron one). The displacement of the metal centre out of the N_4-coordination plane, however, is comparable in all cases (0.6 to 0.8 Å) but the angle around the oxygen in [Fe_2(μ-O)(L)] is particularly obtuse (173°) and the bite angle is smaller than the one

observed for the zincate complexes (15 to 27° in the zinc complexes *vs.* 12° in the iron one); the intermetallic distance is significantly smaller as a result.

Compound	M···M [Å]	Twist [°]	Interplanar Angle[a] [°]	M-X [Å]	M-X-M [°]	M···N_4 [Å]
$[Zn_2(L)]^a$	4.98	34.2	8.4	n/a	n/a	0.14
$[K(THF)_6]$ $[Zn_2(\mu\text{-}Cl)(L)]$	4.532(1)	13.8	26.6	2.340(2)/ 2.346(2)	150.54(9)	0.58/ 0.56
$[Li(THF)_4]$ $[Zn_2(\mu\text{-}OH)(L)]$	3.8914(5)	8.4	14.57	1.962(2)/ 1.962(2)	165.1(5)	0.71/ 0.72
$[^nBu_4N]$ $[Zn_2(\mu\text{-}OH)(L)]$	3.871(1)	9.1	16.8	1.978(4)/ 1.969(4)	157.4(3)	0.75/ 0.75
$[Fe_2(\mu\text{-}O)(L)]$	3.295(2)	8.8	11.69	1.795(2)/ 1.799(2)	173.32(8)	0.700/ 0.769
$[Lu_2(\mu\text{-}OH)_2$ $(DPA)]$[34]	3.5230(9)	2.1	15.53	2.246(8)/ 2.206(8)/ 2.186(8)/ 2.223(8)	105.3/ 105.4	1.05/ 1.09

Table 4.3 : Comparison between the calculated structure of $[Zn_2(L)]$, the X-ray structural data of its anion bridged complexes, of $[Fe_2(\mu\text{-}O)(L)]$, and the related complex $[Lu_2(\mu\text{-}OH)_2(DPA)]$. [a] calculated structure.

As a summary of the experimental data, $[Zn_2(L)]$ is a good candidate for the recognition of small anions. In particular, the ^1H NMR spectroscopic data and the computed data suggest the aggregation of the complex compensate for the quite unstable structure of $[Zn_2(L)]$ and this phenomenon will be investigated in the following section. Furthermore, three anion-bridged complexes were obtained either by partial elimination of the salt in salt elimination reactions or by host:guest interaction resulting from the reaction of $[Zn_2(L)]$ with a tetrabutylammonium salt. As a result, $[Zn_2(L)]$ is a potential receptor for anions and more detailed anion binding properties are described in section 4.3. Initial synthetic data suggest the capacity of the molecular cleft in $[Zn_2(L)]$ to accommodate a chloride anion but the binding of fluoride and iodide were not observed. Instead the binding of hydroxide

(presumably derived from a small quantity of water of crystallisation) was favoured, suggesting a stronger energy of binding for this anion compared to the two halides.

4.2 Solution speciation of $[Zn_2(L)]$

4.2.1 NMR study

4.2.1.1 Analysis by ^{1}H NMR spectroscopy

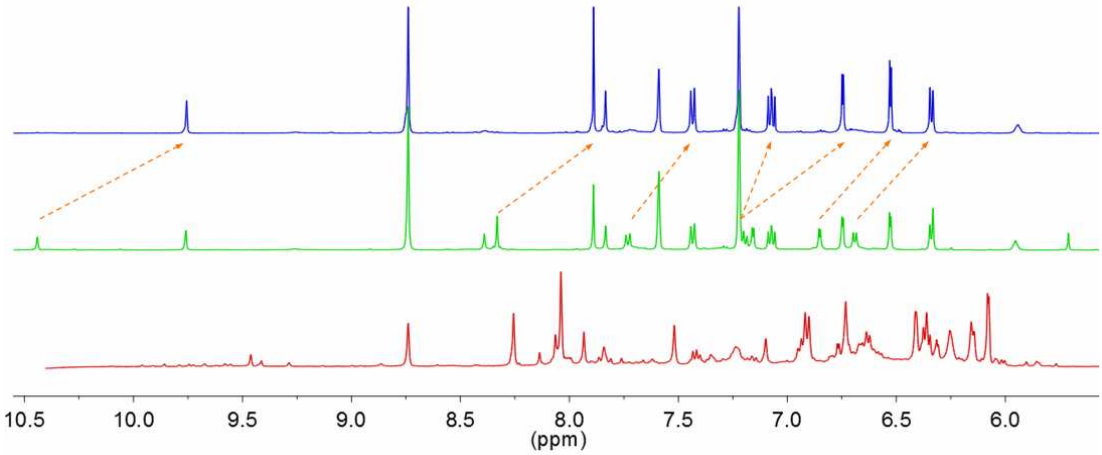

Figure 4.5 : The reaction between $[Zn_2(L)]$ (16 mM) and $^nBu_4NCl$ in d_5-pyridine monitored over time by ^{1}H NMR spectroscopy (only the aromatic region is shown). Bottom, red spectrum: $[Zn_2(L)]$ (16 mM); middle, green spectrum: $[Zn_2(L)]$ (16 mM) and $^nBu_4NCl$ at the end of the titration; top, blue spectrum: $[Zn_2(L)]$ (16 mM) and $^nBu_4NCl$ after 72 hrs equilibration.

The isolation of $[Zn_2(L)]$ that appears pre-disposed towards anion binding, coupled with its poor quality ^{1}H NMR spectroscopic data, encouraged the investigation of aggregation and anion binding phenomena. In the first instance, the ability of $[Zn_2(L)]$ to bind chloride in solution was evaluated by ^{1}H NMR spectroscopy. The addition of an excess of $^nBu_4NCl$ to a d_5-pyridine solution of $[Zn_2(L)]$ caused the ^{1}H NMR spectrum to simplify considerably, leading immediately to signals that are ascribed to a mixture of two compounds (**Figure 4.5**). These signals resolve into a set of resonances consistent with the presence of a single species over the course of 72 h. The presence of a double set of resonances at 2.91/2.45 and 1.41/1.12 ppm for the *meso*-ethyl substituents in the ^{1}H NMR spectrum recorded after equilibration is consistent with the formation of a complex of cofacial geometry, i.e. the ultimate generation of $[^nBu_4N][Zn_2(\mu\text{-}Cl)(L)]$. The second set of resonances seen in the

^{1}H NMR spectrum immediately after the addition of ^{n}Bu$_4$NCl is similarly consistent with a binuclear complex of cofacial structure and is due to the formation of monomeric [Zn$_2$(L)], i.e. the addition of chloride induces de-aggregation (see section 4.2.1.1). The mechanism of this de-aggrgation process was not fully understood but similar results are obtained in THF/d$_6$-bezene.

Numerous examples of the self-assembly of zinc porphyrins, making use of the Lewis acidity of the zinc cation, have been reported and the dissociation of the assembly observed upon solvent addition is compensated by the binding of an extra ligand at the axial position.[18] Considering that the structural properties of cofacial Schiff-base pyrroles are similar to those of cofacial diporphyrins, the propensity of [Zn$_2$(L)] to accept a strong donor ligand is likely and in the absence of a suitable interaction, the underlying coordination deficiency that drives ligand association is compensated by aggregation. Although the interactions leading to the formation of aggregates and their speciation has not yet been determined, the consistent lack of resolution seen in the ^{1}H NMR spectra of [Zn$_2$(L)] and the presence of some signals below 0 ppm are similar to those observed by Balaban and co-workers for the aggregation of zinc porphyrins.[35] In order to understand this aggregation process better, a sequential dilution study of [Zn$_2$(L)] monitored by ^{1}H NMR spectroscopy was carried out in d$_8$-THF (**Figure 4.6**). On successive dilution from 4.8 to 0.1 mM gradual resolution towards a single set of signals is observed. These signals are consistent with de-aggregation to form monomeric [Zn$_2$(L)] at lower concentrations. Better resolved signals are also seen in the ^{1}H NMR spectrum when the dilution experiment is carried out in a strong donor solvent, such as d$_5$-pyridine. Such a finding is consistent with the intuitively reasonable expectation that the monomeric species is stabilised by the pyridine donor ligands.

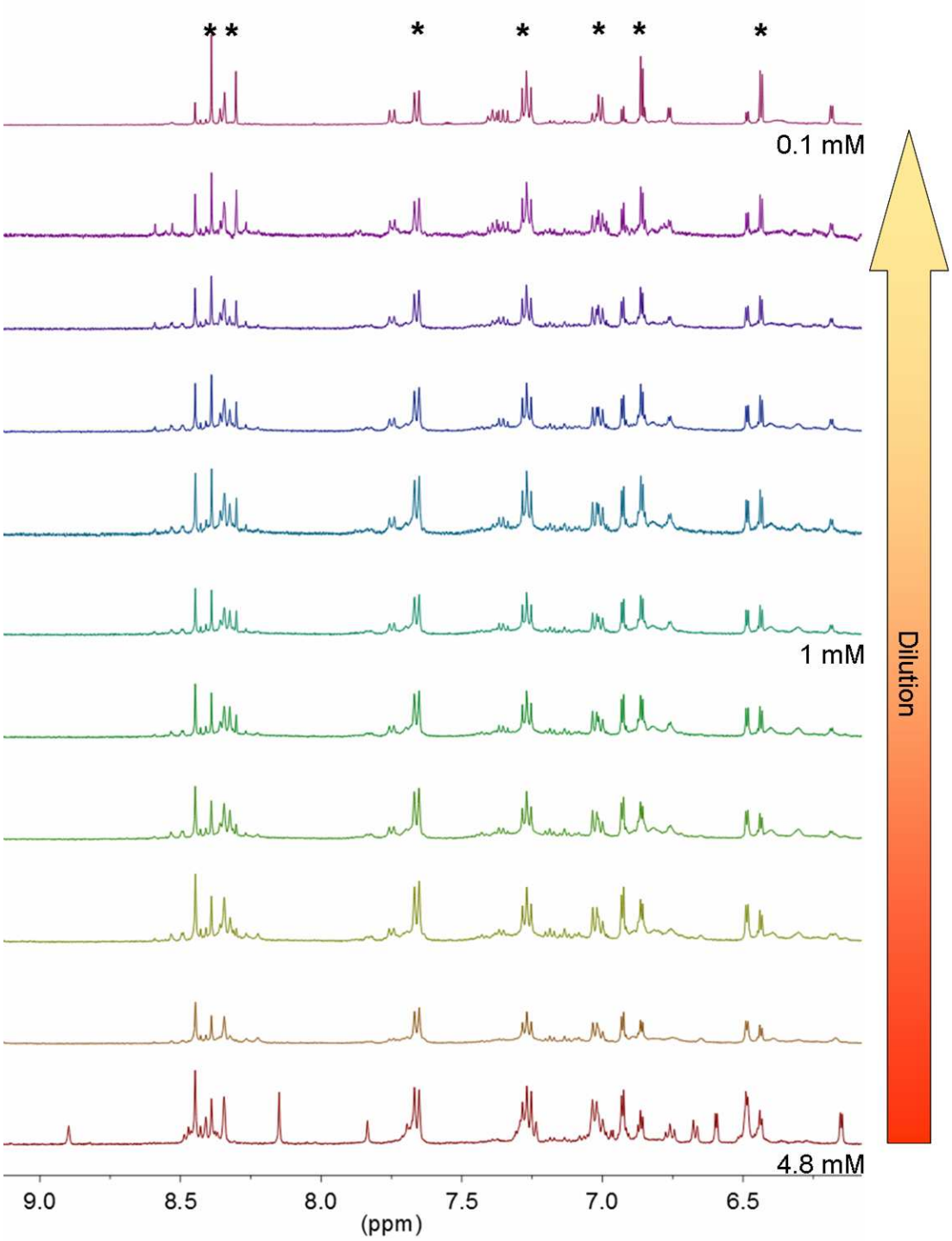

Figure 4.6 : ^{1}H NMR spectra of [Zn_2(L)] in d_8-THF recorded at concentrations ranging from 0.1 mM (top) to 4.8 mM (bottom). The stars indicate the position of the resonances of the monomeric species.

The double-presaturation ^{1}H NMR spectrum recorded straight after the addition of $^{n}Bu_4NCl$ to a THF/d_6-benzene solution of [Zn_2(L)] was compared to the final spectrum of the dilution experiment (recorded in d_8-THF) (**Figure 4.7**). The second set of resonances observed for the chloride containing sample, which disappears with time, was found to be almost identical to set of main resonances observed from the diluted sample and was attributed to de-aggregated [Zn_2(L)]. This confirmed that the addition of $^{n}Bu_4NCl$ and the dilution of the sample cause the same phenomenon: the sample de-aggregates as previously suggested. The minor differences between the two sets of signals were attributed slight difference between the two solvent systems.

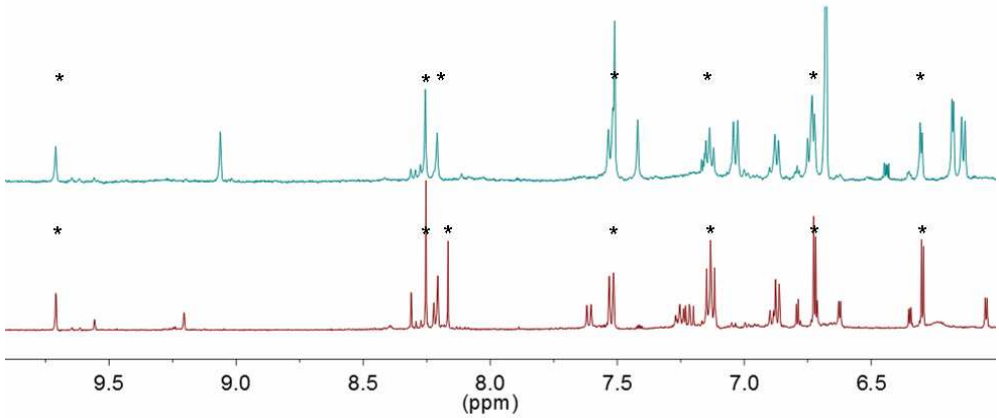

Figure 4.7 : ^{1}H NMR spectra of 0.1 mM [Zn_2(L)] in d_8-THF (top) and a mixture of [Zn_2(L)] (1 mM) and $^{n}Bu_4NCl$ (2.5 mM) in THF/d_6-benzene (bottom). The stars indicate the position of the resonances of the monomeric species.

4.2.1.2 Analysis by diffusion ordered NMR spectroscopy

In an attempt to quantify the speciation of [Zn_2(L)] in solution, diffusion ordered NMR spectroscopy experiment (DOSY) were carried out with the help of Mr J. Bella. This experiment is based on the response of a molecule exposed to a pulsed magnetic field gradient as a function of its diffusion coefficient.[36] A DOSY spectrum is usually presented as a 2D spectrum in which the horizontal axis represents the ^{1}H NMR spectrum of the sample studied and the vertical axis encodes the diffusion coefficient. As a result, resonances for the different chemical species in solution can be separated, allowing an analysis of the content of the solution. Furthermore, as the diffusion coefficient is linked to the size of the molecule, it is also related to its

molecular weight. In particular, the Stokes-Einstein equation **(4.1)** relates the diffusion coefficient (D) to the hydrodynamic radius (R_H) of the species studied. In this equation, R_H correspond to the radius of a sphere that would diffuse the same way as the compound of interest (*i.e.* the approximation is made that the compound has a roughly spherical shape in solution). This approximation seemed appropriate according to the shape of [Zn_2(L)] and complex investigations would be required to reach a more accurate model.[37]

$$D = \frac{kT}{6\pi\eta R_H} \qquad \textbf{(4.1)}$$

Where D is the diffusion coefficient, k the Boltzmann constatnt, η the solvent viscosity and R_H the hydrodynamic radius. With this approximation, the molecular weight M is related to R_H by **(4.2)**:

$$R_H = \sqrt[3]{\frac{3M}{4\pi\rho N_A}} \qquad \textbf{(4.2)}$$

Where R_H is the hydrodynamic radius, M the molecular weight, ρ the density of the species and N_A is Avogadro's number.

The experiment was carried out on a 26 mM solution of [Zn_2(L)] in d_5-pyridine at room temperature. In order to reach a full dissolution, the sample was repeatedly sonicated, heated and was allowed to stand overnight. The diffusion coefficient was measured to be $2.8.10^{-10}$ $m^2.s^{-1}$, which corresponds to a hydrodynamic radius of 8.8 Å. In the solid state structures of binuclear complexes of L, the two furthest atoms were observed to lay 14 to 15 Å apart and the calculated 17.6 Å diameter obtained here appears as a good estimation for a monomeric complex. The de-aggregation can be attributed to the combination of sonication, heating and donor character of pyridine.

In an attempt to observe the aggregated complex, the experiment was carried out in a less coordinated solvent, THF. A lower concentration (5 mM) had to be used to ensure the full solubilisation of the sample. This concentration was actually too low to record the desired signal and only the solvent signal was observed.

4.2.2 Isothermal microcalorimetry study

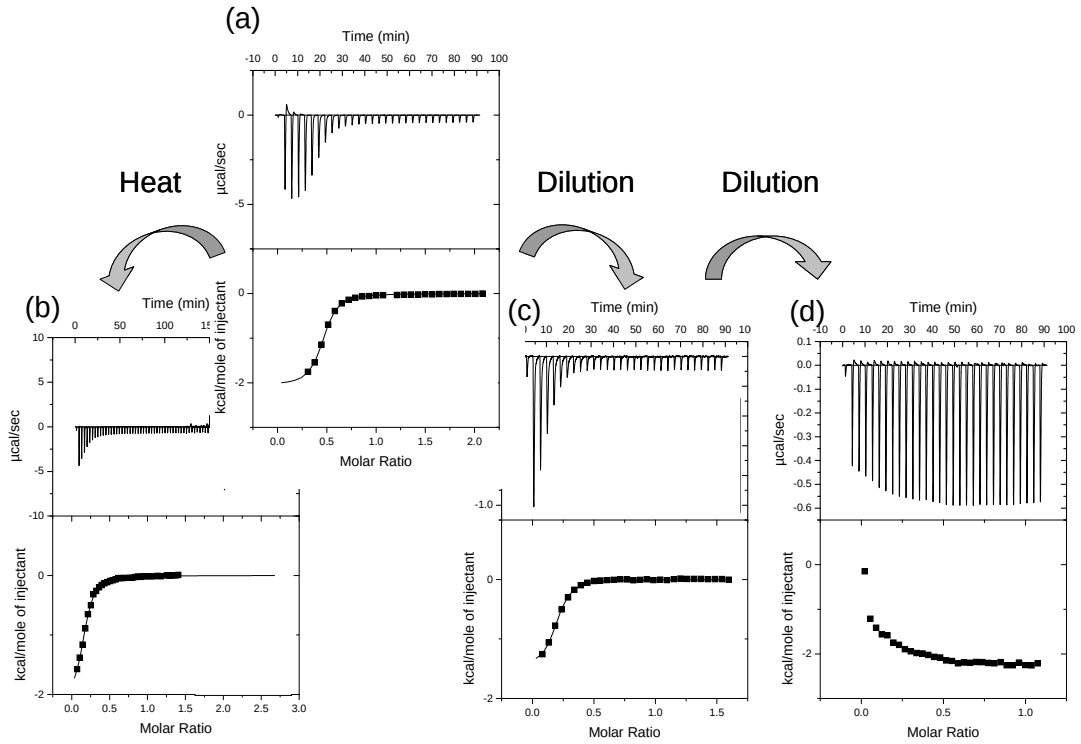

Figure 4.8 : ITC traces for the titration of $[Zn_2(L)]$ with $^{n}Bu_4NCl$ in DMF: (a) 25 ^{o}C, 0.67 mM, n = 0.44; (b) 50 ^{o}C, 1.12 mM, n = 0.17; (c) 25 ^{o}C, 0.34 mM, n = 0.18; (d) 25 ^{o}C, 0.13 mM, n = n/a (the concentration cited correspond to $[Zn_2(L)]$, $[Zn_2(L)]/[^{n}Bu_4NCl\ )] = 20$); n is the guest:host ratio at the equivalence.

The aggregated nature of $[Zn_2(L)]$ was also studied by isothermal micro-calorimetry (ITC). Each experiment comprised the sequential addition of a solution of anionic guest to a mM solution of $[Zn_2(L)]$ which acts a host; the heat generated is measured and allows access to the thermodynamic parameters of the phenomenon. Usually, ITC is used to investigate the binding of anions within a receptor; in this case the guest:host ratio at the equivalence is given by the stoichiometry, n, and the strength of the binding is given by the binding constant, K. The de-aggregation phenomenon was studied using $^{n}Bu_4NCl$ as an anion source as this was shown by ^{1}H NMR spectroscopy to promote de-aggregation; and DMF as a solvent, as $[Zn_2(L)]$ proved to be soluble enough to carry out ITC experiments in this solvent but no evidence of anion binding was observed. In this case, n is indicative of the number of moles of chloride required for the whole $[Zn_2(L)]$ sample to be de-aggregated. ITC experiments were carried out at different temperatures and concentrations, and highlighted that more dilute and/or warmer samples required less anion to reach full

dissociation, a finding that again supports the proposed aggregation/de-aggregation of $[Zn_2(L)]$ (**Figure 4.8**). Furthermore, at lower concentrations, *i.e.* when full dissociation is already achieved before the experiment is carried out a simple dilution pattern was observed (**Figure 4.8**, d).

4.2.3 Attempted UV-visible study

UV-visible dilution and temperature variation experiments were attempted to evaluate further the speciation of $[Zn_2(L)]$ in solution. Several factors prevented these experiments from being successful: (1) at mM concentrations, where the compound is aggregated in solution, saturation of the spectrometer prevented the observation of the spectrum and at μM concentration (which was appropriate for the recording of the spectrum) the sample was already de-aggregated; (2) at low concentrations, the sensitivity of $[Zn_2(L)]$ towards traces of water is intensified and even small traces can lead to a non-negligible $[H_2O]/[Zn_2(L)]$ concentration ratio which can lead to the formation of a bridged hydroxide species and/or decomposition of the binuclear zinc complex.

The Balaban group published a UV-visible method to attest of the aggregated nature of a complex where the intensity and wavelength of the signals are observed in a solvent in which aggregation occurs and in the presence of a coordinating solvent (typically methanol) which causes the de-aggregation.[35] Again, attempts to carry out this type of experiment were unsuccessful due to the very high absorption coefficient of $[Zn_2(L)]$ preventing the observation of the aggregate ($\ln \varepsilon_{max} = 10.58$ in THF).

4.2.4 Attempted fluorescence study

Fluorescence spectroscopy was also considered to elucidate the nature of $[Zn_2(L)]$ in solution. In this case, experiments were carried at concentrations even lower than for the UV-visible experiments, and the observation of the aggregate was prevented once again. However, fluorescence experiments were attempted to study the anion binding phenomenon (see paragraph 4.3.4).

4.3 Anion recognition by $[Zn_2(L)]$

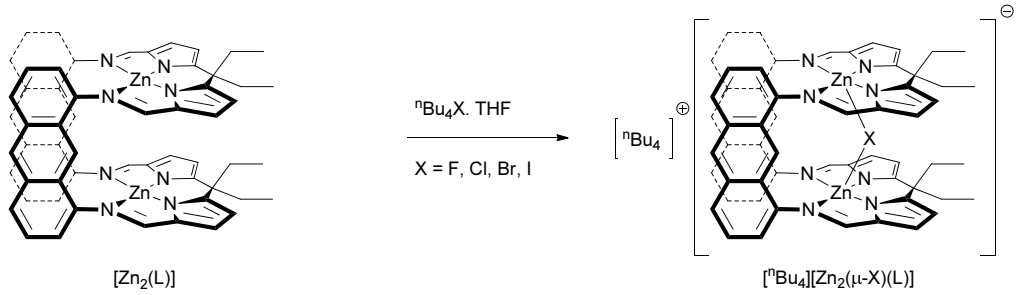

Scheme 4.7 : Anion recognition titration of $[Zn_2(L)]$ by the tetrabutylammonium salts of halides.

Anion binding titrations were carried out by sequential addition of tetrabutylammonium salt solutions of the anion considered to a $[Zn_2(L)]$ solution (**Scheme 4.7**). The effect on the system was followed by different analytic techniques including ^{1}H NMR spectroscopy, ITC, UV-visible and fluorescence spectroscopy.

4.3.1 NMR study

Ideally, a solution of the fully de-aggregated $[Zn_2(L)]$ would be required to carry out the anion binding studies. Unfortunately, a balance had to be found between the ability of a solvent to solvate $[Zn_2(L)]$ and its own binding ability, *i.e.* a strong enough donor solvent is required to dissociate the aggregate but too good a donor binds strongly to the zinc centres of the metal complex, thereby competing with the anion binding event. Furthermore, the highly hygroscopic nature of the host complex required dry conditions to inhibit the formation of the hydroxyl-bridged species.

Likewise, the presence of water could weaken significantly the strength of anion-metal cation interactions. Finally, ^{1}H NMR spectroscopy requires mM concentration of the compounds studied to be recorded in a reasonable time. As a result, ^{1}H NMR spectroscopy anion binding experiments were carried out in 1 mM solutions of $[Zn_2(L)]$ in THF/d_6-bezene or d_5-pyridine and care was taken to exclude moisture.

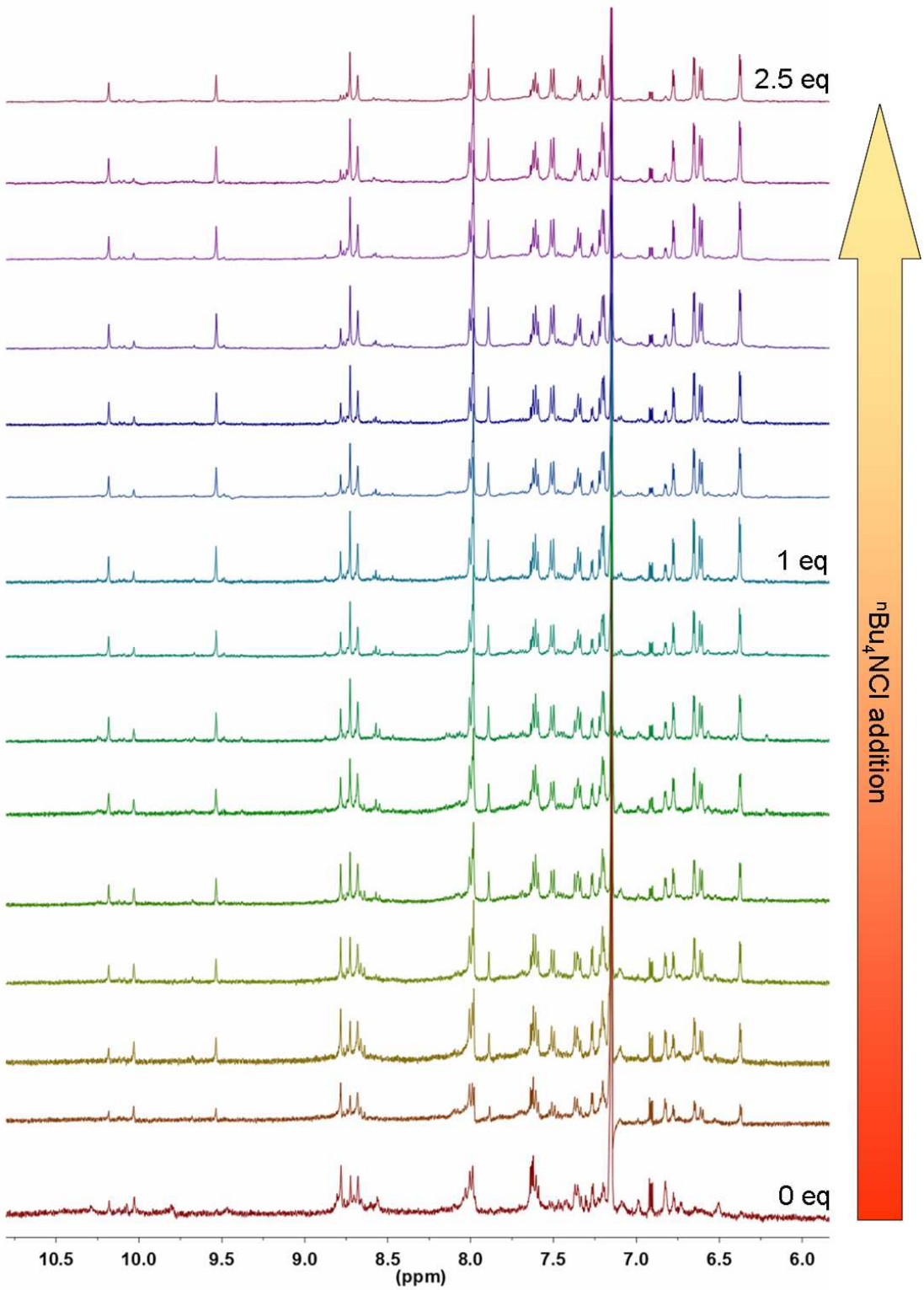

Figure 4.9 : ^{1}H NMR spectroscopic titration of $[Zn_2(L)]$ (1 mM) with $^{n}Bu_4NCl$ (12 mM) in THF/d_6-bezene, showing the region between 11 and 6 ppm only.

On sequential addition of $^{n}Bu_4NCl$, the ^{1}H NMR spectrum of $[Zn_2(L)]$ in THF/d_6-benzene becomes more resolved and the signals for the chloride complex appear while the resonances for the free host vanish. This is just as is expected for a de-aggregation event followed by anion binding (**Figure 4.9**). Unfortunately, the aggregated nature of the host does not allow for accurate integration of the resonances. While this lack of precision prevented a Job plot analysis, a split of, for example, the signal for the 9*H*-anthracene proton from 9.65 ppm into 9.80 ppm and 9.16 ppm is observed, as would be expected given this two step chemical transformation (i.e., de-aggregation followed by anion-cation interaction). The same experiment carried out in d_5-pyridine led to similar observations; two sets of well resolved signals were observed corresponding to the monomeric $[Zn_2(L)]$ from dilution and anion-bound $[Zn_2(\mu\text{-}Cl)(L)]^{-}$. As noted above (paragraph 4.2.1.1), equilibration over 72 hours afforded a single set of signals that are consistent with the formation of $[^{n}Bu_4N][Zn(\mu\text{-}Cl)(L)]$ as the final, stable product. While such a conversion is consistent with all available data, the dynamic nature of the transformation renders quantitative measurements difficult using NMR spectroscopy. Therefore, ITC was considered to be a more useful method to investigate the proposed anion binding events.

4.3.2 Isothermal microcalorimetry study

ITC binding experiments were carried out in DMF and THF and were focused mainly on halides, which were studied in the form of their tetrabutylammonium salts. No reliable data were obtained for fluoride, possibly due to its hygroscopic nature and the potential for formation of a hydroxyl adduct. Therefore, fluoride ion was excluded from the study and the investigations focused on chloride, bromide and iodide. In DMF, the dissociation of the aggregate is observed on chloride addition but no evidence of anion binding was detected (see paragraph 4.2.2), suggesting that DMF competes strongly with the anion at the binding site.

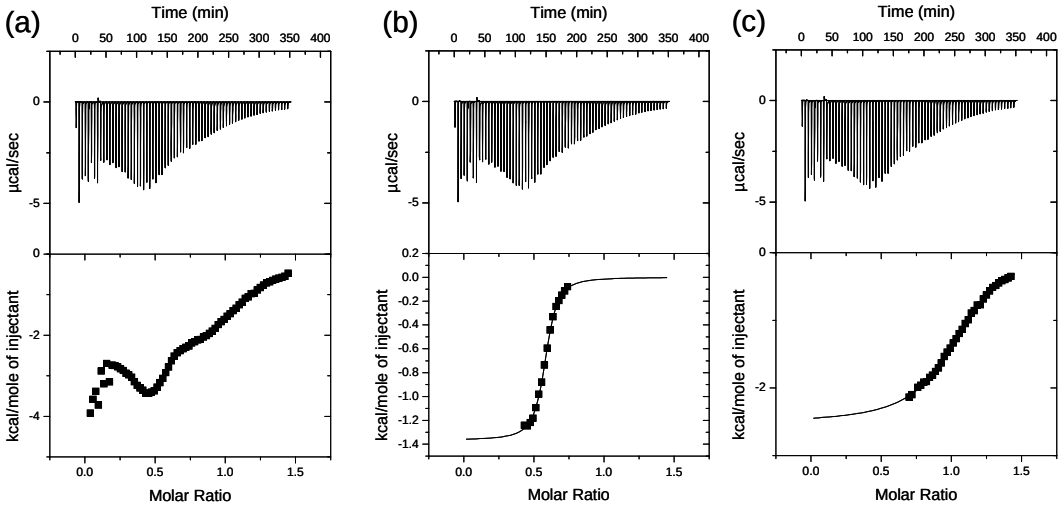

Figure 4.10 : ITC traces of the titration of 0.5 mM [Zn_2(L)] by $^{n}Bu_4NCl$ in THF: (a) full trace; (b) fitting profile for the de-aggregation phenomenon (n = 0.6); and (c) fitting profile for the binding event (n = 1.1).

The addition of bromide and iodide salts both lead to patterns typical of dilution only, which is consistent with their lower electronegativity and softer character compared to chloride. When a less coordinating solvent such as THF is used, changes consistent with de-aggregation followed by anion binding of chloride are observed sequentially (**Figure 4.10**). Furthermore, the underlying data are consistent with a 1:1 binding event and are thus in full accord with the solid state structures in which the anion is bound within the cavity of the Pacman-shaped molecule. The host complex [Zn_2(L)] also exhibits selectivity for Cl^- over Br^- and I^- as only de-aggregation phenomena are observed for the latter halides in THF (**Figure 4.11**).

In all cases, it should be noted that only small quantities of heat were generated during de-aggregation and anion-binding events and so reliable thermodynamic data were difficult to reproduce; typically, the de-aggregation and binding events for Cl^- amount to 7.4 and 6.1 kcal.mol^{-1} respectively (**Figure 4.14**). Unfortunately, the poor solubility of [Zn_2(L)] in THF limited the accessible concentration range and therefore prevented the determination of more accurate values. The titrations were carried out at different host [H] and guest [G] concentration (at [H]/[G] of 1 mM/20 mM, 1 mM/10 mM and 0.5 mM/10 mM) and these variations did not affect the overall

nature of the binding isotherms, thus providing important support for the proposed selective binding of chloride and with a 1:1 host:guest ratio (**Table 4.4**).

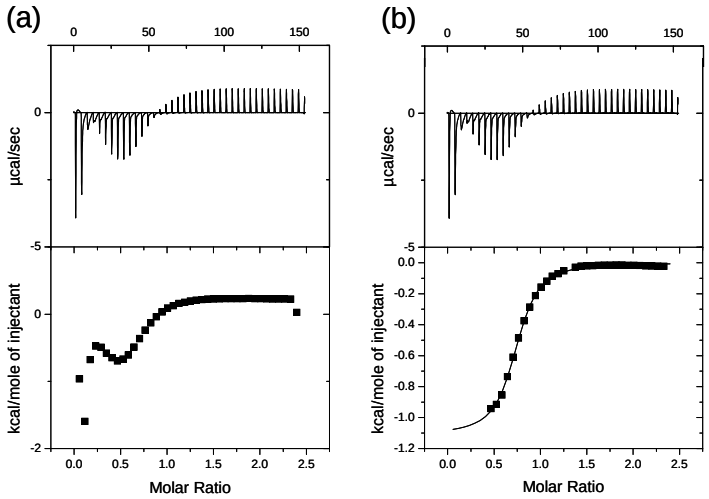

Figure 4.11 : ITC traces of the titration of a 1 mM solution of [Zn_2(L)] by a 18 mM solution of $^{n}Bu_4NBr$ in THF: (a) full trace; (b) fitting profile for the de-aggregation phenomenon (n = 0.7).

Anion	Solvent	De-aggregation		Binding	
		Equivalence	K (M^{-1})	Equivalence	K (M^{-1})
Cl^-	DMF	0.44	158000 ±1.2x10^4	not observed	n/a
Br^-	DMF	not observed	n/a	not observed	n/a
I^-	DMF	not observed	n/a	not observed	n/a
Cl^-	THF	0.58	271000 ±1.5x10^4	1.07	32200 ±1x10^3
Br^-	THF	0.73[a]	40000 ±1.5x10^4	not observed	n/a

Table 4.4 : ITC data in DMF and THF for the titration of a 1 mM solution of [Zn_2(L)] and by a10 mM solution of anion. [a] 20 mM guest solution.

In an attempt to elucidate the mechanism of the salt elimination reaction between an alkali metal salt of L and a zinc halide, which generates the halide-bridged "-ate" complex, the titration of [Zn_2(L)] by LiCl (the THF soluble equivalent of KCl) was carried out in THF. As expected from the tight ion pair introduced, only the

de-aggregation phenomenon was observed at n = 0.7 equivalents for host and guest concentrations of 1 mM and 20 mM respectively. This observation confirms that [K][Zn(μ-Cl)(L)] results from the incomplete elimination of KCl (as opposed to a full elimination followed by a binding event).

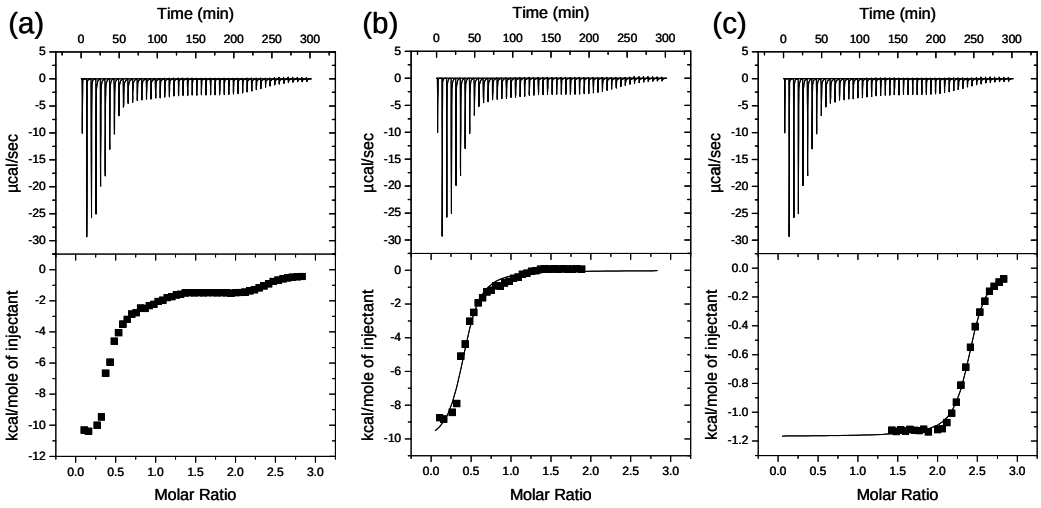

Figure 4.12 : ITC traces of the titration of 1 mM [Zn_2(L)] by 20 mM $^{n}Bu_4NH_2PO_4$ in DMF: (a) full trace; (b) fitting profile for the de-aggregation phenomenon (n = 0.4); and (c) fitting profile for the binding event (n = 2.4).

On top of spherical anions, a series of anions of different shape (linear, trigonal, and tetragonal) was also investigated in DMF as an initial study of the ability of [Zn_2(L)] to bind anions. As expected from the data obtained for halides, most anions did not promote the binding event and only the de-aggregation (or a dilution pattern) was observed. The phosphate anion was the only exception: its was found to bind to [Zn_2(L)] even in DMF (**Figure 4.12**). In this case a very different binding was observed with a 1:2 host guest ratio (n = 2.4), a binding constant of 210000 M^{-1} and a binding energy of 7.2 kcal.mol^{-1}. This binding appears quite strong compared to the binding of halides, especially considering that the measure was carried out in a good donor (*i.e.* competing) solvent. Furthermore, the binding event occurs at 2 equivalents, two very distinct signals were observed for the de-aggregation (at n = 0.4) and the binding. The binding of phosphates at zinc centres is quite common but usually occurs in a 1:1 fashion for di-zinc complexes.[8, 12] In the present case the 1:2 ratio suggests a binding of one phosphate on each zinc atom, outside the molecular cleft, which can be rationalised by steric considerations. Further

investigations would be required to confirm the exact nature of the phenomenon as well as the energy of binding in THF as a comparison point to halides. The preliminary results are promising because phosphates ions are biologically relevant and the binding to $[Zn_2(L)]$ occurs here in an unusual fashion and ratio.

4.3.3 Attempted UV-visible study

UV-visible spectroscopy was considered to study the anion recognition properties of $[Zn_2(L)]$. The main advantage offered was the ability to work at μM concentration which prevented the observation of the de-aggregation phenomenon and was expected to simplify considerably the data obtained. Unfortunately, the change observed in the spectrum upon addition of an anion was not significant enough to obtain reliable data (**Figure 4.13**): the spectrum of $[Zn_2(L)]$ consists mainly of two intense and broad absorptions at 359 (ln ε = 10.52) and 434 nm (ln ε = 10.48) and the spectrum of $[^nBu_4N][Zn_2(\mu\text{-}Cl)(L)]$ presents similar features at 360 (ln ε = 10.46) and 435 (ln ε = 10.39). Fluorescence spectroscopy experiments were carried out to try and overcome this issue.

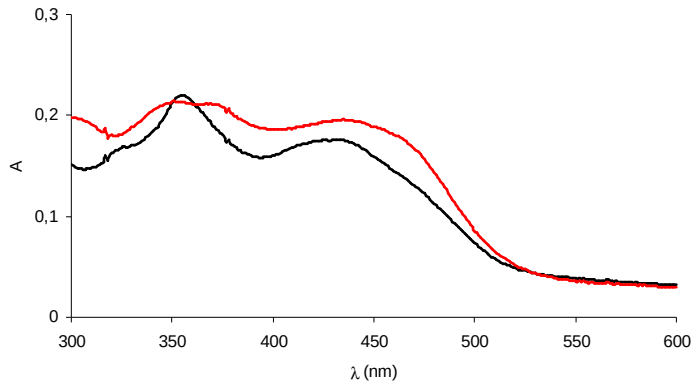

Figure 4.13 : UV-visible spectrum of a 6 μM solution of $[Zn_2(L)]$ in THF on its own (black trace) and in the presence of a large excess of $^nBu_4NCl$ (red trace).

4.3.4 Attempted fluorescence study

Attempts to observe the binding of anions by $[Zn_2(L)]$ by fluorescence spectroscopy proved to be very challenging and no conclusive data could be obtained. It is believed that the moisture sensitivity of the complex was exacerbated under the

highly dilute conditions required by fluorescence spectroscopy. Indeed, the analysis of the emission and excitation spectra for the titration of $[Zn_2(L)]$ by $^{n}Bu_4NCl$ suggested the presence of at least three different species in solution and were consistent with a mixture of $[Zn_2(L)]$, $[^{n}Bu_4N][Zn_2(\mu\text{-}OH)(L)]$ and $[^{n}Bu_4N][Zn_2(\mu\text{-}Cl)(L)]$. Unfortunatelly, the equipment available was not suited for experiments under dry conditions and once again no conclusive data could be obtained.

4.3.5 DFT calculations

In order to gain extra insight on the structure of $[Zn_2(L)]$ in solution, its ability to recognise anions, the structure of the anion-bound complexes as well as the energy of the binding event, Density Functional Theory (DFT) calculations were carried out by Dr P. Richardson. The computational details and the choice of computational tools used are published elsewhere;[38] only the outline of the calculations carried out will be discussed here together with the results.

Several functionals and basis sets were considered to carry out the calculations and the results were compared to the experimental data available (X-ray diffraction solid state structure and binding energy extracted from ITC data). The combination of M05-2X, the Zhao and Truhlar functional,[28] and LANL2DZ, the Hay and Wadt basis set,[29] was found to yield a satisfying accuracy at a reasonable computing cost. The bulk solvent interactions were accounted for using the self-consistent reaction field (SCRF) using the polarisable continuum model (PCM)[30] with the default parameters for THF within Gaussian 09. The other basis set and functional combination tried to model the binuclear zinc complexes yielded significantly over estimated values of the anion binding energy and will not be discussed further here.

The solid state structure of $[Pd_2(L)]$ (described in **Chapter 2**) was used as a starting point for the calculations and unconstrained geometry optimisations were carried out replacing the palladium cations by zinc ones. The structure obtained for $[Zn_2(L)]$ is described in section 4.1.1 and is consistent with the spatial arrangement expected and

the aggregation observed experimentally which results from the relatively constrained structure. The introduction of anions to the calculations generated "-ate" structures in which an anion bridged the two zinc atoms within the molecular cavity, as expected from the known X-ray structures. Interestingly, no exogenous anion binding was observed.

Space fill representations of the geometry optimised structures are depicted on **Figure 4.14** with anion binding energy for each binuclear zincate complex. In the geometry optimised structure of the binuclear zinc hydroxylate complex, zinc cations are displaced away from their N_4-donor plane towards the cavity by 0.68 Å resulting in a distorted square-base pyramidal geometry around the metal centres. As a result of this displacement, the intermetallic separation is shortened to 3.90 Å (*vs.* 4.98 Å in the structure of $[Zn_2(L)]$) and an obtuse 153.4° angle is observed. The molecular twist is largely reduced to 8° (*vs.* 34.2° in the structure of $[Zn_2(L)]$) while the two N_4-donor plane deviate slightly more from coplanarity (15.5° *vs.* 8.4° in the structure of $[Zn_2(L)]$). These geometrical parameters resemble closely those observed in the experimentally-determined structures and the differences observed are of the same order of magnitude as the differences observed between the two experimental structures (**Table 4.5**). Similarly, the geometrical parameters for the calculated and the experimental structure of $[Zn_2(\mu\text{-}Cl)(L)]^-$ are in good agreement. This argues again in favour of an accurate model as the counter ion effect and the packing interactions are not accounted for in computed model.

Qualitatively, the hydroxide anion appears as a definite best fit within the cavity while the accommodation of bigger halide anions appear to force the cavity to open (*i.e.* the bite angle is increased and the complex deviates form cofaciality). The stability of the "-ate" complex resulting from the binding was quantified by the energy of binding ΔE defined by **(4.3)**:

$$\Delta E = E([Zn_2(\mu - X)(L)] + ZPE) - E([Zn_2(L)] + ZPE) - E(X) \qquad \textbf{(4.3)}$$

where $E([Zn_2(\mu\text{-}X)(L)])$ is the energy of the solvated host:guest complex for the anion X, $E([Zn_2(L)])$ is the energy of the solvated binuclear zinc complex alone,

E(X) is the energy of the solvated anion X alone and ZPE is the zero-point energy correction for each component.

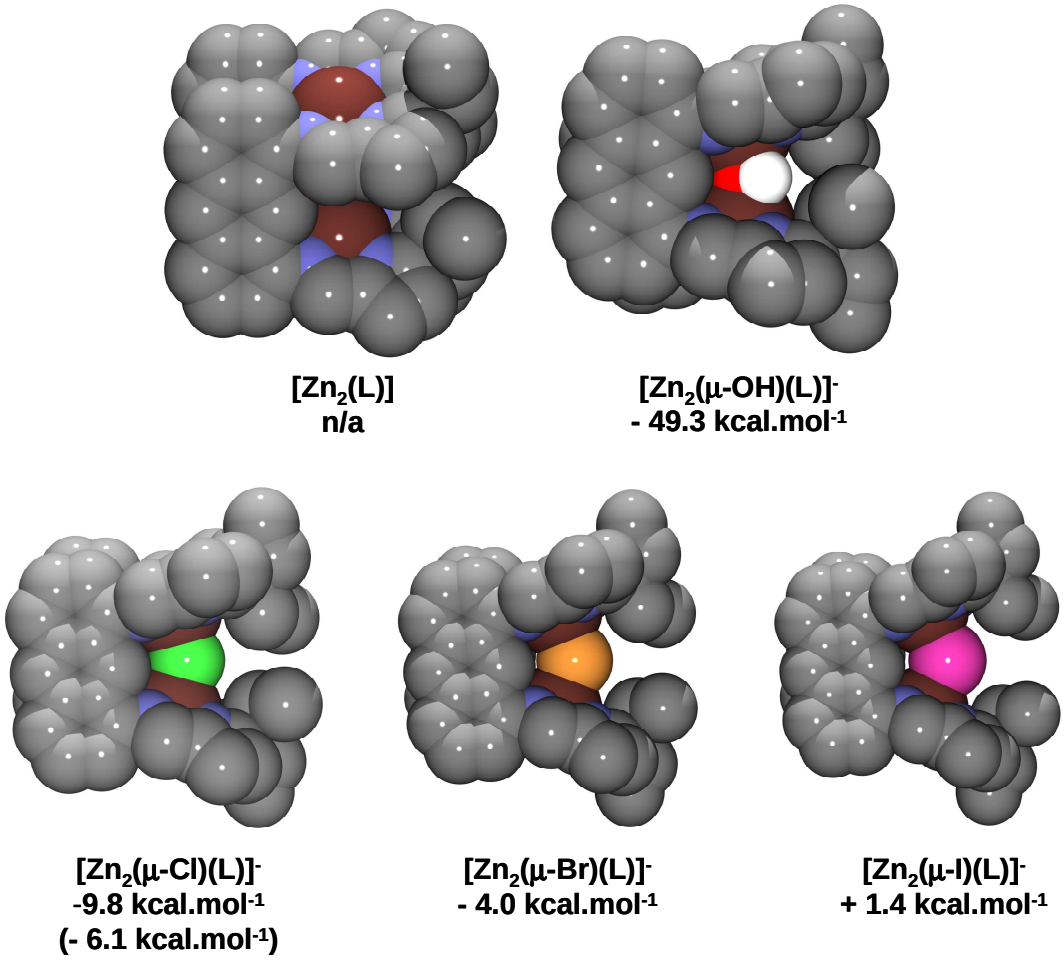

Figure 4.14 : Spacefill representation of the geometry optimised structures of $[Zn_2(L)]$ and its host:guest complex with hydroxide, chloride, bromide and iodide; side views. The anion binding energy for each complex is presented below the corresponding structure (the experimental value, obtained by ITC, is presented in brackets when available).

Only the energy of binding for the chloride anion was determined experimentally by ITC and the corresponding calculated value (- 9.8 kcal.mol^{-1}) is similar to the experimental value (- 6.1 kcal.mol^{-1}), which validates the model. The binding of the hydroxide anion within the molecular cleft appears to generate an important - 49.3 kcal.mol^{-1} stabilisation to the system which is consistent with the experimentally observed high propensity of $[Zn_2(L)]$ to react with atmospheric water and generate the hydroxide complex. Among the halides, the accommodation of chloride anion is slightly favoured. Considering that the binding energy for the chloride anion is slightly overestimated (by *ca* 3.7 kcal.mol^{-1}), the actual value for

the binding energy of bromide, estimated at -4.0 kcal.mol^{-1}, is probably above -1 kcal.mol^{-1} indicating that the bromide anion, like the iodide anion (ΔE = + 1.4 kcal.mol^{-1}), is effectively unbound (or extremely weakly bound) to the binuclear zinc unit. This is consistent with the ITC experimental data in which the chloride anion was found to bind weakly within the molecular cleft in THF and no binding interaction was observed for the other halides. The $OH^- >> Cl^- > Br^- > I^-$ trend in the binding strength follows the anionic radius[39] trend as well as the electronegativity[40] trend: the smaller the anion and the more electronegative the element, the stronger the binding (**Table 4.5**).

Compound	M···M [Å]	Twist [°]	Interplanar Angle[a] [°]	M-X [Å]	M-X-M [°]	M···N_4 [Å]
$[Zn_2(L)]$	**4.98**	**34.2**	**8.4**	**n/a**	**n/a**	**0.14**
$[Li(THF)_4]$ $[Zn_2(\mu\text{-}OH)(L)]$	3.8914(5)	8.4	14.57	1.962(2)/ 1.962(2)	165.1(5)	0.71/ 0.72
$[^nBu_4N]$ $[Zn_2(\mu\text{-}OH)(L)]$	3.871(1)	9.1	16.8	1.978(4)/ 1.969(4)	157.4(3)	0.75/ 0.75
$[Zn_2(\mu\text{-}OH)(L)]^-$	**3.90**	**8.5**	**15.5**	**2.00**	**153.4**	**0.68**
$[K(THF)_6]$ $[Zn_2(\mu\text{-}Cl)(L)]$	4.532(1)	13.8	26.6	2.340(2)/ 2.346(2)	150.54(9)	0.58/ 0.56
$[Zn_2(\mu\text{-}Cl)(L)]^-$	**4.68**	**11.2**	**28.9**	**2.42**	**150.5**	**0.54**
$[Zn_2(\mu\text{-}Br)(L)]^-$	**4.84**	**9.3**	**35.0**	**2.59**	**138.9**	**0.54**
$[Zn_2(\mu\text{-}I)(L)]^-$	**5.03**	**8.8**	**40.7**	**2.77**	**130.1**	**0.53**

Table 4.5 : Structural parameters of the calculated (bold) and the X-ray diffraction structures of binuclear zinc complexes of L.

4.4 Conclusion

The anthracenyl-hinged Schiff-base pyrrole macrocycle H_4L proved to be suitable for the complexation of two zinc cations and the resulting complex $[Zn_2(L)]$ was characterised together with two of its "-ate" compounds in which a chloride or hydroxide anion bridges the two metals within the binuclear cofacial molecular cleft. The anion-free complex, $[Zn_2(L)]$, was found be an aggregate in solution and its dissociation was observed as a result of dilution, heating, or upon addition of certain anions (**Figure 4.15**). Significantly, in an appropriate solvent, $[Zn_2(L)]$ was found to accommodate selectively a chloride anion over the other halides as inferred from ITC experiments, while evidence of favoured hydroxyl binding was also obtained.

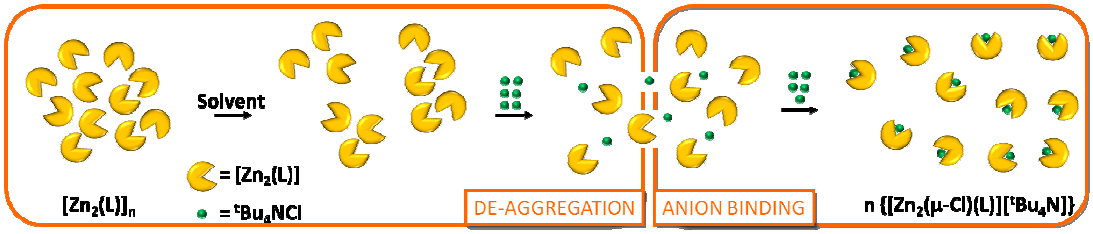

Figure 4.15 : Schematic representation of de-aggregation and anion binding by $[Zn_2(L)]$.

These host:guest interactions were found to be weak, a result that was corroborated by DFT calculations carried out at the M05-2X/LANL2DZ level of theory. These latter data revealed a distinct preference for hydroxide over chloride and confirmed the experimentally observed finding that bromide and iodide give rise to much less thermodynamically-stable host:guest interactions. It is clear from this work that the cofacial arrangement of Lewis acidic zinc cations facilitates the weak binding of small anions such as hydroxide and chloride within the molecular cleft. In fact, preliminary results have been obtained that show that $[Zn_2(L)]$ also acts as a receptor for tetrahedral ions such as phosphate and thus may have a broader role to play as an anion recognition and sensing system. The flexible nature of the complex and the ability to respond to various stimuli in different chemical terms, *i.e.* de-aggregation *vs.* anion binding lead to the suggestion that $[Zn_2(L)]$ and its analogues could be employed as a chemically-controlled switching element.

4.5 Bibliography

1 J. L. Sessler, P. A. Gale, and W.-S. Cho, 'Anion Receptor Chemistry', Royal Society of Chemistry, 2006; P. A. Gale and T. Gunnlaugsson, *Chem. Soc. Rev.*, **39**, 3595.

2 A. P. Paiva and P. Malik, *J. Radionucl. Nucl. Chem.*, 2004, **261**, 485.

3 R. A. Coxall, L. F. Lindoy, H. A. Miller, A. Parkin, S. Parsons, P. A. Tasker, and D. J. White, *Dalton Trans.*, 2003, 55; P. G. Plieger, S. Parsons, A. Parkin, and P. A. Tasker, *J. Chem. Soc., Dalton Trans.*, 2002, 3928; M. Wenzel, G. B. Jameson, L. A. Ferguson, Q. W. Knapp, R. S. Forgan, F. J. White, S. Parsons, P. A. Tasker, and P. G. Plieger, *Chem. Commun.*, 2009, 3606; V. Gasperov, S. G. Galbraith, L. F. Lindoy, B. R. Rumbel, B. W. Skelton, P. A. Tasker, and A. H. White, *Dalton Trans.*, 2005, 139; R. S. Forgan, J. E. Davidson, F. P. A. Fabbiani, S. G. Galbraith, D. K. Henderson, S. A. Moggach, S. Parsons, P. A. Tasker, and F. J. White, *Dalton Trans.*, 2010, **39**, 1763; S. G. Galbraith, L. F. Lindoy, P. A. Tasker, and P. G. Plieger, *Dalton Trans.*, 2006, 1134.

4 P. Ballester, *Chem. Soc. Rev.*, 2010, **39**, 3810; J. W. Steed, *Chem. Soc. Rev.*, 2009, **38**, 506; E. J. O'Neil and B. D. Smith, *Coord. Chem. Rev.*, 2006, **250**, 3068; V. Amendola, M. Bonizzoni, D. Esteban-Gómez, L. Fabbrizzi, M. Licchelli, F. Sancenón, and A. Taglietti, *Coord. Chem. Rev.*, 2006, **250**, 1451; R. Vilar, *Eur. J. Inorg. Chem.*, 2008, **2008**, 357; C. R. Rice, *Coord. Chem. Rev.*, 2006, **250**, 3190; J. L. Sessler, 'Anion Receptor Chemistry', 2006; C. Suksai and T. Tuntulani, *Chem. Soc. Rev.*, 2003, **32**, 192; P. D. Beer and E. J. Hayes, *Coord. Chem. Rev.*, 2003, **240**, 167; S. Bayly and P. Beer, in 'Metal-Based Anion Receptor Systems', Heidelberg, 2008; S. K. Kim and J. L. Sessler, *Chem. Soc. Rev.*, 2010, **39**, 3784; D. J. Mercer and S. J. Loeb, *Chem. Soc. Rev.*, 2010, **39**, 3612; S. O. Kang, J. M. Llinares, V. W. Day, and K. Bowman-James, *Chem. Soc. Rev.*, 2010, **39**, 3980; A. Dalla Cort, P. De Bernardin, G. Forte, and F. Yafteh Mihan, *Chem. Soc. Rev.*, 2010, **39**, 3863.

5 P. D. Beer, D. P. Cormode, and J. J. Davis, *Chem. Commun.*, 2004, 414.

6 V. Amendola, L. Fabbrizzi, C. Mangano, P. Pallavicini, A. Poggi, and A. Taglietti, *Coord. Chem. Rev.*, 2001, **219-221**, 821.

7 B. Jacques, C. Dro, S. Bellemin-Laponnaz, H. Wadepohl, and L. H. Gade, *Angew. Chem., Int. Ed. Engl.*, 2008, **47**, 4546; S. Carvalho, R. Delgado, M. G. B. Drew, and V. Felix, *Dalton Trans.*, 2007, 2431; Z.-H. Chen, Y.-B. He, C.-G. Hu, and X.-H. Huang, *Tetrahedron: Asymmetry*, 2008, **19**, 2051; S. Goswami and R. Chakrabarty, *Tetrahedron Lett.*, 2009, **50**, 5994; R. Shen, X. Pan, H. Wang, J. Wu, and N. Tang, *Inorg. Chem. Commun.*, 2008, **11**, 318; S. V. Mattigod, G. E. Fryxell, and K. E. Parker, *Inorg. Chem. Commun.*, 2007, **10**, 646; H. Min Su and H. K. Dong, *Angew. Chem., Int. Ed. Engl.*, 2002, **41**, 3809; S. Mizukami, T. Nagano, Y. Urano, A. Odani, and K. Kikuchi, *J. Am. Chem. Soc.*, 2002, **124**, 3920; V. Stastny, P. Lhoták, I. Stibor, and B. König, *Tetrahedron*, 2006, **62**, 5748; K.-H. Kim, J. S. Park, T. Y. Kang, K. Oh, M.-S. Seo, Y. S. Sohn, M.-J. Jun, W. Nam, and K. M. Kim, *Chem. -Eur. J.*, 2006, **12**, 7078; M. Boiocchi, L. Fabbrizzi, M. Garolfi, M. Licchelli, L. Mosca, and C. Zanini, *Chem.- Eur. J.*, 2009, **15**, 11288; S. Sabiah, B. Varghese, and N.

N. Murthy, *Chem. Commun.*, 2009, 5636; V. Ganesh, M. P. C. Sanz, and J. C. Mareque-Rivas, *Chem. Commun.*, 2007, 5010; V. Ganesh, M. P. C. Sanz, and J. C. Mareque-Rivas, *Chem. Commun.*, 2007, 804; J. B. Love, J. M. Vere, M. W. Glenny, A. J. Blake, and M. Schröder, *Chem. Commun.*, 2001, 2678.

8 Y. D. M. Champouret, W. J. Nodes, J. A. Scrimshire, K. Singh, G. A. Solan, and I. Young, *Dalton Trans.*, 2007, 4565; P. Roy, K. Dhara, M. Manassero, and P. Banerjee, *Inorg. Chim. Acta*, 2009, **362**, 2927; J. B. Fontecha, S. Goetz, and V. McKee, *Dalton Trans.*, 2005, 923; M. J. McDonough, A. J. Reynolds, W. Y. G. Lee, and K. A. Jolliffe, *Chem. Commun.*, 2006, 2971; G. Ambrosi, M. Formica, V. Fusi, L. Giorgi, A. Guerri, E. Macedi, M. Micheloni, P. Paoli, R. Pontellini, and P. Rossi, *Inorg. Chem.*, 2009, **48**, 5901.

9 J. M. Lehn, S. H. Pine, E. Watanabe, and A. K. Willard, *J. Am. Chem. Soc.*, 1977, **99**, 6766.

10 J.-M. Chen, X.-M. Zhuang, L.-Z. Yang, L. Jiang, X.-L. Feng, and T.-B. Lu, *Inorg. Chem.*, 2008, **47**, 3158.

11 C. J. Harding, F. E. Mabbs, E. J. L. MacInnes, V. McKee, and J. Nelson, *J. Chem. Soc., Dalton Trans.*, 1996, **15**, 3227.

12 H. H. Jang, S. Yi, M. H. Kim, S. Kim, N. H. Lee, and M. S. Han, *Tetrahedron Lett.*, 2009, **50**, 6241; B. A. Smith, W. J. Akers, W. M. Leevy, A. J. Lampkins, S. Xiao, W. Wolter, M. A. Suckow, S. Achilefu, and B. D. Smith, *J. Am. Chem. Soc.*, 2009, **132**, 67; A. Ojida, I. Takashima, T. Kohira, H. Nonaka, and I. Hamachi, *J. Am. Chem. Soc.*, 2008, **130**, 12095; W. M. Leevy, S. T. Gammon, H. Jiang, J. R. Johnson, D. J. Maxwell, E. N. Jackson, M. Marquez, D. Piwnica-Worms, and B. D. Smith, *J. Am. Chem. Soc.*, 2006, **128**, 16476; M. Coggins, K, A. Parker, M, A. Mangalum, G. Galdamez, A, and R. Smith, C, *Eur. J. Org. Chem.*, 2009, **2009**, 343; S. Khatua, S. H. Choi, J. Lee, K. Kim, Y. Do, and D. G. Churchill, *Inorg. Chem.*, 2009, **48**, 2993; G. Feng, D. Natale, R. Prabaharan, J. C. Mareque-Rivas, and N. H. Williams, *Angew. Chem., Int. Ed. Engl.*, 2006, **45**, 7056; Y. J. Jang, E. J. Jun, Y. J. Lee, Y. S. Kim, J. S. Kim, and J. Yoon, *J. Org. Chem.*, 2005, **70**, 9603; K. M. DiVittorio, W. M. Leevy, E. O'Neil, J., J. Johnson, R. , S. Vakulenko, J. Morris, D. , K. D. Rosek, N. Serazin, S. Hilkert, S. Hurley, M. Marquez, and B. Smith, D. , *ChemBioChem*, 2008, **9**, 286; D. H. Lee, J. H. Im, S. U. Son, Y. K. Chung, and J.-I. Hong, *J. Am. Chem. Soc.*, 2003, **125**, 7752; H. N. Lee, K. M. K. Swamy, S. K. Kim, J.-Y. Kwon, Y. Kim, S.-J. Kim, Y. J. Yoon, and J. Yoon, *Org. Lett.*, 2006, **9**, 243; J. H. Lee, J. Park, M. S. Lah, J. Chin, and J.-I. Hong, *Org. Lett.*, 2007, **9**, 3729.

13 P. J. Zinn, D. R. Powell, V. W. Day, M. P. Hendrich, T. N. Sorrell, and A. S. Borovik, *Inorg. Chem.*, 2006, **45**, 3484 and references within.

14 M. Y. Udugala-Ganehenege, M. J. Heeg, L. M. Hryhorczuk, L. E. Wenger, and J. F. Endicott, *Inorg. Chem.* , 2001, **40**, 1614; K. T. Szacilowski, P. Xie, A. Y. S. Malkhasian, M. J. Heeg, M. Y. Udugala-Ganehenege, L. E. Wenger, and J. F. Endicott, *Inorg. Chem.*, 2005, **44**, 6019.

15 R. Newell, A. Appel, D. L. DuBois, and M. Rakowski DuBois, *Inorg. Chem.*, 2004, **44**, 365.

16 A. M. Appel, R. Newell, D. L. DuBois, and M. Rakowski DuBois, *Inorg. Chem.*, 2005, **44**, 3046.

17 Y. D. M. Champouret, J. Fawcett, W. J. Nodes, K. Singh, and G. A. Solan, *Inorg. Chem.*, 2006, **45**, 9890; N. Singh, H. J. Jung, and D. O. Jang, *Tetrahedron Lett.*, 2009, **50**, 71.

18 I. Beletskaya, V. S. Tyurin, A. Y. Tsivadze, R. Guilard, and C. Stern, *Chem. Rev.*, 2009, **109**, 1659.

19 C. Bucher, C. H. Devillers, J.-C. Moutet, G. Royal, and E. Saint-Aman, *New J. Chem.*, 2004, **28**, 1584; D. P. Cormode, M. G. B. Drew, R. Jagessar, and P. D. Beer, *Dalton Trans.*, 2008, 6732; C. Lee, D. H. Lee, and J.-I. Hong, *Tetrahedron Lett.*, 2001, **42**, 8665.

20 J. P. Collman, P. S. Wagenknech, and J. E. Hutchison, *Angew. Chem. Int. Ed.*, 1994, **33**, 1537; P. D. Harvey, C. Stern, C. P. Gros, and R. Guilard, *Coord. Chem. Rev.*, 2007, **251**, 401; J. Rosenthal and D. G. Nocera, *Acc. Chem. Res.* , 2007, **40**, 543; J. Rosenthal and D. G. Nocera, *Prog. Inorg. Chem.*, 2007, **55**, 483.

21 D. Jokic, C. Boudon, G. Pognon, M. Bonin, K. Schenk, J. , M. Gross, and J. Weiss, *Chem.-Eur. J.*, 2005, **11**, 4199; S. Yagi, M. Ezoe, I. Yonekura, T. Takagishi, and H. Nakazumi, *J. Am. Chem. Soc.*, 2003, **125**, 4068; C. G. Oliveri, N. C. Gianneschi, S. T. Nguyen, C. A. Mirkin, C. L. Stern, Z. Wawrzak, and M. Pink, *J. Am. Chem. Soc.*, 2006, **128**, 16286; C. G. Oliveri, P. A. Ulmann, M. J. Wiester, and C. A. Mirkin, *Acc. Chem. Res.*, 2008, **41**, 1618; Z. Zai-Chun, L. He, Y.-Z. Zhu, and J.-Y. Zheng, *Chin. J. Chem.*, 2007, **25**, 1632; C.-H. Lee, H. Yoon, and W.-D. Jang, *Chem. -Eur. J.*, 2009, **15**, 9972; J. Brettar, J.-P. Gisselbrecht, M. Gross, and N. Solladie, *Chem. Commun.*, 2001, 733; C. A. Hunter, M. N. Meah, and J. K. M. Sanders, *J. Am. Chem. Soc.*, 1990, **112**, 5773; R. Rein, M. Gross, and N. Solladie, *Chem. Commun.*, 2004, 1992; P. Ballester, A. Costa, A. Castilla, M. , P. Deyà, M. , A. Frontera, R. Gomila, M. , and C. Hunter, A. , *Chem.-Eur. J.*, 2005, **11**, 2196.

22 N. Bampos, V. Marvaud, and J. Sanders, K. M. , *Chem.-Eur. J.*, 1998, **4**, 335; D. Kim, S. Lee, G. Gao, H. Seok Kang, and J. Ko, *J. Organomet. Chem.*, 2010, **695**, 111.

23 M. Gal, C. Marzin, G. Tarrago, I. Zidane, T. Hours, D. Lerner, C. Andrieux, H. Gampp, and J. M. Saveant, *Inorg. Chem.*, 1986, **25**, 1775; T. Muraoka, K. Kinbara, and T. Aida, *J. Am. Chem. Soc.*, 2006, **128**, 11600; T. Carofiglio, E. Lubian, I. Menegazzo, G. Saielli, and A. Varotto, *J. Org. Chem*, 2009, **74**, 9034; Z. Zhou, Y. Zhu, and J. Zheng, *Sci. China, Ser. B*, 2009, **52**, 1353; I. Tabushi and S. Kugimiya, *J. Am. Chem. Soc.*, 1986, **108**, 6926; I. Tabushi, S. Kugimiya, and T. Sasaki, *J. Am. Chem. Soc.*, 1985, **107**, 5159.

24 X. Li, M. Tanasova, C. Vasileiou, and B. Borhan, *J. Am. Chem. Soc.*, 2008, **130**, 1885; M. Tanasova, C. Vasileiou, O. Olumolade, O. , and B. Borhan, *Chirality*, 2009, **21**, 374.

25 D. Sun, F. S. Tham, C. A. Reed, L. Chaker, M. Burgess, and P. D. W. Boyd, *J. Am. Chem. Soc.*, 2000, **122**, 10704; Y. Shoji, K. Tashiro, and T. Aida, *Chirality*, 2008, **20**, 420; L. Tong, H. , J.-L. Wietor, W. Clegg, P. Raithby, R. , S. Pascu, I. , and J. Sanders, K. M *Chem.-Eur. J.*, 2008, **14**, 3035; M. Yanagisawa, K. Tashiro, M. Yamasaki, and T. Aida, *J. Am. Chem. Soc.*, 2007, **129**, 11912; A. Hosseini, S. Taylor, G. Accorsi, N. Armaroli, C. A. Reed, and P. D. W. Boyd, *J. Am. Chem. Soc.*, 2006, **128**, 15903; K. Tashiro

and T. Aida, *Chem. Soc. Rev.*, 2007, **36**, 189; Y. Shoji, K. Tashiro, and T. Aida, *J. Am. Chem. Soc.*, 2006, **128**, 10690.
26 L. Pauling, *J. Am. Chem. Soc.*, 1932, **54**, 3570.
27 R. G. Pearson, *J. Am. Chem. Soc.*, 1963, **85**, 3533; R. G. Pearson, *J. Chem. Educ.*, 1968, **45**, 581; R. G. Pearson, *J. Chem. Educ.*, 1968, **45**, 643.
28 Y. Zhao, N. E. Schultz, and D. G. Truhlar, *J. Chem. Theory Comput.*, 2006, **2**, 364.
29 P. J. Hay and R. W. Willard, *J. Chem. Phys.*, 1985, **82**, 270; R. W. Willard and P. J. Hay, *J. Chem. Phys.*, 1985, **82**, 284; P. J. Hay and R. W. Willard, *J. Chem. Phys.*, 1985, **82**, 299.
30 S. Miertus, E. Scrocco, and J. Tomasi, *Chem. Phys.*, 1981, **55**, 117.
31 F. Allen, *Acta Crystallogr., Sect. B*, 2002, **58**, 380.
32 S. Faure, C. Stern, R. Guilard, and P. D. Harvey, *J. Am. Chem. Soc.*, 2004, **126**, 1253.
33 O. Atsuhiro, N. Satoshi, N. Toshi, M. Kazuhiro, and T. Koshiro, *Angew. Chem., Int. Ed. Engl.*, 1991, **30**, 582; Y. Deng, C. J. Chang, and D. G. Nocera, *J. Am. Chem. Soc.*, 1999, **122**, 410; C. J. Chang, Y. Deng, A. F. Heyduk, C. K. Chang, and D. G. Nocera, *Inorg. Chem.*, 2000, **39**, 959.
34 M. Lachkar, A. Tabard, S. Brandes, R. Guilard, A. Atmani, A. De Cian, J. Fischer, and R. Weiss, *Inorg. Chem.*, 1997, **36**, 4141.
35 T. S. Balaban, R. Goddard, M. Linke-Schaetzel, and J.-M. Lehn, *J. Am. Chem. Soc.*, 2003, **125**, 4233; T. S. Balaban, M. Linke-Schaetzel, A. D. Bhise, N. Vanthuyne, and C. Roussel, *Eur. J. Org. Chem.*, 2004, **2004**, 3919.
36 W. S. Price, *Concepts in Magnetic Resonance*, 1997, **9**, 299; P. S. Pregosin, *Prog. Nucl. Magn. Reson. Spectrosc.*, 2006, **49**, 261; P. S. Pregosin, *Pure Appl. Chem.*, 2009, **81**, 615; P. S. Pregosin, P. G. A. Kumar, and I. Fernández, *Chem. Rev.*, 2005, **105**, 2977; C. S. Johnson Jr, *Prog. Nucl. Magn. Reson. Spectrosc.*, 1999, **34**, 203.
37 S. Floquet, S. Brun, J.-F. Lemonnier, M. Henry, M.-A. Delsuc, Y. Prigent, E. Cadot, and F. Taulelle, *J. Am. Chem. Soc.*, 2009, **131**, 17254.
38 A. M. J. Devoille, P. Richardson, N. Bill, J. L. Sessler, and J. B. Love, *Inorg. Chem.*, 2011, **50**, 3116.
39 R. Shannon, *Acta Crystallogr., Sect. A*, 1976, **32**, 751.
40 L. Pauling, *J. Am. Chem. Soc.*, 1932, **54**, 3570.

Chapter 5 – Towards the activation of other small molecules.

The activation of various small molecules is currently of much interest due to its ecological and economical relevance. For example, the redox chemistry of dihydrogen, coupled to that of dioxygen is essential for the development of hydrogen fuel cell technology, a crucial step towards renewable energy. Furthermore, the activation of carbon dioxide is of interest in order to transform this green house effect gas into useful materials such as polymers. Also, the reduction of dinitrogen, relevant to the fertiliser industry in particular, is highly energy demanding which makes it very expensive both in terms of money and carbon foot print. The macrocyclic ligand H_4L was designed such that its binuclear complexes are suited for the accommodation and transformation of small molecules, in particular dioxygen as detailed in **Chapter 3**. In **Chapter 2**, the versatility of the ligand was highlighted and this property makes it a good candidate for the activation of a variety of small molecules. In this chapter, two types of complexes are investigated: (1) cofacial complexes of early transition metals which are potential catalysts for the reduction of nitrogen and (2) a second binding mode offered by H_4L which leads to bowl-shaped complexes of general formula $[(MX_2)_2(H_4L)]$ in which the intermetallic distance is expected to be more flexible than in cofacial complexes. This second binding mode offers another possibility for the fine tuning of the metal-metal distance which is a fundamental parameter for the activation of small molecules. The reactivity of L towards this new binding mode is investigated for M = Zn and an overview of the possibilities is presented with a range of transition metals.

5.1 Binuclear zirconium cofacial complexes

5.1.1 Synthesis of $[(ZrCl_2)_2(L)]$ from $[K_4(L)]$

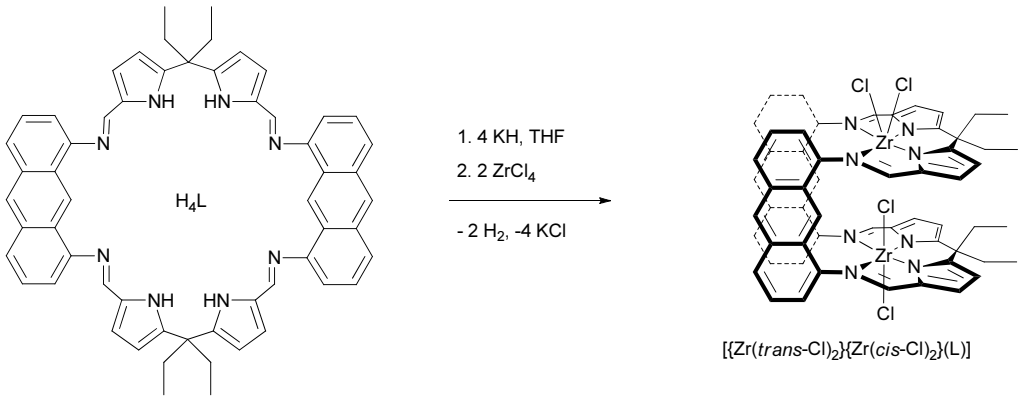

Scheme 5.1: Synthesis of $[(ZrCl_2)_2(L)]$ by salt elimination reaction from $[K_4(L)]$

The *in-situ* synthesis of the potassium salt $[K_4(L)]$ (described in **Chapter 2**) followed by reaction with two equivalents of zirconium tetrachloride in THF on a small scale (0.023 mmol) was monitored by ^{1}H NMR spectroscopy. Within an hour of the addition of the metal chloride, a quantitative reaction was observed. Compared to the ^{1}H NMR spectrum of a symmetric binuclear cofacial complex of L (such as $[Pd_2(L)]$ for example) most of the resonances appear split into two similar signals. This could be indicative of two phenomena: (1) the formation of two symmetrical complexes in a 1:1 ratio or (2) a de-symmetrisation of the complex caused by two non-equivalent metal environments. The absence of pyrrolic N-H resonances (observed at 12.16 ppm for H_4L) confirms that both pockets have been metallated. This implies that each diimino-dipyrrolic coordination site is occupied by a $ZrCl_2^{2+}$ cation and that the two metals have different coordination spheres. Steric considerations lead to the assumption that only one chloride can be accommodated within the molecular cleft and therefore the complex formed would contain both *trans*- and *cis*-geometries, i.e. $[\{Zr(trans\text{-}Cl)_2\}\{Zr(cis\text{-}Cl)_2\}(L)]$ (**Scheme 5.1**). This hypothesis is supported by the observation of two resonance for the aromatic protons at the 9-position on the anthracenyl backbone (10.70 and 8.96 ppm, integrating each for one proton) and one resonance for the 10-position (7.93 ppm, two protons), indicative of the presence of a single asymmetric complex with two non-equivalent 9-H positions (see **Chart C** on the bookmark for the localisation of the anthracenyl 9- and 10-positions). The

unusual deshielding of the resonance for one of the hydrogen atoms at the 9-position, seen at 10.70 ppm in THF/d_6-benzene (*vs.* 10.00 and 9.28 ppm for the corresponding proton in H_4L and $[Pd_2(L)]$), was attributed to hydrogen binding to the *endo*-chloride.

5.1.2 Synthesis of $[(ZrCl_2)_2(L)]$ from $[Li_4(L)]$

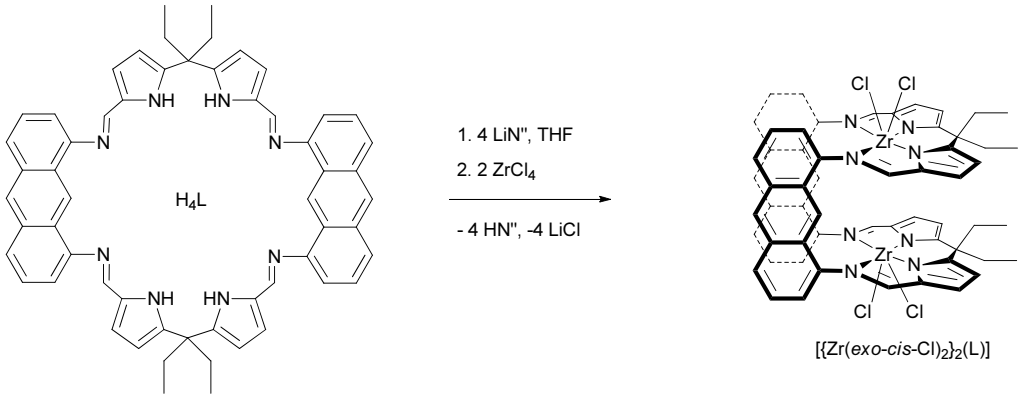

Scheme 5.2: Synthesis of $[(ZrCl_2)_2(L)]$ by salt elimination reaction from $[Li_4(L)]$

In an attempt to isolate $[(ZrCl_2)_2(L)]$ as a solid, a reaction similar to the one previously described was carried out on a bigger scale (0.23 mmol) from the lithium salt $[Li_4(L)]$. After overnight reaction at room temperature with $ZrCl_4{\cdot}2THF$, the product was extracted in dichloromethane and precipitated with diethyl ether to yield $[(ZrCl_2)_2(L)]$ in moderate yield. The ^1H NMR spectrum is consistent with a single, symmetric cofacial complex with two quartets at 2.18/2.13 ppm and two triplets at 0.79/0.74 ppm. The identical substitution in the two diimino-dipyrrolic pockets is further supported by the presence of only five anthracenyl aromatic resonances. In particular a single environment is observed at 8.77 ppm for the proton at the 9-position on the anthracene backbone; this latter resonance is standard and suggests that no hydrogen bonding is occurring to the chloride ligands. The isolation of $[\{Zr(exo\text{-}cis\text{-}Cl)_2\}_2(L)]$ was inferred from these observations (**Scheme 5.2**). The formation of this isomer may be due to a different pre-organisation of the macrocyclic ligand depending on the alkali-metal salt ($[Li_4(L)]$ *vs.* $[K_4(L)]$), a mechanism involving the silylamide by-product of the lithium salt synthesis or a simple isomerisation during the work up or over time; the full explanation of the reaction mechanism would require further investigation. The IR spectrum exhibits

multiple C=N and C=C stretches (1651, 1610, 1555 and 1504 cm^{-1}) that are consistent with the occurrence of metallation. Elemental analyses support the expected molecular composition. Attempted crystallisations by diffusion of an anti-solvent in the reaction mixture in THF of $[(ZrCl_2)_2(L)]$ (without work-up) yielded a mixture of brown block which were not suitable for the diffraction of X-rays and orange crystals which were identified by X-ray diffraction as $[Li(THF)_4][ZrCl_5(THF)]$. This is indicative of a decomposition mechanism occurring or a reaction that competes with the desired metallation of the ligand. No crystals of $[(ZrCl_2)_2(L)]$ suitable for an X-ray diffraction study could be isolated.

5.1.3 Synthesis of $[Zr(NMe_2)_2(H_2L)]$ and $[\{Zr(NMe_2)_2\}_2(L)]$

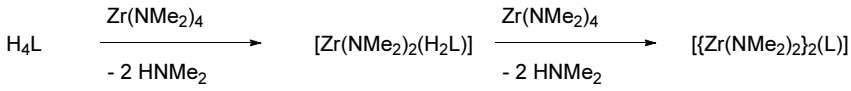

Equation 5.1: Synthesis of $[Zr(NMe_2)_2(H_2L)]$ and $[\{Zr(NMe_2)_2\}_2(L)]$ by stepwise transamination reaction.

The reaction between H_4L and one equivalent of $Zr(NMe_2)_4$ was carried out in THF and monitored by ^1H NMR spectroscopy. After 16 h, the reaction medium consisted of a clean mixture of two compounds: the ligand H_4L and a product of metallation. The presence of ligand and the double presaturation nature of the NMR experiment prevented the analysis of some areas of the spectrum but shows the mono-metallated cofacial complex $[Zr(NMe_2)_2(H_2L)]$ to be the most probable product (**Equation 5.1**). Indeed, a pyrrolic N*H* resonance is observed at 9.51 ppm and suggests that one diimino-dipyrrolic pocket remains protonated. Furthermore, two sets of multiplets are observed in the aliphatic region and the non-equivalence of the *meso*-ethyl groups is indicative of a cofacial arrangement. Even though only two triplets are observed at 0.73/0.61 ppm, the clear presence of three quartets at 2.18/2.09/2.03 ppm confirms the asymmetric nature of the product; the missing quartet and triplets are most probably obscured by the resonances for the *meso*-ethyl groups of the ligand at 0.88 (triplet) and 2.30 ppm (quartet). The mono-substitution is also supported by the resonances observed in the aromatic region: apart from the resonances corresponding

to the 9- and 10-positions on the anthracenyl backbone all the signals appear split into two similar resonances; one set corresponds to the substituted binding pocket, the second to the metal free pocket. Further investigation, including the isolation of the complex, would be required to fully characterise [$Zr(NMe_2)_2(H_2L)$] and confirm its nature. If the mono-metallic complex is proved to be formed and is easily isolated, this could be the first step towards hetero-bimetallic complexes of L which are highly relevant to small molecule activation as they potentially offer cooperative action between the two different metal centres.

A second equivalent of $Zr(NMe_2)_4$ was added to the reaction mixture of H_4L and [$Zr(NMe_2)_2(H_2L)$] in an attempt to force the reaction to completion (reasoning that sterics should prevent the second metallation to occur). After 16 hours of reaction, the concentration of solvent afforded a microcrystalline sample and the formation of a new compound was actually observed. Once again the numerous resonances observed and the solvent suppressed nature of the ^{1}H NMR spectrum recorded in THF rendered the full analysis challenging. However, full conversion was observed and the absence of remaining free ligand reveals the definite presence of four non-equivalent *meso*-methyl groups (triplets at 0.81/0.65/0.48/0.40 ppm, the quartets and the $N(CH_3)_2$ resonances are obscured by the suppressed THF resonance ranging from 1.4 and 2 ppm). Apart from the protons actually linked to the same carbon (i.e. in CH_3 groups), a resonance is observed for every single proton present in the molecule which indicates a complete desymmetrisation of the ligand. The absence of N*H* resonances above 9.3 ppm corroborates the formation of a binuclear complex. The complete lack of symmetry suggests that a very distorted structure is adopted to accommodate the sterically-demanding dimethylamide ligands around the zirconium atoms. An alternative explanation of the NMR data is that a mixture of two asymmetric isomers is obtained. Even thought the exact configuration of the complex cannot be ascertain from ^{1}H NMR spectroscopic data only, the spectrum is consistent with the formation of [$\{Zr(NMe_2)_2\}_2(L)$] (**Equation 5.1**). Attempts to record the ^{1}H NMR spectrum in other solvents to observe all the resonances proved unsuccessful due either to the poor solubility of the product or to extra coordination happening in more solubilising solvents (the spectrum recorded in d_5-pyridine was even more

complex). Elemental analyses were inconclusive and the small size of the crystals obtained by concentration of the liquors prevented their use for an X-ray diffraction study. Further investigation will be required to fully characterise [{Zr(NMe$_2$)$_2$}$_2$(L)]. However, the initial data appear promising and this complex is a potential precursor for a catalyst for the reduction of dinitrogen.

5.1.4 Reduction of [(ZrCl$_2$)$_2$(L)] with KC$_8$

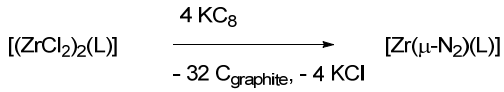

Equation 5.2: Reduction of [(ZrCl$_2$)$_2$(L)] by KC$_8$

On a small scale, [(ZrCl$_2$)$_2$(L)] was reacted with four equivalents of potassium graphite under an atmosphere of nitrogen. The solution turned darker instantly and the formation of a black solid, consistent with the formation of graphite, was observed. The ^{1}H NMR spectrum recorded in situ was consistent with the formation of a major cofacial, symmetric product. In particular, two triplets (at 0.68/0.61 ppm) and two quartets (at 2.03/1.97 ppm) were observed and the single set of resonances in the aromatic region also corroborates the symmetric nature of the product. The presence of minor products prevented the full analysis of the spectrum, in particular the accurate integration of the resonances. The reaction would need to be carried out under more controlled conditions to favour the exclusive formation of the desired product. However, the initial data support the reduction of the metal centre followed by its re-oxidation with possible concomitant binding and reduction of dinitrogen; therefore, the formation of [Zr$_2$(μ-N$_2$)(L)] is proposed (**Equation 5.2**) and further investigations will aim at the reproduction of the reaction as well as the isolation and full characterisation of the product. If the proposed formula is confirmed, this binuclear zirconium complex will have significant potential for reactions with hydrogen, ultimately to form ammonia.

5.2 Bowl-shaped complexes

5.2.1 Synthesis of $[(ZnCl_2)_2(H_4L)]$

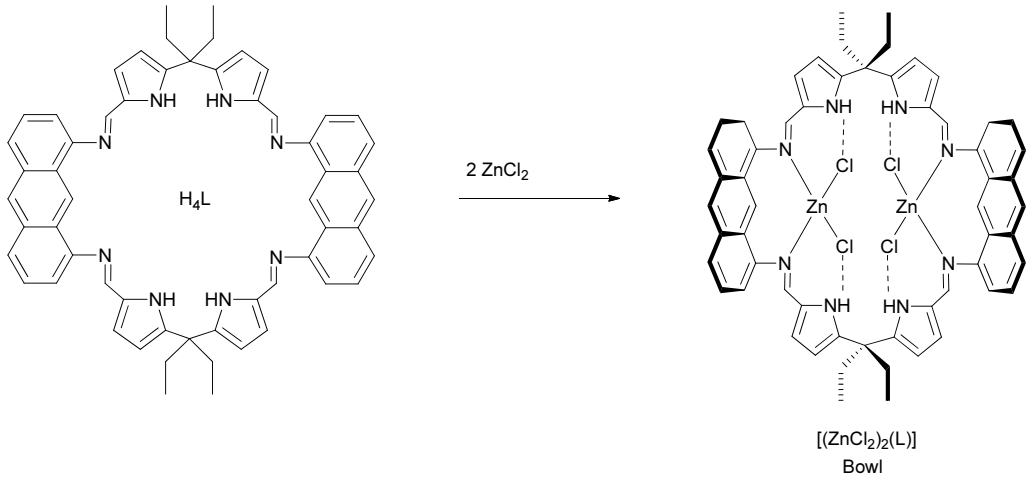

Scheme 5.3: Synthesis of $[(ZnCl_2)_2(L)]$

The macrocycle H_4L was found to react with metal halides MX_n ($n \geq 2$) to yield $[(MX_n)_2(L)]$ as presented in **Chapter 2**. In particular, the reaction of H_4L with $ZnCl_2$ in THF afforded $[(ZnCl_2)_2(H_4L)]$ as an orange solid which was isolated by filtration in good yield. Compared to the ^1H NMR spectrum of the ligand recorded in d_5-pyridine, only small shifts of the resonances are observed and the most affected signals are those corresponding to the proton at the 9-position on the anthracene moiety which shifts from 10.00 ppm in the ligand to 9.90 ppm in $[(ZnCl_2)_2(H_4L)]$ and the pyrrolic N*H* resonance which shifts from 12.16 to 12.00 ppm. In the IR spectrum of $[(ZnCl_2)_2(H_4L)]$, the N-H stretch at 3167 cm^{-1} is consistent with hydrogen-bonding of the pyrrolic N-H (this stretch is observed at 3250 cm^{-1} in H_4L) and the multiplicity of the C=N and C=C stretches (1649, 1618, 1577, 1554 and 1538 cm^{-1} vs. 1613 and 1550 cm^{-1} in H_4L) suggest that $[(ZnCl_2)_2(H_4L)]$ does not have the same symmetry as the unmetallated macrocycle. The bowl-shape structure presented on **Scheme 5.3** was inferred from these data and corresponds to a binding mode proposed by Mitsuo and co-workers[1] for palladium complexes in which a transition metal is coordinated with to anthracene-imine macrocycle through the imino-nitrogen atoms located at the 1 and 8-positions on the anthracene. This is similar to the reactivity observed with the related 1,2-aryl substituted macrocycles[2] and in contrast with the reactivity observed in the Love group with dipyrromethane

ligands.[3] Elemental analysis supports the expected composition. Further investigation, such as an X-ray diffraction study, would be required to confirm the structure of $[(ZnCl_2)_2(H_4L)]$.

5.2.2 Attempted synthesis of $[(MX_2)_2(H_4L)]$, M = Mn, Fe, Ni, Cu ; X = Br, Cl

Equation 5.3: Proposed synthesis of $[(MX_2)_2(L)]$

In an attempt to investigate this possible alternative binding mode further, $[(MCl_2)_2(H_4L)]$ complexes were synthesised on small scale (**Equation 5.3Equation 5.3**). The reaction described above was carried out replacing $ZnCl_2$ by $FeBr_2 \cdot 2THF$, $CoCl_2$, $NiCl_2 \cdot 2DME$ and $CuCl_2$. In all cases, a colour change was observed rapidly (to red for M= Fe, brown for M = Co, Cu and orange for M = Ni). When the reaction was carried out in d_6-benzene, a red microcrystalline solid was isolated from the iron containing sample; the ^1H NMR spectrum in THF/d_6-benzene was paramagnetic and exhibited a few resolved signals (at 35.36 and -8.90 ppm) as well as very broad un-resolved signals. The other reactions were carried out in THF/d_6-benzene only and afforded NMR silent samples. These observations are also consistent with the formation of $[(MX_2)_2(H_4L)]$ complexes, but further investigations will be required to characterise the complexes formed. These preliminary results, however, open up the range of chemistry accessible with H_4L. The study of the new binding mode as well as the redox properties of the bowl shaped complexes formed could lead to a large number of compounds with potential for PCET chemistry. In particular, the reaction with earlier transition metals halide followed by their chemical reduction could promote the activation of nitrogen (as illustrated on **Equation 5.4** for M = $ZrCl_2$) and would offer an alternative to the cofacial complexes presented earlier in this chapter. The main characteristic of the bowl-shape complex would be a much larger range of accessible intermetallic separations.

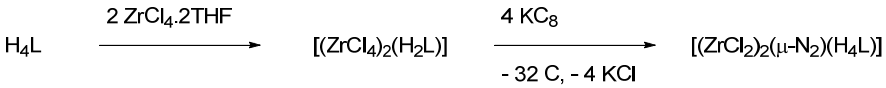

Equation 5.4: Potential activation of nitrogen from a binuclear zirconium bowl-shape complex of H_4L.

5.3 Bibliography

1 H. Mitsuo, Y. Naoki, T. Hiroshi, and U. Kazunori, in 'Organic Luminescent Element', 2002.

2 J. L. Sessler, E. Tomat, T. D. Mody, V. M. Lynch, J. M. Veauthier, U. Mirsaidov, and J. T. Markert, *Inorg. Chem.*, 2005, **44**, 2125; L. L. Cuesta, Vincent M.; Sessler, Jonathan L., *J. Porphyrins Phthalocyanines*, 2010, **14**, 41; E. Tomat, L. Cuesta, V. M. Lynch, and J. L. Sessler, *Inorg. Chem.*, 2007, **46**, 6224; J. M. Veauthier, E. Tomat, V. M. Lynch, J. L. Sessler, U. Mirsaidov, and J. T. Markert, *Inorg. Chem.*, 2005, **44**, 6736; G. Givaja, A. J. Blake, C. Wilson, M. Schroder, and J. B. Love, *Chem. Commun.*, 2005, 4423.

3 S. D. Reid, C. Wilson, A. J. Blake, and J. B. Love, *Dalton Trans.*, 2010, **39**, 418.

Chapter 6 – General conclusion.

The new ligand H_4L, designed to support catalysts for PCET has proved to be very versatile and was shown to be able to accommodate elements ranging from alkali earth metal (Mg) to actinide (UO_2) and a wide range of transition metals (Pd, Fe, Co, Zn, Zr) in various oxidation state in its cofacial binding mode. In particular, cofacial binuclear cobalt complexes of L were found to act as catalysts for the full reduction of oxygen to water with enhanced selectivity and conversion compared to pre-existing systems. Cofacial binuclear zinc complexes were also investigated and were found to bind anions weakly, with a clear preference for hydroxide; they were also found to recognise selectively chlorides over other halides. These results encouraged the synthesis of more soluble analogues of H_4L and xanthenes-based macrocycles are now being investigated within the Love group. Furthermore, initial work on the synthesis of early transition metal complexes of L was carried out and the initial results, in particular in the formation of binuclear zirconium complexes, are very promising; it is expected that these complexes will be able to bind dinitrogen. Finally, a different binding mode of H_4L affording complexes of the formula $[(MX_2)_2(H_4L)]$ was considered and once again the preliminary results are encouraging and further investigation should open the route to broad range of new potential catalysts for PCET.

Chapter 7 – Experimental.

7.1 General

Pyrrole was distilled under reduced pressure prior to use. All other chemicals were used as purchased. Lithium trimethylsilylamide was purchased from Aldrich, recrystallised from hexane and sublimed at 110 °C at 1×10^{-4} Torr. $[PdCl_2(PhCN)_2]$[1] and $[Zr(NMe_2)_4]$[2] were prepared as described in the literature. With the exception of $[Pd_2(L)]$ (alternative route), $[Fe_2(\mu\text{-}O)(L)]$, $[Co_2(\mu\text{-}O_2)(L)]$, $[Li(THF)_6][Zn_2(\mu\text{-}OH)(L)]$ and $[Bu_4N][Zn_2(\mu\text{-}OH)(L)]$, all the complexes of L were synthesised under nitrogen using Schlenk and glovebox techniques. Dry solvents (methanol, THF, DMF, toluene, dichloromethane, acetonitrile and diethyl ether) were purified by passage through Vacuum Atmospheres solvent drying towers; pyridine was distilled from potassium and stored over molecular sieves; benzonitrile was dried over activated alumina, distilled over phosphorus pentoxide and freeze-pump-thaw degassed three times; d-chloroform was dried over activated alumina, trap-to-trap vacuum distilled, and freeze-pump-thaw degassed three times; d_8-THF, d_5-pyridine and d_6-benzene were dried over potassium, trap-to-trap vacuum distilled, and freeze-pump-thaw degassed three times. ^1H NMR spectra were recorded at 298 K on a Bruker ARX250, AVA400,* DMX500, or AVA600 spectrometer operating at 250.13, 399.90, 400.25, 500.13 and 599.81 MHz respectively; $^{13}C\{^1H\}$ NMR spectra were recorded at 298 K on a Bruker ARX250 or DMX500 spectrometer operating at 62.90 and 125.77 respectively, ^7Li NMR spectra were recorded on a Bruker AVA600 spectrometer operating at 193.37 MHz. Dilution experiments and titrations were recorded on a Bruker DMX500 spectrometer. All NMR spectra were referenced to residual protio-solvent resonances. When the solvent is THF, the ^1H NMR experiment was recorded with double-presaturation of

*Two different machines operating at slightly different frequencies (399.90 and 400.25 MHz).

THF with a small quantity of d_6-benzene added as a deuterium lock. The EPR spectra were recorded at 100 K on a Bruker EPX080 spectrometer by Dr Paul Murray at the University of Edinburgh. IR spectra were recorded on a JASCO FT/IR 460 Plus spectrometer in the range 4000-400 cm^{-1}. The UV-Vis spectra were recorded on a Perkin Elmer Lambda 9 UV/Vis/NIR Spectrophotometer. Electrospray mass spectra were recorded using a Thermo LCQ instrument and electron impact mass spectra using a Thermo MAT 900XP spectrometer,[†] the mass spectrum of $[Zn_2(L)]$ was recorded by Mr. Martin De Cecco on a Q-Tof 2 (Micromass Waters Corporation, Manchester, UK) mass spectrometer using a nano-electrospray ionization source. Elemental analyses were carried out by Mr. Stephen Boyer at the London Metropolitan University. Cyclic voltammograms were recording using an Autolab PGstat12 equipment and the data were processed in GPES manager version 4.9. A conventional three-electrode cell made of a platinum wire embedded in glass working electrode, a silver wire reference electrode and a platinum foil counter electrode was used. All the voltammograms were referenced to the ferrocene/ferrocenium couple. Rotating ring disk experiments were recorded using a conventional three-electrode cell made of a glassy carbon disk (area = 0.192 cm^2, Pine Instruments, Sussex, UK) and platinum ring RRDE, a silver/silver chloride reference electrode separated from the bulk by a salt bridge and a platinum wire counter electrode. The RRDE was rotated in the range 100 rpm to 1000 rpm using a Pine Instruments AFMSRCE modulated speed rotator the rotating ring disk. Voltammograms were recorded using a PC-operated AFCBB1 bipotentiostat. All the voltammograms were referenced to the Ag/AgCl reference electrode, and the efficiency of the platinum disk was measured previously at 23%.[3] Microcalorimetric titrations were carried out using a MicroCal VP-ITC instrument and were processed with the Origin software provided. Emission and excitation fluorescence spectra were recorded with a Fluoromax spectrometer and the data were analysed with the DataMax software provided. DFT calculations were carried out by Dr Patricia Richardson at the University of Edinburgh.

[†] Divergences of 2 mass units from teh expected M+1 mass were observed in several spectra and were attributed to a miss-calibration of the spectrometre.

7.2 Synthetic procedures for Chapter 2

Synthesis of 1,8-diaminoanthracene

1,8-diaminoanthracene was prepared as reported in the literature from 1,8-dinitroanthraquinone,[4] except the quinone reduction step was carried out in the dark and the diamine product was kept away from light at all times. The diamine was isolated as a bright yellow solid by filtration, washed with hexane and recrystallised from methanol at -80 °C to yield pale yellow needles in an overall 65% yield. The ^{1}H NMR spectroscopic data are identical to those reported previously (only the data which were not presented in the initial literature are reported here).

^{1}H NMR (d_8-THF, 599.81 MHz): δ_H 8.65 (s, 1H, Ar*H*), 8.18 (s, 1H, Ar*H*), 7.26 (d, 2H, *J* = 8.4 Hz, Ar*H*), 7.16 (t, 2H, *J* = 7.8 Hz, Ar*H*), 6.58 (d, 2H, *J* = 7.1 Hz, Ar*H*), 5.21 (s, 4H, N*H*). IR (nujol): 3427 (N-H), 3373 (N-H), 1583 (C=C), 1549 (C=C) cm^{-1}. UV-Vis (THF): λ_{max} 356 nm (ln ε = 8.35), 375 (8.74), 419 (8.56). Analysis. Found: C, 80.64; H, 5.87; N, 13.38. $C_{14}H_{12}N_2$ requires: C, 80.74; H, 5.81; N, 13.45 %.

Decomposition product of 1,8-diaminoanthracene

1,8-diaminoanthracene was dissolved in deuterated solvent and exposed to light. The decomposition led to a brown solution and a brown solid. The solvent dependant reactivity was studied in a d-chloroform/d_6-DMSO mixture and in d_8-THF, the decomposition product could not be identified.

^{1}H NMR (d-chloroform/d_6-DMSO, 250.13 MHz): δ_H 8.77 (s, 1H), 8.11 (s, 1H), 7.15 (m, 4H), 6.55 (m, 2H), 5.74 (br, 4H); ^{1}H NMR (d_8-THF, 599.81 MHz): δ_H 6.88 (t, 1H, *J* = 7.6 Hz), 6.51 (m, 2H), 4.44 (s, 2H), 3.92 (s, 1H), 3.47 (s, 1H). IR (nujol): 3651, 3357(br), 3240(br), 1757, 1630, 1660, 1564 cm^{-1}. UV-Vis (THF): λ_{max} 497 nm (ln ε = 8.05, broad). EI-MS: 292.2 (55%), 224.1 (32%), 209 (M+1, 43%, diaminoanthracene), 208.1 (M, 100%, diaminoanthracene), 205.2 (50%); FAB-MS: 535.1 (5.5%), 461.1 (12.6%), 401.1 (16.0%), 327.1 (31.8%), 220.3

(88.6%), 207.2 (60.3%), 205.3 (76.8%). Analysis. Found: C, 72.20; H, 6.73; N, 7.71%.

Attempted synthesis of 1,8-diamino-9,10-dihydroanthracene

The synthesis of 1,8-diamino-9,10-dihydroanthracene was carried out as reported in the literature from 1,8-dinitroquinone.[5] The reaction was also carried out in the dark with no success. The ^{1}H NMR spectra in d-chloroform showed a mixture of unknown products containing no starting material and no expected product.

Synthesis of 2,7-di-tert-butyl-9,9-dimethylxanthene and the corresponding spiroketal

The condensation of p-*tert*-butylphenol and acetone was carried out in the presence of methanesulfonic acid as described in the literature[6, 7] and the best results were obtained using a Dean-Stark apparatus to remove the water formed azeotropically.[7] Upon recrystallisation from ethanol, the first two crops yielded a 50:50 mixture of 4,5-diamino-2,7-ditert-butyl-9,9-dimethylxanthene and corresponding spiroketal in moderate yield (3 g, 4%); a third crop yielded pure spiroketal.

^{1}H NMR (d-chloroform, 250.13 MHz): δ_H 7.40 (d, 2H, J = 2.3 Hz, Ar*H*), 7.30* (d, 2H, J = 2.4 Hz, Ar*H*), 7.21 (m, 2H, Ar*H*), 7.04* (m, 2H, Ar*H*), 6.96 (d, 2H, J = 8.5 Hz, Ar*H*), 6.61* (d, 2H, J = 8.5 Hz, Ar*H*), 2.08* (d, 2H, J = 13.9 Hz, CH_2), 1.96* (d, 2H, J = 13.9 Hz, CH_2), 1.65 (s, 6H, CH_3), 1.60* (s, 6H, CH_3), 1.33 (s, 18H, C(CH_3)$_3$), 1.29* (s, 18H, C(CH_3)$_3$). * Resonnances of the spiroketal.

Synthesis of 2,7,9,9-dimethylxanthene

The condensation of p-methylphenol and acetone was carried out in the presence of methanesulfonic acid as described in the literature[6, 7] and the best results were obtained by heating the mixture of starting materials to reflux for 90 h before extraction.[6] After several crystallisation attempts from methanol, the desired product was obtained in moderate yield (1.8 g, 11 %). The ^{1}H NMR spectrum was consistent with the data reported in the literature.

Syntheses of 4,5-diamino-2,7,9,9-dimethylxanthene and 4,5-diamino-2,7-di-tert-butyl-9,9-dimethylxanthene

The nitration and nitro-reduction of 2,7,9,9-dimethylxanthene and 2,7-di-*tert*-butyl-9,9-dimethylxanthene as described in the literature were unsuccessful and were carried out following the procedure for the related spiroketal:[8] the nitrations were carried out using fuming nitric acid in nitric acid and the 4,5-dinitro-xanthenes obtained were reduced with tin powder in hydrochloric acid to yield 4,5-diamino-2,7-di-*tert*-butyl-9,9-dimethylxanthene and 4,5-diamino-2,7,9,9-dimethylxanthene in 10-15% overall yields. The ^{1}H NMR spectrum for 4,5-diamino-2,7-di-*tert*-butyl-9,9-dimethylxanthene was consistent with the data reported in the literature.

4,5-diamino-2,7,9,9-dimethylxanthene: ^{1}H NMR (d-chloroform, 399.90 MHz): δ_H 7.19 (d, 2H, *J* = 1.5 Hz, Ar*H*), 7.00 (m, 2H, Ar*H*), 6.93 (d, 2H, *J* = 8.2 Hz, Ar*H*), 2.34 (s, 6 H, C*H*$_3$), 1.62 (s, 6 H, C*H*$_3$).

Synthesis of *meso*-diethyl-5,5'-diformyl-2,2'dipyrromethane and *meso*-fluorene -5,5'-diformyl-2,2'dipyrromethane

Meso-diethyl-5,5'-diformyl-2,2'dipyrromethane and *meso*-fluorene-5,5'-diformyl-2,2'dipyrromethane were synthesised as described in the literature.[9] The initial condensation between fluorenone and pyrrole was carried out at 0 °C instead of room temperature resulting in a yield increase from 45% to 71%. All the characterisation data were consistent with those reported in the literature.

Synthesis of the anthracenyl-macrocycle H_4L

The reaction and work up were carried out in the dark. A suspension of *meso*-diethyl-5,5'-diformyl-2,2'dipyrromethane (2.46 g, 9.6 mmol) in methanol (40 mL) was warmed until a clear solution was obtained and added to a suspension of 1,8-diaminoanthracene (2.00 g, 9.6 mmol, 1eq) in methanol (40 mL). Neat $(CF_3CO)_2O$ (1.60 mL, 11.5 mmol, 1.2 eq) was added dropwise at room temperature, the reaction mixture was stirred at room temperature for 30 min during which a bright orange precipitate formed. NEt_3 was added

dropwise until the precipitate turned bright yellow. The mixture was stirred for a further 15 min, the solid filtered, washed with methanol (3 x 10 mL), and dried under vacuum to yield H_4L as a yellow solid (2.80 g, 68%) that was stored under a nitrogen atmosphere.

^{1}H NMR (d-chloroform, 250.13 MHz): δ_H 9.28 (s, 4H, N*H*), 9.22 (s, 2H, Ar*H*), 8.42 (s, 2H, Ar*H*), 8.37 (s, 4H, imino), 7.82 (d, 4H, *J* = 8.4 Hz, Ar*H*), 7.43 (t, 4H, *J* = 7.3 Hz, Ar*H*), 6.95 (d, 4H, *J* = 7.0 Hz, Ar*H*), 6.68 (d, 4H, *J* = 3.6 Hz, pyrrole C*H*), 6.23 (d, 4H, *J* = 3.7 Hz, pyrrole C*H*), 2.05 (q, 8H, *J* = 7.4 Hz, CH_2), 0.81 (t, 12H, J = 7.3 Hz, CH_3); ^{1}H NMR (THF/d_6-benzene, 599.81 MHz): δ_H 10.74 (s, 4H, N*H*), 9.37 (s, 2H, Ar*H*), 8.36 (s, 2H, Ar*H*), 8.30 (s, 4H, imino), 7.75 (d, 4H, *J* = 8.1 Hz, Ar*H*), 7.35 (m, 4H, Ar*H*), 6.85 (br, 4H, Ar*H*), 6.77 (br, 4H, pyrrole C*H*), 6.20 (br, 4H, pyrrole C*H*), 2.30 (br, 8H, CH_2), 0.88 (br, 12H, CH_3); ^{1}H NMR (d_5-pyridine, 400.25 MHz): δ_H 12.16 (s, 4H, N*H*), 10.00 (s, 2H, Ar*H*), 8.53 (s, 4H, imino), 8.48 (s, 2H, Ar*H*), 7.87 (d, 4H, *J* = 8.4 Hz, Ar*H*), 7.43 (t, 4H, *J* = 7.7 Hz, Ar*H*), 7.07 (br, 4H, pyrrole C*H*), 6.99 (d, 4H, *J* = 6.8 Hz, Ar*H*), 6.43 (br, 4H, pyrrole C*H*), 2.36 (br d, 8H, *J* = 7.1 Hz, CH_2), 0.92 (t, 12H, *J* = 7.0 Hz, CH_3). ^{13}C{^{1}H} NMR (d-chloroform, 62.90 MHz): δ_C 150.6 (s, imine), 150.1 (s, quaternary), 140.83 (s, quaternary), 132.5 (s, quaternary) 130.6 (s, quaternary), 127.3 (s, quaternary), 126.2 (s, *C*H), 125.8 (s, *C*H), 125.2 (s, *C*H), 118.9 (s, *C*H), 116.9 (s, *C*H), 112.8 (s, *C*H), 110.0 (s, *C*H), 45.5 (s, *meso*-*C*-pyrrole quaternary), 32.2 (s, *C*H_2), 9.1 (s, *C*H_3). IR (nujol): ν 3250 (N-H), 1613 (C=N), 1550 (C=C) cm^{-1}. UV-Vis (THF): λ_{max} 322 nm (ln ε= 9.6), 370 (shoulder), 420 (shoulder). EI-MS: 860.5 (M^+, <1%), 831.5 (M^+-29, <1%, Et loss), 448.2 (M/2+18, 2%, water adduct), 430.2 (M/2, 100%) 401.1 (M/2-28, 86%, Et loss); ESI-MS: 897.27 (M+37, 28%), 861.74 (M, 40%), 431.72 (M/2+2, 40%). TLC: DCM/MeOH 97:3, Rf = 0.62. Analysis. Found: C, 80.84; H, 6.13; N, 12.94. $C_{58}H_{52}N_8$ requires: C, 80.90; H, 6.09; N, 13.01 %

Synthesis of the reduced anthracenyl macrocycle H_8L

$LiAlH_4$ (3.5 mg, 0.09 mmol, 4.5 eq) was added to a solution of H_4L (20 mg, 0.02 mmol) in THF (0.7 mL) under nitrogen. Vigorous gas evolution was

accompanied by a colour change from yellow to deep orange. Upon water addition, more gas was evolved and a bright yellow organic solution was obtained. The compound was studied *in-situ* and its isolation as a solid would require a scale-up of the reaction.

^{1}H NMR (THF/d_6-benzene, 500.13 MHz): δ_H 8.67 (s, 2H, Ar*H*), 8.06 (s, 2H, Ar*H*), 7.13 (m, 8H, Ar*H*), 6.40 (d, 4H, *J* = 6.6 Hz, Ar*H*), 5.95 (br, 4H, pyrrole C*H*), 5.87 (d, 4H, *J* = 3.02 Hz, pyrrole C*H*), 4.34 (s, 4H, CH_2N*H*), 4.26 (s, 8H, C*H*$_2$NH)), 0.62 (br, 12H, C*H*$_3$), the C*H*$_2$ resonance was obscured by the THF resonances, the observation of the pyrrolic N*H* would require dry conditions.

Attempted synthesis of the naphthyl-macrocycle H_4L'

The syntheses of H_4L' was attempted under conditions similar to the ones of the synthesis of H_4L, using hydrochloric acid as a catalyst. As the diamine is not light sensitive, the reaction was carried out in light. No imine resonance was observed in the ^{1}H NMR spetrum.

Synthesis of the xanthenyl-macrocycle H_4L"

Meso-diethyl-5,5'-diformyl-2,2'dipyrromethane (104 mg, 0.40 mmol, 1 eq) and 4,5-diamino-2,7-di-*tert*-butyl-9,9-dimethylxanthene (144 mg, 0.41 mmol, 1.01 eq) were suspended in methanol (2.5 mL) at room temperature and 1 drop of trifluoroacetic acid was added. The reaction mixture was stirred at room temperature for 15 min and the deep orange solution was neutralised with 10 drops of KOH saturated methanol. A yellow solid precipitated and was isolated and dried under vacuum to yield a mixture of compounds (60 mg, 25%).

^{1}H NMR (d-chloroform, 400.25 MHz): δ_H 9.42 (s, C*H*O), 9.34 (s, C*H*O), 9.24 (s, C*H*O), 8.84 (s, Ar*H*), 8.73 (s, Ar*H*), 8.64 (s, Ar*H*), 8.38 (s, imino), 8.27 (s, imino), 8.25-8.05 (m, Ar*H*), 7.25-5.90 (m, Ar*H* and pyrrole C*H*), 4.94 (br, N*H*), 4.73 (br, N*H*), 4.46 (br, N*H*), 2.23 (m, ethyl C*H*$_2$), 2.09 (m, ethyl C*H*$_2$), 1.95 (m, ethyl C*H*$_2$), 1.65 (s, methyl C*H*$_3$), 1.62 (s, methyl C*H*$_3$), 1.59 (s, methyl C*H*$_3$), 1.40 (s, *tert*-butyl C(C*H*$_3$)$_3$), 1.35 (s, C(C*H*$_3$)$_3$), 1.24 (s, C(C*H*$_3$)$_3$), 1.05-0.65 (m, aliphatic resonances), 0.60 (t, CH_2C*H*$_3$), 0.44 (t, ethyl CH_2C*H*$_3$). Only the signals that could be identified in

the poorly resolved spectrum are described, the others are cited as multiplets within a displacement range, no integration or coupling constant could be obtained. ESI-MS: 1149.63 (M, 23%), 593.36 (M/2+18, water adduct, 11%), 575.40 (M/2, 100%), 546.42 (M/2-29, ethyl loss, 12%).

Synthesis of the xanthenyl-macrocycle H_4L"'

A suspension of *meso*-fluorene-5,5'-diformyl-2,2'dipyrromethane (0.075 g, 0.21 mmol) in methanol (10 mL) was warmed to enhance the solubility and 4,5-diamino-2,7-di-*tert*-butyl-9,9-dimethylxanthene (0.075 g, 0.21 mmol, 1 eq) was added. Neat CF_3CO_2H (a few drops, catalytic) was added at room temperature, the reaction mixture was stirred at ambient temperature for 45 min after which the solvent volume was reduced to about 5 mL and a few drops of NEt_3 were added until the solution turned pale yellow. The mixture was stirred for a further 15 min, the solvent was removed under reduced pressure and the pale yellow solid was isolated by successive trituration in hexane and diethyl ether (0.023 g, 16%).

^{1}H NMR (d-chloroform, 250.13 MHz): δ_H 8.16 (s, 3H, imino), 7.82 (d, 4H, J = 7.3 Hz, fluorenyl Ar*H*), 7.56 (d, 4H, J = 7.1 Hz, fluorenyl Ar*H*), 7.41 (t, 4H, J = 7.0 Hz, fluorenyl Ar*H*), 7.27 (m, 12H, fluorenyl Ar*H* + xanthene Ar*H* x2), 6.71 (br, 3H, pyrrole C*H*), 5.58 (br, 3H, pyrrole C*H*), 1.73 (s, 12H, CH_3), 1.41 (s, 36H, C(CH_3)$_3$). ESI-MS: 1355.63 (M+18, water adduct, <1%), 1337.60 (M, 11%), 687.31 (M/2+18, water adduct, 32%), 669.38 (M/2, 100%), 353.28 (dialdehyde and diamine starting materials, 17%).

Synthesis of $[K_4(L)]\cdot 2.65$ THF

To a stirred mixture of H_4L (0.50 g, 0.58 mmol) and KH (0.12 g, 2.90 mmol, 5 eq) was added THF at -78 ºC under nitrogen. The resulting solution was stirred for 1 h at -78 ºC, allowed to reach room temperature and stirred for a further 4 h. The deep red solution was decanted from the excess KH and the solvent was

removed under reduced pressure to yield the potassium salt as a red solid (0.70 g, 74 %).

^{1}H NMR (d_5-pyridine, 500.13 MHz): δ_H 10.02 (s, Ar*H*), 8.55 (s, Ar*H*), 8.41(s, Ar*H*), 8.34 (br, Ar*H*), 7.74 (br, Ar*H*) 7.69 (br, Ar*H*), 7.41 (br, Ar*H*), 7.31 (br, Ar*H*), 7.22 (m, Ar*H*), 6.87 (br, pyrrole C*H*), 6.80 (br, pyrrole C*H*), 6.76 (br, pyrrole C*H*), 3.67 (m, THF), 3.24 (br, CH_2), 3.14 (br, CH_2), 2.79 (br, CH_2), 2.73 (br, CH_2), 1.63 (m, THF), 1.20 (br m, CH_3). IR (nujol): ν 1583 (C=N), 1549 (C=C) cm^{-1}. Analysis. Found: C, 68.41; H, 5.66; N, 9.54. $C_{58}H_{48}K_4 \cdot 2.65(C_4H_8O)$ requires: C, 68.40; H, 5.79; N, 9.30%.

Synthesis of [Li_4(L)]

To a solution of H_4L (0.100 g, 0.12 mmol) in THF (5 mL) at -78 °C was added a solution of lithium *tris*-(dimethylsilyl)amide (LiN") (0.077g, 0.48 mmol 4 eq) in THF (5 mL) at -78 °C. The mixture was allowed to reach room temperature and was reacted for 4 h to yield [Li_4(L)] as an orange solution in THF in a 95% yield by in situ NMR spectroscopy. The solvent was removed under reduced pressure and the solid was washed with toluene to afford [Li_4(L)] as a yellow solid (0.170 g, 83%).

^{1}H NMR (THF/d_6-benzene, 500.13 MHz): δ_H 9.39 (s, 2H, Ar*H*), 8.28 (s, 2H, Ar*H*), 8.07 (s, 4H, imino), 7.56 (d, 4H, *J* = 8.4 Hz, Ar*H*), 7.28 (m, 4H, Ar*H*), 6.80 (d, 4H, *J* = 6.9 Hz, Ar*H*), 6.57 (d, 4H, *J* = 3.3 Hz, pyrrole C*H*), 6.08 (d, 4H, *J* = 3.3 Hz, pyrrole C*H*), 2.08 (dd, 4H, *J* = 14.4 Hz, 7.0 Hz, CH_2 part obscured by THF suppression signal), 0.69 (t, 13H, *J* = 7.3 Hz, CH_3), 0.01 (s, 63H, HN"), -0.16 (s, 24H, excess LiN"). ^{13}C{^{1}H} NMR (THF/d_6-benzene, 125.77 MHz): δ_C 159.97 (s, quaternary), 155.55 (s, imino), 153.69 (s, quaternary), 138.81 (s, quaternary), 133.51(s, quaternary), 128.45 (s, *C*H), 126.09 (s, *C*H), 126.00 (s, *C*H), 122.16 (s, *C*H), 121.66 (s, *C*H), 113.53 (s, *C*H), 112.67 (s, *C*H), 107.68 (s, quaternary), 48.32 (s, quaternary, *meso*-C), 31.97 (s, *C*H_2), 9.78 (s, *C*H_3), 5.56 (s, *C*H_3, excess LiN"), 2.12 (s, *C*H_3, HN"). ^{7}Li NMR (THF/d_6-benzene, 194.37 MHz): 1.76 (br, [Li_4(L)]), 1.64 (s, br, [Li_4(L)]), 1.56 (shoulder, [Li_4(L)]), 0.82 (br, excess LiN").

Synthesis of $[Mg_2(L)]\cdot 2THF$

To a solution of H_4L (0.120 g, 0.14 mmol) in THF (5 mL) at -78 °C was added dropwise a solution of 0.5 M dibutylmagnesium in heptane (0.55 mL, 0.28 mmol, 2 eq). The mixture was allowed to reach room temperature and was reacted for an extra 16 h. The solution was cooled to 0°C and hexane (10 mL) was layered carefully resulting in, after 16 h, the formation of an orange micro-crystalline solid (0.035g, 27%) (Note: the ^{1}H NMR spectrum of the liquors exhibits mainly resonances corresponding to $[Mg_2(L)]$ and yield is limited by the re-crystallisation step).

^{1}H NMR (THF/d_6-benzene, 599.81 MHz): δ_H 8.92 (s, 2H, Ar*H*), 8.00 (s, 2H, Ar*H*), 7.96 (s, 4H, imino), 7.34 (d, 4H, *J* = 8.1 Hz, Ar*H*), 6.77 (br, 4H, Ar*H*), 6.67 (s, 4H, pyrrole C*H*), 6.18 (br, 8H, Ar*H* and pyrrole C*H*), 2.05 (q, 4H, *J* = 6.9 Hz, CH_2), 0.85 (t, 6H, *J* = 7.0 Hz, CH_3), 0.60 (t, 6H, *J* = 7.0 Hz, CH_3) (one of the CH_2 resonances is obscured by the THF suppressed signal); ^{1}H NMR (d_5-pyridine, 399.90 MHz): δ_H 9.42 (s, 2H, Ar*H*), 8.35 (s, 4H, imino), 8.19 (s, 2H, Ar*H*), 7.53 (d, 4H, *J* = 8.3 Hz, Ar*H*), 6.98 (d, 4H, *J* = 3.4 Hz, pyrrole C*H*), 6.90 (t, 4H, *J* = 7.7 Hz, Ar*H*), 6.38 (m, 8H, Ar*H* and pyrrole C*H*), 3.66 (m, 8H, THF), 2.03 (m, 4H, CH_2), 1.62 (m, 8H, THF), 1.48 (m, 4H, CH_2), 0.68 (t, 6H, *J* = 7.1 Hz, CH_3), 0.07 (t, 6H, *J* = 7.2 Hz, CH_3). ^{13}C{^{1}H} NMR (THF/d_6-benzene, 125.76 MHz) δ_C 157.77 (s, imino), 156.74 (s, quaternary), 148.88 (s, quaternary), 135.77 (s, quaternary), 132.41 (s, quaternary), 127.67 (s, quaternary), 126.49 (s, quaternary), 125.95(s, quaternary), 124.41 (s, *C*H), 122.58 (s, *C*H), 119.63 (s, *C*H), 118.30 (s, *C*H), 114.72 (s, *C*H), 111.75 (s, *C*H), 47.84, (s, quaternary, *meso*-C), 40.51 (s, *C*H_2), 30.35 (s, *C*H_2), 9.99 (s, *C*H_3), 9.24 (s, *C*H_3). IR (nujol): ν 1610 (w), 1572 (*C*=*N*), 1549 (*C*=*C*) cm^{-1}. Analysis. Found: C, 76.84; H, 5.44; N, 12.24. $C_{58}H_{48}N_8Mg_2$ requires: C, 76.92; H, 5.34; N, 12.37%.

Synthesis of $[Pd_2(L)]$

A mixture of H_4L (0.13 g, 0.15 mmol) and KH (0.03 g, 0.75 mmol, 5 eq) was combined in THF at -78 ºC, allowed to warm to room temperature, and stirred for a further 4 h. The resulting mixture was transferred by filter cannula into a solution of $[PdCl_2(PhCN)_2]$ (0.15 g, 0.39 mmol, 3 eq) in THF, shielded from light

and stirred for 20 days. The mixture was filtered, the solvent reduced under vacuum, and the product was recrystallised at -78 °C to yield a yellow microcrystalline solid (0.04 g, 23 %).

^{1}H NMR (d_8-THF, 500.13 MHz): δ_H 9.28 (s, 2H, Ar*H*), 7.80 (s, 2H, Ar*H*), 7.74 (s, 4H, imino), 7.34 (d, 4H, *J* = 8.8 Hz, Ar*H*), 6.93 (m, 4H, Ar*H*), 6.84 (m, 4H, Ar*H*), 6.81 (d, 4H, *J* = 4.0 Hz, pyrrole C*H*), 6.11 (d, 4H, *J* = 4.0 Hz, pyrrole C*H*), 2.15 (q, 4H, *J* = 7.2 Hz, CH_2), 1.89 (q, 4H, *J* = 7.3 Hz, CH_2), 0.51 (t, 6H, *J* = 7.2 Hz, CH_3), 0.27 (t, 6H, *J* = 7.3 Hz, CH_3). ^{13}C{^{1}H} NMR (d_8-THF, 125.77 MHz) δ_C 160.6 (s, imine), 145.0 (s, quaternary), 146.9 (s, quaternary), 138.2 (s, quaternary), 132.8 (s, quaternary), 127.9 (s, *C*H), 126.8 (s, quaternary), 126.6 (s, *C*H), 125.1 (s, *C*H), 120.7 (s, pyrrole *C*H), 119.4 (s, *C*H), 116.8 (s, *C*H), 109.0 (s, pyrrole *C*H), 40.0 (s, *C*H_2), 36.6 (s, *C*H_2), 11.2 (s, *C*H_3), 10.4 (s, *C*H_3). The poor solubility of the compound prevented the assignment of the quaternary *meso*-carbon. IR (nujol): ν 1616 (w), 1570 (*C=N*), 1552 (*C=C*) cm^{-1}. UV-Vis (THF): λ_{max} 314 nm (ln ε= 11.0), 411 (10.1), 433 (9.9). ESI-MS: 1095.21 (M+2+23, 44%, Na^+ adduct), 1094.23 (M+1+23, 46%, Na^+ adduct), 1093.16 (M+23, 64%, Na^+ adduct), 1092.19 (M-1+23, 57%, Na^+ adduct), 1091.2 (M-2+23, 63%, Na^+ adduct), 1090.2 (M-3+23, 52%, Na^+ adduct). 1072.3 (M+2, 29%), 1071.2 (M+1, 34%), 1070.2 (M, 34%), 1069.2 (M-1, 31%), 1068.2 (M-2, 31%), 1067.1 (M-3, 24%). Analysis. Found: C, 64.89; H, 4.86; N, 9.93. $C_{58}H_{48}N_8Pd_2$ requires: C, 65.11; H, 4.52; N, 10.47%.

Alternative synthesis of [Pd_2(L)]

A solution of [$PdCl_2(PhCN)_2$] (0.02 g, 0.06 mmol, 1eq) in THF (1 mL) was added to a solution of H_4L (0.05 g, 0.06 mmol) in THF (4 mL) and stirred at room temperature for 30 min. A few drops of NEt_3 were added and the reaction mixture was stirred for a further 3 days at room temperature. The mixture was treated with toluene (1 mL) and solvent was removed under reduced pressure. The crude mixture was analysed by ^{1}H NMR spectroscopy in d-chloroform from which crystals suitable for an X-ray diffraction study deposited.

^{1}H NMR (d-chloroform, 250.13 MHz): δ_H 9.08 (s, 2H, Ar*H*), 8.27 (s, 2H, Ar*H*), 8.22 (s, 4H, Ar*H*), 7.67 (d, 4H, *J* = 8.70 Hz, Ar*H*), 7.27 (m, 4H, Ar*H*), 6.78 (m, 4H, Ar*H*), 6.58 (d, 4H, *J* = 3.72 Hz, pyrrole C*H*), 6.10 (d, 4H, *J* = 3.73 Hz, pyrrole C*H*), 1.54 (m, 4H CH_2).

Synthesis of [$(FeCl)_2$(L)]

To a stirred mixture of H_4L (0.100 g, 0.11 mmol) and LiN" (0.079 g, 0.47 mmol, 4.1 eq) at -78 ºC was added THF (5 mL) and the mixture was allowed to reach room temperature. After 4 h, the resulting solution was added dropwise to a suspension of $FeCl_3$ (0.038 g, 0.23 mmol, 2 eq) in THF (1 mL) at -78 °C, the mixture was allowed to reach room temperature slowly and was stirred for 16 h during which a deep red solid formed. The solvent was removed under reduced pressure, the product was extracted in dichloromethane and the solvent was removed under reduced pressure (25 mg, 22 %).

^{1}H NMR (THF/d_6-benzene, 400.25 MHz): δ_H 39.33 (s), 38.21 (s), 25.46 (br), 22.99 (s), 15.33 (br), 7.97 (s), -0.54 (s), -5.71 (s), -15.08 (s), -19.05 (br), -26.57 (br), -37.07 (s), -63.74 (br). IR (nujol): ν 1615(w), 1644 (C=N), 1575 (*C*=*N*), 1551 (*C*=*C*) cm^{-1}. ESI-MS: inconclusive. Analysis. Found: C, 67.28; H, 4.90; N, 9.45. $C_{58}H_{48}N_8Fe_2Cl_2 \cdot 2(C_4H_8O)$ requires: C, 67.42; H, 4.80; N, 9.53%.

Synthesis of [Fe_2(L)] from [K_4(L)]

To a stirred mixture of H_4L (0.100 g, 0.11 mmol) and KH (0.023 g, 0.57 mmol, 4.8 eq) at -78 ºC was added THF (5 mL) and the mixture was allowed to reach room temperature. After 4 h, the resulting suspension was added dropwise to a suspension of [$FeBr_2(THF)_2$] (0.082 g, 0.23 mmol, 2eq) in THF (1 mL) at -78 °C, the mixture was allowed to reach room temperature slowly and was stirred for 16 h during which it turned deep red and solid formed. Filtration and solvent removal under reduced pressure resulted in the product as a brown solid. ^{1}H NMR (in situ before work-up): silent, ^{1}H NMR (of the isolated product): shows resonances for the oxygenated

compound [Fe_2(μ-O)(L)]. Full characterisation, including a yield, would require a scale up of the reaction.

Synthesis of [Fe_2(L)] from [Li_4(L)]

To a stirred mixture of H_4L (0.100 g, 0.11 mmol) and LiN" (0.078 g, 0.46 mmol, 4.2 eq) at -78 ºC was added THF (5 mL) and the mixture was allowed to reach room temperature. After 4 h, the resulting solution was added dropwise to a suspension of [$FeBr_2(THF)_2$] (0.084 g, 0.23 mmol, 2eq) in THF (1 mL) at -78°C, the mixture was allowed to reach room temperature slowly and was stirred for 16 h during which it turned deep red. The solvent was evaporated to dryness and the product was extracted in dichloromethane.

^{1}H NMR (THF/d_6-benzene, recorded *in situ* before work-up, presumably [Li$(THF)_4$][Fe_2(μ-Br)(L)], 599.81 MHz): δ_H 56.05 (s), 28.01 (s), 23.60 (s), 11.39 (s), 11.01 (s), -16.04 (s), -29.29 (s), -64.17 (s), -65.57 (s). ^{1}H NMR (of the isolated product): NMR silent.

Synthesis of [Fe_2(L)] from the reduction of [$(FeCl)_2$(L)]

[$(FeCl)_2$(L)] was synthesised as described above in a THF/d_6-benzene solution on a 0.012 mmol scale in an NMR tube under nitrogen atmosphere and its formation was monitored by ^{1}H NMR spectroscopy. C_8K (0.0048 g, 0.036 mmol, 3 eq.) was added to the suspension, dissolution occurred with a subtle colour change and a black solid was observed. The ^{1}H NMR spectrum was recorded after filtration and was silent which is consistent with [Fe_2(L)]. Exposure of the NMR sample to air afforded a spectrum consistent with the formation of [Fe_2(μ-O)(L)]. Full characterisation, including a yield, would require a scale up of the reaction.

Synthesis of [Fe_2(μ-O)(L)]

[Fe_2(L)] was synthesised from the potassium salt of H_4L as described above in a THF solution on a 0.11 mmol scale. After filtration of the solid, the solution was exposed

to air and the solvent was removed under reduced pressure to afford the $[Fe_2(\mu\text{-}O)(L)]$ as a black shiny solid (39 mg, 36%).

^{1}H NMR (THF/d_6-benzene, 599.81 MHz): δ_H 44.15 (br), 23.46 (s), 10.76 (s), 9.44 (s), 4.66 (s), 2.31 (s), 1.12 (s), 0.80 (s), -0.32 (s). ESI-MS: inconclusive. IR (nujol): ν 1612(br), 1577 (br, *C=N*), 1552 (br, *C=C*) cm^{-1}. Analysis. Found: C, 70.72; H, 4.83; N,11.25. $C_{58}H_{48}N_8Fe_2O$ requires: C, 70.74; H, 4.91; N, 11.38%

Synthesis of $[(UO_2)_2(L)]$

The synthesis and full characterisation of this complex were carried out by Guy Jones and will be described elsewhere.

7.3 Synthetic procedures for Chapter 3

Synthesis of $[Co_2(L)]$

To a stirred mixture of H_4L (0.200 g, 0.23 mmol) and LiN" (0.156 g, 0.93 mmol, 4.1 eq) at -78 ºC was added THF (5 mL) and the mixture was allowed to reach room temperature. After 4 h, the resulting solution was added dropwise to a suspension of $CoCl_2$ (0.060 g, 0.46 mmol, 2 eq) in THF (2 mL) at -78 °C, the mixture was allowed to reach room temperature slowly and was stirred for 16 h during which a deep red solid formed. The reaction mixture was maintained at -20 °C for 24 h, the solid was isolated by decantation of the supernatant liquid and dried under reduced pressure (0.115 g, 51%).

^{1}H NMR (THF/d_6-benzene, 599.81 MHz): δ_H 35.7 (br s, 4H), 23.7 (s, 4H), 2.75 (s, 2H), 0.01 (s, 1H), -2.11 (s, 4H), -13.2 (s, 4H), -15.5 (br s, 3H), -16.0 (s, 4H), -17.1 (s, 4H), -18.2 (s, 5H), -31.4 (s, 4H), -55.6 (br, 3H). EPR (benzonitrile, 100 K, N_2): very weak and broad feature, g ~ 2.0. IR (nujol): ν 1616 (w), 1580 (*C=N*), 1555 (*C=C*) cm^{-1}. UV-Vis (benzonitrile, N_2): λ_{max} 355 nm (shoulder, ln ε= 11.04), 430 (10.69). ESI-MS (THF-acetonitrile): 974 ($[M]^+$, 20%, $[Co_2(L)]$), 991 ($[M + 17]^+$, 69%, water loss on $[Co_2(O_2H_3)(L)]^-$), 962 ([M + 17 - 29], 100%, single Et loss and water loss on $[Co_2(O_2H_3)(L)\ ]^-$), 945 ($[M - 29]^+$, 18%, single Et loss on$[Co_2(L)]$), 933

([M + 17 - 58], 85%, double Et loss and water loss on $[Co_2(O_2H_3)(L)]^-$), 916 ($[M - 58]^+$, <1%, double Et loss on$[Co_2(L)]$). Analysis. Found: C, 71.43; H, 5.03; N, 11.38. $C_{58}H_{48}N_8Co_2$ requires: C, 71.45; H, 4.96; N, 11.49 %.

Synthesis of $[Co_2(L)][BF_4]$

To a solution of $[Co_2(L)]\cdot THF$ (6 mg, 0.005 mmol) in benzonitrile containing a drop of tetramethylsilane was added $AgBF_4$ (1 mg, 0.005 mmol, 1eq). After a few hours at room temperature, the sample was filtered.

^1H NMR (benzonitrile/d_6-benzene capillary, 400.25 MHz): δ_H 8.20 (br), 5.11 (br), -1.40 (br), -2.22 (br), -3.30 (br). Large regions are obscured by solvent signals in the aromatic region and impurities in the aliphatic region, and accurate integration was prevented by the poor quality of the spectrum. Δ_{ppm} = 0.033 (measured on one sample only), μ_{eff} = 1.25 B.M. When left in solution, this sample evolves with time to yield the doubly-oxidised product $[Co_2(L)][BF_4]_2$. Full characterisation of the product would require a scale up of the reaction.

Synthesis of $[Co_2(L)][BF_4]_2$

To a solution of $[Co_2(L)]\cdot THF$ (6 mg, 0.005 mmol) in benzonitrile was added $AgBF_4$ (10 mg, 0.05 mmol, 10 eq). After a few hours at room temperature, the grey precipitate was filtered. No further reactivity was observed upon exposure to air.

^1H NMR (benzonitrile/d_6-benzene capillary, 400.25 MHz): δ_H 9.29 (s), 8.76 (s), 7.99 (s), 7.89 (s), 7.82 (s), 6.90 (s), 1.22 (m), 0.87 (m), 0.44 (m), 0.38 (t), 0.29 (t), 0.23 (t). Large regions are obscured by solvent signals in the aromatic region and impurities in the aliphatic region, and accurate integration was prevented by the poor quality of the spectrum. Full characterisation of the product would require a scale up of the reaction.

Synthesis of [K][Co_2(L)]

To a solution of [Co_2(L)]·THF (20 mg, 0.02 mmol) in THF/d_6-benzene (0.7 mL) was added KC_8 (2.6 mg, 0.019 mmol, 0.9 eq). After 1 h at room temperature, a brown precipitate had formed which dissolved upon addition of d_5-pyridine. The black solid remaining in suspension was filtered.

^{1}H NMR (THF/d_6-benzene, 400.25 MHz): δ_H 7.4 (br), 4.9 (br), -1.8 (br), -2.3 (br), -3.9 (br), -13.2 (br). Full characterisation of the product would require a scale up of the reaction.

Synthesis of [K]$_2$[Co_2(L)]

To a solution of [Co_2(L)]·THF (11 mg, 0.01 mmol) in THF/d_6-benzene (0.7 mL) was added KC_8 (2.8 mg, 0.02 mmol, 2 eq). After 1 h at room temperature, a brown precipitate had formed which dissolved upon addition of d_5-pyridine. The black solid remaining in suspension was filtered.

^{1}H NMR (THF/d_6-benzene, 400.25 MHz): silent. Full characterisation of the product would require a scale up of the reaction.

Oxidation of [K]$_2$[Co_2(L)] by air

A sample of [Co_2(L)]·THF (11 mg, 0.01 mmol) previously reduced by C_8K (2.8 mg, 0.02 mmol, 2 eq) was exposed to air in a THF/d_6-benzene/d_5-pyridine mixture.

^{1}H NMR (THF/d_6-benzene/d_5-pyridine, 400.25 MHz): δ_H 60.0 (br), 34.0 (br), 29.8 (br), 8.7 (br), 7.7 (br), 6.7 (br), 5.9 (br), 4.9 (br), 0.8 (br), -0.6 (br), -2.9 (br), -9.5 (br). Full characterisation of the product would require a scale up of the reaction.

Synthesis of [$Co_2(O_2)$(L)]

[Co_2(L)] was dissolved in benzonitrile (typically to a 1 mM solution, 20 μM for UV-Visible experiment) under nitrogen, freeze-pump-thaw degassed three times and exposed to oxygen. The isolation of [$Co_2(O_2)$(L)] as a solid was prevented by the reversible nature of the binding of oxygen.

^{1}H NMR (benzonitrile/d_6-benzene capillary, 400.25 MHz): mainly NMR silent, a minor paramagnetic compound is observed at δ_H 20.47 (br), 10.14 (br), -2.79 (br), -5.09 (br), -6.59 (br), -7.63 (br), -8.08 (br), -11.39 (br). Large regions are obscured by solvent signals in the aromatic region and impurities in the aliphatic region, and accurate integration was prevented by the poor quality of the spectrum. ^{1}H NMR (benzonitrile/H_6-benzene/d_6-benzene capillary, 400.25 MHz): μ_{eff} = 1.97 B.M. (average over three concordant measures). EPR (benzonitrile, O_2, 100 K): g ~ 2.07, no resolved hyperfine coupling. UV-Vis (benzonitrile, O_2): λ_{max} 358 nm (shoulder, ln ε = 11.36), 449 (10.79).

7.4 Synthetic procedures for Chapter 4

Synthesis of $[Zn_2(L)]$ from diethyl zinc

To a solution of H_4L (1 g, 1.16 mmol) in THF (10 mL) at -78 ºC was added a solution of 1.1 M diethyl zinc in toluene (3.5 mL, 3.85 mmol, 3.3 eq) dropwise, the mixture was allowed to reach room temperature and was heated to reflux for 16 h. The orange suspension was treated with diethyl ether (20 mL) and the supernatant decanted by cannula transfer. The resulting orange solid was washed with diethyl ether (20 mL) and dried under vacuum (0.584 g, 51%).

^{1}H NMR (d_5-pyridine, 500.13 MHz): Broad overlapping resonances in the range 10-0.5 ppm. IR (nujol): ν 1610 (w), 1574 (*C=N*), 1546 (*C=C*) cm^{-1}. UV-Vis (THF, 12 µM): λ_{max} 238 nm (ln ε= 10.59), 266 (10.85), 359 (10.52), 434(10.48). Nano-ESI-MS: 1068 ($[M+82]^+$, <1%, bis-CH_3CN adduct), 1004 ($[M+18]^+$, 2.5%, H_2O adduct), 861 ($[M – 2\ Zn]^+$, 15%, ligand), 803 ($[M - 2\ Zn - 58]^+$, 74%, double Et loss on ligand), 429 ($[(M - 2\ Zn) /2 - 1]^+$, 33%), 413 ($[(M - 2\ Zn) /2 - 17]^+$, 33%, double Me loss on ligand, doubly charged species). Analysis. Found: C, 70.41; H, 4.84; N, 11.23. $C_{58}H_{48}N_8Zn_2$ requires: C, 70.52; H, 4.90; N, 11.34 %.

Synthesis of [K][Zn_2(μ-Cl)(L)]

To a stirred mixture of H_4L (0.200 g, 0.23 mmol) and KH (0.044 g, 1.15mmol, 5eq) at -78 ºC was added THF (10 mL) and the mixture was allowed to reach room temperature. After 4 h, the resulting solution was added dropwise to a solution of $ZnCl_2$ (0.063 g, 0.46 mmol, 2 eq) in THF (1 mL) at room temperature. The red solution turned yellow almost instantly and a solid appeared. The resulting mixture was stirred for 16 h after which it consisted of a thick suspension. Complete filtration was prevented by the very fine solid and NMR data were recorded directly from the liquors.

^{1}H NMR (THF/d_6-benzene, 500.13 MHz): δ_H 8.91 (s, 2H, Ar*H*), 7.67 (br, 4H, imino), 7.64 (br, 2H, Ar*H*), 7.20 (d, 4H, *J* = 8.4 Hz, Ar*H*), 6.84 (t, 4H, *J* = 8.4 Hz, Ar*H*), 6.44 (d, 4H, *J* = 3.3 Hz, pyrrole C*H*), 6.33 (d, 4H, *J* = 6.8 Hz, Ar*H*), 6.08 (d, 4H, *J* = 3.3 Hz, pyrrole C*H*), 2.10 (m, 8H, CH_2), 0.99 (t, 6H, *J* = 6.88 Hz, CH_3), 0.79 (t, 6H, *J* = 7.27 Hz, CH_3). ^{13}C{^{1}H} NMR (THF/d_6-benzene, 125.77 MHz): δ_C 157.15 (s, imino), 155.00 (s, quaternary), 151.16 (s, quaternary), 134.85 (s, quaternary), 131.98 (s, quaternary), 127.07 (s, quaternary), 126.42 (s, *C*H), 125.13 (s, *C*H), 124.99 (s, *C*H), 120.30 (s, C*H*), 117.29 (s, *C*H), 116.7 (s, *C*H),111.42 (s, *C*H), 47.31 (s, *C*H_2), 39.19 (s, *C*H_2), 10.72 (s, *C*H_3) 9.90 (s, *C*H_3) . The resonance for to *meso*-quanternary carbon is obscured by resonances of THF.

Synthesis of [Zn_2(L)] from [Li_4(L)]

A solution of [Li_4(L)] (0.02 g, 0.023 mmol) in THF (0.5 mL) was added to a solution of Zn_2I (0.015 g, 0.048 mmol, 2.1 eq) in THF (0.5 mL) and reacted at room temperature for 16 h. A ^{1}H and ^{7}Li NMR spectra were recorded.

^{1}H NMR (THF/d_6-benzene, 599.81 MHz): overlapping signals in the range 11-0 ppm. ^{7}Li NMR (THF/d_6-benzene, 194.37 MHz): δ_{Li} 0.46 (s, LiI).

Synthesis of [Li][Zn_2(μ-OH)(L)]

A solution of [Zn_2(L)] prepared *in situ* from [Li_4(L)] was exposed to air for 72 h. A ^{1}H NMR spectrum was recorded.

^{1}H NMR (THF/d_6-benzene, 599.81 MHz): δ_H 9.31 (s, Ar*H*), 7.73 (s, imino), 7.64 (s, Ar*H*), 7.26 (m, Ar*H*), 6.95 (m, Ar*H*), 6.45 (m, pyrrole C*H*), 6.34 (m, Ar*H*), 6.20 (m, pyrrole C*H*), 4.55 (br, μ-O*H*), 2.74 (br, *H*$_2$O), 2.55 (m, C*H*$_2$), 2.30 (m, C*H*$_2$), 1.31 (m, C*H*$_3$), 0.95 (m, C*H*$_3$). Signals integration and multiplets analysis were prevented by the poor quality of the spectrum due to decomposition.

Synthesis of [^{n}Bu$_4$N][Zn$_2$(μ-Cl)(L)]

N-tetrabutylammonium chloride (28 mg, 0.1 mmol, 10 eq) was added to a suspension of [Zn$_2$(L)] (10 mg, 0.01 mmol) in d_5-pyridine and the system was allowed to equilibrate for 64 h during which full dissolution of the sample occurred. Quantitative reaction was observed by ^{1}H NMR spectroscopy.

^{1}H NMR (d_5-pyridine, 500.13 MHz): δ_H 9.79 (s, 2H, Ar*H*), 7.89 (s, 4H, imino), 7.83 (s, 2H, Ar*H*), 7.43 (d, 4H, *J* = 8.5 Hz, Ar*H*), 7.07 (m, 4H, Ar*H*), 6.75 (d, 4H, *J* = 3.3 Hz, pyrrole C*H*), 6.53 (d, 4H, *J* = 3.3 Hz, pyrrole C*H*), 6.34 (d, 4H, *J* = 6.8 Hz, Ar*H*), 3.67 (m, free ^{n}Bu$_4$NCl), 2.91 (m, 4H, C*H*$_2$), 2.45 (m, 4H, C*H*$_2$), 1.88 (m, free ^{n}Bu$_4$NCl), 1.41 (t, 6H, *J* = 7.22 Hz, C*H*$_3$), 1.34 (m, free ^{n}Bu$_4$NCl), 1.12 (t, 6H, *J* = 7.53 Hz, C*H*$_3$), 0.88 (t, *J* = 7.3 Hz, free ^{n}Bu$_4$NCl). Resonances of the [^{n}Bu$_4$N]$^+$ counter cation of [Zn$_2$(μ-Cl)L]$^-$ overlap with the resonances for free ^{n}Bu$_4$NCl. UV-Vis (THF, 12 μM): λ_{max} 257 nm (ln ε= 11.24), 359 (10.52), 434(10.48).

Synthesis of [N(^{n}Bu)$_4$][Zn$_2$(*μ*-OH)(L)]

Solid ^{n}Bu$_4$NOH·30H$_2$O (74 mg, 0.09 mmol) was added to a suspension of [Zn$_2$(L)] (50 mg, 0.05 mmol) in THF (5 mL) at room temperature and the mixture stirred for 48 h during which full dissolution of the solids occurred. The solvent volume was reduced to 0.5 mL under reduced pressure, diethyl ether (20 mL) was added and the orange precipitate that formed was isolated, washed with diethyl ether (5 mL) and dried under vacuum to yield [^{n}Bu$_4$N][Zn$_2$(μ-OH)(L)] as an orange solid (37 mg, 57%).

^{1}H NMR (599.81 MHz, THF/d_6-benzene): δ_H 9.28 (s, 2H, Ar*H*), 7.70 (s, 4H, imino), 7.60 (s, 2H, Ar*H*), 7.21 (d, 4H, *J* = 8.4 Hz, Ar*H*), 6.91 (m, 4H, Ar*H*), 6.40 (d, 4H,

J = 3.3 Hz, pyrrole C*H*), 6.32 (d, 4H, *J* = 6.7 Hz, Ar*H*), 6.14 (d, 4H, *J* = 3.3 Hz, pyrrole C*H*), 2.81 (br, 15H, $^{n}Bu_4N$), 2.49 (m, 4H, CH_2), 2.25 (m, 4H, CH_2), 1.26 (t, 6H, *J* = 7.2 Hz, CH_3), 1.09 (br m, 40H, $^{n}Bu_4N$), 0.89 (t, 6H, *J* = 7.3 Hz, CH_3), 0.67 (br m, 52H, $^{n}Bu_4N$). Over time, [$^{n}Bu_4N$][Zn_2(μ-OH)(L)] reacts with water (solvent of crystallization from $^{n}Bu_4NOH{\cdot}30H_2O$ or from the atmosphere) and de-metallation of the complex occurs. This prevented the isolation of a high purity sample of [$^{n}Bu_4N$][Zn_2(μ-OH)(L)] and repeated attempts at obtaining satisfactory elemental analytical data proved unsuccessful.

7.5 Synthetic procedures for Chapter 5

Synthesis of [$(ZrCl_2)_2$(L)] from [K_4(L)]

In an NMR tube, [K_4(L)] was generated *in situ* by reacting H_4L (20 mg, 0.023 mmol) and KH (5 mg, 0.125 mmol, 5.4 eq) in THF/d_6-benzene, the sample was freeze-pump-thaw degassed and [$ZrCl_4(THF)_2$] (11 mg, 0.047 mmol, 2 eq) was added to the reaction mixture. The ^{1}H NMR spectrum of the orange solution formed was recorded immediately.

^{1}H NMR (THF/d_6-benzene, 500.13 MHz): δ_H 10.70 (s, 1H, Ar*H*), 8.96 (s,1H, Ar*H*), 8.18 (s, 2H, imino), 8.14 (s, 2H, imino), 7.93 (s, 2H, Ar*H*), 7.59 (d, 2H, *J* = 8.4 Hz, Ar*H*), 7.51 (d, 2H, *J* = 8.5 Hz, Ar*H*), 7.39 (d, 2H, *J* = 6.9 Hz, Ar*H*), 7.26 (m, 3H, Ar*H*), 7.14 (m, 2H, Ar*H*), 6.83 (d, 2H, *J* = 3.7 Hz, pyrrole C*H*), 6.70 (d, 3H, *J* = 7.0 Hz, Ar*H*), 6.56 (d, 2H, *J* = 3.2 Hz, pyrrole C*H*), 6.29 (d, 2H, *J* = 3.7 Hz, pyrrole C*H*), 6.02 (d, 2H, *J* = 3.3 Hz, pyrrole C*H*), 2.23 (m, 2H, CH_2), 2.13 (m, 2H, CH_2), 2.02 (m, 2H, CH_2), 1.94 (m, 2H, CH_2), 1.00 (t, 3H, *J* = 7.2 Hz, CH_3), 0.95 (t, 3H, *J* = 7.2 Hz, CH_3), 0.71 (t, 3H, *J* = 7.0 Hz, CH_3), 0.53 (t, 3H, *J* = 7.4 Hz, CH_3).

Synthesis of [$(ZrCl_2)_2$(L)] from [Li_4(L)]

To a stirred mixture of H_4L (0.200 g, 0.23 mmol) and LiN" (0.156 g, 0.93 mmol, 4.1 eq) at -78 ºC was added THF (5 mL) and the mixture was allowed to reach room temperature. After 4 h, the resulting solution was added dropwise to a

suspension of $[ZrCl_4(THF)_2]$ (0.175 g, 0.47 mmol, 2 eq) in THF (2 mL) at -78 ºC, the resulting mixture was allowed to reach room temperature slowly and was stirred for 16 h. The deep orange solution was evaporated to 3 mL under reduced pressure, diethyl ether was added and the mixture was stored at 0 ºC to afford $[(ZrCl_2)_2(L)]$ as an orange precipitate (30 mg, 11%). ^{1}H NMR (THF/d_6-benzene, 499.81 MHz): δ_H 8.77 (s, 2H, Ar*H*), 8.34 (s, 2H, Ar*H*), 8.04 (s, 4H, imino), 7.75 (d, 4H, *J* = 8.6 Hz, Ar*H*), 7.46 (m, 4H, Ar*H*), 7.34 (d, 4H, *J* = 6.9 Hz, Ar*H*), 6.92 (d, 4H, *J* = 3.7 Hz, pyrrole C*H*), 6.33 (d, 4H, *J* = 3.7 Hz, pyrrole C*H*), 2.17 (q, 4H, *J* = 7.3 Hz, CH_2), 2.13 (q, 4H, *J* = 7.4 Hz, CH_2), 0.79 (t, *J* = 7.2 Hz, CH_3), 0.74 (t, *J* = 7.3 Hz, CH_3). IR (nujol): ν 1651 (C=N), 1610 (*C=N*), 1555 (*C=C*), 1504 (w) cm^{-1}. Analysis. Found: C, 58.80; H, 4.18; N, 9.60. $C_{58}H_{48}N_8Zr_2Cl_4$ requires: C, 58.97; H, 4.10; N, 9.49 %.

Attempted synthesis of $[Zr(NMe_2)_2(H_2L)]$

To a solution of H_4L (100 mg, 0.12 mmol) in THF (20 mL) was added dropwise a solution of $Zr(NMe_2)_4$ (31 mg, 0.12 mmol, 1 eq) in THF (20 mL) at -78 ºC, the mixture was allowed to reach room temperature and was reacted for 16 h. An aliquot was taken and ^{1}H NMR spectrum was recorded.

^{1}H NMR (THF/d_6-benzene, 599.81 MHz): δ_H 9.50 (s, N*H*), 8.71 (s, Ar*H*), 8.27 (s, imino), 8.07 (s, imino), 7.95 (s, Ar*H*), 7.70 (d, Ar*H*), 7.62 (d, Ar*H*), 7.43 (d, Ar*H*), 7.32 (m, Ar*H*), 7.24 (m, Ar*H*), 6.92 (d, pyrrole C*H*), 6.67 (d, Ar*H*), 6.57 (d, pyrrole C*H*), 6.35 (d, pyrrole C*H*), 6.03 (d, pyrrole C*H*), 2.27 (m, CH_2), 2.19 (m, CH_2), 2.09 (m, CH_2), 2.03 (m, CH_2), 0.72 (t, CH_3), 0.60 (t, CH_3). A set of resonances corresponding to free ligand was also observed, two of the CH_3 resonances are obscured by the CH_3 resonance of the free ligand. Superimposition of signals prevented the proper integration of the signals and the accurate measurement of the coupling constants; as such the present interpretation is qualitative.

Attempted synthesis of [(Zr{NMe_2}$_2$)$_2$(L)]

To the solution of [$Zr(NMe_2)_2(H_2L)$] prepared *in situ* as detailed above was added a solution of $Zr(NMe_2)_4$ (31 mg, 0.12 mmol, 1 eq) in THF (20 mL) at -78 ºC, the mixture was allowed to reach room temperature and was reacted for 40 h. Concentration of the liquors under reduced pressure induced crystallisation and [(Zr{NMe_2}$_2$)$_2$(L)] was isolated as an orange microcrystalline solid (40 mg, 22%)
^{1}H NMR (THF/d_6-benzene, 400.25 MHz): δ_H 9.28 (s, 1H, Ar*H*), 8.90 (s, 1H, Ar*H*), 8.30 (s, 1H, Ar*H* or imino), 8.08 (s, 1H, Ar*H* or imino), 7.98 (s, 1H, Ar*H* or imino), 7.87 (d, 1H, *J* = 8.5 Hz, Ar*H*), 7.80 (s, 1H, Ar*H* or imino), 7.68 (s, 1H, Ar*H* or imino), 7.54 (m, 1H, Ar*H*), 7.48 (d, 1H, *J* = 8.4 Hz, Ar*H*), 7.38 (d, 1H, *J* = 8.4 Hz, Ar*H*), 7.24 (s, 1H, Ar*H*), 7.13 (m, 3H, Ar*H*), 7.03 (d, 1H, *J* = 3.8 Hz, pyrrole C*H*), 6.86 (m, 2H, pyrrole C*H* and Ar*H*), 6.74 (m, 3H, pyrrole C*H* and Ar*H*), 6.47 (t, 1H, *J* = 7.8 Hz, Ar*H*), 6.32 (d, 1H, *J* = 3.8 Hz, pyrrole C*H*), 6.28 (d, 1H, *J* = 6.7 Hz, Ar*H*), 6.26 (d, 1H, *J* = 3.7 Hz, pyrrole C*H*), 6.14 (d, 1H, *J* = 3.6 Hz, pyrrole C*H*), 5.76 (d, 1H, *J* = 3.1 Hz, pyrrole C*H*), 5.60 (d, 1H, *J* = 2.3 Hz, pyrrole C*H*), 5.35 (d, 1H, *J* = 7.2 Hz, Ar*H*), 0.80 (t, 3H, *J* = 7.2 Hz, CH_3), 0.66 (t, 3H, *J* = 7.4 Hz, CH_3), 0.47 (t, 3H, *J* = 7.2 Hz, CH_3), 0.38 (t, 3H, *J* = 7.2 Hz, CH_3). The ethyl-CH_2 and the Zr(NCH_3)signals are obscured by the THF suppressed resonances. Analysis. Found: C, 42.96; H, 2.69; N, 5.43. $C_{62}H_{60}N_{10}Zr_2$ requires: C, 65.20; H, 5.97; N, 13.82 %.

Reduction of [($ZrCl_2$)$_2$(L)]

To a solution of [($ZrCl_2$)$_2$(L)] (13 mg, 0.011 mmol) (generated from [Li_4(L)]) in THF/d_6-benzene in a Youngs-tapped NMR tube was added C_8K (7 mg, 0.046 mmol, 4.2 eq). The solution turned darker orange and a black solid formed, consistent with the generation of graphite. A ^{1}H NMR spectrum was recorded.
^{1}H NMR (THF/d_6-benzene, 499.81 MHz): δ_H 8.85 (s, Ar*H*), 7.97 (s, imino), 7.75 (s, Ar*H*), 7.45 (d, *J* = 8.5 Hz, Ar*H*), 7.12 (m, Ar*H*), 7.01 (d, *J* = 6.8 Hz, Ar*H*), 6.60 (d, *J* = 3.5 Hz, pyrrole C*H*), 6.05 (d, *J* = 3.4 Hz, pyrrole C*H*), 2.03 (q, *J* = 7.1 Hz, CH_2), 1.96 (q, *J* = 6.8 Hz, CH_2), 0.68 (m, CH_3), 0.61 (t, *J* = 7.2 Hz, CH_3). Only the resonances corresponding to the main product are reported, the presence

of minor diamagnetic products prevented the accurate integration of the signals.

Synthesis of $[(ZnCl_2)_2(H_4L)]$

To a suspension of H_4L (0.300 g, 0.35 mmol) in THF was added $ZnCl_2$ (0.150g, 1.10 mmol, 3.1 eq). A bright orange precipitate formed instantly and the reaction mixture was stirred at room temperature for 5 h. The supernatant was decanted by cannula transfer, the product was washed twice with THF and dried under vacuum (197 mg, 50%).

^{1}H NMR (d_5-pyridine, 250.13 MHz): δ_H 12.00 (s, 4H, N*H*), 9.90 (s, 2H, Ar*H*), 8.48 (s, 4H, imino), 8.45 (s, 2H, Ar*H*), 7.85 (d, 4H, *J* = 8.6 Hz, Ar*H*), 7.43 (t, 4H, *J* = 7.7 Hz, Ar*H*), 7.02 (s, 2H pyrrole C*H*), 6.96 (d, 4H, *J* = 7.1 Hz, Ar*H*), 6.40 (s, 4H, pyrrole C*H*), 2.33 (m, 8H, , *J* = 7.3Hz, CH_2), 0.91 (t, 12H, *J* = 7.1 Hz, CH_3). IR (nujol): ν 3167 (br, N-H), 3118 (br, N-H), 1651(*C=N*), 1616 (*C=N*), 1576 (*C=N*), 1554 (*C=C*), 1538 (C=C) cm^{-1}. UV-Vis (pyridine, 5 μM): λ_{max} 327 nm (ln ε = 11.96), 419 (11.34). Analysis. Found: C, 70.41; H, 4.84; N, 11.23. $C_{58}H_{48}N_8Zn_2$ requires: C,70.52; H, 4.90; N, 11.34 %

Synthesis of $[(MX_2)_2(H_4L)]$ (MX_2 = $MnCl_2$, $FeBr_2$, $NiCl_2$, $CuCl_2$)

Complexes of formula $[(MX_2)_2(H_4L)]$ were prepared on small scale (0.023 mmol) from $MnCl_2$, $[FeBr_2(THF)_2]$, $[NiCl_2(DME)_2]$ and $CuCl_2$ following the procedure described for $[(ZnCl_2)_2(H_4L)]$. Obvious colour changes were observed and NMR silent samples were obtained for all metals other than iron for which a few resonances were observed.

$[(FeBr_2)_2(H_4L)]$: ^{1}H NMR (THF/d_6-benzene, 500.13 MHz): δ_H 35.36 (s), -8.90 (s). Some resonances might be obscured by the THF suppressed signals, others cannot be observed due to the paramagnetic nature of the sample.

7.6 Analytic procedures

Magnetic measurement by the Evans method

Three samples of [Co_2(L)] (2 mg, 1 mg and 4.3 mg respectively) were dissolved in a mixture of 10:1 THF/d_6-benzene and resulted in samples of 1.6008 g, 0.6151 g and 4.0201g respectively. The ^{1}H NMR spectrum of each sample was recorded in the presence of a H_6-benzene capillary and the chemical shift separation Δ_{ppm} between the d_6-benzene resonance and the H_6-benzene resonance was measured. A similar experiment was carried out in benzonitrile/tetramethylsilane.

^{1}H NMR (THF/d_6-benzene, 599.81 MHz): Δ_{ppm} 0.467, 0.474 and 0.464 respectively, μ_{eff} = 3.55 B.M. ^{1}H NMR (benzonitrile/TMS, 400.25 MHz): μ_{eff} = 1.69 B.M.

Typical cyclic voltametry (CV) procedure

Cyclic voltammograms were recorded in a 1 mM [Co_2(L)] solution in benzonitrile with ^{n}BuN_4BF_4 (0.2 M) as an electrolyte under nitrogen. Voltammograms were recorded at scan rates in the range 25 mV.s^{-1} to 1 V.s^{-1}.

Typical catalytic measurement by rotating ring disk electrode (RRDE) experiment

RRDE experiments were recorded in an air saturated 1 M aqueous TFA solution. The platinum ring was held at +1.00 V versus Ag/AgCl and the ring-disk assembly was rotated in the range 100 rpm to 1000 rpm; voltammograms were recorded at 50 mV.s^{-1}. Before each experiment, the glassy carbon disk was cleaned with methanol, polished with an alumina 5 μm suspension, sonicated in distilled water, rinsed with methanol, and dried. The disk was drop coated using a freshly made solution of [Co_2(L)] in THF.

Typical catalytic measurement by UV-Vis[10]

A 1.0 mM [Co_2(L)] solution, a 0.3 M TFA solution and a 0.3 M ferrocene solution were initially prepared under nitrogen. The [Co_2(L)] solution was freeze-pump-thaw

degassed three times and placed under oxygen (in this solution: $[O_2]$ = 8.5 mM). The catalytic medium was made up using the three solutions cited above and diluting with oxygen or nitrogen saturated benzonitrile to reach the concentrations required. For example, 0.6 mL of the $[Co_2(L)]$ solution, 1.0 mL of the ferrocene solution and 0.4 mL of nitrogen saturated benzonitrile were placed in a UV-Vis quartz cell fitted with an air-tight screw cap with a septum top. At t = 0 s, 1.0 mL of the TFA solution was added through the septum affording an initial 3 mL reaction mixture with the following concentrations: $[Co_2(L)]$ = 0.2 mM, [TFA] = 0.1 M, [Fc] = 0.1 M and $[O_2]$ = 1.7 mM. The mixture was shaken to homogenise and the formation of ferrocenium was monitored over time at 620 nm (where $\varepsilon_{max}(Fc^+) = 330\ M^{-1}.cm^{-1}$).

H_2O_2 titration

A sample (5 μL) of the catalytic reaction mixture was degassed to stop the reaction and diluted with nitrogen-saturated benzonitrile (3 mL). NaI (5 mg, large excess) was added and the formation of I_3^- was monitored by UV-vis at λ_{max} = 365 nm ($\varepsilon_{max} = 28000\ M^{-1}.cm^{-1}$).

^{1}H NMR spectroscopic dilution experiments and titrations

The dilution experiment was carried out using a 5 mM sample of $[Zn_2(L)]$ in dry d_8-THF with successive dilutions down to 0.1 mM. To ensure a suitable signal-to-noise, the number of scans was increased accordingly. NMR titrations were carried out in THF with double presaturation by the addition of an *ca.* 1mM $[Zn_2(L)]$ and *ca.* 12 mM $^nBu_4N.Cl$ solution to an *ca.* 1mM $[Zn_2(L)]$ solution, or in d_5-pyridine by addition of an *ca.* 17 mM $[Zn_2(L)]$ and *ca.* 195 mM $^nBu_4N.Cl$ solution to an *ca.* 16 mM $[Zn_2(L)]$ solution (in each case, the highest concentration was limited by the solubility of $[Zn_2(L)]$).

Microcalorimetric titration

Titrations were carried out by the automated sequential addition of the salt solution to a $[Zn_2(L)]$ solution at 298 K, with the help of Nathan Bill and Prof. Jonathan Sessler of the University of Texas, Austin. Extensive efforts were made to exclude moisture from the sample as this could both decompose the binuclear zinc complex and weaken the receptor-anion interactions. Host solutions were prepared under argon atmosphere in a glove box at least 16 h in advance to allow full dissolution, stored under argon and used within 24 h of opening. The guest samples were also prepared with dry solvents and used within 12 h. For each anion investigated, at least three concordant titrations were carried out with different host and guest concentrations.

UV-Vis dilution experiment and titration attempts

The dilution experiment was carried out using a 400 μM sample of $[Zn_2(L)]$ in dry THF with successive dilutions down to 1 μM. The feasibility of a titration was assessed by recording the spectra in dry THF of *ca.* 6 μM $[Zn_2(L)]$ and *ca.* 9 μM $^{n}Bu_4N.Cl$ solution and of *ca.* 6 μM $[Zn_2(L)]$. The spectra obtained were consistent with those described in the synthetic procedures for $[^{n}Bu_4N][Zn_2(\mu\text{-}Cl)(L)]$ and $[Zn_2(L)]$ respectively.

Fluorescence dilution experiment and titration attempts

The dilution effect was studied by comparison of the spectra recorded with 400, 40 and 6 μM solutions of $[Zn_2(L)]$ in THF. For each sample, a range of spectra were recorded. Emission spectra were recorded for excitation wavelengths $350 \leq \lambda_{ex} \leq 570$ nm. Excitation spectra were recorded for emission wavelengths $460 \leq \lambda_{em} \leq 520$ nm. Fluorescence titrations were carried out in THF either by the addition of *ca.* 6 μM $[Zn_2(L)]$ and *ca.* 500 μM $^{n}Bu_4N.Cl$ solution to *ca.* 6 μM $[Zn_2(L)]$ solution or by the addition of *ca.* 0.6 μM $[Zn_2(L)]$ and *ca.* 50 μM $^{n}Bu_4N.Cl$ solution to *ca.* 0.6 μM $[Zn_2(L)]$ solution. Emission spectra were recorded

for λ_{ex} = 410 nm for which the emission is maximal (maximal emission seen at λ_{em} = 520 nm); excitation spectra were recorded for λ_{em} = 520 nm.

7.7 DFT calculations

DFT calculations were carried out by Dr P. Richardson. Initial structures of the [Zn_2(L)] and [Zn_2(L)]:anion complexes were built using ArgusLab[11], based on the crystal structure of the binuclear palladium complex [Pd_2(L)], and used as starting points for unconstrained geometry optimisations. The absence of imaginary frequencies was used to confirm that each calculated structure was a minimum on the molecular potential energy surface. All calculations were carried out using Gaussian09,[12] running under Linux. Geometry optimisations and binding energy calculations were conducted at several levels of theory. The M05-2X functional of Zhao and Truhlar,[13] in combination with the LANL2DZ[14] basis set gave the most satisfactory results. Bulk solvent interactions were modelled via the self-consistent reaction field (SCRF) using the polarisable continuum model (PCM),[15] employing the default parameters for THF within Gaussian 09.

Ligand-anion binding energies were calculated using:

ΔE = E[[Zn2(μ-X)(L)] + ZPE] - E[[Zn2(L)] + ZPE] - E[(X)] + BSSE

where E[Zn2(μ-X)(L)] is the energy of the solvated host:guest complex, E[Zn2(L)] is the energy of the solvated complex alone, E[X] is the energy of the solvated anionic species, and the ZPE are the appropriate zero-point energy corrections for each component. The counterpoise method of Boys and Bernardi[16] was employed to correct for basis set superposition errors (BSSE) in the calculated binding energies, arising as a consequence of the incompleteness of the basis set.

7.8 Crystallographic details

X-Ray diffraction data for H_4L, [Mg_2(L)], [Pd_2(L)], [Fe_2(μ-O)(L)], [K][Zn_2(μ-Cl)(L)] and [^{n}Bu_4N][Zn_2(μ-OH)(L)] were collected at 150 K on a Bruker SMART APEX diffractometer equipped with a CCD detector using graphite monochromated using Mo Kα radiation (λ= 0.71073 Å). The data from

single crystals of $[Co_2(exo\text{-}THF)_2(L)][Co_2(L)]$ were collected at 93.15 K using graphite monochromated Mo Kα radiation (λ = 0.71073 Å) on a Rigaku MM007 diffractometer equipped with a high brilliance Saturn 70 CCD detector. X-Ray diffraction data on the two sets of single crystals of $[Co_2(exo\text{-}py)_2(L)]$ and $[Co_2(O_2H_3)(exo\text{-}py)_2(L)][BF_4]$ were collected at 100 K using an Oxford Cryosystems low temperature device attached to an Oxford Diffraction SuperNova dual wavelength diffractometer equipped with an Atlas CCD detector and operating mirror monochromated Cu*K*α radiation mode (λ = 1.54184Å). Details of the individual data collections and refinements are given in **Appendix 2**. The structures were solved by direct methods (for H_4L, $[Pd_2(L)]$, $[K(THF)_6][Zn_2(\mu\text{-}Cl)(L)]$, $[Li(THF)_4][Zn_2(\mu\text{-}OH)(L)]$, $[^nBu_4N][Zn_2(\mu\text{-}OH)(L)]$) or using SUPERFLIP[17] (for $[Mg_2(L)]$, $[Fe_2(\mu\text{-}O)(L)]$, $[Co_2(THF)_2(L)][Co_2(L)]$, $[Co_2(py)_2(L)]$, $[Co_2(O_2H_3)(py)_2(L)]$, $[Li(THF)_4][ZrCl_5(THF)]$) within the WinGX program suite[18] and refined using full-matrix least square refinement on $|F|^2$ using SHELXL-97.[19] Unless otherwise stated, all non-hydrogen atoms were refined with anisotropic displacement parameters and all hydrogen atoms were placed at calculated positions and were included as part of a riding model. The solvent of crystallisation in H_4L was diffuse and could not be modelled accurately so the corresponding electron density was accounted for using the SQUEEZE routine of PLATON. Three voids were found which equated to 2 molecules of CH_2Cl_2 and 6.5 molecules of methanol in the unit cell. In the asymmetric unit of the structure of $[Pd_2(L)]$, one molecule of chloroform was disordered about an inversion centre and what appeared to be one molecule of disordered triethylamine was modelled using the SQUEEZE routine of PLATON. Two distinct voids were found within the unit cell with electron density appropriate for one molecule of NEt_3 per asymmetric unit. In the structure of $[Fe_2(\mu\text{-}O)(L)]$, hexane solvent molecules located on the 3-fold axis were diffuse and disordered. The use of the SQUEEZE routine of PLATON revealed 3 voids located along the 3-fold axis in the unit cell with a total solvent accessible volume of 2091.4 $Å^3$ and 141 electrons for each void. This was attributed to 8.5 molecules of hexane per unit cell (which require 50 electrons each). The refinement was much more stable after modelling with SQUEEZE. In the structure of $[Co_2(exo\text{-}THF)_2(L)][Co_2(L)]$, some crystallisation toluene molecules

were disordered and some of their carbon atoms (C3A3 and C3B3, C4A3 and C4B3, C4A2 and C4B2) were refined using an isotropic model. In the structure of $[Co_2(O_2H_3)(exo\text{-}py)_2(L)][BF_4]$, the hydrogen atom of the hydroxyl hydrate anion H100 and H101 were located using a 2-site free-variable refinement procedure and refined with fixed thermal parameters. The structure presents a disordered pyridine solvent molecule on the 2-fold axis which was refined using an isotropic model. In each unit cell, two BF_4 units could not be located and the structure exhibits large diameter channels along the c axis. The use of the SQUEEZE routine of PLATON revealed voids located within the channels with a total solvent accessible volume of 1432.5 $Å^3$ and 422 electrons in the unit cell. This was attributed to two tetrafluoroborate unit (which require 41 electrons each) and 8 diffuse pyridine molecules (which require 42 electrons each) in the asymmetric unit. The refinement was much more stable after modelling with SQUEEZE. The bridging hydroxyl hydrogen atom H900 in the structure of $[Li(THF)_6][Zn_2(\mu\text{-}OH)(L)]$ and H001 in $[^nBn_4N][Zn_2(\mu\text{-}OH)(L)]$ were located using a 2-site free-variable refinement procedure and refined with fixed thermal parameters.

7.9 Bibliography

1 J. Lahaye and R. Lagarde, *J. Catal.*, 1979, **60**, 270.

2 D. C. Bradley and I. M. Thomas, *J. Chem. Soc. (Resumed)*, 1960, 3857.

3 M. Volpe, H. Hartnett, J. W. Leeland, K. Wills, M. Ogunshun, B. J. Duncombe, C. Wilson, A. J. Blake, J. McMaster, and J. B. Love, *Inorg. Chem.*, 2009, **48**, 5195.

4 A. Dahan, T. Ashkenazi, V. Kuznetsov, S. Makievski, E. Drug, L. Fadeev, M. Bramson, S. Schokoroy, E. Rozenshine-Kemelmakher, and M. Gozin, *J. Org. Chem.*, 2007, **72**, 2289; J. L. Sessler, T. D. Mody, D. A. Ford, and V. Lynch, *Angew. Chem., Int. Ed. Engl.*, 1992, **31**, 452.

5 C.-Z. Zhang, H. Yang, D.-L. Wu, and G.-Y. Lu, *Chin. J. Chem.*, 2007, **25**, 653.

6 A. J. Caruso and J. L. Lee, *J. Org. Chem.*, 1997, **62**, 1058.

7 J. Herwig, H. Bohnen, P. Skutta, S. Sturm, P. W. N. M. Van Leeuwen, and R. Bronger, in 'Novel diphosphines and method for their production', 2002.

8 S. Xavier, J. G. S. Eduardo, F. Zoraida, B.-B. Jordi, and P. W. N. M. van Leeuwen, *Eur. J. Org. Chem.*, 2008, **2008**, 6197.

9 M.-Y. Song, H.-K. Na, E.-Y. Kim, S.-J. Lee, K. I. Kim, E.-M. Baek, H.-S. Kim, D. K. An, and C.-H. Lee, *Tetrahedron Lett.*, 2004, **45**, 299; E. Askarizadeh, A. M. J. Devoille, D. M. Boghaei, A. M. Z. Slawin, and J. B. Love, *Inorg. Chem.*, 2009, **48**, 7491.
10 S. Fukuzumi, K. Okamoto, C. P. Gros, and R. Guilard, *J. Am. Chem. Soc.*, 2004, **126**, 10441.
11 M. A. Thompson, in 'ArgusLab 4.0.1', Seattle, WA.
12 M. J. Frisch, G. W. Trucks, H. B. Schlegel, G. E. Scuseria, M. A. Robb, J. R. Cheeseman, G. Scalmani, V. Barone, B. Mennucci, G. A. Petersson, H. Nakatsuji, M. Caricato, X. Li, H. P. Hratchian, A. F. Izmaylov, J. Bloino, G. Zheng, J. L. Sonnenberg, M. Hada, M. Ehara, K. Toyota, R. Fukuda, J. Hasegawa, M. Ishida, T. Nakajima, Y. Honda, O. Kitao, H. Nakai, T. Vreven, J. A. Montgomery Jr., J. E. Peralta, F. Ogliaro, M. Bearpark, J. J. Heyd, E. Brothers, K. N. Kudin, V. N. Staroverov, R. Kobayashi, J. Normand, K. Raghavachari, A. Rendell, J. C. Burant, S. S. Iyengar, J. Tomasi, M. Cossi, N. Rega, N. J. Millam, M. Klene, J. E. Knox, J. B. Cross, V. Bakken, C. Adamo, J. Jaramillo, R. Gomperts, R. E. Stratmann, O. Yazyev, A. J. Austin, R. Cammi, C. Pomelli, J. W. Ochterski, R. L. Martin, K. Morokuma, V. G. Zakrzewski, G. A. Voth, P. Salvador, J. J. Dannenberg, S. Dapprich, A. D. Daniels, Ö. Farkas, J. B. Foresman, J. V. Ortiz, J. Cioslowski, and D. J. Fox, in 'Gaussian 09', 2009.
13 Y. Zhao, N. E. Schultz, and D. G. Truhlar, *J. Chem. Theory Comput.*, 2006, **2**, 364.
14 P. J. Hay and W. R. Wadt, *J. Chem. Phys.*, 1985, **82**, 299; P. J. Hay and W. R. Wadt, *J. Chem. Phys.*, 1985, **82**, 284; P. J. Hay and W. R. Wadt, *J. Chem. Phys.*, 1985, **82**, 270.
15 S. Miertus, E. Scrocco, and J. Tomasi, *Chem. Phys.*, 1981, **55**, 117.
16 S. F. Boys and F. Bernadi, *Mol. Phys.*, 1970, **19**, 533.
17 L. Palatinus and G. Chapuis, *J. Appl. Crystallogr.*, 2007, **40**, 786.
18 L. Farrugia, *J. Appl. Crystallogr.*, 1999, **32**, 837.
19 G. Sheldrick, *Acta Crystallogr., Sect. A*, 2008, **64**, 112.

Appendix 1 – ^{1}H NMR spectra of H_4L and $[Pd_2(L)]$

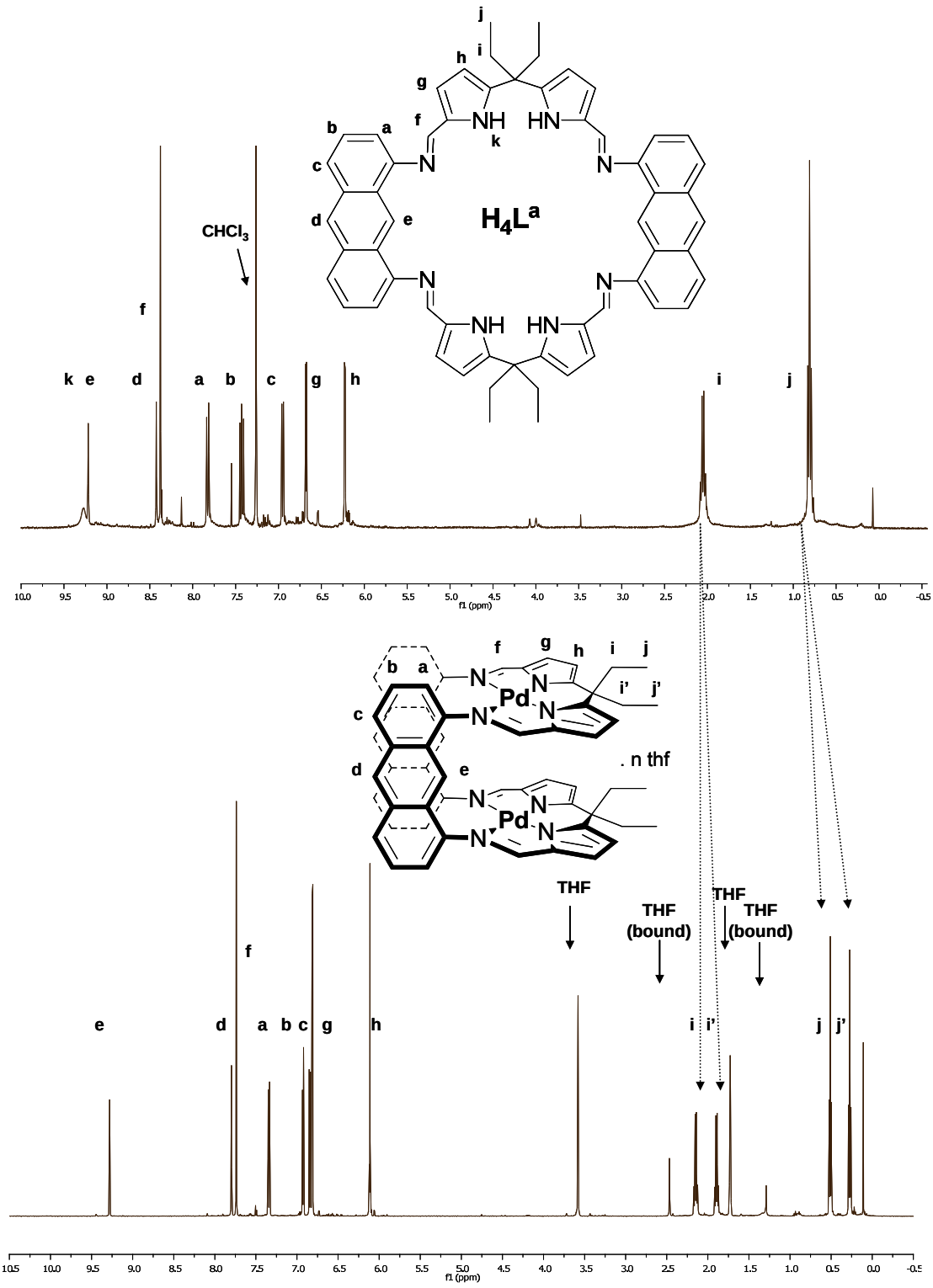

Figure A1.1 : ^{1}H NMR spectra of H_4L in d-chloroform (top) and [Pd_2(L)] in THF/d_6-benzene (bottom) showing the splitting of the ethyl resonances, characteristic of a Pacman arrangement.

Appendix 2 – Crystal data for H_4L and its bimetallic cofacial complexes

	$H_4L.(CH_2Cl_2)_2.(CH_3OH)_{6.5}$	$[Mg_2(endo\text{-}Py)(endo\text{-}Py)_2(L)].5Py$	$[Pd_2(L)].(NEt_3).(CHCl_3)$
Cell setting, space group	Monoclinic, *P-1*	Triclinic, *P*-1	Monoclinic, *C* 2/*c*
a , *b* , *c* (Å)	13.6736 (3), 15.7991 (4), 16.2295 (4)	14.6535 (3), 15.5131 (3), 20.1732 (4)	12.453 (3), 24.437 (6), 19.712 (5)
α, β, γ (°)	71.049 (1), 87.508 (2), 72.914 (1)	67.706 (1), 69.500 (1), 81.902 (1)	90, 103.965 (5), 90
V (Å^3)	3164.44 (13)	3974.14 (14)	5822 (2)
Z	2	2	4
D_x (Mg m^{-3})	1.101	1.286	1.472
Crystal size (mm)	0.53 × 0.33 × 0.24	0.41 × 0.16 × 0.10	0.20 × 0.10 × 0.10
Absorption correction	Multi-scan	Multi-scan	Multi-scan
T_{min}	0.942	0.662	0.701
T_{max}	0.965	0.745	1
No. of measured, independent and observed reflections	80872, 17650, 14732	63282, 16038, 11007	23819, 5241, 4687
θ_{max} (°)	30.5	26.2	25.5
$R[F^2 > 2\sigma(F^2)]$, $wR(F^2)$, *S*	0.109, 0.281, 0.93	0.056, 0.149, 1.02	0.071, 0.200, 1.09
No. of parameters	598	1071	348
H-atom treatment	Riding	Riding	Mixture of independent and constrained refinement
Δr_{max}, Δr_{min} (e Å^{-3})	0.68, −0.32	0.61, −0.60	0.78, –0.98

Table A2.1 : Crystal data for H_4L and its bimetallic cofacial complexes.

	$[Fe_2(\mu\text{-}O)(L)].0.5Hex$	$[Co_2(exo\text{-}THF)_2(L)][Co_2(L)].Tol$	$[Co_2(exo\text{-}Py)_2(L)]$
Cell setting, space group	Trigonal, *R*-3	Triclinic, *P*-1	Monoclinic, $P\,1_2 1/c\,1$
a , *b* , *c* (Å)	27.2173 (5), 27.2173 (5), 39.3148 (8)	15.777 (8), 19.297 (9), 21.128 (11)	13.2413 (7), 27.2716 (10), 16.2006 (8)
α, β, γ (°)	90, 90, 120	108.942 (8), 110.955 (5), 90.469 (7)	90, 111.900 (6), 90
V (Å^3)	25221.8 (8)	5625 (5)	5428.0 (4)
Z	18	1	4
D_x (Mg m^{-3})	1.167	1.372	1.315
Crystal size (mm)	0.47 × 0.46 × 0.44	0.20 × 0.10 × 0.05	0.22 × 0.18 × 0.03
Absorption correction	Multi-scan	Multi-scan	Analytical
T_{min}	0.778	0.723	0.394
T_{max}	0.79	1	0.86
No. of measured, independent and observed reflections	82342, 11527, 9990	57646, 20434, 17081	50956, 10785, 3945
θ_{max} (°)	26.5	25.4	77.7
$R[F^2 > 2\sigma(F^2)]$, $wR(F^2)$, *S*	0.041, 0.112, 1.05	0.075, 0.215, 1.07	0.431, 0.793, 2.64
No. of parameters	627	1498	249
H-atom treatment	Riding	Riding	Mixture of independent and constrained refinement
Δr_{max}, Δr_{min} (e Å^{-3})	0.68, −0.24	0.98, −0.88	10.81, −3.32

Table A2.1 : Crystal data for H_4L and its bimetallic cofacial complexes.

	$[Co_2(exo\text{-}Py)_2(L)].4THF$	$[Co_2(O_2H_3)(exo\text{-}Py)_2(L)][BF_4].1.8Py$	$[K(THF)_6][Zn_2(\mu\text{-}Cl)(L)].2THF$
Cell setting, space group	Monoclinic, $P2_1/n$	Hexagonal, $P\text{-}3C1$	Monoclinic, $P2_1/n$
a, b, c (Å)	14.9616 (3), 16.2706 (3), 28.8075 (6)	27.5796 (4), 27.5796 (4), 15.5052 (3)	13.7180 (5), 23.2233 (8), 26.1448 (9)
α, β, γ (°)	90, 91.944 (2), 90	90, 90, 120	90, 100.094 (2), 90
V (Å^3)	7008.7 (2)	10213.7 (3)	8200.2 (5)
Z	4	12	4
D_x (Mg m^{-3})	1.347	1.232	1.328
Crystal size (mm)	0.20 × 0.13 × 0.10	0.26 × 0.14 × 0.07	0.38 × 0.36 × 0.24
Absorption correction	Multi-scan	Multi-scan	Multi-scan
T_{min}	0.616	0.689	0.52
T_{max}	1	1	0.745
No. of measured, independent and observed reflections	68295, 13901, 9847	50108, 6781, 4322	52898, 8558, 6689
θ_{max} (°)	73.4	73.3	20.9
$R[F^2 > 2\sigma(F^2)]$, $wR(F^2)$, S	0.085, 0.244, 0.90	0.058, 0.180, 0.75	0.071, 0.155, 1.16
No. of parameters	900	393	988
H-atom treatment	Riding	Mixture of independent and constrained refinement	Riding
Δr_{max}, Δr_{min} (e Å^{-3})	1.28, −0.65	0.81, −0.42	0.46, −0.31

Table A2.1 : Crystal data for H_4L and its bimetallic cofacial complexes.

	$[Li(THF)_4][Zn_2(\mu\text{-}OH)(L)].2THF$	$[^nBu_4N][Zn_2(\mu\text{-}OH)(L)]$	$[Li(THF)_4][ZrCl_5(THF)]$
Cell setting, space group	Triclinic, *P*-1	Monoclinic, $P2_1/n$	Monoclinic, $P2_1/n$
a, b, c (Å)	11.9461 (4), 13.4711 (4), 23.2772 (8)	20.593 (3), 15.3523 (17), 21.653 (3)	10.267 (5), 16.288 (5), 17.848 (5)
α, β, γ (°)	79.147 (2), 77.062 (2), 83.350 (2)	90, 111.061 (7), 90	90.000 (5), 106.217 (5), 90.000 (5)
V (Å^3)	3574.9 (2)	6388.2 (13)	2865.9 (18)
Z	2	4	4
D_x (Mg m^{-3})	1.342	1.297	1.474
Crystal size (mm)	0.68 × 0.35 × 0.12	0.57 × 0.34 × 0.10	0.20 × 0.10 × 0.10
Absorption correction	Multi-scan	Multi-scan	Multi-scan
T_{min}	0.599	0.547	0.852
T_{max}	0.745	0.745	1
No. of measured, independent and observed reflections	34379, 14542, 11705	50481, 12934, 11069	46463, 9676, 8277
θ_{max} (°)	26.4	26.4	32.2
$R[F^2 > 2\sigma(F^2)]$, $wR(F^2)$, S	0.050, 0.120, 1.05	0.105, 0.208, 1.34	0.024, 0.063, 1.05
No. of parameters	348	787	289
H-atom treatment	Mixture of independent and constrained refinement	Mixture of independent and constrained refinement	Mixture of independent and constrained refinement
Δr_{max}, Δr_{min} (e Å^{-3})	0.72, −0.37	1.22, −0.90	0.56, −0.76

Table A2.1 : Crystal data for H_4L and its bimetallic cofacial complexes.

Appendix 3 – Selected bond lengths and angles for H_4L and its binuclear cofacial complexes.

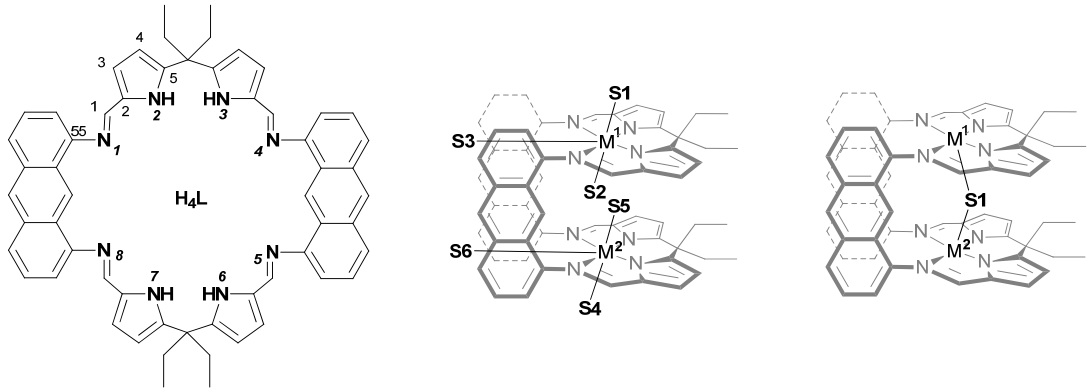

Figure A3.1 : representation of H_4L with partial numbering scheme (left) for nitrogen (bold italic) and carbon (standard font), representation of a bimetallic cofacial complex of L with numbering scheme for the metals and the extra ligands in the general case (middle) and in the case of a single bridging ligand. (right).

Following pages:

Table A3.1: Selected bond lengths and angles for H_4L and its bimetallic cofacial complexes determined by X-ray crystallography.

	H_4L	$[Mg_2(endo\text{-}Py)(exo\text{-}Py)_2(L)]$	$[Pd_2(L)]$	$[Fe_2(\mu\text{-}O)(L)]$	$[(UO_2)_2(Py)_2(L)]$
N1-C1	1.270 (6)	1,321 (3)	1.325 (8)	1.305 (2)	1.322 (9)
N1-C55	1.422 (6)	1,419 (3)	1.416 (7)	1.430 (2)	1.425 (9)
C1-C2	1.427 (7)	1,417 (3)	1.399 (10)	1.408 (3)	1.402 (10)
C2-C3	1.380 (6)	1,399 (3)	1.398 (9)	1.398 (3)	1.394 (10)
N2-C2	1.380 (5)	1,378 (3)	1.373 (7)	1.376 (2)	1.399 (8)
N2-C5	1.361 (6)	1,1,345 (3)	1.361 (8)	1.355 (2)	1.347 (9)
C3-C4	1.406 (7)	1,393 (4)	1.373 (10)	1.387 (3)	1.374 (10)
C4-C5	1.370 (6)	1,411 (3)	1.405 (8)	1.406 (3)	1.423 (10)
M1-N1	-	2,147 (2)	2.082 (5)	2.1574 (16)	2.558 (6)
M1-N2	-	2,063 (2)	1.933 (5)	2.0477 (15)	2.417 (6)
M1-N3	-	2,051 (2)	1.927 (5)	2.0395 (15)	2.430 (6)
M1-N4	-	2,210 (2)	2.068 (4)	2.1483 (15)	2.595 (6)
M2-N5	-	2,224 (2)	-	2.1993 (17)	2.542 (6)
M2-N6	-	2,077 (2)	-	2.0180 (17)	2.423 (6)
M2-N7	-	2,068 (2)	-	2.0382 (17)	2.415 (5)
M2-N8	-	2,242 (2)	-	2.1423 (17)	2.570 (6)
M1-S1	-	2,147 (2)	-	1.7986 (12)	1.779 (4)
M1-S2	-	-	-	-	1.747 (4)
M1-S3	-	-	-	-	2.610 (6)
M2-S4	-	2,264 (2)	-	1.7955 (12)	1.778 (4)
M2-S5	-	2,264 (3)	-	-	1.764 (4)
M2-S6	-	-	-	-	2.566 (6)
S2-S5	-	-	-	-	-
M1•••M2	-	6,272 (1)	5.377 (1)	3,5880 (5)	5,6994 (3)
C1-N1-C55	115.9 (4)	118.00 (19)	119.3 (5)	115.70 (15)	120,2 (6)
N1-M1-N2	-	78.28 (8)	80.4 (2)	78.36 (6)	69,0 (2)
N2-M1-N3	-	80.24 (8)	87.7 (2)	78.65 (6)	70,3 (2)
N3-M1-N4	-	78.39 (8)	81.03 (18)	77.25 (6)	67,9 (2)
N4-M1-N1	-	117.02 (8)	110.7 (2)	99.97 (6)	150,8 (2)
M1-S1-M2	-	-	-	173.33 (8)	-
N4-M1-S3	-	-	-	-	72,8 (2)
NS3-M1-N1	-	-	-	-	83,9 (2)
	-	**S1 = N11, S4 = N10, S5 = N9**	-	**S1 = O1**	**S1 = O2, S2 = O1, S3 = N9, S4 = O4, S5 = O3, S6 = N10**

	$[Co_2(exo\text{-}THF)_2(L)][Co_2(L)]$	$[Co_2(exo\text{-}Py)_2(L)]$	$[Co_2(\mu\text{-}O_2H_3)(exo\text{-}Py)_2(L)]$
N1-C1	1.329 (5) / 1.331 (5)	1.318 (5)	1.319 (4)
N1-C55	1.433 (6) /1.439 (5)	1.419 (5)	1.431 (4)
C1-C2	1.413 (6) / 1.403 (6)	1.403 (6)	1.403 (5)
C2-C3	1.400 (6) /1.405 (6)	1.395 (6)	1.399 (5)
N2-C2	1.375 (5) / 1.375 (5)	1.375 (5)	1.383 (4)
N2-C5	1.341 (6) / 1.345 (5)	1.341 (5)	1.346 (4)
C3-C4	1.394 (7) / 1,394(6)	1.388 (6)	1.389 (5)
C4-C5	1.427 (6) / 1,415(6)	1.419 (6)	1.407 (5)
M1-N1	1.998 (4) / 1.976 (4)	2.013 (3)	1.990 (3)
M1-N2	1.876 (4) / 1.846 (3)	1.881 (4)	1.859 (3)
M1-N3	1.861 (4) / 1.855 (4)	1.875 (3)	1.865 (3)
M1-N4	2.001 (3) / 1.967 (3)	2.013 (4)	2.049 (3)
M2-N5	2.033 (4) / 1.956 (3)	2.009 (3)	-
M2-N6	1.869 (4) / 1.856 (4)	1.873 (4)	-
M2-N7	1.867 (4) / 1.841 (3)	1.871 (4)	-
M2-N8	1.979 (3) / 1.965 (4)	2.008 (3)	-
M1-S1	2.001 (3) / -	2.146 (4)	1.973 (3)
M1-S2	-	-	1.929 (2)
M1-S3	-	-	-
M2-S4	2.243 (3) / -	2.142 (4)	-
M2-S5	-	-	-
M2-S6	-	-	-
S2-S5	-	-	2,455 (5)
M1•••M2	5,710 (2) / 5,471 (2)	5,8374 (9)	5,5739 (7)
C1-N1-C55	117.3 (4) / 114.9 (3)	117.1(3)	120,4 (3)
N1-M1-N2	82.51 (15) / 83.17 (15)	82.0(1)	83,4 (1)
N2-M1-N3	86.81 (15) / 87.27 (15)	86.8(1)	87,8 (1)
N3-M1-N4	83.04 (15) / 83.17 (15)	82.3(1)	82,5 (1)
N4-M1-N1	107.45 (14) / 106.37 (14)	107.1(1)	106,1 (1)
M1-S1-M2	-	-	-
N4-M1-S3	-	-	-
NS3-M1-N1	-	-	-
	S1 = O1, S4 = O2	**S1 = N9, S4 = N10**	**S1 = N9, S4 = O1, S2/S5 = $(O_2H_3)^-$**

	$[K(THF)_6][Zn_2(\mu\text{-}Cl)(L)]$	$[Li(THF)_4][Zn_2(\mu\text{-}OH)(L)]$	$[^nBu_4N][Zn_2(\mu\text{-}OH)(L)]$
N1-C1	1.307 (8)	1.309 (3)	1.293 (7)
N1-C55	1.425 (8)	1.416 (3)	1.415 (8)
C1-C2	1.402 (9)	1.411 (4)	1.416 (8)
C2-C3	1.389 (9)	1.403 (4)	1.398 (8)
N2-C2	1.374 (8)	1.372 (3)	1.376 (7)
N2-C5	1.320 (8)	1.345 (3)	1.351 (7)
C3-C4	1.366 (9)	1.382 (4)	1.383 (9)
C4-C5	1.434 (9)	1.410 (4)	1.413 (8)
M1-N1	2.155 (6)	2.176 (2)	2.411 (5)
M1-N2	2.023 (5)	2.075 (2)	2.031 (5)
M1-N3	2.024 (5)	2.032 (2)	2.105 (5)
M1-N4	2.186 (5)	2.261 (2)	2.139 (4)
M2-N5	2.156 (5)	2.188 (2)	2.160 (5)
M2-N6	2.019 (5)	2.079 (2)	2.057 (5)
M2-N7	2.040 (5)	2.036 (2)	2.050 (5)
M2-N8	2.197 (5)	2.255 (2)	2.347 (5)
M1-S1	2.3462 (18)	1.9625 (18)	1.978 (4)
M1-S2	-	-	-
M1-S3	-	-	-
M2-S4	2.3398 (18)	1.9620 (18)	1.969 (4)
M2-S5	-	-	-
M2-S6	-	-	-
S2-S5	-	-	-
M1•••M2	4,532 (1)	3,9814 (5)	3,871 (1)
C1-N1-C55	117,9 (5)	116.7 (2)	115.3 (5)
N1-M1-N2	78,6 (2)	79.13 (8)	76.05 (18)
N2-M1-N3	81,9 (2)	80.81 (9)	81.78 (18)
N3-M1-N4	78,9 (2)	77.29 (9)	79.34 (19)
N4-M1-N1	103,8 (2)	97.47 (8)	95.66 (17)
M1-S1-M2	150,54 (8)	165.11 (12)	157.4 (3)
N4-M1-S3	-	-	-
NS3-M1-N1	-	-	-
	S1 = Cl^-	**S1 = OH^-**	**S1 = OH^-**

Appendix 4 – Abstracts of the publications based on the work presented.

Part of the content of this thesis, has been published or will be published as the peer reviewed publications cited below:

Ligand Modifications For Tailoring The Binuclear Microenvironment In Schiff-Base Calixpyrrole Pacman Complexes**

E. Askarizadeh, A. M. J. Devoille, D. M. Boghaei, A. M. Z. Slawin, and J. B. Love,* *Inorg. Chem.*, 2009, **48**, 7491.

** E. Askarizadeh and A. M. J. Devoille contributed equally to this work.

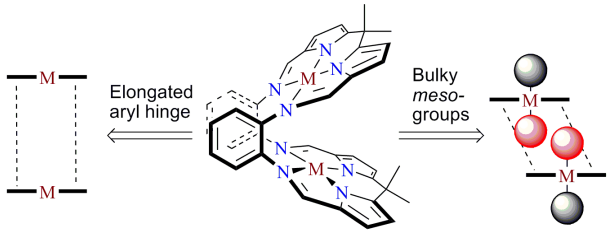

ABSTRACT.† The synthesis and structures of two new octadentate, Schiff-base calixpyrrole macrocycles are presented in which modifications at the *meso*-substituents (L^{10}) or the aryl spacer between the two pyrrole-imine donor compartments (L) are introduced. The outcomes of these changes are highlighted in the structures of binuclear Pacman complexes of these macrocycles, [$M_2(L^{10})$] and [$M_2(L)$]. Both palladium and cobalt complexes of the fluorenyl-*meso*-substituted macrocycle H_4L^{10} adopt rigid, but laterally twisted geometries with enclosed bimetallic microenvironments; a consequence of this spatial constraint is an *exo*-*exo*-bonding mode of pyridine in the dicobalt complex [$Co_2(py)_2(L^{10})$]. In contrast, the use of an anthracenyl backbone between the two donor compartments (H_4L) generates a binuclear palladium complex in which the two PdN_4 environments are approximately cofacial and separated by 5.3 Å, so generating a bimetallic complex that is structurally very similar to binuclear compounds of cofacial diporphyrins.

† Compared to the published abstract, the notations have been modified in agreement with those used within this thesis.

Double-Pillared Cobalt Pacman Complexes: Synthesis, Structures and Four-Electron Oxygen Reduction Catalysis

A. M. J. Devoille, F. White and J. B. Love,* *Manuscript submitted*, 2011.

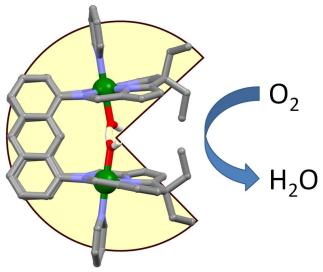

ABSTRACT. The syntheses and structures of binuclear cobalt complexes of a double-pillared cofacial Schiff-base pyrrole macrocycle (L) were determined and their activity as catalysts for the oxygen reduction reaction evaluated. The new binuclear cobalt complex, [Co_2(L)], was formed in good yield using a salt-elimination method and was characterized as adopting a cofacial structure in solution by ^{1}H NMR spectroscopy and as its THF and pyridine solvates in the solid state by X-ray crystallography. Using a variety of spectroscopic techniques, this complex was found to react reversibly with dioxygen, forming a paramagnetic complex that was assigned tentatively as the superoxo cation by EPR spectroscopy. In acidified benzonitrile solution, [Co_2(L)] was shown to act as a catalyst for the selective four-electron reduction of dioxygen to water and showed large improvement in efficacy compared to its *o*-phenylene Schiff-base analogues, becoming comparable to that exhibited by single-pillared cofacial diporphyrin complexes.

Selective Anion Binding by a Cofacial Binuclear Zinc Complex of a Schiff-Base Pyrrole Macrocycle

A. M. J. Devoille, P. Richardson, N. Bill, J. L. Sessler, and J B. Love*, *Inorg. Chem.*, 2011, **50**, 3116.

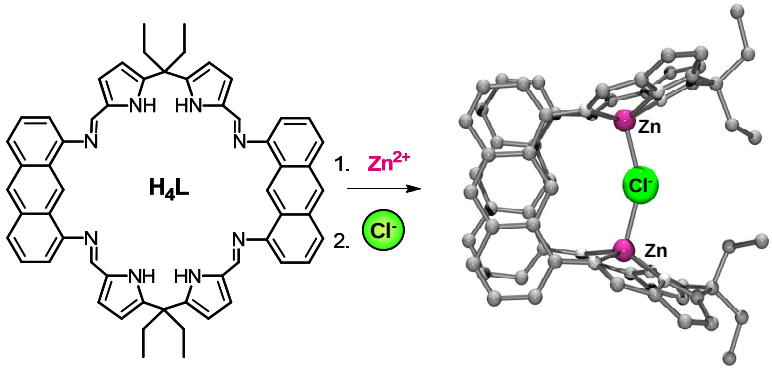

ABSTRACT. The synthesis of the new cofacial binuclear zinc complex $[Zn_2(L)]$ of a Schiff-base pyrrole macrocycle is reported. It was discovered that the binuclear microenvironment between the two metals of $[Zn_2(L)]$ is suited for the encapsulation of anions, leading to the formation of $[K(THF)_6][Zn_2(\mu\text{-}Cl)(L)].2THF$ and $[Bu^n{}_4N][Zn_2(\mu\text{-}OH)(L)]$ which were characterized by X-ray crystallography. Unusually obtuse Zn-X-Zn angles (X = Cl: 150.54(9)° and OH: 157.4(3)°) illustrate the weak character of these interactions and the importance of the cleft pre-organization to stabilize the host. In the absence of added anion, aggregation of $[Zn_2(L)]$ was inferred and investigated by successive dilutions and by the addition of coordinating solvents to $[Zn_2(L)]$ solutions using NMR spectroscopy as well as isothermal microcalorimetry (ITC). On anion addition, evidence for de-aggregation of $[Zn_2(L)]$, combined with the formation of the 1:1 host-guest complex, was observed by NMR spectroscopy and ITC titrations. Furthermore, $[Zn_2(L)]$ binds to Cl^- selectively in THF as deduced from the ITC analyses, while other halides induce only de-aggregation. These conclusions were reinforced by DFT calculations, which indicated that the binding energies of OH^- and Cl^- were significantly greater than for the other halides.